^{31}P Nuclear Magnetic Resonance Spectroscopy Studies of Cardiac Energetics and Function in the Perfused Rat Heart

Vol. 1

by

Richard Glenn Stevens Spencer

B.A., University of California at Berkeley
(1977)

M.A., University of California at Berkeley
(1981)

SUBMITTED TO THE DEPARTMENT OF
MEDICAL ENGINEERING AND MEDICAL PHYSICS
IN PARTIAL FULFILLMENT OF THE REQUIREMENTS FOR THE DEGREE OF

DOCTOR OF PHILOSOPHY
IN
MEDICAL PHYSICS

at the

MASSACHUSETTS INSTITUTE OF TECHNOLOGY

April 1987

Signature of Author _____
Department of Medical Engineering and Medical Physics
April 1987

Certified by _____
Associate Professor Joanne S. Ingwall
Thesis Supervisor

Accepted by _____
Professor Roger G. Mark
Co-Director of the Harvard-MIT Division of
Health Sciences and Technology

DEDICATION

To My Parents

For Their Unlimited Love and Support
Throughout the Years

and

To My Wife

For Her Help and Understanding

Habe nun, ach! Philosophie,
Juristerei und Medizin
Und leider auch Theologie
Durchaus studiert, mit heißem Bemühn.
Da steh ich nun, ich armer Tor,
Und bin so klug als wie zuvor!
Heiße Magister, heiße Doktor gar
Und ziehe schon an die zehen Jahr
Herauf, herab und quer und krumm
Meine Schüler an der Nase herum--
Und sehe, daß wir nichts wissen können!

Johann Wolfgang Goethe
Faust, Erster Teil, Nacht

I have pursued, alas, philosophy,
Jurisprudence, and medicine,
And, help me God, theology,
With fervent zeal through thick and thin,
And here, poor fool, I stand once more,
No wiser than I was before.
They call me Magister, Doctor, no less,
And for some ten years, I would guess,
Through ups and downs and tos and fros
I have led my pupils by the nose--
And see there is nothing we can know!

Johann Wolfgang Goethe
Faust, Part One, Night
Translated by Walter Arndt

ACKNOWLEDGEMENTS

It has been my very good fortune to carry out this research in the Harvard Medical School Nuclear Magnetic Resonance Laboratory, under the direction of Joanne Ingwall. To her I offer my sincere thanks, for her careful guidance of my work, her willingness to move in new directions, and her (almost) infinite patience.

Scientific cooperation and personal camaraderie among denizens of the NMR lab have contributed in no small measure to making my tenure there enjoyable and productive. I would particularly like to thank Jim Balschi and John Bittl for invaluable assistance and discussion.

I am grateful to my Thesis Committee, W. Grossman, M. Kushmerick, L. Neuringer, and F. Villars, for their reading of my thesis and for their comments. Productive collaboration with James Scheuer and Peter Buttrick is also acknowledged.

I would also like to acknowledge three of my early mentors, Chun-Ming Leung, then of the National Radio Astronomy Observatory in Charlottesville, Virginia, Jon Arons, in the Department of Astronomy at U.C. Berkeley, and especially Allan Kaufman, in the Department of Physics at Berkeley. These individuals' impeccable scientific standards and personal integrity provided me with the most favorable possible start in research.

My home computer was tamed largely through the tireless efforts of Herb Gordon; the hours he devoted to this task are much appreciated.

My wife, Christine, has put up with a variety of privations as a result of this work. To her go my thanks and my love.

TABLE OF CONTENTS

^{31}P NMR Spectroscopy Studies of Cardiac Energetics and Function in the Perfused Rat Heart

by

Richard Glenn Stevens Spencer

31P nuclear magnetic resonance (NMR) spectroscopy provides the ability to measure the concentration and turnover of high-energy phosphate compounds in the heart while simultaneously assessing hemodynamic function. Thus, relationships between cardiac function and metabolism may be investigated directly.

ATP is the dominant substrate for energy-dependent processes in the heart, while creatine phosphate (CP), through the creatine kinase (CK) reaction, serves the function of an energy buffer, allowing ATP levels to be maintained at times of acute stress. In terms of phosphorus flux, the CK reaction is the dominant reaction in which ATP participates. Measurements of flux through the CK reaction in the isolated perfused heart using the NMR technique of saturation transfer have shown that the flux towards ATP synthesis is greater than that towards CP synthesis. Explanations for this apparent violation of detailed balance include metabolic compartmentation, and the participation of ATP in reactions besides ones catalyzed by CK. Direct tests of these hypotheses have been difficult, because the conventional magnetization transfer techniques widely employed in NMR spectroscopy to assess reaction kinetics cannot be applied to systems of coupled reactions. Accordingly, an extension of this technique, double saturation transfer, has been developed which can be applied to systems with competing reactions. Applied to the CK system, we find that ATP homeostasis can be directly demonstrated by using our double saturation technique to properly account for myofibrillar ATPase and mitochondrial ATP synthesis reactions. In addition, our results indicate that exchange between CP and NMR-invisible, saturable, ATP is not a dominant component of the CK reactions in the heart; thus, we may expect that overall ATP concentration as measured by NMR reflects the functional energetic status of the heart.

In order to achieve quantitatively reliable, high-time-resolution measurements of physiologic samples, signal-to-noise (S/N) considerations are paramount. One common method of increasing S/N is to allow partial saturation of spectral resonances during data acquisition. This partial saturation can be accounted for using saturation factors to obtain correct abundances only if the measured metabolites are not undergoing chemical exchange. In general, this is not the case in organ physiology. Accordingly, we have developed the theory of saturation factors in the presence of chemical exchange. We find that the error which results from neglect

of exchange depends on: 1) the changes in the ratio of metabolite abundances, 2) the reaction rate, 3) the difference in T_1's of the exchanging metabolites, and 4) the interpulse delay and flip angle used.

Based on the preceding considerations, we have used ^{31}P NMR spectroscopy to study two important problems of modern cardiac physiology: cardiac hypertrophy and diastolic function. Recent clinical studies indicate that diastolic dysfunction, which is often a prominent feature of hypertrophy, may be as important as systolic dysfunction as a cause of congestive heart failure.

Cardiac hypertrophy may represent a state of diminished cardiac reserve rather than a state of inability to function under normal conditions. Accordingly, we compared the response to prolonged global hypoxia of normal rat hearts and rat hearts which had hypertrophied secondary to chronic hypertension. During hypoxia, [ATP] was an excellent predictor of diastolic (but not systolic) dysfunction, while [CP] was an excellent predictor of systolic (but not diastolic) dysfunction. Further, the additional diastolic stiffening due to hypertrophy could be accounted for by increased muscle mass, without the need to invoke a defect in high-energy phosphate metabolism. This is consistent with the parallel replication of normal sarcomeres which may occur in pressure-overload hypertrophy.

Cardiac hypertrophy also occurs secondary to exercise. If a diastolic defect proportional to increased muscle mass occurs in this setting as well, it would be strong evidence for a maladaptation of exercised hearts. Instead, we found that hearts from animals exercised by chronic swimming exhibited a marked preservation of diastolic function during prolonged global hypoxia. This result could not be explained by preservation of metabolic energy stores or by the series replication of sarcomeres which may occur in volume-overload hypertrophy. To test other possible mechanisms, we also performed kinetic studies using saturation transfer, and biochemical analyses of cardiac enzymes, in this model of exercise hypertrophy. Although we found small increases in the rate constant of the CK reaction and in mitochondrial CK activity, these changes may be too small to adequately account for the improved diastolic performance of the hearts from exercised animals.

These studies showed a direct relationship between loss of ATP and impaired diastolic function during hypoxia. However, the rate of ATP depletion was unchanged for either type of hypertrophy, so that we could not directly demonstrate that attenuation of hypoxic diastolic dysfunction accompanies preservation of ATP. By superimposing a negative inotropic intervention (mild acidosis) on the hypoxic state, we were able to demonstrate this.

Thesis Supervisor: Dr. Joanne Ingwall, Associate Professor of Physiology and Biophysics in the Department of Medicine, Harvard Medical School

Introduction

Cardiac biochemistry encompasses an exceedingly wide range of processes. These range in scale from the organ level, where the overall neurohormonal regulation of cardiac function is exerted by the intact organism, to the submolecular level of myosin light-chain control of contractile protein ATPase activity. However, despite the complexity of cardiac function, the ultimate purpose of the heart is to pump, and the sine qua non of this activity is energy. Chemical energy is provided to tissues in a variety of forms. For example, the heart preferentially metabolizes circulating free fatty acids, but it has considerable adaptability with respect to substrate. However, in spite of this vast potential for heterogeneity of metabolic input, it is part of the general plan of metabolic processes to produce a single class of compounds, the high-energy phosphates, whose hydrolysis provides energy for active cellular function.

Of the various high-energy phosphate compounds found in the heart, ATP is the metabolite which is most directly related to function. The production and utilization of this compound are both highly regulated and highly sensitive to cardiac functional demands. Phosphocreatine (PCr) is the next-most important high-energy phosphate in the heart. At the least, it serves as an energy buffer, allowing ATP levels to be maintained during times of acute stress through the creatine kinase (CK) reaction

$$ADP + PCr \underset{\longleftarrow}{\overset{\longrightarrow}{\rightleftharpoons}} ATP + Cr$$

between ATP and PCr. In terms of phosphorus flux, the CK reaction is, moreover, the dominant reaction in which ATP participates. Thus, an understanding of the role of PCr and of the properties of the CK reaction is an essential part of the understanding of cardiac biochemistry.

In recent years, ^{31}P nuclear magnetic resonance (NMR) spectroscopy has proved to be an extraordinarily versatile

technique for studying cardiac physiology, primarily because it provides the ability to monitor phosphate metabolites of physiologic significance while simultaneously assessing hemodynamic function. Thus, relationships between cardiac function and metabolism may be investigated directly. In this context, it is worth commenting on the exceptional nature of the relationship between function and metabolism in the heart. In no other organ can these two aspects of overall activity be so readily distinguished. For example, in the kidney, liver, or brain, function and biochemistry are largely one and the same, i.e., the main function of the organ <u>is</u> biochemical. In the heart, on the other hand, biochemical activity is to a great extent subservient to mechanical activity; the purpose of cardiac biochemistry is to provide energy for cardiac function. It is precisely this fact that lends to cardiac physiology its exceptional richness and fascination. It is also a prime reason that NMR studies of the heart, allowing simultaneous assessment of function and metabolism, can be so illuminating.

NMR spectroscopy has the capability of providing insight into metabolic processes at two distinctly different levels, through the use of kinetic and steady-state techniques.

Kinetic experiments may be performed to study reaction rates and metabolite fluxes through reactions in steady-state systems. In effect, this constitutes an assessment of the instantaneous behavior of a dynamic system. NMR is unique in its ability to provide such kinetic data on specific, enzyme-catalyzed reactions in whole organs and living systems. Chemical fluxes can thereby be directly related to the physiologic state of the preparation. On the other hand, standard biochemical techniques for studying isolated reactions <u>in vitro</u>, involving, for example, radioactive tracer uptake, generally use homogeneous tissue preparations as samples. Thus, biochemical studies are highly controlled and versatile, but lack the physiologic context of whole-

organ studies. Therefore, these two general types of kinetic studies, NMR and biochemical, are complementary.

Steady-state NMR can be used to provide measurements of net metabolite abundances. In general terms, this may be thought of as an integration with respect to time of kinetic measurements. However, it is more than that, because the system need not be in a steady state for these types of studies. The time evolution of metabolite abundances can therefore be followed after pharmacologic or other interventions. In this role, NMR is not unique, since such serial measurements of metabolites have been performed for decades using standard biochemical techniques. However, NMR still provides tremendous advantages in certain instances. While standard biochemical techniques require the destruction of the sample prior to measurement, NMR measurements are non-invasive, so that the same preparation may be followed throughout the length of the experiment. With NMR, then, not only does each sample serve as its own control, but it also becomes practical to accumulate measurements with reasonably high temporal resolution since each sample can be studied for the duration of the protocol. This eliminates the need to prepare separate samples for each time point. Consider, for example, an experiment in which a control measurement is followed by measurements every three minutes, for 24 minutes, after an intervention. Such an experiment is described in Chapter 3, Part 1, in which measurements are performed on a total of 14 hearts using NMR. To accumulate the equivalent data using a destructive technique such as freeze clamping, 126 hearts, as opposed to the 14 actually used, would be required. This ability to obtain high temporal resolution with NMR is especially important in relating function to metabolism, and so can be used to great advantage in studies of the heart. Finally, we mention that NMR provides the ability to monitor non-invasively true intracellular pH during the course of an experiment; again, this capability is of considerable importance in studies of cardiac physiology.

Next, we briefly summarize the methods used in this Thesis. The NMR system consists of an Oxford Instruments 360 wide-bore superconducting magnet (field strength 8.45 Tesla) interfaced with a Nicolet 1280 spectrometer. The phosphorus spectra obtained allow the measurement of relative abundances of ATP, PCr, and inorganic phosphate. In addition, intracellular pH is monitored by measurement of the chemical shift between phosphocreatine and inorganic phosphate.

Hearts are perfused retrograde through the aorta by phosphate-free Krebs-Henseleit buffer, gassed with a mixture of O_2, N_2, and CO_2, depending on the oxygenation and pH desired. The system may be configured for either constant-pressure or constant-flow-rate perfusion. A water-filled latex balloon is inserted into the left ventricle of the perfused heart through an incision in the left atrium, via the mitral valve, to permit hemodynamic measurements. These measurements are obtained via a water-filled tube running from the intraventricular balloon to a Stratham pressure transducer, producing a continuous record of systolic and end-diastolic pressure and heart rate, which are recorded on a Hewlett-Packard chart recorder. Coronary flows are measured either by timed collection of coronary effluent or with an in-line flow gauge. See Figure 1.

We now describe the specific applications we have made of ^{31}P NMR spectroscopy to further elucidate the relationship of cardiac function to high-energy phosphate metabolism.

In measurements of flux through the CK reaction in the isolated perfused heart using the NMR technique of saturation transfer, it has been consistently found that the flux towards ATP synthesis is greater than that towards PCr synthesis. This result is in apparent violation of detailed balance. Plausible explanations for this apparent paradox include certain types of metabolic compartmentation, in which ATP exists in two (or more) separate pools in the myocyte which have different exchange properties with PCr, and the participation of ATP in many other reactions besides the one

catalyzed by CK. Direct tests of these hypotheses have been difficult, because the conventional magnetization transfer techniques widely employed in NMR spectroscopy to assess reaction kinetics can only be applied to systems of coupled reactions in certain restrictive circumstances. To overcome this limitation, we have developed a technique, called double saturation transfer, which can be applied to systems with competing reactions. This is described in Chapter 1. Applied to the CK system, we found that ATP homeostasis could be directly demonstrated using our double saturation technique to properly account for myofibrillar ATPase and mitochondrial ATP synthesis reactions.

The ability to describe ATP homeostasis in the heart in this way provides an important step in the validation of steady-state NMR measurements of metabolite concentrations. If exchange between PCr and an NMR-invisible pool of ATP were a dominant feature of the kinetics of ATP reactions, then the interpretation of overall abundance measurements would be complicated enormously. Our results provide support for the notion that overall ATP concentration measurements do indeed reflect the functional energetic status of the heart. Thus, we may make steady-state measurements with some confidence in their relevance to cardiac energetics.

In order to make high-quality steady-state measurements of physiologic samples, such as the perfused hearts used in this Thesis, signal-to-noise (S/N) considerations are paramount. Reasons for this include, first of all, the fact that the preparations themselves are always more or less unstable, so that speed in obtaining the required measurements is essential. In addition, for experiments which follow the time course of metabolic changes following an intervention (such as hypoxia), high time-resolution is desirable. This is important in the hypoxia studies we will describe, for example, because of our interest in developing explicit functional relationships between cardiac mechanical performance and metabolic state during hypoxia. These

relationships can be constructed only from data having high temporal resolution, so that data points do not represent simply the time-average of very different physiologic states. Finally, to establish such quantitative relationships, it is obviously essential to have quantitatively reliable data, and high S/N facilitates this as well.

One way in which S/N is commonly increased is to allow partial saturation of spectral resonances during data acquisition. This occurs when the interpulse delay time is insufficient to allow complete relaxation of nuclear spins between pulses. Partial saturation can be accounted for by using saturation factors to obtain correct abundances only if the measured metabolites are not undergoing chemical exchange, as has been assumed in previous treatments of saturation factors. While this may be the case for many NMR applications in organic chemistry and solution biochemistry, it is in general not true for intact organ physiology.

Accordingly, we have developed the theory of saturation factors in the presence of chemical exchange, as described in Chapter 2. This treatment extends the powerful S/N enhancement technique of saturation factors so that it may be properly applied to systems with exchange. We found that chemical exchange alters the fundamental character of the problem, in that it causes the magnitude of saturation factors to be dependent on metabolite abundances. Neglect of this fact results in an error in abundance calculations, whose magnitude depends on the reaction rate, on the difference in T_1's of the exchanging metabolites, on the changes in the ratio of metabolite abundances, and on the interpulse delay and flip angle used. In contrast, our development allows for a rigorous treatment of saturation factors so that abundances may be determined accurately.

Two of the outstanding problems of modern cardiac physiology are the understanding of cardiac hypertrophy and diastolic function. While the hypertrophy which accompanies certain pathologic states has long been recognized as an

extremely important cardiac adaptation, with both beneficial and deleterious aspects, the importance of diastolic function has come to be appreciated only recently. In fact, recent clinical studies suggest that diastolic dysfunction may be as important a factor as systolic dysfunction in the etiology of congestive heart failure. Furthermore, the problem of hypertrophy is linked to this by the fact that such diastolic dysfunction is very often found in the setting of cardiac hypertrophy.

Hypoxia is an appropriate setting to study the function of hypertrophied hearts because cardiac hypertrophy may represent a state of diminished cardiac reserve, rather than a state of inability to function under normal conditions. In fact, it is likely that the clinically important increased susceptibility of pathologically hypertrophied hearts to ischemic injury is a manifestation of a variety of cellular and organ-level alterations which accompany the hypertrophy process. To study this, we performed experiments, described in Chapter 3, Part 1, comparing the response to prolonged global hypoxia of normal rat hearts and rat hearts which had hypertrophied secondary to chronic hypertension. In this investigation, we were especially interested in alterations in the relationship between metabolic and functional deficits which may occur in the state of mild compensated hypertrophy, with particular emphasis on diastolic function. We found that during hypoxia, for both control and hypertrophied hearts, [ATP] was an excellent predictor of diastolic (but not systolic) dysfunction, while [PCr] was an excellent predictor of systolic (but not diastolic) dysfunction. In addition, we found that the additional diastolic stiffening exhibited by the hypertrophied hearts could be accounted for by their increased muscle mass, without the need to invoke a defect in high-energy phosphate metabolism. This is consistent with the parallel replication of normal sarcomeres which may occur in pressure-overload hypertrophy.

Cardiac hypertrophy occurs not only in pathologic states, but also secondary to exercise. Because the diastolic defect seen in the pathologically hypertrophied rat hearts appears to be a direct result of their increased mass, we examined the response to hypoxia of hypertrophied hearts from rats which had been trained by chronic swimming. These experiments are described in Chapter 3, Part 2. If we had again found a diastolic defect proportional to increased muscle mass, this would be strong evidence for a maladaptation of exercised hearts. Instead, we found that the hearts from exercised animals exhibited a marked preservation of diastolic function during prolonged global hypoxia, as compared with controls. This result was independent of mass normalization, and so could not be explained by the series replication of sarcomeres which may occur in volume-overload hypertrophy. To test other possible mechanisms, we performed kinetic studies using the NMR technique of saturation transfer, and biochemical analyses of cardiac enzymes, in this model of exercise hypertrophy, as discussed in Chapter 3, Part 3. Although we found a small increase in the rate constant of the CK reaction and in mitochondrial CK activity, these changes may be too small to adequately account for the improved diastolic performance of the hearts from exercised animals.

These studies showed a direct relationship between loss of ATP and impaired diastolic function during hypoxia. However, the rate of ATP depletion was unchanged for either type of hypertrophy, so that we were unable to directly demonstrate that attenuation of hypoxic diastolic dysfunction accompanies preservation of ATP. In Chapter 4, we describe experiments in which we did demonstrate this by superimposing a negative inotropic intervention (mild acidosis) on the hypoxic state. In addition, we find that the hearts subjected to mild acidosis during hypoxia exhibit markedly improved recovery of function during reoxygenation.

In summary, in this Thesis we have considered the relationship between cardiac function and high-energy phosphate metabolism by using ^{31}P NMR spectroscopy to assess both instantaneous metabolite turnover and time-dependent changes in metabolite concentrations. The problem of detailed balance for reactions involving ATP as a substrate was addressed by developing an extension of standard NMR kinetic techniques. Correctly accounting for chemical exchange was also the underlying motivation for our development of the theory of saturation factors in the presence of exchange. Finally, the ability of NMR spectroscopy to make measurements of metabolite abundances with high temporal resolution was used to develop explicit relationships between functional and metabolic parameters for normal rat hearts and for rat hearts which had undergone either pathologic or physiologic hypertrophy.

Figure 1. Schematic diagram of the isolated heart perfusion apparatus used for this Thesis. The composition of both the buffer in the temperature-controlled reservoir and of the gas with which it is bubbled may be altered to suit the requirements of a particular experimental protocol. Outflow from the reservoir can be either under a constant gravitational pressure head or maintained at a constant flow rate by a variable-speed peristaltic pump. The inflow line to the heart is water-jacketed to maintain the desired temperature. The hearts are perfused directly through the aorta in a retrograde fashion against a competent aortic valve, allowing for perfusion of the coronary arteries and coronary vasculature. A water-filled catheter runs from the left ventricle to a pressure transducer through a side-port, permitting measurement of pressures and heart rate. A glass NMR tube is placed around the heart as shown.

Figure 1

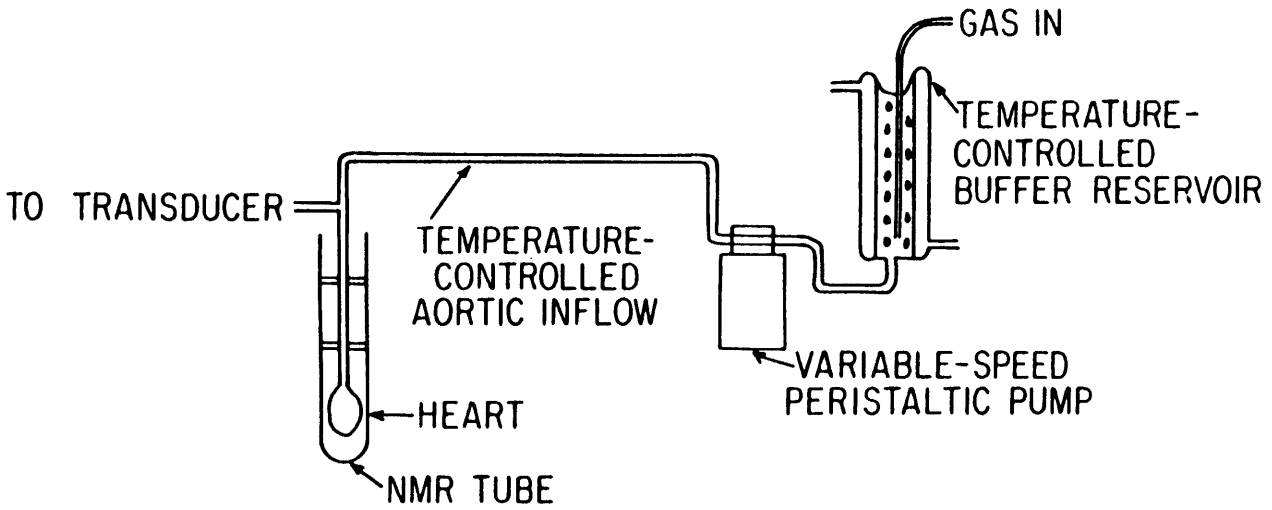
GAS IN
TEMPERATURE-
CONTROLLED
BUFFER RESERVOIR
TO TRANSDUCER
TEMPERATURE-
CONTROLLED
AORTIC INFLOW
VARIABLE-SPEED
PERISTALTIC PUMP
HEART
NMR TUBE

Chapter 1

Double Saturation Transfer Measurements of ATP Synthesis and Degradation in the Perfused Rat Heart at High Workload

Abstract

A limitation of magnetization transfer techniques for studying enzyme kinetics with NMR has been the difficulty of treating systems with more than two exchanging species. This problem was addressed in the original papers on saturation transfer, and since then a number of approaches have been taken to work with these complex situations. Here, we present a simplified method based on the transient saturation transfer experiment in which spin-lattice relaxation time constants and reaction rates are obtained from the same data, and which is particularly suitable for biological samples. We apply the method to evaluate flux balance in the three-site linear exchange network comprised of creatine phosphate, adenosine triphosphate, and inorganic phosphate in the heart.

Introduction

Saturation transfer methods can directly yield kinetic information characterizing two-site exchange when applied to a system in which there are only two reactants, or in which reactions between all but two species may be neglected. In addition, one can by this method obtain the spin-lattice relaxation times, T_1, of both species. However, biologic and other complex chemical systems are frequently characterized by the presence of multiple, competing, reactions. In these cases, application of standard saturation transfer techniques leads to a problem of complicated and ambiguous data analysis in which competing reactions can only be clearly accounted for in certain limiting cases. If competing reactions are significant, moreover, approaches which neglect them can lead to results which are inconsistent with known facts about the system under study. In particular, one may obtain apparent violations of the principle of detailed balance in spite of constant metabolite levels.

Thus, an extension of usual saturation transfer methods is required to account properly for competing reactions. This problem was recognized by Forsén and Hoffman[1], who presented a direct extension of their original theory[2,3] to the N-site system, allowing for simultaneous exchange between each pair of sites. Since then, other work[4,5] which has appeared on the multisite exchange problem has centered on steady-state saturation techniques in which spin-lattice relaxation times are determined in one set of experiments, and then used along with the results of a separate protocol to derive kinetic constants. Both the transient method of Forsén and Hoffman and these steady-state methods extend the single-resonance saturation technique of standard saturation-transfer experiments by saturating two resonances simultaneously. Ugurbil[5,6], adapting the steady-state approach, was the first to apply a multiple saturation technique to an in vivo system, the creatine kinase (CK)

reaction between creatine phosphate (CP) and adenosine triphosphate (ATP) in the perfused rat heart:

$$CP \underset{k_r}{\overset{k_f}{\rightleftharpoons}} ATP$$

The subscripts f and r denote respectively the forward and reverse directions of the reaction with respect to ATP synthesis. This reaction scheme as written may be referred to as the two-site model for phosphorus exchange.

This particular enzyme system has been the subject of a number of recent studies, out of which an apparent paradox has emerged. Nunnally and Hollis[7], Matthews et al.[8], and Bittl and Ingwall[9] all performed saturation transfer experiments in which Γ-ATP or CP was saturated, and all three investigations found that the flux towards ATP synthesis, $F_f = [CP]k_f$, was greater than the flux towards CP synthesis, $F_r = [ATP]k_r$. This result is inconsistent with the known steady-state of these metabolites in the well-oxygenated perfused heart. Because CP participates only in the CK reaction, saturation transfer provides, in principle, a reliable measure of CP breakdown. However, ATP is known to participate in a number of other reactions, the fluxes through which depend on the physiologic state of the heart (e.g., membrane transport and contractile demands). These competing reactions invalidate straightforward saturation transfer measurements of flux from ATP to CP. Therefore, the value obtained for F_f by saturating CP could differ from the value obtained for F_r by saturating Γ-ATP, to a degree dependent upon the relative flux of ATP through competing reactions.

Matthews et al.[8] suggested that participation of ATP in processes besides the CK and ATPase reactions leads to this apparent inequality. However, the method they employed did not allow them to explicitly treat ATPase flux.

Alternatively, Nunnally and Hollis[7] attributed the discrepancy to intracellular compartmentation of ATP.

Ugurbil's work has provided support for the notion that, when treating the CK system in a manner which can explicitly account for competing reactions, the three-site reaction network for phosphorus

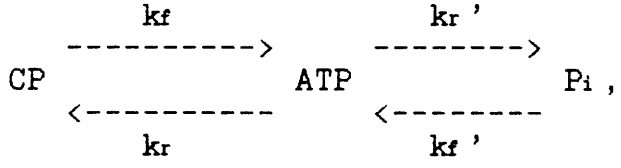

which explicitly includes flux through ATPases, is in fact adequate to describe CK flux measurements.

In this Chapter, we study this same enzymatic system using a variation of the original Forsén and Hoffman transient saturation transfer method, which has two important advantages over steady-state methods for <u>in vivo</u> studies. First, in our transient experiments, the reaction rates and spin-lattice relaxation times are derived from the same data set rather than from data produced in independent experiments. This insures that both quantities reflect the same state of the sample. This is a nontrivial issue, given the inherent instability of most biological samples and the duration of a saturation-transfer experiment. Second, as discussed by Koretsky and Weiner[10], there is a fundamental difference between the T_1's obtained by the two methods if one of the reactants is composed of two NMR-visible pools, one of which is in exchange and another which is not. In this case, as we will show in the next section, steady-state methods will necessarily yield a T_1 which is a hybrid of the T_1's of the two pools, while the reaction rate itself can be derived only if the relative magnitudes of the exchanging and nonexchanging pools are known or assumed, and if the T_1 of the exchanging pool is known. Transient methods, on the other hand, allow for the determination of the true T_1 of the

exchanging pool and of the rate constant of the exchange, uncontaminated by the effects of the nonexchanging pool.

Using a transient saturation technique, we obtain results that are in overall agreement with Ugurbil's, that the three-site reaction scheme above is adequate to describe NMR-derived CK fluxes in the perfused rat heart.

Theory

We will first describe in some detail the steady-state and transient saturation-transfer methods mentioned above, in order to provide motivation for our choice of method. Consider a system of two exchanging species, A and B:

$$1)\qquad A \underset{k_{AB}}{\overset{k_{BA}}{\rightleftharpoons}} B$$

where k_{AB} and k_{BA} denote pseudo-first order rate constants. The Bloch equations for the evolution of this system following a perturbation are

$$2)\quad dM(A)/dt = (M_0(A) - M(A))/T_1(A) - k_{AB}M(A) + k_{BA}M(B)$$

$$3)\quad dM(B)/dt = (M_0(B) - M(B))/T_1(B) - k_{BA}M(B) + k_{AB}M(A)$$

where $T_1(S)$ denotes the longitudinal relaxation time, $M_0(S)$ is the equilibrium magnetization, and $M(S)$ is the instantaneous value of the magnetization, for species S. Saturation transfer methods allow one to avoid fitting data to the solution of these coupled equations, which would require data of much higher quality than is generally available.

In the steady-state form of saturation transfer, a long-time saturation is applied at, for example, B, so that the magnetization at A reaches a new steady-state, which will, from Eq. 2), be given by

$$4)\quad M_{ss}(A)/M_0(A) = (\tau(A)/T_1(A))$$

where $\tau(A)^{-1} = T_1(A)^{-1} + k_{AB}$.

$\tau(A)$ is then determined in a separate experiment, such as an inversion recovery protocol during which B must be continuously saturated so that M(A) evolves according to a

simplified form of Eq. 2) in which the coupling to Eq. 3) has been eliminated:

$$5)\quad dM(A)/dt = (M_0(A) - M(A))/T_1(A) - k_{AB}M(A).$$

The appropriate initial condition for an inversion-recovery experiment is $M(A)(t=0) = -M_0(A)$, and the solution to Eq. 5) is then

$$6)\quad M(A)(t) = M_0(A)[\tau(A)/T_1(A) - (\tau(A)/T_1(A) + 1)\exp(-t/\tau(A))]$$

where t is the recovery time for M(A) between the inversion and the observation pulses. Variable recovery-time data for A can be fit to the monoexponential Eq. 6) to give the time constant $\tau(A)$, and so, with $\tau(A)/T_1(A)$ obtained by using Eq. 4), k_{AB} and $T_1(A)$ can be determined.

In the transient saturation-transfer experiment, closer to the one introduced by Forsén and Hoffman[1,2,3], B is saturated for different lengths of time, during which A again evolves according to Eq. 5), and M(A) is measured at the end of each saturation period. k_{AB} and $T_1(A)$ may now be obtained from a two-parameter fit of the data to the solution of Eq. 5) with the appropriate initial condition $M(A)(t=0) = M_0(A)$:

$$7)\quad M(A)(t) = M_0(A)(1-k_{AB}\tau(A)(1-\exp(-t/\tau(A))))$$

where t is the duration of saturation. Forsén and Hoffman described essentially just this method. They proposed obtaining $\tau(A)$ by writing 7) as

$$8)\quad (M(A) - (\tau(A)/T_1(A))M0(A)) = (1 - \tau(A)/T_1(A))\exp(-t/\tau(A))$$

and fitting the saturation data to a plot of $\log(M(A) - (\tau(A)/T_1(A))M0(A))$ to obtain $\tau(A)$. $\tau(A)/T_1(A)$ is then obtained as above from Eq. 4) following a long-time

saturation at site B. However, the two-parameter fit described above obviates the need to observe this steady-state, resulting in a considerable savings in experimental time.

Both of the saturation-transfer methods described are symmetric in A and B, so that, just as saturation at B gives k_{AB} and $T_1(A)$, saturation at A gives k_{BA} and $T_1(B)$. k_{AB} and k_{BA} contain redundant information for the system 1) , as they are related by the principle of detailed balance:

9) $k_{AB}/k_{BA} = M_0(B)/M_0(A)$.

However, independent derivation of k_{AB} and k_{BA} provides an important check on the validity of the assumed exchange network 1), or, in cases in which the network may be considered known, on the quality of the data. We will consider this point further, in the Discussion.

In order to correctly account for an exchange network more complex than 1), we have developed a simple modification of the transient experiment described above, which resolves the paradox of unequal forward and reverse fluxes through the CK reaction in the perfused heart, and which can be generalized to treat a variety of systems of competing reactions. The experimental method is based on simultaneous saturation transfer from two peaks, and may be described as follows.

Consider the following simple system of competing reactions:

10) $$A \underset{k_{BA}}{\overset{k_{AB}}{\rightleftharpoons}} B \underset{k_{CB}}{\overset{k_{BC}}{\rightleftharpoons}} C \quad .$$

In the model of cardiac energetics we are concerned with, we will take species A = CP, B = ATP, and C = P_i, so that the reaction between A and B is the CK reaction, and the reaction

between B and C represents a variety of ATPases. The equations of motion are:

$$11)\ dM(A)/dt = (M\emptyset(A) - M(A))/T_1(A) - k_{AB}M(A) + k_{BA}M(B)$$

$$12)\ dM(B)/dt = (M\emptyset(B) - M(B))/T_1(B) - (k_{BA} + k_{BC})M(B) + k_{AB}M(A) + k_{CB}M(C)$$

$$13)\ dM(C)/dt = (M\emptyset(C) - M(C))/T_1(C) - k_{CB}M(C) + k_{BC}M(B)$$

First, a conventional saturation transfer experiment may be performed on this system in which the magnetization of species B is nulled. While M(B) = Ø, the evolutions of M(A) and M(C) are governed by:

$$14)\ dM(A)/dt = M\emptyset(A)/T_1(A) - M(A)/\tau(A)$$

$$15)\ dM(C)/dt = M\emptyset(C)/T_1(C) - M(C)/\tau(C)$$

where $1/\tau(A) = 1/T_1(A) + k_{AB}$ and $1/\tau(C) = 1/T_1(C) + k_{CB}$. Eqs. 14) and 15) are of the same form as Eq. 5) and have the solution

$$16)\ M(S)(t)/M\emptyset(S) = \tau_S k_{SB} \exp(-t/\tau_S) + \tau_S/T_1(S),$$

where the species label S = A or B. This solution could also be written in the same form as Eq. 7), of course.

Obtaining measurements for a sequence of saturation times t yields a curve of $M(S)(t)/M\emptyset(S)$ vs t, which is parameterized by the constants k_{SB} and $T_1(S)$. As discussed above, a two-parameter fit of the data to Eq. 16) then yields the spin-lattice relaxation times $T_1(S)$ and the rate constants k_{SB}. Defining the flux from species S to species R by $F_{SR} = k_{SR}M\emptyset(S)$, we see that from the k_{SB}'s and measurements of $M\emptyset(S)$ in the absence of saturation, we may obtain the magnetization fluxes $F_{AB} = k_{AB}M\emptyset(A)$ from A to B and $F_{CB} = k_{CB}M\emptyset(C)$ from C to B.

If we now invoke the steady-state conditions $F_{BA} = F_{AB}$, $F_{BC} = F_{CB}$, we need go no further in investigating the fluxes

out of B into A and C. Using detailed balance, the remaining rate constants may be derived from the two already obtained. However, this ignores the possibility that the reaction scheme as written is incomplete, which is an important part of the question being addressed. Therefore, we desire a direct measurement of the total flux out of B, $F_{BA} + F_{BC} = (k_{BA} + k_{BC})M_0(B)$, for comparison with the total flux into B, $F_{AB} + F_{CB}$. In order to draw an analogy, consider again the two-site model of the CK system discussed in the Introduction. Recall that when a direct saturation-transfer measurement of the forward (saturating Γ-ATP) and reverse (saturating CP) CK fluxes is made, a discrepancy is found. Obviously, this discrepancy could not occur if the flux had been measured in only a single direction, with the reverse flux assumed to be equal (to satisfy detailed balance).

Returning to the three-site model Eq. 10), and repeating the procedure which led to Eqs. 14) and 15) with saturation at A rather than at B, we obtain the following modified version of Eq. 12):

$$17)\quad dM(B)/dt = (M_0(B) - M(B))/T_1(B) - (k_{BA} + k_{BC})M(B) + k_{CB}M(C).$$

To proceed most simply, the exchange between B and C must be approximated as zero, which is equivalent to setting

$$18)\quad k_{BC} = k_{CB} = 0.$$

The resulting equation

$$19)\quad dM(B)/dt = M_0(A)/T_1(B) - (k_{BA} + 1/T_1(B))M(B)$$

is simple to solve in the same way as Eqs. 14) and 15), but is only applicable under the assumption used in deriving it, namely, Eq. 18). Thus, we expect the flux F_{BA} obtained from the solution of Eq. 19) to be equal to the value of F_{AB}

obtained from the solution of Eq. 14) only when exchange between B and C is negligible. This is consistent with the analysis of the CK system in Ref. 9, in which the forward and reverse fluxes through CK become disparate in situations when one expects a relatively significant flux through the competing (ATPase) reactions (i.e. at high workload).

We can now examine the outcome if the results of a single saturation at A of the network Eq. 1Ø) were used to estimate either k_{BA} or $(k_{BA} + k_{BC})$. Consideration of the steady-state saturation-transfer experiment allows us to show that this would lead to an underestimate of these quantities, and hence of F_{BA} or of $(F_{BA} + F_{BC})$.

For the network 1Ø), a long-time saturation of A yields the pair of algebraic equations

$$2Ø)\quad Ø = (M_Ø(B) - M(B))/T_1(B) - (k_{BA} + k_{BC})M(B) + k_{AB}M(A) + k_{CB}M(C)$$

$$21)\quad Ø = (M_Ø(C) - M(C))/T_1(C) - k_{CB}M(C) + k_{BC}M(B).$$

Solving simultaneously for the steady-state measured value of M(B), one finds readily

$$22)\quad M_{ss}(B)/M_Ø(B) = (1 + k_{BC}T_1(B) + k_{CB}T_1(C))/(1 + (k_{BA} + k_{BC})T_1(B) + k_{CB}T_1(C) + k_{BA}k_{CB}T_1(B)T_1(C)).$$

Now suppose that one interprets Eq. 22) as reflecting the k_{BA} obtained in the two-site model Eq. 1) with resonance A saturated. Assuming $T_1(B)$ is known, the derived k', which may be regarded as an estimate of k_{BA} or of $(k_{BA} + k_{BC})$, would satisfy

$$23)\quad M_{ss}(B)/M_Ø(B) = 1/(1 + T_1(B)k').$$

Solving Eqs. 22) and 23) for k', we find

24) $k' = k_{BA}[1 - \{k_{BC}T_1(B)/(1 + k_{CB}T_1(C) + k_{BC}T_1(B))\}]$.

Note that this k' satisfies $k' < k_{BA} < k_{BA} + k_{BC}$. Thus, such a measurement will underestimate the flux out of B by an amount depending on the relative magnitudes of $k_{BC}T_1(B)$ and $k_{CB}T_1(C)$.

Hence, we are still left with the problem of achieving an independent measurement of flux into and out of ATP in order to show whether a proper treatment of the three-site model is capable of accounting for the apparent discrepancy in forward and reverse CK fluxes at high cardiac workload.

This can be done in the following fashion. Consider the three-site model Eqs. 10)-13). By simultaneously saturating sites A and C for a time t, we obtain, for the evolution of M(B) during the saturation,

25) $dM(B)/dt = M_0(B)/T_1(B) - (k_{BA} + k_{BC} + 1/T_1(B))M_0(B)$.

This is an equation in a single variable, of the same form as Eq. 5). Eq. 25) is similar to Eq. 19), except that in the latter the assumption $k_{BC} = 0$ was required. Eq. 25) can be solved readily to yield a solution identical in form to the solution of Eq. 5):

26) $M(B)(t) = M_0(B)\{1-(k_{BA} + k_{BC})\tau(B)(1 - \exp(-t/\tau(B)))\}$

where $1/\tau(B) = 1/T_1(B) + (k_{BA} + k_{BC})$. The two-parameter fit to Eq. 26) of experimental double-saturation data now gives $(k_{BA} + k_{BC})$ and $T_1(B)$. From the former, we can calculate the total magnetization flux out of B, $F_{BA} + F_{BC} = (k_{BA} + k_{BC})M_0(B)$.

If the three-site exchange network shown in Eq. 10) is adequate to describe NMR-observable fluxes between species A, B, and C, we expect that the sum of F_{AB} (derived from fitting data to the solution of Eq. 14)) and F_{CB} (derived from fitting data to the solution of Eq. 15)) will be equal to

(F_{BA} + F_{BC}) (derived from fitting data to the solution of Eq. 25)):

27) F_{AB} + F_{CB} = F_{BA} + F_{BC}.

We will apply just this approach to study flux balance in the CK system.

We now turn to a direct comparison of the steady-state and transient saturation-transfer techniques. As stated earlier, transient methods have two significant advantages in biological NMR. First, biological preparations are generally deteriorating to a greater or lesser extent throughout the duration of an experiment. In addition, many other experimental factors, such as the temperature of the preparation or effectiveness of oxygenation of the perfusate, may vary somewhat over time. As a result, if T_1 and k values are obtained from separate protocols performed necessarily at separate times, as in the steady-state experiment, there is no assurance that they reflect the same physiologic state of the preparation. However, in the transient experiment, these quantities are obtained from the same data set, so that this concern is not as severe.

The second and more important advantage of the transient experiment is particularly of interest in the CK/ATPase system, due to the possible compartmentation of intracellular ATP into a cytosolic pool in fast exchange with CP, and a mitochondrial pool which is in slow exchange. To illustrate, consider a modification of Eq. 1) in which A is composed of two pools, one, A^e, exchanging with B, and another, A^n, not exchanging:

28)
$$A^e \underset{k_{AeB}}{\overset{k_{BAe}}{\rightleftharpoons}} B \qquad + \qquad A^n$$

The appropriate Bloch equations for this system are

$$29)\quad dM(A^e)/dt = (M_0(A^e) - M(A^e))/T_1(A^e) - k_{AeB}M(A^e) + k_{BAe}M(B)$$

$$30)\quad dM(A^n)/dt = (M_0(A^n) - M(A^n)/T_1(A^n)$$

$$31)\quad dM(B)/dt = (M_0(B) - M(B))/T_1(B) - k_{BAe}M(B) + k_{AeB}M(A^e).$$

With saturation at B, these reduce to

$$32)\quad dM(A^e)/dt = M_0(A^e)/T_1(A^e) - M(A^e)/\tau(A^e)$$

$$33)\quad dM(A^n)/dt = (M_0(A^n) - M(A^n))/T_1(A^n)$$

where $1/\tau(A^e) = 1/T_1(A^e) + k_{AeB}$.

Consider first a determination of T_1 by an inversion-recovery experiment, performed with saturation at B. Here, the appropriate initial conditions for Eqs. 32) and 33) are

$$M(A^e)(t=0) = -M_0(A^e), \quad M(A^n)(t=0) = -M_0(A^n).$$

Solving Eqs. 32) and 33) with these initial conditions and adding the solutions, one obtains for the time course of recovery of the observed pool of A after inversion,

$$\begin{aligned} 34)\quad M(A)(t) &= M(A^e)(t) + M(A^n)(t) \\ &= M_0(A^e)\{\ \tau(A^e)/T_1(A^e) \\ &\quad - (\tau(A^e)/T_1(A^e)) + 1)\exp(-t/\tau(A^e))\ \} \\ &\quad + M_0(A^n)\{\ 1 - 2\exp(-t/T_1(A^n))\ \}. \end{aligned}$$

This is of the form

$$35)\quad M(A)(t) = K_1 - K_2\exp(-t/\tau(A^e)) - K_3\exp(-t/T_1(A^n)),$$

showing explicitly that, in general, measuring this recovery from inversion cannot give $\tau(A_e)$ by itself.

Further, consider a long-time saturation of B, so that A reaches steady-state; then from Eqs. 32) and 33) we have

$$36)\quad M_{ss}(A)(t) = M_0(A^n) + M_0(A^e)(\tau(A^e)/T_1(A^e)).$$

Even supposing $\tau(A^e)$ were known, it is clear that the contributions of the two pools cannot be separated to obtain information about $T_1(A^e)$ or k_{AeB} unless an assumption is made about the relative magnitudes of $M_0(A^e)$ and $M_0(A^n)$.

However, now consider a transient saturation-transfer experiment performed on this system as described above. The appropriate initial conditions are

$$M(A^e)(t=0) = M_0(A^e), \quad M(A^n)(t=0) = M_0(A^n).$$

Adding the solutions of Eqs. 32) and 33) with these initial conditions, one obtains for the time course of A after saturation at B

$$\begin{aligned} 37)\quad M(A)(t) &= M(A^e)(t) + M(A^n)(t) \\ &= M_0(A^e)\{\ \tau(A^e)k_{AeB}\exp(-t/\tau(A^e)) \\ &\quad + \tau(A^e)/T_1(A^e)\ \} + M_0(A^n). \end{aligned}$$

Thus, the presence of the nonexchanging pool merely results in an offset, and saturation data fitted to Eq. 37) will yield values for k_{AeB} and $\tau(A^e)$, and hence for $T_1(A^e)$ as well.

Therefore, in situations in which metabolite compartmentation of the type described above may be important, the results of a transient experiment are more relevant and much simpler to interpret than are the results obtained from steady-state saturation. In the case of the CK/ATPase system, we consider the possibility that part of the ATP is in a very slowly exchanging, NMR-visible mitochondrial compartment, while the balance is cytosolic, and in rapid exchange with CP and P_i. In terms of the

preceding discussion, we would like to allow for the possibility

A^e = cytosolic ATP
A^n = mitochondrial ATP
B = cytosolic P_i and CP.

Accordingly, we have applied the foregoing theory of the transient saturation transfer experiment to the CK/ATPase system in the perfused rat heart to determine whether the simplest three-site model for phosphorus exchange

$$\text{38)}\qquad CP \underset{k_r}{\overset{k_f}{\rightleftharpoons}} ATP \underset{k_f'}{\overset{k_r'}{\rightleftharpoons}} P_i$$

with the associated Bloch equations

$$\text{39)}\quad dM(CP)/dt = (M_0(CP) - M(CP))/T_1(CP) - k_f M(CP) + k_r M(\Gamma\text{-ATP})$$

$$\text{4Ø)}\quad dM(\Gamma\text{-ATP})/dt = (M_0(\Gamma\text{-ATP}) - M(\Gamma\text{-ATP}))/T_1(\Gamma\text{-ATP}) - (k_r + k_r')M(\Gamma\text{-ATP}) + k_f M(CP) + k_f' M(P_i)$$

$$\text{41)}\quad dM(P_i)/dt = (M_0(P_i) - M(P_i))/T_1(P_i) - k_f' M(P_i) + k_r' M(\Gamma\text{-ATP})$$

is adequate to describe NMR-observable fluxes of phosphorus in this system. We have in fact found this three-site network to be adequate, and conclude that the apparent inequality of fluxes through the CK reaction as found in Refs. 1-3 is caused by the application of Eqs. 18) and 19) to a case in which they do not apply, namely, significant flux through the ATPase reaction, that is, significant $F_f' = k_f'[P_i]$ and $F_r' = k_r'[ATP]$).

Methods

Heart Perfusion

Male Sprague-Dawley rats weighing 350-400 grams were anesthetized with an intraperitoneal injection of 40 mg sodium pentobarbital. Hearts, with some adjacent tissue, were then rapidly excised and immersed in ice cold buffer (see below). The aorta was then dissected free and the heart perfused retrograde through the aorta by 37° phosphate-free Krebs-Henseleit buffer gassed with a mixture of 95% O2 and 5% CO_2 (pH 7.4), as previously described[11]. The buffer was composed of (mM) NaCl (118), KCl (4.7), EDTA (.5), $MgSO_4$ (1.2), $CaCl_2$ (1.75), $NaHCO_3$ (25), and glucose (11). A constant-pressure system was used, providing a perfusion pressure of 100 mm Hg under gravity feed.

Hemodynamic measurements

A water-filled latex balloon was inserted into the left ventricle through an incision into the left atrium, via the mitral valve. The volume of this balloon was adjustable, so that preload, and hence the rate-pressure product (RPP), could be adjusted in all hearts. Pressures were obtained via a water-filled tube running from the latex balloon to a pressure transducer, connected to a Hewlett-Packard chart recorder. Systolic and diastolic pressures were monitored continuously throughout the experiment. By adjusting preload, we created two groups of hearts, with RPP of 22,000 and 32,000 mm Hg/min, respectively. Hearts were excluded if their rate-pressure products could not be closely adjusted to one of these two values.

NMR measurements

The perfused hearts were placed into a 20 mm NMR sample tube and inserted into the bore of an Oxford Instruments 360 wide-bore magnet (field strength, 8.46 Tesla, operating at 145.75 MHz for phosphorus), interfaced with a Nicolet 1280

computer.

Experiments were performed with 6Ø° broad-band observation pulses with a minimum interpulse delay of 3 seconds. Each spectrum was the Fourier transform of the average of 76 free-induction decays, with an applied line broadening of 2Ø Hz. Low-power saturations were applied either at Γ-ATP or at P_i and CP for Ø, .3, .6, 1.2, 2.4, and 4.8 seconds for each set of kinetic data acquisition. Loss of intensity due to saturation transfer for each time-point was assessed by measurement of peak heights (after fitting the spectral lines to a Lorentzian form).

Spillover to the adjacent CP peak during single saturation at Γ-ATP was measured by moving the saturating frequency upfield of CP by an amount equal to the frequency separation between Γ-ATP and CP. Measured in this way, direct spillover saturation of CP during Γ-ATP saturation was found to be less than 1Ø%.

For the simultaneous saturation at P_i and CP, we mixed the output of an audio frequency oscillator with a low-power narrowband radio frequency carrier signal from the spectrometer. The carrier signal was placed halfway between the P_i and CP resonances, and the audio frequency mixed was equal to one-half of this spacing. The spectrum of the mixer output during the double-saturation configuration is shown in Fig. 1, and a typical spectrum is shown in Fig. 2. The two central peaks (1 and 1') in Fig. 1 are at the appropriate frequency to saturate P_i and CP when the carrier frequency is located halfway between P_i and CP, position CF_2 in Fig. 2, while the smaller peaks in Fig. 1 are higher-order harmonics. Γ-ATP is located midway between the mixer output peaks labeled 1' and 2' in Fig. 1, so that, judging from the power output spectrum of the mixer, little spillover is to be expected at Γ-ATP. To assess this more directly, we first moved the spectrometer carrier frequency to a position CF_2 downfield of Γ-ATP by an amount equal to the distance the carrier frequency was located upfield of Γ-ATP during a

double-saturation experiment (that is, position CF_1 of Fig. 2). However, the frequency separation between P_i and CP is almost exactly twice that between CP and Γ-ATP. Consideration of this fact and of the overtone spectrum of the mixer shows that positioning the carrier at CF_2 results in direct saturation of CP by the large first sideband labeled 2 in Fig. 1; this saturation at CP was carried to Γ-ATP through the CK reaction, rendering impossible such an assessment of direct "spillover" saturation of Γ-ATP during simultaneous saturation at P_i and CP. Instead, this effect was estimated by placing the carrier at position CF_3 in Fig. 2, upfield of β-ATP by an amount equal to the upfield distance of the carrier from Γ-ATP during double saturation. Assessed in this way, spillover, as averaged from such baseline saturations of seven hearts, was found to be $\lesssim$ 1Ø% during the double saturation experiments.

Hearts were excluded from the study if they showed metabolic instability (defined as a 1Ø% or greater change in NMR-measured metabolite levels) or hemodynamic instability (defined as a 1Ø% or greater change in RPP) during the course of each protocol. Both single (Γ-ATP) and double (P_i and CP) saturation measurements were obtained on each heart included in the study.

Data analysis

The results of each transient saturation transfer protocol comprised of the full sequence of saturation times were fitted to the form

$$f(t;a,b,c) = a \cdot \exp(-t/b) + c$$

by the nonlinear least-squares routine of the RS/1 software of BBN Research Systems, Cambridge, Mass. From the best-fit values of a,b, and c, the corresponding k and T_1 for each of the two saturation protocols on each heart were calculated according to

$$T_1 = [(a + c)b/c]$$

and

$$k = a/[(a + c)b].$$

These T_1's and k's were then averaged; errors are given as the standard error of the mean (SEM) of this average.

Fluxes were derived from the k's and from relative metabolite levels obtained by integrating the P_i, β-ATP, and CP peaks of each heart, with the integral of β-ATP arbitrarily set to 1ØØ magnetization units. In each heart, the metabolite levels were measured independently at the beginning and end of each of the two protocols to confirm metabolic stability.

All errors are presented as ± SEM. Final values of the fluxes ± SEM were derived under the assumption that the error in the k's and in the metabolite levels were independent. Thus, the formula for the derived error[1,2] in a function f of two variables x and y becomes

$$\sigma_f = \sqrt{(df/dx)^2\sigma_x^2 + (df/dy)^2\sigma_y^2}$$

where σ_f denotes the standard deviation of the derived quantity f(x,y), and σ_x and σ_y are the standard deviations of the independent variables x and y. For flux,

$$F = M_Ø k,$$

this formula becomes

$$\sigma_F = \sqrt{(M_Ø)^2\sigma_k^2 + k^2\sigma_{M_Ø}^2}.$$

Thus, $F \pm \sigma_F = kM_Ø \pm \sqrt{(M_Ø)^2\sigma_k^2 + k^2\sigma_{M_Ø}^2}$. Similarly, the error in the ratio R of two quantities x and y was derived from the formula

$$\sigma_R = \sqrt{\sigma_x^2/y^2 + x^2\sigma_y^2/y^4}.$$

Results

Figure 3 shows stacked spectra obtained from the two saturation protocols, with saturation times of Ø, .3, .6, 1.2, 2.4, and 4.8 seconds. In Fig. 3A, Γ-ATP was saturated as described above. Transfer of saturation from Γ-ATP to P_i and to CP is shown by the gradual decline of their magnetizations as the saturation time increases. From these monoexponential declines, we derived values for k_f, k_f', $T_1(P_i)$, and T_1(CP). Fig. 3B shows spectra obtained from simultaneous saturation of P_i and CP. Transfer of saturation to Γ-ATP is shown by the monoexponential decline of its magnetization as a function of saturation time, from which $(k_r + k_r')$ and T_1(Γ-ATP) are obtained.

In both groups of hearts, k_f, k_f', and $(k_r + k_r')$, where k_f, k_f', k_r, and k_r' are the pseudo first-order rate constants defined by the proposed three-site exchange network Eq. 38) and the Bloch Eqs. 39)-41), were obtained by the two transient saturation transfer protocols. These were combined with equilibrium magnetizations obtained from spectra without saturation to derive the fluxes $F_f = k_f[CP]$, $F_f' = k_f'[P_i]$, and $F_r + F_r' = k_r[ATP] + k_r'[ATP]$. With these quantities, we can assess the adequacy of Eq. 38) to account for ATP homeostasis in the heart. This is done by checking that the total phosphorus flux of ATP synthesis equals the total flux of ATP degradation, $F_f + F_f' = F_r + F_r'$, as required by detailed balance.

A complete set of experiments was performed at each of two workloads, defined respectively by RPP = 22,ØØØ mm Hg/min and RPP = 32,ØØØ mm Hg/min. The lower workload was selected to match the one workload in Ref. 9 in which a statistically significant difference between F_f and F_r was found. The higher workload provided an additional check on the method in a regime of higher energy demands, in which the flux discrepancy as measured by standard single-peak saturation transfer would be expected to be still greater due to greater

activity of ATPase systems.

The quantities measured in the NMR experiments at each workload were the relative concentrations of CP, Γ-ATP, and P_i, the spin-lattice relaxation times T_1(CP), T_1(Γ-ATP), and $T_1(P_i)$, and the kinetic constants k_f, $(k_r + k_r')$, and k_f'. Note that of these, the double-saturation technique is required to obtain correct values only for T_1(Γ-ATP) and $(k_r + k_r')$, while standard saturation-transfer experiments suffice to obtain T_1(CP), $T_1(P_i)$, k_f, and k_f'.

From the experimental data, we derived

F_{syn} = total ATP synthesis = k_f[CP] + k_f'[P_i],

F_{deg} = total ATP degradation = $(k_r + k_r')$[Γ-ATP],

F_{CK} = flux through the CK reaction = k_f[CP],

and

F_{ATPase} = flux through ATPases = k_f'[P_i].

The values of the measured quantities and the fluxes are given in Table 1. There were no significant differences in any of the measured or derived quantities between the two workloads investigated. The derived ratio of phosphorus flux through the ATPase reaction to the flux through the CK reaction was greater by a factor of two at the higher workload, but the increase was not statistically significant due to the size of the errors.

The main result of this study is that the three-site model Eq. 38) is indeed adequate to show detailed balance in the combined CK-ATPase system of the heart, and suffices to demonstrate ATP homeostasis directly. As shown in Table 1, the ratio of the phosphorus flux of ATP synthesis to the flux of ATP degradation at each of the two workloads was indistinguishable from unity: at RPP = 22,ØØØ mm Hg/min, F_{syn}/F_{deg} = .94 ± .18, while at RPP = 32,ØØØ mm Hg/min, F_{syn}/F_{deg} = 1.18 ± .18.

It is useful to make a direct comparison of our results to those of Ref. 9, in which a similar series of experiments was carried out but with the difference that the reverse CK reaction was analyzed with saturation applied only at CP, rather than at both CP and P_i, as in the present study.

In Fig. 4, the left-hand panel displays our values for the fluxes F_{deg} and F_{syn}, derived from the spectroscopic data as discussed above. At both workloads, $F_{deg} \approx F_{syn}$. To calculate F_{syn} and F_{deg} from the data of Ref. 9, we used $F_{syn} = k_f[CP] + k_f'[P_i]$, as in the present study, and $F_{deg} = k_r[\Gamma\text{-ATP}]$. The right-hand panel of Fig. 4 shows these fluxes. As discussed in the Theory section of this Chapter, the validity of this derivation of F_{deg} rests on assumptions which may not be valid at these workloads. Here, we see that F_{syn} and F_{deg} are substantially different.

Fig. 5 shows a direct comparison between the double-saturation experiments of the present study and the results of Ref. 9, with respect to apparent balance between ATP synthesis and ATP degradation. As shown explicitly in the Theory section of this Chapter, single-saturation would be expected to underestimate the rate of ATP degradation. In fact, as seen in Fig. 5, at a workload of 22,ØØØ mm Hg/min, the single-saturation experiment underestimated F_{deg} to the extent that the apparent $F_{syn}/F_{deg} = 1.51 \pm .25$. In contrast, the double-saturation treatment of F_{deg} lowers this to $.94 \pm .18$, a value indistinguishable from unity. At the higher workload of 32,ØØØ mm Hg/min, the discrepancy between synthesis and degradation flux is still greater in Ref. 9, $F_{syn}/F_{deg} = 1.69 \pm .33$, while in the present study this ratio is $F_{syn}/F_{deg} = 1.18 \pm .18$, again indistinguishable from unity.

Discussion

At this point, it is worthwhile to reemphasize exactly what type of information one obtains in a saturation transfer experiment. The chemistry of a kinetic system in steady-state is fully characterized by two sets of relationships. First are the appropriate statements of the law of detailed balance, which must hold in steady state when all reactants are properly accounted for. Second, to interpret the saturation transfer data, an assumption must be made about the form of the exchange network. Since detailed balance is always true in the steady-state, and is also an underlying assumption of all present saturation transfer-techniques, the saturation transfer experiment itself provides no further information about that set of relationships. However, the relations of detailed balance themselves furnish internal checks on the kinetic constants derived from the data, and provide the ability to test the validity of an assumed reaction network.

To take the simplest example, consider again the simple two-site exchange, 1):

$$1)\qquad A \underset{k_{AB}}{\overset{k_{BA}}{\rightleftharpoons}} B \qquad .$$

Either steady-state or transient experiments may be performed to determine $T_1(A)$ and k_{AB}, and, in a separate experiment, $T_1(B)$ and k_{BA}. If the reaction network as written is correct, then

$$42)\quad k_{AB} = k_{BA}(M_0(B)/M_0(A))$$

should be obtained. Provided that this relation is satisfied within experimental error, one may assume that departures from the scheme Eq. 1), such as enzymatic intermediates or

side reactions (including reactions involving NMR-invisible pools) are negligible. In that case, the values obtained for k_{AB} and k_{BA} may be regarded as reflecting the true kinetics of the reaction. However, verifying the internal consistency of the data according to Eq. 42) is a crucial step in reaching this conclusion.

Suppose on the other hand that, performing the above experiment, it is found that

43) $k_{AB} \neq k_{BA}(M_0(B)/M_0(A))$.

This would imply that the network Eq. 1) does not adequately account for the main features of the reaction, and so a modification of Eq. 1) must be introduced, and verified experimentally.

This is precisely the situation found in Refs. 1,2,and 3 with respect to the CK reaction. One could modify the simplest, two-site, model of the phosphorus-exchange system in the heart, diagrammed in Sec. I, in a number of ways. These might involve NMR-invisible metabolites, nonexchanging pools, additional sites, or a combination of these. In this study, we have chosen to apply the most straightforward modification of the two-site system, that is, explicit inclusion of a third site for phosphorus, P_i. This was also the choice made by Ugurbil[5,6]. Our conclusions are substantially the same as those of Ref. 6, namely that the discrepancy in the forward and reverse fluxes through the CK reaction can be resolved by correctly accounting for the presence of ATPase reactions.

The chief advantage of the technique of Refs. 5) and 6) is that it allows for the formal elimination of the competing reaction from the Bloch equations describing the reaction system. On the other hand, as described in detail in the earlier section on theory, the transient experiment we employ may have an advantage in the CK system, or in other biological systems in which metabolic compartmentation may be

a feature, in that kinetic constants and spin-lattice relaxation times are derived from the same data set. In certain circumstances, as detailed in the theory section, this would allow one to sidestep the considerable complications introduced when the T_1 of a metabolite may vary according to compartment.

Finally, we note that although our technique as presented allows only for the direct measurement of the sum of k_r and k_r' in the CK/ATPase system, while the technique of Ref. 5 provides k_r by itself, the sum ($k_r + k_r'$) suffices to confirm flux balance and the adequacy of the three-site model 38) for this system. This in turn validates a derivation of k_r and k_r', using detailed balance, from k_f and k_f'

$$44)\quad k_r = k_f([CP]/[\Gamma\text{-ATP}]),\quad k_r' = k_f'([P_i]/[\Gamma\text{-ATP}]),$$

which standard single-saturation techniques provide. Moreover, k_r may be obtained separately, if desired, by applying a long-time saturation at P_i, so that the other resonances reach a steady-state. Eq. 39) then becomes

$$45)\quad \emptyset = (M_\emptyset(CP) - M_{ss}(CP))/T_1(CP) - k_f M_{ss}(CP) + k_r M_{ss}(\Gamma\text{-ATP}),$$

which may be solved explicitly for k_r, since $T_1(CP)$ and k_f have already been determined. Similarly, a long-time saturation at CP would allow k_r' to be obtained directly.

To summarize, we have extended the NMR technique of transient saturation transfer in order to properly account for the kinetics of the creatine kinase reaction in the perfused rat heart. Previous work, allowing for only two sites of exchange for phosphorus, has resulted in an apparent violation of detailed balance in this system. Our treatment, appropriate for a three-site network, resolves this paradox and allows a direct demonstration of ATP homeostasis.

1. S. Forsén and R. A. Hoffman, Exchange rates by nuclear magnetic multiple resonance. III. Exchange reactions in systems with several nonequivalent sites. J. Chem. Phys. 40, 1189 (1964).

2. S. Forsén and R. A. Hoffman, A new method for the study of moderately rapid chemical exchange rates employing nuclear magnetic double resonance. Acta Chem. Scand. 17, 1787 (1963).

3. S. Forsén and R. A. Hoffman, Study of moderately rapid chemical exchange reactions by means of nuclear magnetic double resonance. J. Chem. Phys. 39, 2892 (1963).

4. C. L. Perrin and E. R. Johnston, Saturation-transfer studies of three-site exchange kinetics. J. Mag. Res. 33, 619 (1979).

5. K. Ugurbil, Magnetization-transfer measurements of individual rate constants in the presence of multiple reactions. J. Mag. Res. 64, 207 (1985).

6. K. Ugurbil, M. Petein, R. Maidan, S. Michurski, and A. H. L. From, Measurement of an individual rate constant in the presence of multiple exchanges: application to myocardial creatine kinase reaction. Biochem. 25, 100 (1986).

7. R. L. Nunnally and D. P. Hollis, Adenosine triphosphate compartmentation in living hearts: a phosphorus nuclear magnetic resonance saturation transfer study. Biochem. 18, 3642 (1979).

8. P. M. Matthews, J. L. Bland, D. G. Gadian, and G. K. Radda, A ^{31}P-NMR saturation transfer study of the regulation of creatine kinase in the rat heart. Biochim. Biophys. Acta. 721, 312 (1982).

9. J. A. Bittl and J. S. Ingwall, Reaction rates of creatine kinase and ATP synthesis in the isolated rat heart. J. Biol. Chem. 260, 3512 (1985).

10. A. P. Koretsky and M. W. Weiner, ^{31}Phosphorus nuclear magnetic resonance magnetization transfer measurements of exchange reactions in vivo. In: Biomedical magnetic resonance, eds. A. Margulis and T. James (1984)

11. J. S. Ingwall, Phosphorus Nuclear Magnetic Resonance Spectroscopy of Cardiac and Skeletal Muscles. Am J Physiol 242, H729-H744 (1982).

12. P. R. Bevington, Data reduction and error analysis for the physical sciences, McGraw, (1969).

Table. Measured and Derived NMR and Kinetic Parameters

	RPP = 22,000 mm Hg/min n = 5			RPP = 32,000 mm Hg/min n = 5		
Measured Quantities						
	CP	Γ-ATP	Pi	CP	Γ-ATP	Pi
M0	1090 ± 38	1000 ± 35	281 ± 13	1100 ± 54	1000 ± 47	343 ± 24
T1	2.78 ± .16	.64 ± .13	2.4 ± .31	3.00 ± .46	.82 ± .12	1.92 ± .22
	k_f	$k_r + k_r'$	k_f'	k_f	$k_r + k_r'$	k_f'
	.90 ± .08	1.15 ± .19	.37 ± .09	.92 ± .06	1.04 ± .13	.63 ± .22
Derived Quantities						
	F_f	k_r		F_f	k_r	
	981 ± 94	.98 ± .10		1012 ± 87	1.02 ± .10	
	F_f'	k_r'		F_f'	k_r'	
	104 ± 26	.10 ± .03		216 ± 50	.22 ± .05	
	F_{syn}	F_{deg}		F_{syn}	F_{deg}	
	1085 ± 93	1150 ± 192		1228 ± 100	1040 ± 137	
	F_{syn}/F_{deg}	F_{CK}/F_{ATPase}		F_{syn}/F_{deg}	F_{CK}/F_{ATPase}	
	.94 ± .18	9.4 ± 2.5		1.18 ± .18	4.68 ± 1.16	

NMR-derived reaction rates and spin-lattice relaxation times are shown for all metabolites at both workloads. Fluxes are derived as described in the text. The derived k_r and k_r' are obtained from detailed balance, and so are not used in the calculation of F_{deg}. Instead, F_{deg} is derived from the measured sum ($k_r + k_r'$).

Figure 1. Spectrum of the spectrometer carrier frequency mixed with an audio frequency equal to one-half of the frequency separation between P_i and CP. When the carrier was positioned at position CF_1 of Figure 2, the main peaks of the mixer output, 1 and 1', were positioned to saturate P_i and CP with little spillover to Γ-ATP. The small unlabeled peak between 1 and 1' is carrier breakthough.

Figure 1

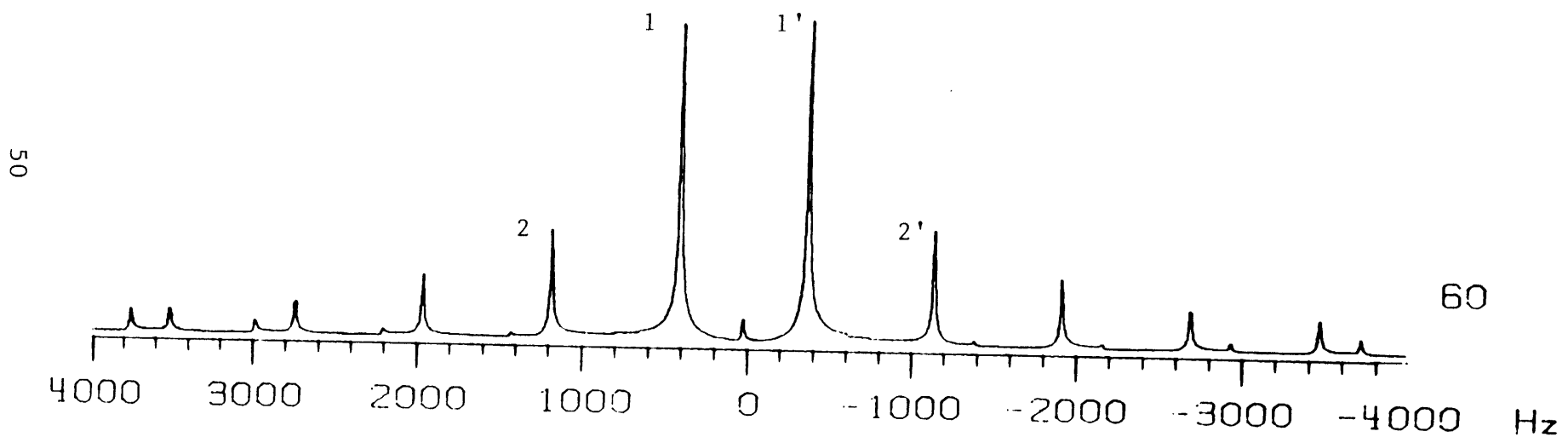

Figure 2. Typical ^{31}P-NMR spectrum of a perfused rat heart, obtained as the average of 76 free-induction decays following broad-band pulses of 60°, with an interpulse delay time of three seconds. The spectrum is displayed on the same frequency scale as Figure 1 to facilitate comparison. During the double saturation experiments, the carrier frequency was placed at position CF_1. Positioning the carrier at CF_2 in an attempt to assess spillover during these experiments failed, since the sideband labeled 2 in Figure 1 is then positioned directly on CP. Instead, spillover was estimated by observing β-ATP when the carrier was positioned at CF_3.

Figure 2

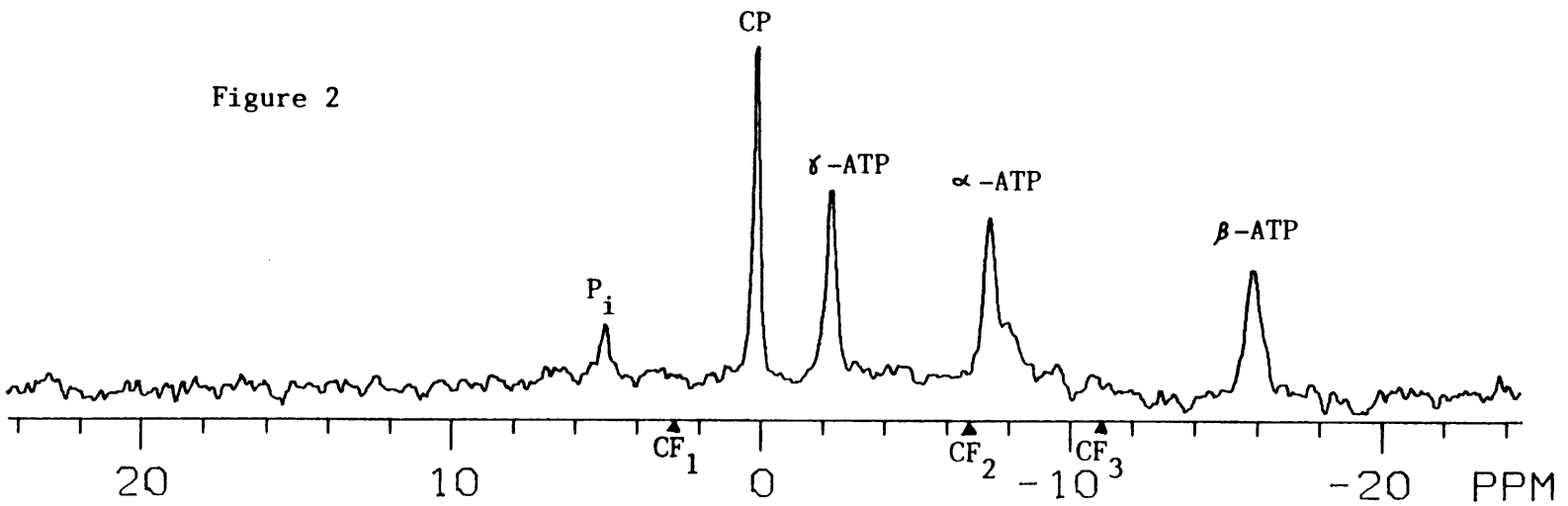

Figure 3. Stacked spectra from the two saturation protocols. Time of saturation is indicated to the right of each spectrum.

A. Transient saturation of Γ-ATP, allowing measurement of $T_1(P_i)$, $T_1(CP)$, k_f', and k_f.

B. Simultaneous transient saturation of P_i and CP, allowing measurement of T_1(Γ-ATP) and $(k_r + k_r')$.

Figure 3A

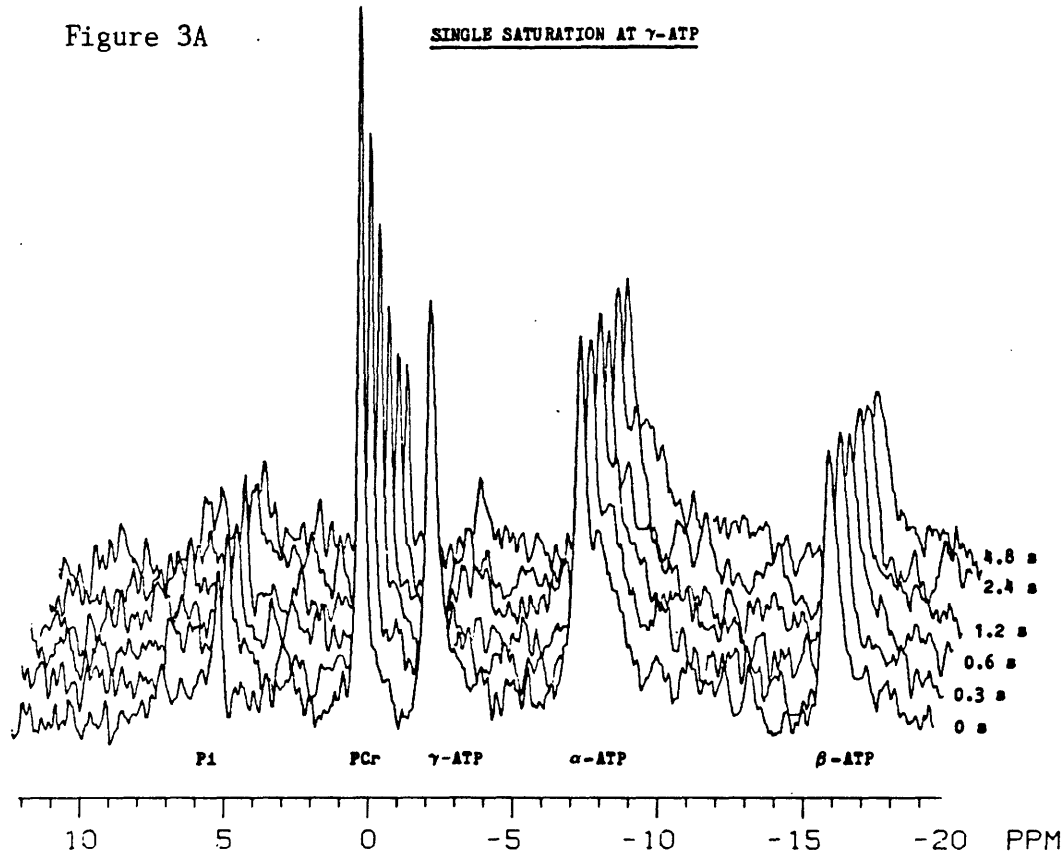

Figure 3B

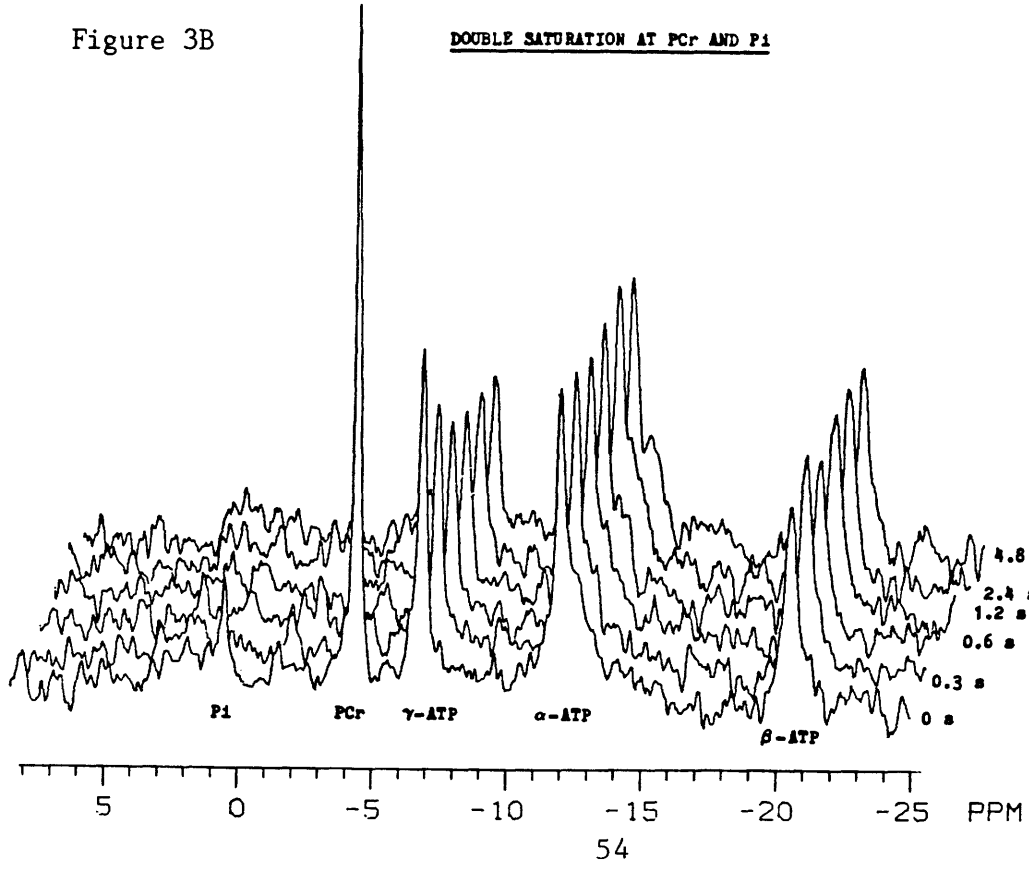

Figure 4. Comparison of the values for F_{deg} and F_{syn} derived at rate-pressure products of 22,ØØØ and 32,ØØØ in the present study and in Ref. 9. In Ref. 9, F_{deg} and F_{syn} were different at these two workloads, while in the present study they were equal.

Figure 4

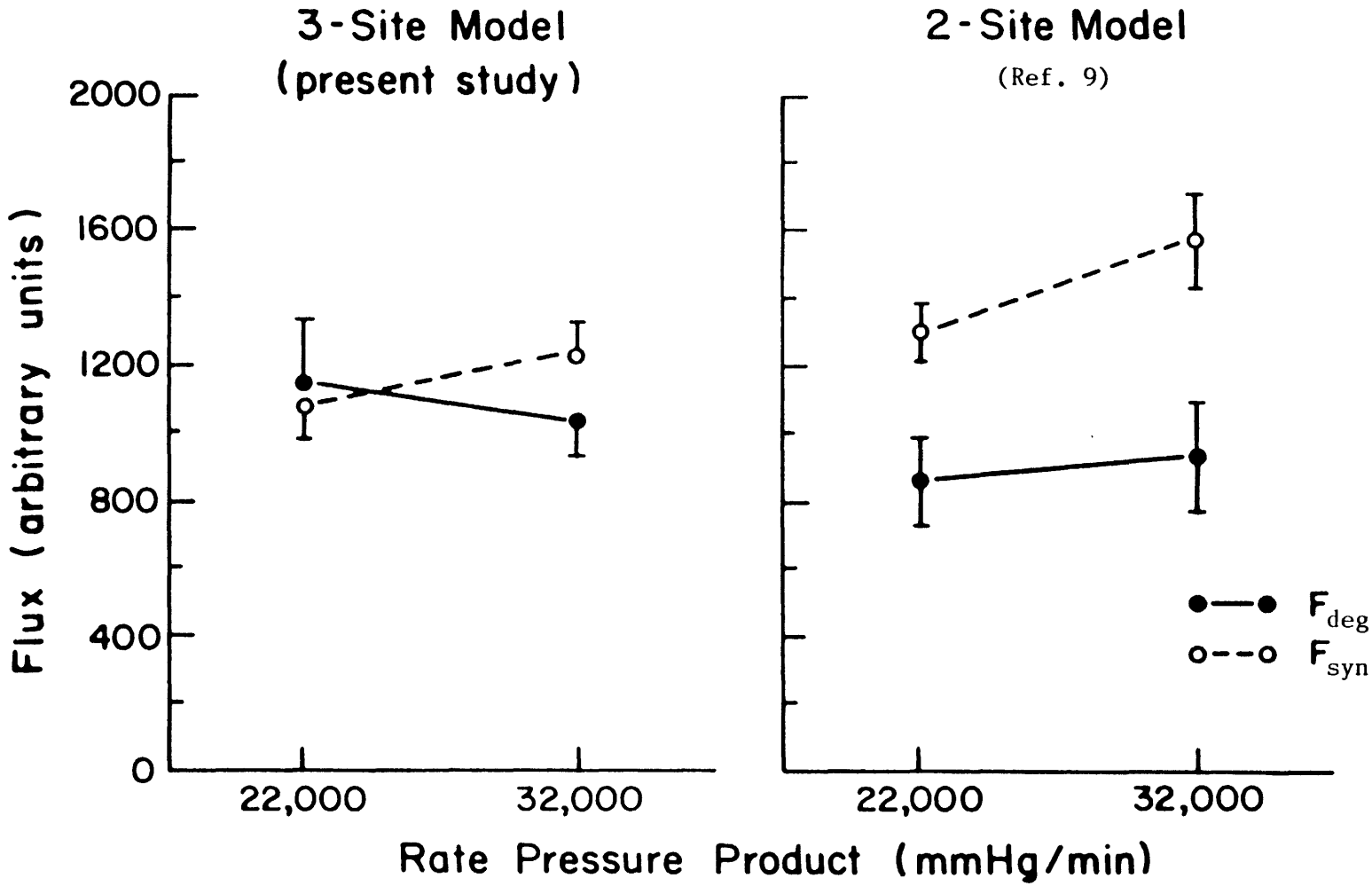
3-Site Model
(present study)
2-Site Model
(Ref. 9)
Flux (arbitrary units)
2000
1600
1200
800
400
0
22,000
32,000
22,000
32,000
Rate Pressure Product (mmHg/min)
F_{deg}
F_{syn}

Figure 5. Ratio of F_{syn} to F_{deg} derived at rate-pressure products of 22,000 and 32,000 in the present study and in Ref. 9. In Ref. 9, this ratio differed from unity, while in the present study it did not.

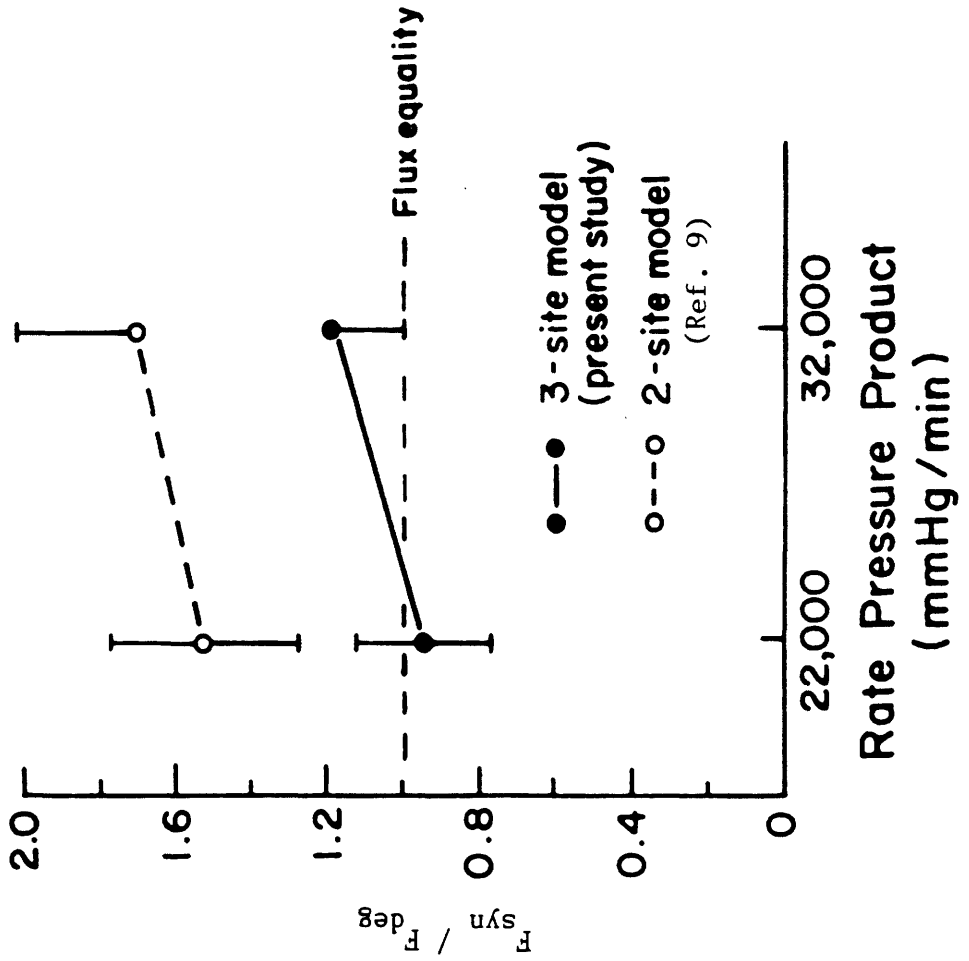
2.0
1.6
1.2
0.8
0.4
0
F_{syn} / F_{deg}
22,000
32,000
Rate Pressure Product
(mmHg/min)
Flux equality
3-site model
(present study)
2-site model
(Ref. 9)

Figure 5

CHAPTER 2

NMR SATURATION FACTORS IN THE PRESENCE OF CHEMICAL EXCHANGE

Abstract

Rapid pulsing is frequently employed in NMR spectroscopy to increase spectral signal-to-noise. In general, this results in partial saturation and diminished magnetization amplitudes, so that observed metabolite abundances must be corrected with saturation factors to obtain true abundances. Saturation factors may be derived from known T_1's or obtained experimentally. However, an underlying assumption of both of these procedures is that there is no chemical exchange between metabolites with different T_1's. This is almost never the case in biological samples, so that the usual development of saturation factors, appropriate for systems which do not exhibit exchange, must be modified in order to properly apply this powerful technique of signal-to-noise enhancement to biological NMR spectroscopy. For this reason, we have extended the theory of saturation factors to allow for the effects of chemical exchange. We found that for systems with chemical exchange: (1) saturation factors are not independent of abundances, in contrast to the case without exchange, and (2) in a particular case, the error in abundance measurements which results from the traditional application of saturation factors depends on the reaction rate, on the difference in T_1's of the exchanging metabolites, on the changes in the ratio of metabolite abundances, and on the interpulse delay and flip angle used. For reasonable choices of kinetic and pulse parameters, this error can reach 10% or more. In contrast, our development allows for a rigorous treatment of saturation factors so that abundances may be determined accurately. If the reaction constant and T_1's are known, the effect of exchange on apparent metabolite abundances may be derived. Alternatively, pulse parameters may be defined which will result in a predetermined upper limit on the error resulting from neglect of exchange.

Introduction

Maximizing spectral signal-to-noise (S/N) is critically important in physiologic NMR for at least three reasons. First, most physiologic samples, such as perfused organs, are unstable to some degree, so that measurements should be obtained as quickly as possible. Second, in these experiments one frequently makes high time resolution measurements during the response of a system to an intervention, such as hypoxia or inflow of a shift reagent. Finally, NMR spectroscopy is being employed increasingly as a quantitative technique, such as in magnetization transfer studies in which reaction rates are determined, rather than simply to obtain qualitative information about a sample. Accuracy, and hence S/N considerations, are of overriding concern in these quantitative studies. As a result of these considerations, the conflict between experimental speed and maximal time resolution on the one hand, and accurate assessment of relative abundances on the other, is acute.

One common method of increasing S/N is to use a flip angle (θ) of less than 90° for the broad-band observation pulse, combined with an interpulse delay T of less than $5 \cdot T_1$. This causes partial saturation of the spectral resonances. In order to obtain a reference to determine true abundances during measurements of metabolite levels, two series of measurements must be made. One is made using θ = 90° and $T \geq 5 \cdot T_1$, this being the combination which gives no amplitude distortion. The second measurement is made using a choice of θ and T_1 which is more favorable from a S/N standpoint. The ratio of these two[1], called the saturation factor (SF):

$$SF = \frac{\text{magnetization (preferred } \theta \text{ and } T)}{\text{magnetization } (\theta = 90°,\ T = 5 \cdot T_1)}$$

---

[1] According to this definition, convenient for the present study, the saturation factor we discuss is actually the reciprocal of the one defined by Gadian, op. cit.

may then be used to correct subsequent measurements performed with the more favorable θ and T. If the spectrum contains more than one resonance, the SF will in general be different for each.

This formulation depends upon the assumption that the SF's are independent of metabolite abundances, which in turn rests upon the assumption that there is no chemical exchange between NMR-visible metabolites with different T_1's. Clearly, this is almost never the case in physiologically intact samples, although this complication is ignored in published treatments of SF's[1,2]. Thus, the theory of SF's, developed for systems which do not exhibit chemical exchange, must be modified so that this powerful method of S/N enhancement may be applied properly to physiologic NMR spectroscopy.

Therefore, we have developed the theory of saturation factors in the presence of exchange by considering the problem of two interacting spin systems. We have derived the closed-form steady-state solution for a train of pulses of angle θ followed by relaxation intervals of duration T, and have written computer codes to implement this solution for arbitrary kinetic and pulse parameters. The most important conclusion (which can be seen from either the closed-form solution or examples with the computer codes), is that the presence of chemical exchange alters the fundamental character of the problem, in that <u>saturation factors are no longer independent of the abundances of the species present</u>. As a consequence, one sample, or one time-period of a physiologic experiment, cannot necessarily be used as a reference to derive saturation factors which will be applicable for the rest of the experiment. The amount of error in a particular case depends on the changes in the ratio of metabolite abundances during the course of the experiment, the difference in the T_1's of the metabolites, the reaction rate, the flip angle of the observation pulse, and the interpulse delay. We have explored the problem for

reasonable choices of these parameters, and found that the errors introduced by naive application of saturation factors can certainly amount to 10%.

This chapter is divided into two parts. Part 1, Saturation Factors in the Absence of Chemical Exchange, is a thorough review of the usual theory of saturation factors. Although our presentation of this differs somewhat from treatments found in the literature, it contains nothing fundamentally new. We include it as a reference, and to set the stage for what follows. Part 2, Saturation Factors in the Presence of Chemical Exchange, is a presentation of our extension of the theory of Part 1 to systems of two chemically exchanging spins.

Part 1.

Saturation Factors in the Absence of Chemical Exchange

To fully understand the problem of saturation factors, a brief review of certain NMR principles may be helpful. The simple classical theory which we will discuss may be regarded as the ensemble average of the corresponding quantum statistical approach[3], and is adequate to treat the present problem.

The nuclei of a particular species of NMR-visible atom, such as phosphorus, have net magnetic moments. When placed in a strong, static, magnetic field, B, these magnetic moments become preferentially oriented along the field direction, according to Boltzmann statistics. The net bulk moment so induced, M_0, is proportional to the abundance of the species in question. In order to measure the magnitude of this moment, thereby measuring the abundance of the chemical species producing it, a strong radio-frequency (RF) pulse is applied to the sample, in order to tip the net magnetic moment out of alignment with the static magnetic field, which is assumed to be oriented along the $\hat{z}$ axis. After this RF pulse, called the observation pulse, the net magnetic moment has a component in the $\hat{x}$-$\hat{y}$ plane. The angle between the net magnetic moment vector and the $\hat{z}$ axis defines the flip angle θ. As this tipped magnetization precesses in response to the $M_0 \times B$ torque which is now present, it induces a voltage in the receiver coil which surrounds the sample. It is this voltage which is the NMR signal.

The signal is proportional to the magnitude of the projection of M_0 in the $\hat{x}$-$\hat{y}$ plane, which in turn depends on the magnitude of M_0 and on θ. Clearly, a 90° flip angle gives the maximum signal for a single accumulation of data. Since the noise is independent of tip angle, a 90° flip also gives maximum S/N. However, the situation is complicated by the need to sample multiple flips in order to achieve reasonable S/N. After a flip, while the voltage in the

receiver coil is being measured, the spin system relaxes (exponentially in time) towards its equilibrium along the $\hat{z}$ axis. After an interpulse delay time T, the spin system is again flipped and the voltage is again measured. This sequence is repeated as many times as desired, more flips increasing the S/N but also increasing the time required for the measurement. The relaxation of the spin system between flips increases the pre-flip $\hat{z}$ component of M_0, and hence the post-flip $\hat{x}$-$\hat{y}$ component, and is therefore fundamental to the measurement. The exponential time constant of this relaxation, T_1, is called the spin-lattice relaxation time, and the equation describing the relaxation[4] is:

$$1) \quad dM/dt = (M_0 - M)/T_1$$

where M refers to the component of M_0 along $\hat{z}$: $M = M_0 \cdot \hat{z}$.

The repetitively pulsed system asymptotically approaches a steady-state, in the sense that between pulses, it relaxes to the same state (same value of M) that it was in when previously pulsed. Consideration of this steady-state, reached for all practical purposes after four or five flips, allows us to define the <u>saturation factor</u> for a given interpulse delay T and flip angle θ. The largest possible value of the projection of M_0 into the $\hat{x}$-$\hat{y}$ plane is clearly equal to the magnitude of M_0. This is achieved with 90° flips and long T's (e.g., $T \geq 5 \cdot T_1$). For smaller θ's and shorter T's, the projection of M_0 into the $\hat{x}$-$\hat{y}$ plane will be less than this, resulting in a decreased apparent abundance of the species under consideration. Assuming without loss of generality that after the flip M_0 is in the $\hat{z}$-$\hat{y}$ plane, the saturation factor is defined by

$$2) \quad SF\ (T,\theta) = M_0 \cdot \hat{y} / M_0$$

where the notation indicates that the numerator depends on the choice of T and θ. It is clear from the above discussion

that species with different T_1's can be expected to have different saturation factors.

With respect to S/N, the following considerations apply to the choice of θ and T. For an experimental time D, the total number, N_0, of flip-and-measure sequences which are signal-averaged is $N_0 = D/T$. Clearly, S/N is improved as N_0 is increased, since the signal is proportional to N_0 while noise is proportional to $\sqrt{N_0}$. From this standpoint, a small T is desirable. However, a larger T would allow more relaxation towards the $\hat{z}$-axis, and hence more magnetization in the $\hat{x}$-$\hat{y}$ plane after a flip, and so a greater induced voltage across the receiver coil. In order that the T required to achieve this not be too large, θ must be small. However, this means that the projection of M_0 into the $\hat{x}$-$\hat{y}$ plane will be small. To determine the appropriate compromise, one must derive the steady-state of the spin system[5], and the corresponding S/N, for arbitrary T and θ, given D, M_0, and noise for a single measurement. This has been done in Appendix 1a. In Appendix 1c, the maximal S/N, achieved with the optimal choice of T and θ, is derived. This maximal S/N (achieved with $T \longrightarrow 0$ and $\theta = \theta_E$, the Ernst angle to be defined below), serves as an appropriate normalization for other values of S/N. Thus, from Appendix 1a, we have

3) $S/N(T,\theta) \;/\; S/N(\text{maximum}) =$

$$\frac{\sqrt{2}}{\sqrt{(T/T_1)}} \qquad \frac{(1 - E_1)\sin\theta}{(1 - E_1\cos\theta)}$$

where $E_1 = \exp(-T/T_1)$. This equation is plotted in Fig. 1. It is clear from Eq. 3) and Fig. 1 that as T/T_1 increases (i.e., as more complete relaxation is allowed between flips), the flip angle at which S/N is maximized increases; however, that maximum itself is decreasing. Using only this information, one would obviously choose a small T/T_1 to insure a large S/N. However, as discussed in general terms

above, this would result in distortion of resonance line amplitudes, that is, development of saturation factors different from unity. In Appendix 1a, we have derived the saturation factor for arbitrary T and θ, for a species of given T_1:

$$4) \quad SF = M_0 \cdot \hat{y}(T,\theta)/M_0 = \frac{(1 - E_1)\sin\theta}{(1 - E_1\cos\theta)} .$$

It is important to note that the SF is independent of M_0. Eq. 4) is plotted in Fig. 2, as a function of θ for various T/T_1. We see that as T/T_1 decreases, the saturation factors decrease, so that the measured amplitude M becomes an increasingly distorted reflection of M_0. In fact, comparing Figs. 1 and 2, we see that the saturation factors only begin to approach 1 (the most desirable number) as T/T_1 gets sufficiently large to seriously impair S/N.

In order to show this tradeoff even more clearly, in Appendix 1b we have calculated the flip angle at which the curves in Fig. 1 are at their maximum. The result is the well-known formula for the Ernst angle θ_E,

$$5) \quad \cos(\theta) = \exp(-T/T_1),$$

which we have plotted in Fig. 3. This represents the maximization of S/N with respect to θ, for a given T/T_1. Inserting this condition into Eq. 3), and again normalizing by the full maximum, gives the expression for S/N achieved for given T/T_1, with optimally chosen θ:

$$6) \quad \frac{S/N(T/T_1,\theta_E)}{S/N(\text{maximum})} = \frac{2^{1/2}}{(T/T_1)^{1/2}} \quad \frac{(1 - E_1)}{(1 - E_1{}^2)^{1/2}} .$$

Fig. 4 shows this relation, plotted as a function of T/T_1. Essentially, then, Fig. 4 is a plot of the maxima of the

curves in Fig. 1. Note first that, as expected from Fig. 1 and as shown in Appendix 1c, it is in the limit of small T that maximum S/N is achieved. Second, there is a severe reduction in S/N as one moves towards longer T's.

Using Eq. 5) in Eq. 4) gives the saturation factors corresponding to the choice $\theta = \theta_E$:

7) $$SF(T/T_1, \theta_E) = (1 - E_1)/(1 - E_1^2)^{1/2}.$$

This is plotted in Fig. 5. In effect, Fig. 5 is a plot of a cross-section of the family of curves of Fig. 2, with the cross-section taken through each curve at $\theta = \theta_E$. Note that as in Fig. 2, this steady-state solution exhibits significant departures from SF = 1 for most choices of parameters, so that here too the determination of the amount of material present cannot be made from such measurements alone. Second, comparing Figs. 4 and 5, we see clearly that the desire to have a steady-state in which $M \cdot \vartheta = M_0$ (that is, SF = 1) in order to accurately assess concentration is in direct conflict with maximizing S/N. The maxima of the two functions $SF(T/T_1; \theta_E)$ and $S/N(T/T_1; \theta_E)$ are simply at opposite ends of the T/T_1 range. In fact, the SF approaches zero for choices of parameters which maximize S/N. Further, there is no intermediate value at which one can avoid either significant amplitude distortion or significant loss of S/N.

These results taken together imply the following. Suppose that one had several samples, each with an unknown amount of a certain NMR-visible species. In order to assess the true amount present in each, but still work with high S/N, i.e., to perform the measurement in the minimum amount of time, one may follow the following procedure. On sample 1, make two measurements, the first with high S/N--choose a small T (generally bounded below by the acquisition time), and the corresponding θ_E. We may refer to these choices as optimal parameters. Then, for the second measurement, use $\theta = 90^\circ$, and choose T such that $T/T_1 >> 1$ (e.g., $T \geq 5 \cdot T_1$) to

get full projection of M_0 into the $\hat{x}$-$\hat{y}$ plane, and full relaxation between flips. From Eq. 4), we see that with these latter parameters the steady-state of the spin system will accurately reflect M_0, and the abundance may be directly measured. In addition, the saturation factor may be calculated from Eq. 7). Now, for all of the other samples, repeat the measurements with the optimal NMR parameters only, and, to get the true amount of the observed species in these samples, simply divide by the saturation factor derived for sample 1 (that is, apply Eq. 2)). There is no need to perform a measurement designed to obtain a full projection of M_0 into the $\hat{x}$-$\hat{y}$ plane, since, again, the saturation factor is independent of M_0. It is also important to note that this algorithm does not require knowledge of T_1, which is, in general, not known (although in isolated spin systems it may be determined without too much difficulty).

In the type of system described in the above example, the value of the saturation factor is unimportant, since, once it is determined, it can be applied appropriately to different samples. Or, as the case may be, it can be applied to the same sample, at different times following an intervention.

The above discussion dealt with a single spin system. We now consider the case in which two (or more) spin systems are present, but are non-interacting. This will always mean nuclei of the same atomic species, but with different chemical shifts. In general, these systems will have different T_1's, and therefore, for a given choice of pulse parameters (θ and T), different saturation factors. This implies that the ratio of the areas of their peaks on the NMR spectrum will in general not be the same as the ratio of their true abundances in the sample. The distortion is simply the ratio of their saturation factors (SF), as shown in Appendix 1d. Thus, as discussed in Appendix 1d, an appropriate measure of the distortion of apparent relative abundances may be termed the <u>relative saturation factor</u> (RSF):

8) $RSF(A,X) = SF(A) / SF(X)$,

where A and X denote two nuclear species present. The expression for RSF(A,X) is clearly, from Eq. 4),

9) $$RSF(A,X) = [(1 - E_1(A))/(1 - E_1(X))] \cdot [(1 - E_1(X)\cos\theta)/(1 - E_1(A)\cos\theta)]$$

where $T_1(A)$ and $T_1(X)$ are the spin-lattice relaxation times of species A and X, $E_1(A) = \exp(-T/T_1(A))$, and $E_1(X) = \exp(-T/T_1(X))$.

Figs. 6a - 6f show the RSF's (that is, distortions of relative amplitude) for a variety of parameter choices. Relative saturation factors are plotted as a function of flip angle. Each of the figures is for a given $T/T_1(X)$, and displays a family of curves parameterized by $T/T_1(A)$. We have included curves for a range of $T/T_1(X)$ from .1 (corresponding to little relaxation, but high S/N, as we have seen previously) to 5 (full relaxation, poor S/N). The family of $T/T_1(A)$ curves on each plot covers the same range: $T/T_1(A)$ = .1, .3, .5, 1, 3, and 5. Note that whenever $T_1(A) = T_1(X)$, the saturation factor of X equals that of A, so that the RSF = 1 for any flip angle. This is, however, the only case in which RSF(A,X) is independent of θ.

The most important observation is the following. Suppose that, as is frequently the case, all that one cares about is the relative abundance of A and X. It might then seem from the figures that by choosing a small enough flip angle, the desired combination of an RSF close to one and a high S/N will be obtained. Recall that a small flip angle corresponds to a small T/T_1 in the optimization condition Eq. 5), and we have seen that it is exactly in the small T limit that maximum S/N is obtained. And, although we have also seen that small saturation factors arise in the small T limit, it

is only the relative saturation factor which is of concern when we are trying to assess the ratio of concentrations of two species. And indeed, from Figs. 6a-6f, it is clear that for a small enough θ, the RSF is close to 1.

Unfortunately, these qualitative conclusions break down upon further consideration. Consider Fig. 6a; here, with $T/T_1(X) = .1$ (small T/T_1, and hence good S/N), we would select a θ of approximately $\theta_E = \cos^{-1}(\exp -.1) = 25^\circ$. But, reading the figure at the abscissa value of 25°, we see that there is a severe distortion of apparent relative abundances for $T/T_1(A) = .2$ (not shown) or .3. Hence, significant distortion results if the T_1's of A and X differ by amounts commonly seen in actual systems. One might conclude that the selection of $T/T_1(X) = .1$ was too restrictive, and that we could perhaps do better by sacrificing S/N to a certain extent. Consider then Fig. 6c, in which $T/T_1(X) = .5$, at a small sacrifice in S/N, but, as is clear from Fig. 4, not a very large sacrifice. The appropriate θ_E is now 53°; looking along the abscissa to this point, we see that again, unfortunately, departures from a RSF = 1 are quite significant for modest differences between $T_1(X)$ and $T_1(A)$. Similar comments apply to the other figures. In Fig. 6d we see large distortions of relative amplitudes at the flip angle of 68°, selected for $T/T_1(X) = 1$. From Figs. 6e and 6f, it is clear that, for given $T_1(X)$ and $T_1(A)$, the distortion of relative amplitudes can be reduced by moving to larger values of T. In the limit of large T, of course, there is no distortion of amplitudes at all. However, the choice of a larger T results in poorer S/N.

Nevertheless, these problems can be overcome by following the procedure outlined above for the case of several samples with an unknown concentration of a single species. The reason is simply that with two (or more) spin systems which are non-interacting (i.e., not in chemical exchange with each other), nothing has really changed from the case of a single isolated system, so that all that is needed is to again make two

measurements on the first sample as described above for the single spin system. From these, one can easily derive a saturation factor for each species present, and then have all the information required to interpret measurements of the remaining samples (or remaining time periods of the experiment) made with parameters which produce superior S/N.

Note that the pulse parameters T and θ can be selected to maximize S/N for only one of the T_1's represented. However, it can be seen from Fig. 1 that what is optimal for the species with the largest T_1 will be fairly close to optimal for the other T_1's, provided they are within a factor of, say, five of this largest value. Alternatively, if there is a species present in low concentration, or which is of particular interest, one could choose to optimize with respect to that species. In any case, it is in general not difficult to select pulse parameters which will result in high S/N across the entire spectrum of two or more peaks.

These considerations are adequate to treat the problem of selecting optimal pulse parameters (T and θ) for non-interacting spin systems. However, in making measurements of physiologic systems, one is usually dealing with species which are interacting, so that the above analysis does not apply. The problem arises because the evolution equation (Eq. 1)) for an isolated spin system is no longer valid, so that the steady-state solutions derived in Appendix 1a are no longer valid. To avoid this complication, one would like to obtain a high S/N with a saturation factor close to one. However, we have seen in detail that this is, in general, not possible. This then leads to the more difficult problem of the derivation of saturation factors in the presence of chemical exchange, as presented in Part 2 which follows.

Part 2. Saturation Factors in the Presence of Chemical Exchange

In the presence of exchange between n chemical species, the evolution equation Eq. 1) given above must be replaced by a coupled system of n equations. We will discuss the case of n = 2, considering exchange between two spin systems A and B:

$$10) \quad A \underset{k_{BA}}{\overset{k_{AB}}{\rightleftharpoons}} B,$$

where k_{AB} and k_{BA} are pseudo first-order rate constants of the reaction. Under certain assumptions, the evolution equations for the magnetizations M(A) and M(B) may be written[6]

$$11) \quad dM(A)/dt = (M_0(A) - M(A))/T_1(A) - k_{AB} \cdot M(A) + k_{BA} \cdot M(B)$$

$$12) \quad dM(B)/dt = (M_0(B) - M(B))/T_1(B) - k_{BA} \cdot M(B) + k_{AB} \cdot M(A),$$

where $M_0(A)$ and $M_0(B)$ are the equilibrium values of the net magnetic moments of species A and B, and $T_1(A)$ and $T_1(B)$ are their spin-lattice relaxation times. In order for chemical equilibrium to be maintained, we have the additional relationship

$$13) \quad k_{AB} = k_{BA}(M_0(B)/M_0(A)).$$

The appropriate saturation factors for the steady-state attained with a train of pulses of flip angle θ and interpulse delay T can be obtained, using Eq. 2), from the steady-state (in the sense of Part 1) solution to Eqs. 11) and 12). The first step is to explicitly solve Eqs. 11) and 12) for arbitrary initial conditions. For a system of n

inhomogeneous linear first-order equations with constant coefficients, this solution is in principle trivial, but laborious to obtain in practice. For the case n = 2 we are concerned with, however, it is still practical to solve the system in closed form. The solution is presented in Appendix 2a.

This solution may now be used in obtaining the steady-state of the interacting spin systems, in a fashion analogous to the derivation of Eq. A9) in Appendix 1a. The problem is again to solve for the initial conditions of M(A) and M(B), $M_1(A)$ and $M_1(B)$, such that, starting with these net magnetization vectors, they are again reached after an observation pulse of flip angle θ followed by an interpulse delay time T (during which the spins evolve according to Eqs. 11) and 12)). This analysis is carried out in Appendix 2b, which is the main result of this chapter. To summarize, the analysis gives the saturation factors for A and B for arbitrary $M_0(A)$, $M_0(B)$ (that is, metabolite levels), $T_1(A)$, $T_1(B)$, k_{AB} (and the corresponding k_{BA}, determined by detailed balance), interpulse delay T, and flip angle θ.

The most important conclusion which can be drawn from the analytic solution of this problem is that the magnitudes of the saturation factors are indeed dependent on metabolite concentrations. In this sense, the presence of chemical exchange alters the fundamental character of the problem, so that saturation factors cannot be applied in the same naive fashion as in the case of noninteracting spin systems. In fact, it can be shown from the analytic solution that the extent to which the saturation factors in the presence of exchange are different from those which would be expected in the absence of exchange depends on the extent of the departure from four conditions. If any one of these conditions is satisfied (which is in general not the case), then chemical exchange does not alter the saturation factors. The conditions are:

1) $k_{AB} \longrightarrow \emptyset$

If k_{AB} (and hence k_{BA}) = Ø, exchange plays no role. The greater the departure from this condition, the greater the importance of exchange in the final result for the saturation factors.

2) $M_0(A)/M_0(B)$ = constant

The analytic solution can be written (c.f. Appendix 2c) so that $M_0(A)$ and $M_0(B)$ enter only as this ratio. Therefore, if it is constant, the saturation factors are independent of concentration changes (i.e., independent of changes in $M_0(A)$ and $M_0(B)$), as in the case of no exchange. A special case of this condition is $M_0(A)$ = constant, $M_0(B)$ = constant.

3) $T_1(A) = T_1(B)$

Intuitively, if this condition is satisfied, the nucleus does not "care" whether it happens to be a member of A or B. The two species are in this case equivalent sites for magnetic relaxation, which therefore occurs independently of exchange between A and B. Note that this conclusion holds even though k_{AB} may not equal k_{BA} (if $M_0(A) \neq M_0(B)$)

4) $T >> T_1(A), T_1(B)$

If this condition is satisfied, then, no matter how complicated (because of exchange) the approach to equilibrium may be, the final result is full relaxation between pulses. Thus, the saturation factors will depend only on the flip angle.

We can now derive explicitly the errors introduced in abundance measurements by neglect of chemical exchange. For a given $M_0(A)$, $M_0(B)$, $T_1(A)$, $T_1(B)$, T, and θ, the effect of increasing k_{AB} on the saturation factor for A (SF(A)), the saturation factor for B (SF(B)), and another quantity, the distortion of relative saturation factors (DRSF), can be calculated. To define the DRSF, we recall from Eq. 8) that the relative saturation factor for two species, A and B, is defined as RSF(A,B) = SF(A)/SF(B). For the case in which k_{AB} = Ø, we denote this by RSF(A,B;Ø). The RSF for non-zero k_{AB}, RSF(A,B;k_{AB}), will in general differ from this. The ratio of

the two, $RSF(A,B;k_{AB})/RSF(A,B;\emptyset)$, may be called the distortion of the RSF (due to exchange):

14) $DRSF = RSF(A,B;k_{AB})/RSF(A,B;\emptyset)$.

The significance of the DRSF is the following. Recall that from SF(A) and the measured M(A), one can obtain $M\emptyset(A)$. A similar statement holds for B. Frequently, however, as discussed in Part 1, it is only the relative concentrations of A and B which are of interest. This can be obtained from the RSF(A,B) and the measured M(A):

15) $M\emptyset(A)/M\emptyset(B) = M(A)/M(B)/RSF(A,B)$.

Consider an observed value for M(A). The saturation factor appropriate for the case without exchange may be denoted $SF(A;\emptyset)$, while the true saturation factor may be denoted $SF(A;k_{AB})$. The calculated $M\emptyset(A)$, assuming the saturation factor equals $SF(A;\emptyset)$, is

16) $M\emptyset(A)(apparent) = M(A)/SF(A;\emptyset)$,

while the true abundance is

17) $M\emptyset(A)(true) = M(A)/SF(A;k_{AB})$.

The proportional error introduced is then

18) $M\emptyset(A)(true)/M\emptyset(A)(apparent) = SF(A;\emptyset)/SF(A;k_{AB})$.

In an exactly analogous fashion, it is easy to derive the error due to the neglect of chemical exchange in the determination of <u>relative</u> amplitudes, using Eq. 18):

19) $[M_0(A)/M_0(B)](\text{true})/[M_0(A)/M_0(B)](\text{apparent}) =$

$[M_0(A)(\text{true})/M_0(B)(\text{true})]/[M_0(A)(\text{apparent})/M_0(B)(\text{apparent})]$

$=$

$[M_0(A)(\text{true})/M_0(A)(\text{apparent})]/[M_0(B)(\text{true})/M_0(B)(\text{apparent})]$

$= [SF(A;\emptyset)/SF(A;k_{AB})]/[SF(B;\emptyset)/SF(B;k_{AB})]$

$= [SF(A;\emptyset)/SF(B;\emptyset)]/[SF(A;k_{AB})/SF(B;k_{AB})]$

$= RSF(A,B;\emptyset)/RSF(A,B;k_{AB})$

$= 1/DRSF.$

In Figs. 7a-7h, we show the results of calculations of saturation factors for non-zero k_{AB}, and the DRSF introduced as a result of the exchange. The magnitude of the saturation factors and the DRSF, correctly accounting for chemical exchange, is plotted on the vertical axis. The horizontal axis is the magnitude of k_{AB}, so that chemical exchange becomes more important as one moves to the right along that axis. The values of the SF's and the DRSF which would be appropriate for no exchange are the values corresponding to $k_{AB} = \emptyset$.

Fig. 7a shows an example for reasonable values of pulse and chemical parameters; $M_0(A) = 3 \cdot M_0(B)$, $T_1(A) = 3 \cdot T_1(B)$, $\theta = 30^\circ$, and $T = .5$ sec. For $k_{AB} = \emptyset$, the saturation factors are $SF(A) = .287$ and $SF(B) = .414$, and the DRSF = 1. Note that by definition, DRSF always equals 1 for $k_{AB} = \emptyset$, since the distortion referred to is that due to exchange. For $k_{AB} = 2$, the saturation factors are distinctly different from the $k_{AB} = \emptyset$ values: $SF(A) = .334$ (an increase of 16%) and $SF(B) = .347$ (a decrease of 16%). Similarly, the DRSF has become 1.39. According to Eqs. 18) and 19), the effects of exchange can therefore significantly alter estimates of $M_0(A)$, $M_0(B)$, and the ratio $M_0(A)/M_0(B)$.

In Fig. 7b, we see that the situation worsens if T is held constant, but θ is increased. With $\theta = 60^\circ$ (as opposed to the value of 30° in Fig. 7a), SF(A) is 30 % greater when $k_{AB} = 2$ than when $k_{AB} = \emptyset$, while SF(B) is decreased by 30%. At the same time, the DRSF has reached 1.85. Generally, for

such a flip angle, one would choose a somewhat longer T, based on the S/N considerations of Part 1. Fig. 7c shows the effects of selecting a longer T. While the errors introduced by the assumption $k_{AB} = \emptyset$ are still significant, they are smaller than in the previous case. This is further demonstrated in Fig. 7d, in which the interpulse delay is yet longer. Here, with T = 3, the errors due to non-zero k_{AB} for $k_{AB} = 2$ are 12% for SF(A) and 9% for SF(B). Of course, this trend towards smaller errors for larger T is consistent with the analytic result discussed above, that is, zero error for $T >> T_1(A), T_1(B)$. This is shown numerically in Fig. 7e, in which $T = 5 \cdot T_1(A)$ and $T = 15 \cdot T_1(B)$. The problem, of course, is that after a point, S/N decreases significantly with increasing T.

Fig. 7f is provided for comparison with Fig. 7d. In the former, the metabolite with the greater concentration has the greater T_1, while in Fig. 7d, the metabolite with the greater concentration has the smaller T_1. In general, this latter situation has been found to result in smaller errors. Similarly, comparing Fig. 7g with Fig. 7c, we see an illustration of the general result that a greater error results from a larger flip angle, everything else being held constant. The reason for this is that with a greater flip angle, the numerators of the relaxation terms in the Bloch equations are larger throughout the relaxation, so that the difference in the T_1's is in effect magnified.

Finally, Fig. 7h shows explicitly that for $T_1(A) = T_1(B)$, no error is introduced by exchange, as discussed above.

In Fig. 8 we change perspective somewhat from Fig. 7, and, rather than show the effect of increasing k_{AB}, we fix kinetic and pulse parameters, assume a fixed k_{AB}, and consider the errors introduced by a change in $M\emptyset(A)/M\emptyset(B)$ as the experiment progresses. This corresponds to an experimental situation in which saturation factors are determined at the outset, and then applied to calculate the true abundances from the observed abundances for the rest of

the experimental data. As discussed above and demonstrated in Appendix 2c, if the ratio $M_0(A)/M_0(B)$ changes, this procedure will, in general, lead to an error. Let R_i denote the ratio $M_0(A)/M_0(B)$ at the beginning of the experiment, and let R_f denote the ratio at a certain later time. The corresponding saturation factors for A may be denoted $SF(A;R_i)$ and $SF(A;R_f)$, respectively. For an observed value of M(A) at the later time, the abundance calculated using the $SF(A;R_i)$ determined at the beginning of the experiment will be

$$M_0(A)(\text{calculated}) = M(A)/SF(A;R_i),$$

while the true abundance will be

$$M_0(A)(\text{true}) = M(A)/SF(A;R_f).$$

The ratio of these two will be the fractional error in the determination of $M_0(A)$:

$$\begin{aligned}\text{fractional error} &= M_0(A)(\text{calculated})/M_0(A)(\text{true}) \\ &= SF(A;R_f)/SF(A;R_i),\end{aligned}$$

which is the quantity plotted in Fig. 8 as a function of the final $M_0(A)/M_0(B)$, or R_f.

Fig. 8a) shows an example for reasonable values of pulse and kinetic parameters: $T_1(A) = 3 \cdot T_1(B)$, initial concentrations of A and B equal, $k_{AB} = 2$, interpulse delay = 2, and flip angle = 60°. If the ratio of the abundance of A to B increases by a factor of two between the initial and later measurement, the fractional error introduced by the exchange will be 5% for both $M_0(A)$ and $M_0(B)$. If the abundance increases by a factor of four, the error will increase to 9% for the estimate of $M_0(A)$ and to 10% for the estimate of $M_0(B)$. In Figs. 8b and 8c the effect of varying θ is shown. For a 90° flip, the percent error for the

situation in which the ratio of abundances increases by a factor of four is 15% for Mø(A) and 17% for Mø(B). On the other hand, a smaller flip of 3Øº results in a smaller error for such an R_f, only 3% for both Mø(A) and Mø(B). These results are consistent with those in Fig. 7 in that the errors increase with increasing θ.

Of course, in all of the plots of Fig. 8, the ratio of calculated-to-true values of the metabolite levels equals 1 whenever $R_f = R_i$. Thus, in Figs. 8a-8c, the curves pass through a value of 1 for Mø(A)/Mø(B) = 1. In the same way, for an initial ratio of concentrations of 2, the curves pass through a value of 1 for Mø(A)/Mø(B) = 2. This is illustrated in Fig. 8d, which is similar to Fig. 8c except that $R_i = 1$ in Fig. 8c while $R_i = 2$ in Fig. 8d.

Fig. 8e, when compared with Fig. 8d, shows that a greater difference in the T_1's of the two metabolites results in a greater fractional error in the assessment of concentrations. The only difference between the parameters in these two figures is that in Fig. 8d, the T_1's differ by a factor of three, while in Fig. 8e they differ by a factor of two. Quantitatively, for a decrease in Mø(A)/Mø(B) from $R_i = 2$ to $R_f = 6$, the percent error shown in Fig. 8d is 8% for Mø(A) and 9% for Mø(B), while in Fig. 8e the corresponding errors are only 4% and 5%, respectively. In Fig. 8f we have presented an example of a more extreme difference in T_1's, $T_1(A) = 12 \cdot T_1(B)$. The errors are correspondingly greater than those in Figs. 8d or 8e.

The effects of more rapid pulsing are show explicitly by comparing Fig. 8e with Fig. 8g, in which the interpulse delay is decreased by a factor of ten. However, at a rapid pulse rate, S/N considerations would dictate that a much smaller θ be used, and, as discussed above and shown in Fig. 8h, this would tend to reduce the errors introduced by exchange.

Finally, Figs. 8i-8k show three limiting cases in which, as expected from the analytic result, no errors result. Fig.

8i is an example with $k_{AB} = \emptyset$, Fig. 8j shows a case in which $T >> T_1(A), T_1(B)$, and in Fig. 8k, $T_1(A) = T_1(B)$.

Plots such as those in Figs. 7 and 8 can be generated ad infinitum, and, with the sizeable ranges of values over which the several pulse, abundance, and kinetic parameters may realistically vary, it would be impossible to assemble anything like a library of results. However, the examples presented here serve to illustrate the main features of the problem, and to show that significant errors may result if chemical exchange is neglected. If the reaction rate constant and spin-lattice relaxation times are known, these errors may now be eliminated. In general, however, this is not the case, and experimentally, it is only feasible to apply saturation factors in the naive way, ignoring exchange. A more complete experimental evaluation of correct saturation factors throughout an experiment would completely defeat their purpose, which is to save experimental time. However, by consideration of the theory of saturation factors in the presence of exchange, a knowledge of approximate rate constants and T_1's allows selection of pulse parameters for which the errors introduced by the standard application of saturation factors can be made arbitrarily small.

1. D. G. Gadian. Nuclear Magnetic Resonance and its Applications to Living Systems, pp 142-143, Clarendon Press, Oxford (1981).

2. E. D. Becker, J. A. Ferretti, and P. N. Gambhir. Selection of Optimum Parameters for Pulse Fourier Transform Nuclear Magnetic Resonance, Analytical Chem. 51:1413-142Ø (1979).

3. C. P. Slichter. Principles of Magnetic Resonance, Chapter 2, Springer-Verlag, Berlin (1978).

4. F. Bloch. Nuclear Induction, Physical Rev. 7Ø:46Ø-474 (1946).

5. R. R. Ernst and W. A. Anderson. Application of Fourier Transform Spectroscopy to Magnetic Resonance, Rev. Sci. Instruments 37:93-1Ø2 (1966).

6. H. M. McConnell. Reaction Rates by Nuclear Magnetic Resonance, J. Chem. Physics 28, 43Ø-431 (1958).

Appendix 1a. Saturation factors and signal-to-noise for an isolated spin system, with arbitrary pulse parameters θ and T

Expressions for the saturation factor and resultant signal-to-noise for an isolated spin system subject to a train of pulses of flip angle θ and interpulse delay T follow readily from the expression for the steady-state which we will now derive.

The timing diagram for this repetitive pulse sequence is

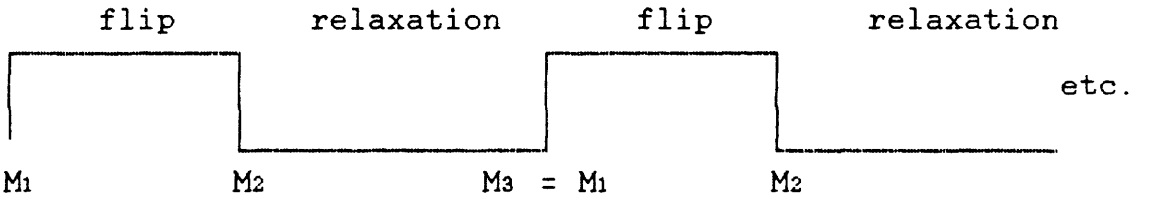

where M_1 denotes the steady-state magnetization vector prior to the pulse of flip angle θ, M_2 denotes this vector immediately after the pulse, and M_3 denotes the magnetization vector after relaxation for a time T after the pulse. As indicated, the condition for steady-state is that $M_3 = M_1$, that is, that the spin system relaxes to the same state it was in prior to the previous pulse.

In the following, we will assume that the transverse relaxation time, T_2, is much smaller than the longitudinal relaxation time, T_1.

In this case, the evolution of the spin magnetization vector due to the pulse is given simply by the rotation

$$A1) \qquad M_2 = \begin{bmatrix} 1 & \emptyset & \emptyset \\ \emptyset & \cos\theta & \sin\theta \\ \emptyset & -\sin\theta & \cos\theta \end{bmatrix} \cdot M_1, \qquad M_1 = \begin{bmatrix} \emptyset \\ \emptyset \\ M_1 \end{bmatrix}$$

so that

A2) $M_2 \cdot \hat{z} = M_1 \cos\theta$.

In considering the evolution from M_2 to M_3, it suffices to consider only $\hat{z}$ components of the vectors, since we have assumed $T_2 << T_1$ so that transverse relaxation is assumed to be, in effect, instantaneous. In the following, therefore, the symbol for a vector will denote its $\hat{z}$ component.

During the relaxation time T, the $\hat{z}$ component of the spin system evolves according to the Bloch equation

A3) $dM/dt = (M_0 - M)/T_1$

with the initial condition

A4) $M(t=0) = M_2$.

Here, M_0 denotes the maximum, equilibrium, value for the net magnetization vector M.

The solution to A3) and A4) is

A5) $M(t) = M_0 - (M_0 - M_2)\exp(-t/T_1)$.

The condition for a steady-state is that, at the end of an interpulse delay, that is, after evolution for a time T starting from M_2, $M(t = T) = M_3$ satisfies

A6) $M_3 = M_1 = M_0 - (M_0 - M_1\cos\theta)\exp(-T/T_1)$

where we have made use of Eq. A2). Solving Eq. A6) for M_1, we find readily

A7) $M_1 = M_0(1 - E_1)/(1 - E_1\cos\theta)$

where

A8) $E_1 = \exp(-T/T_1)$.

The detected receiver signal is proportional to the $\hat{y}$ component of M_2; recalling that the right-hand side of Eq. A7) is the steady-state value for the $\hat{z}$ component of M_1, and using Eq. A1), we finally arrive at the detected steady-state signal

A9) $M_2 \cdot \hat{y} = M_0(1 - E_1)\sin\theta/(1 - E_1\cos\theta)$.

By definition, the saturation factor is

A10) $SF = M_2 \cdot \hat{y}/M_0$

so that

A11) $SF(\theta,T) = (1 - E_1)\sin\theta/(1 - E_1\cos\theta)$

where the functional dependence on flip angle θ and interpulse delay T has been indicated. Note that, as claimed, the saturation factor depends only on the pulse parameters θ and T, and is independent of M_0. (Of course, the fact that this statement no longer holds for systems in exchange forms the basis for this Chapter.)

To derive the corresponding S/N, consider an experiment of total duration D, with Ω denoting the S/N for a single acquisition. The total number N_0 of acquisitions during the experiment will be $N_0 = D/T$, so that, using A9), the total signal will be

A12) $\text{Signal} = (D/T)\cdot M_0(1 - E_1)\sin\theta/(1 - E_1\cos\theta)$.

Assuming random noise, the total noise for N_0 acquisitions will be

A13) $\quad$ Noise $= \Omega\sqrt{N\phi} = \Omega\sqrt{(D/T)}$.

From Eqs. A12) and A13), and using $\sqrt{N\phi} = \sqrt{(D/T_1)}\cdot\sqrt{(1/(T/T_1))}$, the expression for signal-to-noise is then

$$\text{A14)} \quad S/N = \frac{D^{1/2}}{\Omega \quad T_1{}^{1/2}} \cdot M\phi \quad \frac{(1 - E_1)\sin\theta}{(T/T_1)^{1/2}\,(1 - E_1\cos\theta)}$$

for an experiment of duration D.

Appendix 1b. Derivation of the Ernst angle, maximizing S/N for a fixed T, and corresponding saturation factor and signal-to-noise

To obtain the expression for the Ernst angle, θ_E, which maximizes S/N for a fixed interpulse delay T, one simply solves

A15) d/dcosθ (right-hand side of Eq. A14)) = Ø,

obtaining after some algebra

A16) $\cos\theta_E = E_1$.

Inserting this into Eq. A11), the corresponding saturation factor is

A17) $$SF(\theta = \theta_E, T) = \frac{(1 - E_1)}{(1 - E_1^2)^{1/2}}.$$

Similarly, the S/N is obtained by substituting Eq. A16) into Eq. A14):

A18) $$S/N(\theta_E, T) = \frac{D^{1/2}}{\Omega \; T_1^{1/2}} \cdot M_\emptyset \; \frac{(1 - E_1)}{(T/T_1)^{1/2} (1 - E_1^2)^{1/2}}$$

for an experiment of duration D. To emphasize, the difference between the pair A11) and A14) and the pair A17) and A18) is that in the former, the two independent pulse parameters, θ and T, appear. In the latter, only T appears, with θ given in terms of T by Eq. A16); this is the flip angle which maximizes S/N for a given T.

Appendix 1c. Full maximization of signal-to-noise, maximizing with respect to T, for $\theta = \theta_E$

Here, we obtain the pulse parameters resulting in the theoretical maximum S/N, and the corresponding S/N. In Appendix 1b, S/N was maximized with respect to θ for a fixed T, yielding the Ernst angle condition. To continue, we maximize with respect to T by solving

A19) $d/d(T/T_1)$ (right-hand side of Eq. A18)) = Ø,

obtaining

A2Ø) $T/T_1 = Ø$

(and correspondingly, $\cos\theta = E_1 = 1$, or $\theta = Ø^o$).

One can show, by carefully taking limits, that

$$\text{A21)} \quad \lim_{T/T_1 \text{ ---> } Ø} \frac{1}{(T/T_1)^{1/2}} \frac{(1 - E_1)}{(1 - E_1{}^2)^{1/2}} = \frac{1}{2^{1/2}}$$

so that, using Eq. A18),

$$\text{A22)} \quad S/N(\theta_E, T/T_1 \text{ ---> } Ø) = \frac{D^{1/2}}{\Omega} \frac{1}{T_1{}^{1/2}} M_Ø \cdot \frac{1}{2^{1/2}} .$$

Further,

$$\text{A23)} \quad \lim_{T/T_1 \text{ --->} Ø} \frac{(1 - E_1)}{(1 - E_1{}^2)^{1/2}} = Ø$$

so that, from Eq. A17), the corresponding saturation factor is

A24) $SF(\theta_E, T/T_1 \text{ ---> } Ø) = Ø.$

What this result implies is simply that, as S/N is increased by decreasing the interpulse delay T, the distortion of amplitude worsens.

Appendix 1d. Distortion of relative amplitudes of two non-interacting spin systems

We denote the $\hat{x}$-$\hat{y}$ magnetization components of two non-interacting spin systems, M(A), and M(B), following a pulse of tip angle θ, by $M_0(A)\cdot\hat{y}$ and $M_0(B)\cdot\hat{y}$. The distortion of the abundance ratio of these two species is

A25) $$\frac{M_0(A)\cdot\hat{y}}{M_0(B)\cdot\hat{y}} = \frac{(M_0(A)\cdot\hat{y}/M_0(A))\cdot M_0(A)}{(M_0(B)\cdot\hat{y}/M_0(B))\cdot M_0(B)}$$

$$= \frac{M_0(A)}{M_0(B)} \cdot \frac{SF(A)}{SF(B)} = \frac{M_0(A)}{M_0(B)} \cdot RSF(A,B)$$

where the relative saturation factor, RSF, is defined as

A26) $$RSF(A,B) = \frac{SF(A)}{SF(B)} .$$

For non-interacting spins, using Eq. A11),

A27) $$RSF(A,B) = \frac{(1 - E_1(A))}{(1 - E_1(B))} \frac{(1 - E_1(B)\cos\theta)}{(1 - E_1(A)\cos\theta)}$$

where $E_1(A) = \exp(-T/T_1(A))$ and $E_1(B) = \exp(-T/T_1(B))$.

Appendix 2a. Analytic solution to two inhomogeneous coupled first-order linear ordinary differential equations with constant coefficients

The system to solve is

$$dx/dt = c_1 - b_1 \cdot x + a_1 \cdot y$$

A28)

$$dy/dt = c_2 - b_2 \cdot y + a_2 \cdot x$$

with initial conditions

$$x(t = \emptyset) = x\emptyset$$

A29)

$$y(t = \emptyset) = y\emptyset .$$

The solution is:

$$x(t) = \alpha \exp(D_+ t) + \beta \exp(D_- t) + \Sigma$$

A3Ø)

$$y(t) = \alpha\Gamma \exp(D_+ t) + \beta\delta \exp(D_- t) + \Phi$$

where

A31) $$\Sigma = (b_2 c_1 + a_1 c_2)/(b_1 b_2 - a_1 a_2)$$

$$\Phi = (a_2 c_1 + b_1 c_2)/(b_1 b_2 - a_1 a_2)$$

$$D+ = \frac{-(b_1 + b_2) + [(b_1 + b_2)^2 + 4a_1 a_2]^{1/2}}{2}$$

$$D- = \frac{-(b_1 + b_2) - [(b_1 + b_2)^2 + 4a_1 a_2]^{1/2}}{2}$$

$$\Gamma = (D+ + b_1)/a_1$$

$$\delta = (D- + b_1)/a_1$$

$$\alpha(x_0, y_0) = (\delta x_0 - y_0 + \Phi - \Sigma\delta)/(\delta - \Gamma)$$

and

$$\beta(x_0, y_0) = (y_0 - \Gamma x_0 + \Sigma\Gamma - \Phi)/(\delta - \Gamma).$$

Appendix 2b. Derivation of the steady-state for two interacting spin systems, with arbitrary pulse parameters θ and T

As in Appendix 1a, the timing diagram for the pulse sequence is simply

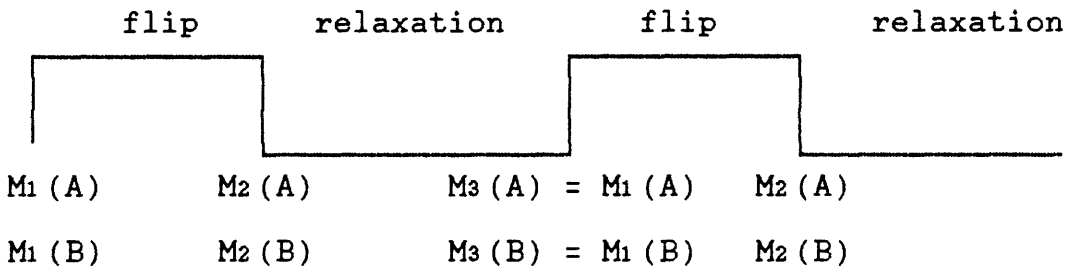

where, as in Appendix 1a, M_1 denotes steady-state magnetization vectors prior to the pulse of flip angle θ, M_2 denotes these vectors after the pulse, and M_3 denotes the magnetization vectors after relaxation for a time T after the pulse. As indicated, the condition for steady-state is that $M_3 = M_1$, so that the spin systems relax to the same state they were in prior to the previous pulse.

Again, we will assume that the transverse relaxation time, T_2, is much smaller than the longitudinal relaxation time, T_1. In this case, again following Appendix 1a, the evolution from $M_1(A)$ and $M_1(B)$ to $M_2(A)$ and $M_2(B)$ is simply

$$M_2(A)\cdot \hat{z} = M_1(A)\cos\theta$$

A32)

$$M_2(B)\cdot \hat{z} = M_1(B)\cos\theta.$$

In considering the evolution from $M_2(A)$ and $M_2(B)$ to $M_3(A)$ and $M_3(B)$, we consider only $\hat{z}$ components of the vectors, based on the assumption $T_2 << T_1$. In the following, then, the symbol for a vector will denote its $\hat{z}$ component.

During the relaxation time T, the $\hat{z}$ component of the spin systems evolve according to the Bloch equations (see Eqs. 10)-12) of the text)

A33) $$dM(A)/dt = (M_0(A) - M(A))/T_1(A) - k_{AB}\cdot M(A) + k_{BA}\cdot M(B)$$

A34) $$dM(B)/dt = (M_0(B) - M(B))/T_1(B) - k_{BA}\cdot M(B) + k_{AB}\cdot M(A),$$

with initial conditions

A35) $$M(A)(t = 0) = M_2(A),$$

A36) $$M(B)(t = 0) = M_2(B).$$

where $M_0(A)$ and $M_0(B)$ denote the maximum, equilibrium, values for the net magnetization vectors M(A) and M(B).

This system is of the form discussed in Appendix 2a,with the correspondences

A37)

$$x = M(A) \qquad y = M(B)$$

$$c_1 = M_0(A)/T_1(A) \qquad c_2 = M_0(B)/T_1(B)$$

$$b_1 = 1/T_1(A) + k_{AB} \qquad b_2 = 1/T_1(B) + k_{BA}$$

$$a_1 = k_{BA} \qquad a_2 = k_{AB}$$

$$x_0 = M(A)(t = 0) = M_1(A)\cos\theta$$

and

$$y_0 = M(B)(t = 0) = M_1(B)\cos\theta.$$

Again, for a steady-state, the initital conditions at time $t = T$ are $M_3(A) = M_1(A)$ and $M_3(B) = M_1(B)$, that is,

relaxation occurs through an angle equal to the flip angle during the relaxation period.

We can solve Eqs. A33) to A36) using the results of Appendix 2a. Then, equating the solutions for M(A) and M(B) at t = T to $M_1(A)$ and $M_1(B)$, respectively, we obtain the simple equations

A38) $$M_1(A) = \alpha(M_1(A)\cos\theta, M_1(B)\cos\theta)E+ + \beta(M_1(A)\cos\theta, M_1(B)\cos\theta)E- + \Sigma$$

A39) $$M_1(B) = \alpha(M_1(A)\cos\theta, M_1(B)\cos\theta)((D+ + b_1)/a_1)E+ + \beta(M_1(A)\cos\theta, M_1(B)\cos\theta)((D- + b_1)/a_1)E- + \Phi$$

where

A4Ø) $$E+ = \exp(D+T)$$

A41) $$E- = \exp(D-T),$$

and where the constants and the functions α and β are defined in Eq. A31) and Eq. A37).

Eqs. A38) and A39) are of the simple form

A42) $$A = g1 \cdot A + h1 \cdot B + k1$$

A43) $$B = g2 \cdot A + h2 \cdot B + k2$$

with $A = M_1(A)$ and $B = M_1(B)$, and where, collecting terms and using the notation for the discriminant

A44) $$disc = \left[(b_1 - b_2)^2 + 4a_1 a_2\right]^{1/2},$$

the coefficients are

A45) $$g1 = \left[\frac{(D+ + b_1)E- - (D- + b_1)E+}{disc}\right] \cos\theta$$

A46) $$h1 = \left[\frac{a_1(E+ + E-)}{disc}\right] \cos\theta$$

A47) $$k1 = \left[\frac{-a_1[(\Phi - \Sigma\delta)E+ + (\Sigma\Gamma - \Phi)E-]}{disc}\right] + \Sigma$$

A48) $$g2 = \left[\frac{(D+ + b_1)}{disc}\ \frac{(D- + b_1)}{a_1}\ (E- + E+)\right] \cos\theta$$

A49) $$h2 = \left[\frac{(D+ + b_1)E+ - (D- + b_1)E-}{disc}\right] \cos\theta$$

A5Ø) $$k2 = \left[\frac{-(\Phi - \Sigma\delta)(D+ + b_1)E+ - (\Sigma\Gamma - \Phi)(D- + b_1)E-}{disc}\right] + \Phi.$$

The solution to Eqs. A42)-A43) is

A51) $$A = \frac{1}{(1 - g1)(1 - h2) - g2 \cdot h1}\ [(1 - h2)k1 + h1 \cdot k2]$$

A52) $$B = \frac{1}{(1 - g1)(1 - h2) - g2 \cdot h1}\ [g2 \cdot k1 + (1 - g1)k2]\ .$$

Eqs. A51)-A52) are then the explicit steady-state for the exchanging system A33)-A34), giving $M_1(A)$ and $M_1(B)$, the net magnetization vectors before the pulse. Using Eq. A1), these are related to the magnitudes of the observed ($\hat{y}$ component) magnetizations after the pulse by

A53) $$M_2(A) \cdot \hat{y} = M_1(A)\sin\theta$$

$$M_2(B) \cdot \hat{y} = M_1(B)\sin\theta.$$

The saturation factors are simply, as in the case of isolated spins,

A54) $$SF(A) = M_2(A)\cdot \hat{y}/M_0(A)$$

$$SF(B) = M_2(B)\cdot \hat{y}/M_0(B).$$

The corresponding expressions for signal-to-noise are

A55) $$S/N(A) = \left[\frac{D^{1/2}}{\Omega\, T(A)^{1/2}(T/T_1(A))^{1/2}} \right] \cdot M_2(A)\cdot \hat{y}$$

and

A56) $$S/N(B) = \left[\frac{D^{1/2}}{\Omega\, T(B)^{1/2}(T/T_1(B))^{1/2}} \right] \cdot M_2(B)\cdot \hat{y}$$

where again, Ω is the noise from a single acquisition and D is the total duration of the experiment. Of course, expressions A53)-A56) are essentially just definitions, and are the same expressions as were used in Appendix 1a; the only difference is the actual steady-state solutions for $M_1(A)$ and $M_1(B)$.

Appendix 2c. Demonstration that metabolite abundances enter only as a ratio in the expressions for saturation factors in the presence of exchange

As in the text, let

A57) $R = M_0(A)/M_0(B)$.

Then, from Eqs. A31) and A37), the expression for Σ can be written

A58) $\Sigma = M_0(A)\Sigma'$

where

A59) $$\Sigma' = \frac{b_2/T_1(A) + (a_1/T_1(B))(1/R)}{b_1 b_2 - a_1 a_2}.$$

Similarly, we can write

A60) $\Phi = M_0(A)\Phi'$

where

A61) $$\Phi' = \frac{a_2/T_1(A) + (b_1/T_1(B))(1/R)}{b_1 b_2 - a_1 a_2}.$$

In the same way, k1 and k2 can each be rewritten as the product of $M_0(A)$ and a term, k1' or k2', through which $M_0(A)$ and $M_0(B)$ enter only as R:

A62) $k1 = M_0(A)k1'$

A63) $k2 = M_0(A)k2'$.

The right-hand sides of Eqs. A51) and A52) are linear

combinations of k1 and k2, so that they too may be written (recalling that A = $M_1(A)$ and B = $M_1(B)$)

A64) $$M_1(A) = M_0(A)\cdot M_1(A)'$$

and

A65) $$M_1(B) = M_0(A)\cdot M_1(B)'$$

where, in $M_1(A)'$ and $M_1(B)'$, $M_0(A)$ and $M_0(B)$ enter only through the ratio R.

Finally, using these and the expressions Eqs. A53) and A54), we have for the saturation factors

A66) $$\begin{aligned} SF(A) &= M_2(A)\cdot \hat{y}/M_0(A) \\ &= M_1(A)\sin\theta/M_0(A) \\ &= M_0(A)\cdot M_1(A)'\sin\theta/M_0(A) \\ &= M_1(A)'\sin\theta \end{aligned}$$

and similarly,

A67) $$SF(B) = M_1(B)'\sin\theta.$$

From these expressions, it is clear that since $M_1(A)'$ and $M_1(B)'$ depend on $M_0(A)$ and $M_0(B)$ only through R, the same is true for SF(A) and SF(B).

Figure 1. Ratio of experimental signal-to-noise for arbitrary pulse parameters, to maximum signal-to-noise, as a function of flip angle, for a variety of T/T_1 values.

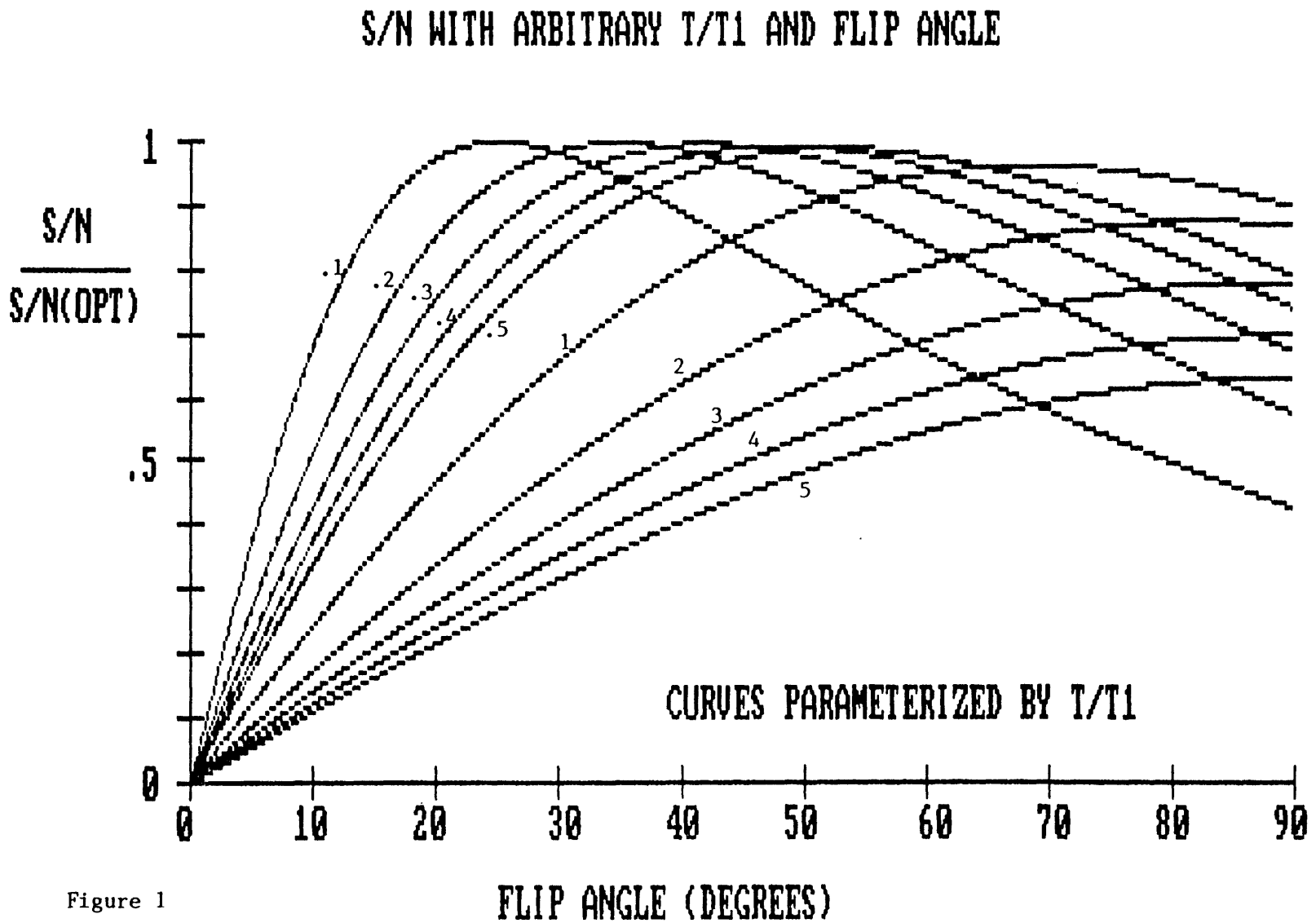
S/N WITH ARBITRARY T/T1 AND FLIP ANGLE
S/N
S/N(OPT)
1
.5
0
.1
.2
.3
.4
.5
1
2
3
4
5
CURVES PARAMETERIZED BY T/T1
0
10
20
30
40
50
60
70
80
90
FLIP ANGLE (DEGREES)

Figure 1

Figure 2. Saturation factors for arbitrary pulse parameters, as a function of flip angle, for a variety of T/T1 values.

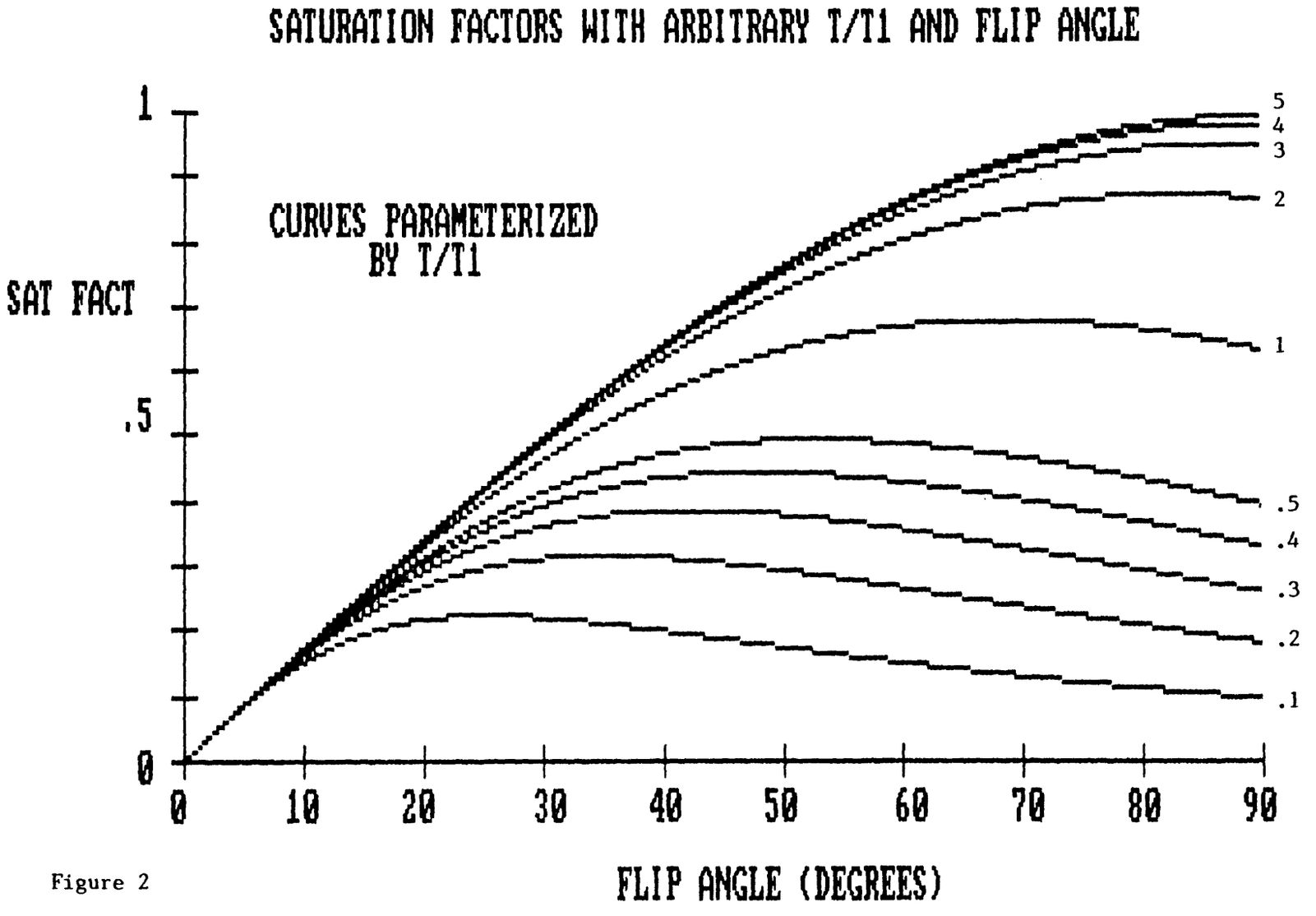
SATURATION FACTORS WITH ARBITRARY T/T1 AND FLIP ANGLE
CURVES PARAMETERIZED
BY T/T1
SAT FACT
1
.5
0
5
4
3
2
1
.5
.4
.3
.2
.1
0
10
20
30
40
50
60
70
80
90
FLIP ANGLE (DEGREES)

Figure 2

Figure 3. Ernst angles, the flip angles giving the maximum signal-to-noise for a fixed interpulse delay.

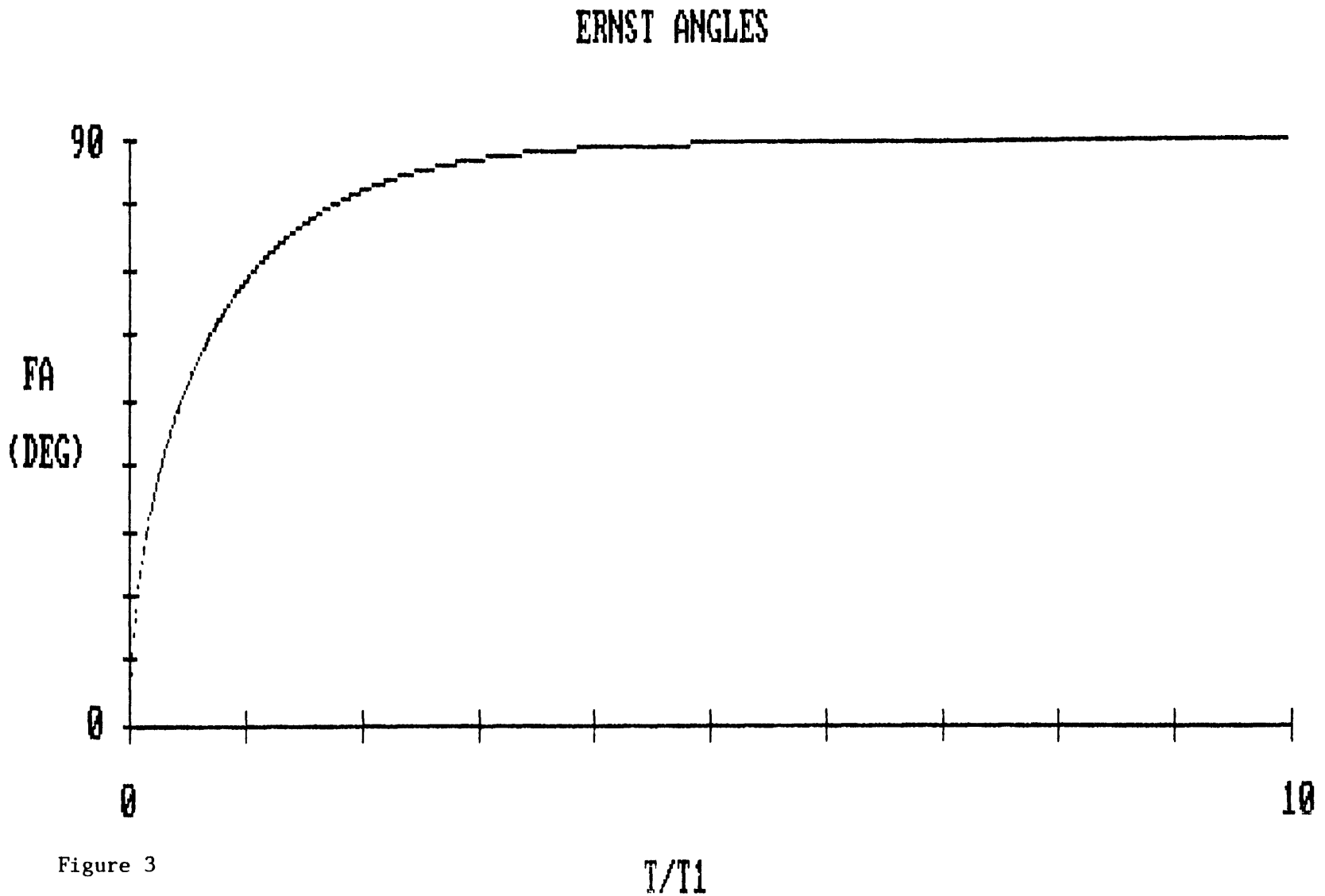

Figure 3

Figure 4. Ratio of experimental signal-to-noise with flip angle given by the Ernst angle, to maximum signal-to-noise, as a function of T/T_1.

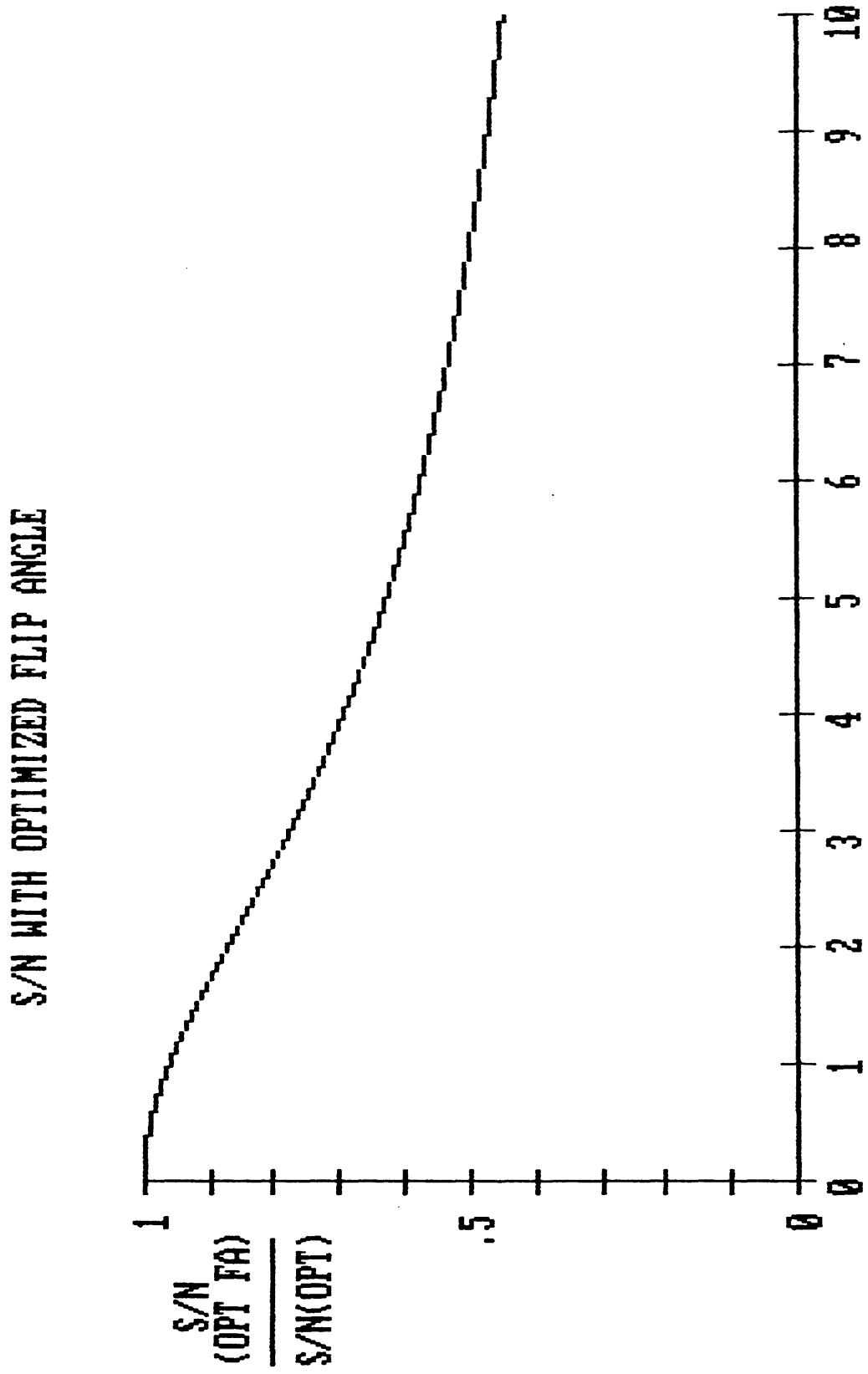
S/N WITH OPTIMIZED FLIP ANGLE
S/N (OPT FA) / S/N(OPT)
1
.5
0
0 1 2 3 4 5 6 7 8 9 10
T/T1

Figure 4

Figure 5. Saturation factors with flip angle given by the Ernst angle, as a function of T/T_1.

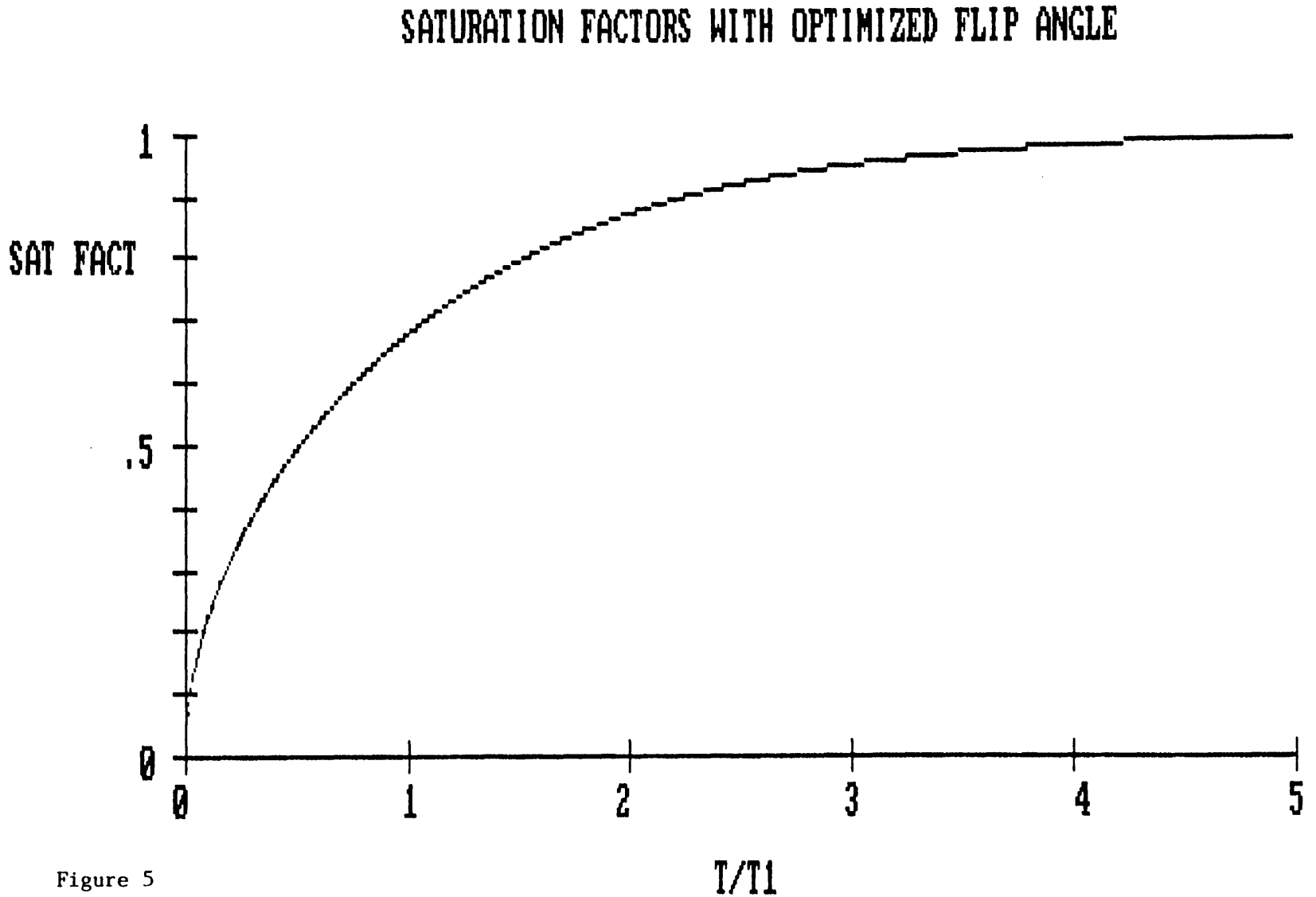
SATURATION FACTORS WITH OPTIMIZED FLIP ANGLE
SAT FACT
1
.5
0
0
1
2
3
4
5
T/T1

Figure 5

Figure 6a)-6f). Relative saturation factors for two noninteracting species A and B, as a function of flip angle, for a variety of T_1(A) and T_1(B) values.

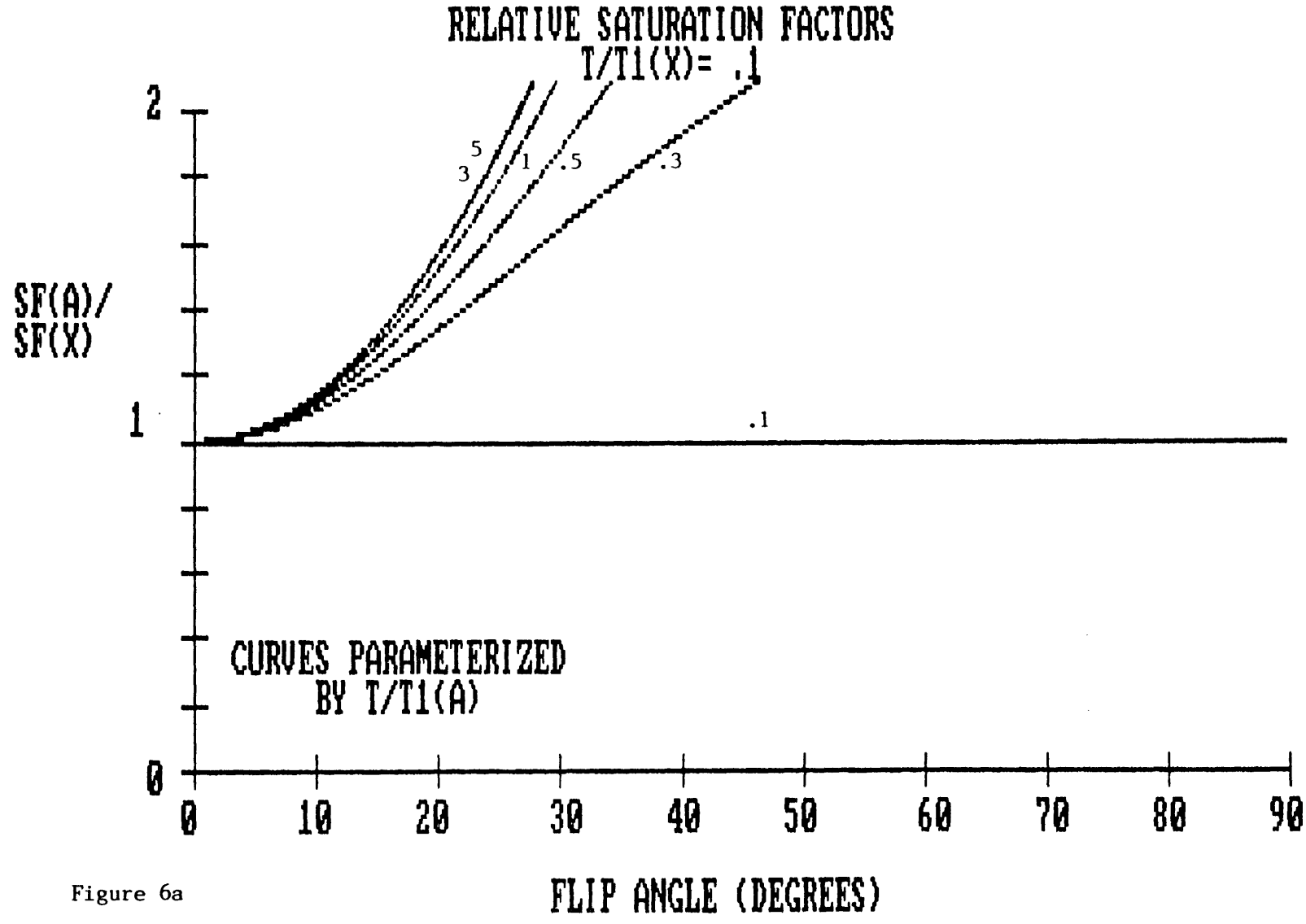
RELATIVE SATURATION FACTORS
T/T1(X)= .1
2
1
0
SF(A)/
SF(X)
5
3
1
.5
.3
.1
CURVES PARAMETERIZED
BY T/T1(A)
0
10
20
30
40
50
60
70
80
90
FLIP ANGLE (DEGREES)

Figure 6a

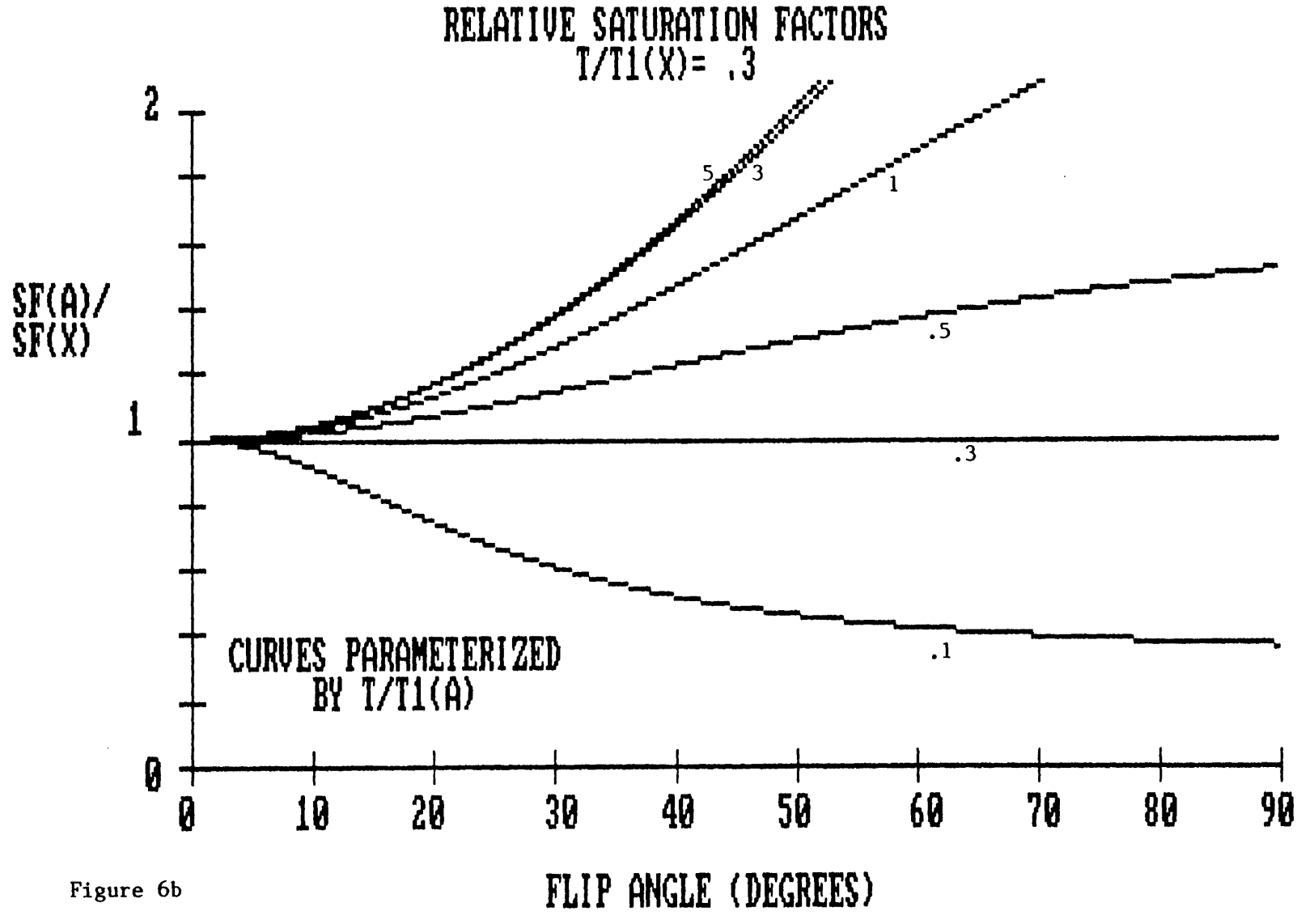
RELATIVE SATURATION FACTORS
T/T1(X)= .3
SF(A)/
SF(X)
2
1
0
5
3
1
.5
.3
.1
CURVES PARAMETERIZED
BY T/T1(A)
0
10
20
30
40
50
60
70
80
90
FLIP ANGLE (DEGREES)

Figure 6b

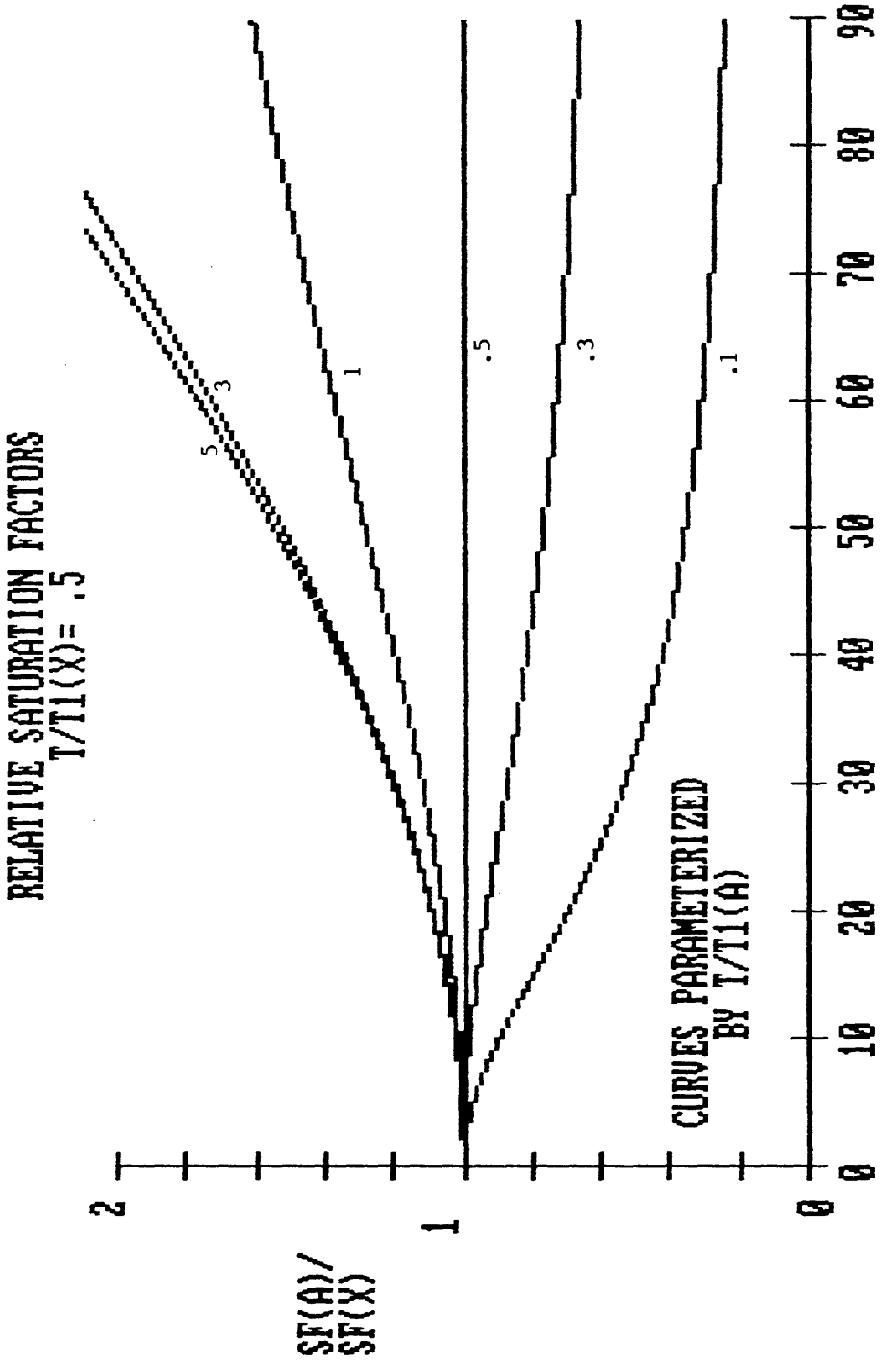
RELATIVE SATURATION FACTORS
T/T1(X)= .5
SF(A)/
SF(X)
2
1
0
0
10
20
30
40
50
60
70
80
90
FLIP ANGLE (DEGREES)
CURVES PARAMETERIZED
BY T/T1(A)
5
3
1
.5
.3
.1

Figure 6c

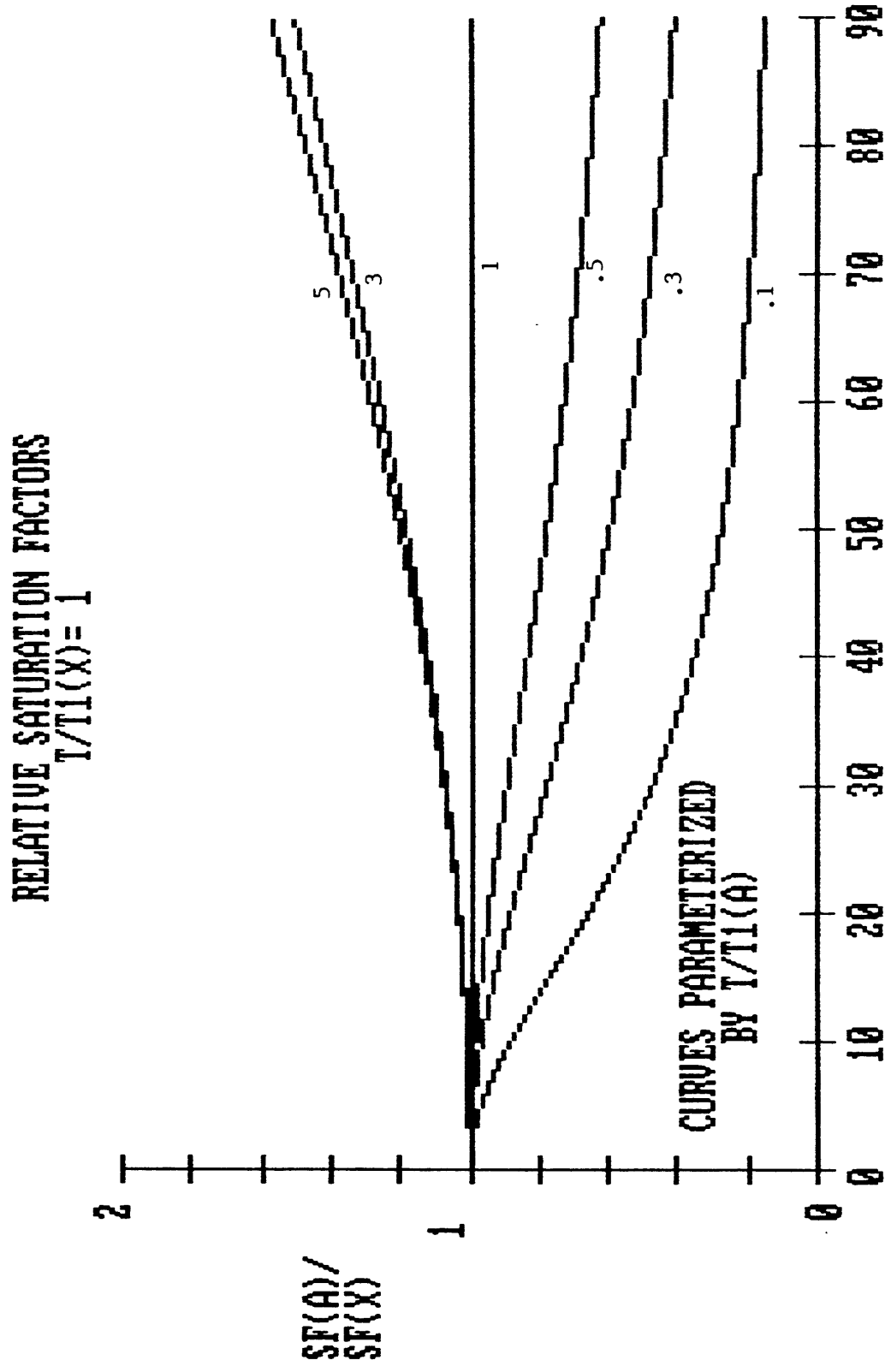
RELATIVE SATURATION FACTORS
T/T1(X)= 1
SF(A)/
SF(X)
2
1
0
0
10
20
30
40
50
60
70
80
90
FLIP ANGLE (DEGREES)
5
3
1
.5
.3
.1
CURVES PARAMETERIZED
BY T/T1(A)

Figure 6d

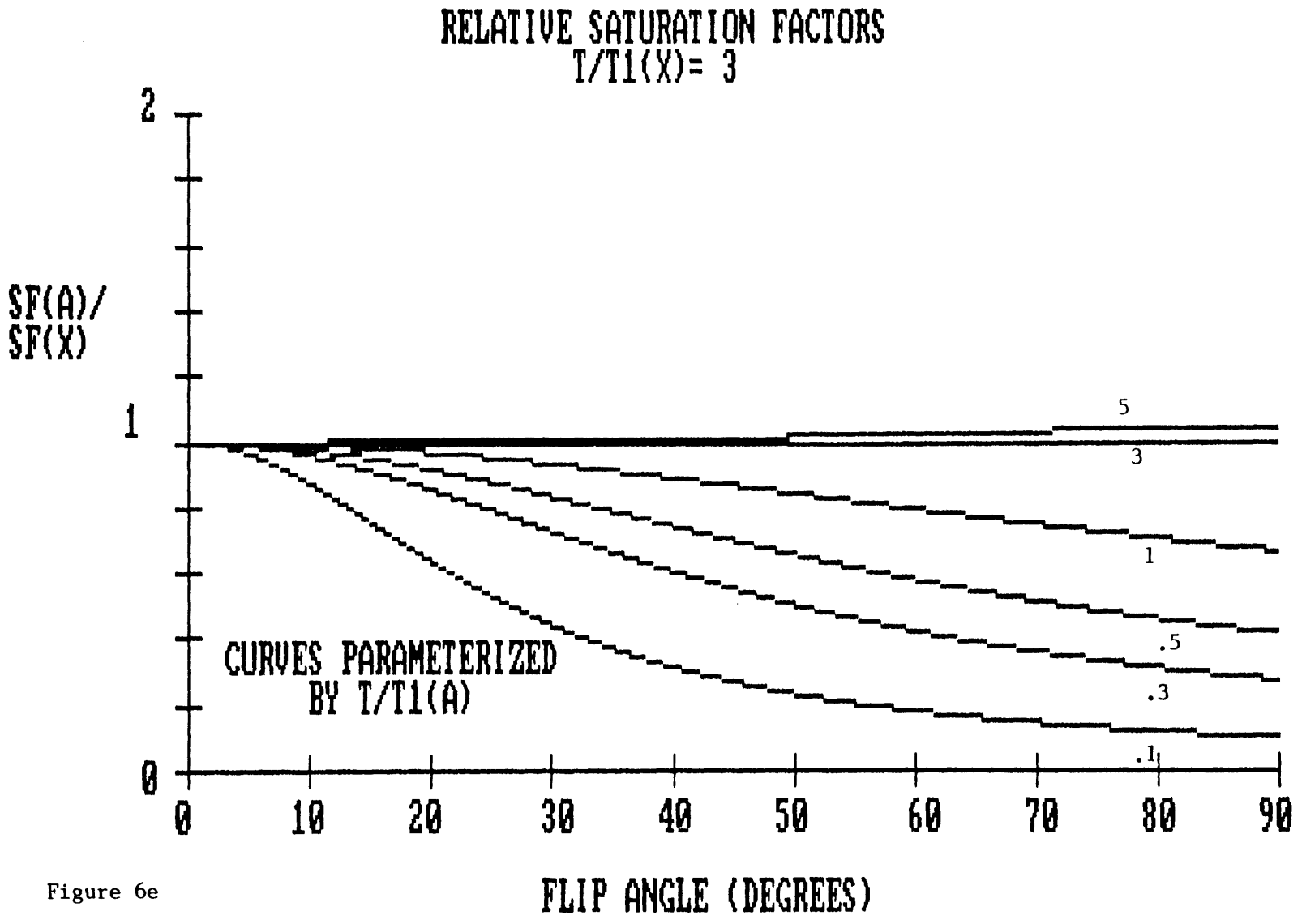
RELATIVE SATURATION FACTORS
T/T1(X)= 3
SF(A)/
SF(X)
2
1
0
5
3
1
.5
.3
.1
CURVES PARAMETERIZED
BY T/T1(A)
0
10
20
30
40
50
60
70
80
90
FLIP ANGLE (DEGREES)

Figure 6e

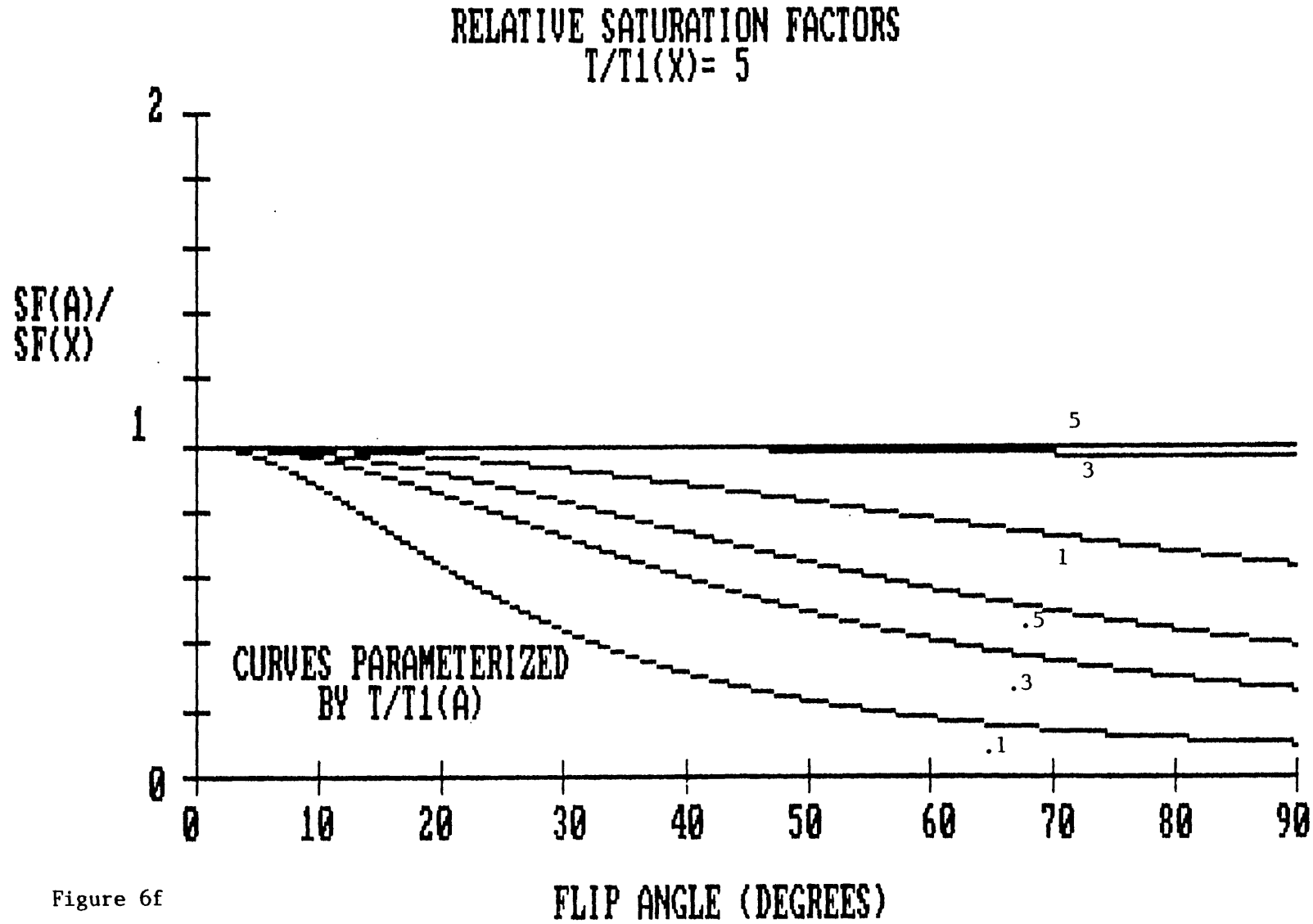
RELATIVE SATURATION FACTORS
T/T1(X)= 5
SF(A)/
SF(X)
2
1
0
5
3
1
.5
.3
.1
CURVES PARAMETERIZED
BY T/T1(A)
0
10
20
30
40
50
60
70
80
90
FLIP ANGLE (DEGREES)

Figure 6f

Figure 7a-7h). Effect of exchange on the saturation factors for two interacting species A and B, and the corresponding distortion of their relative saturation factor, for a variety of pulse, kinetic, and abundance parameters.

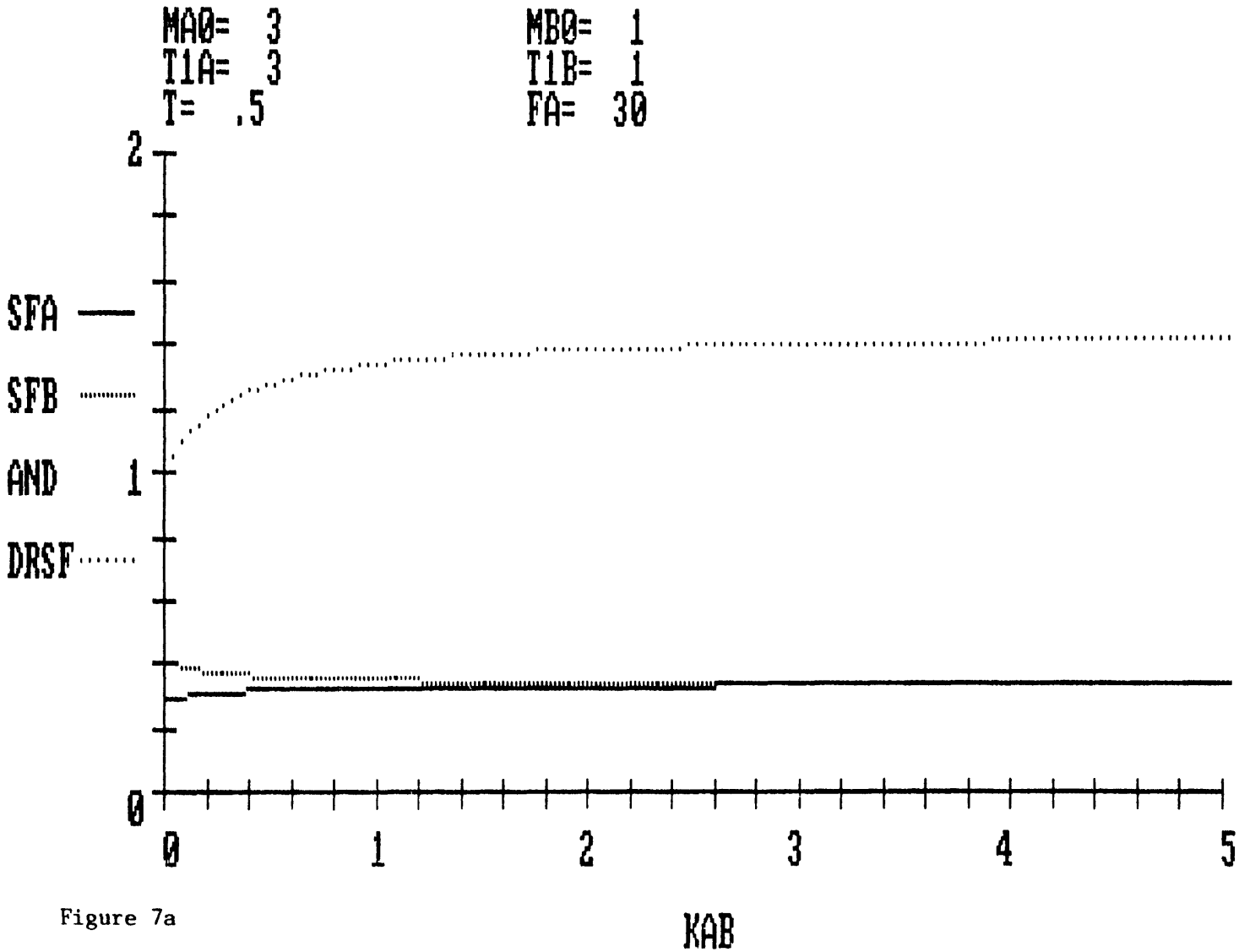

Figure 7a

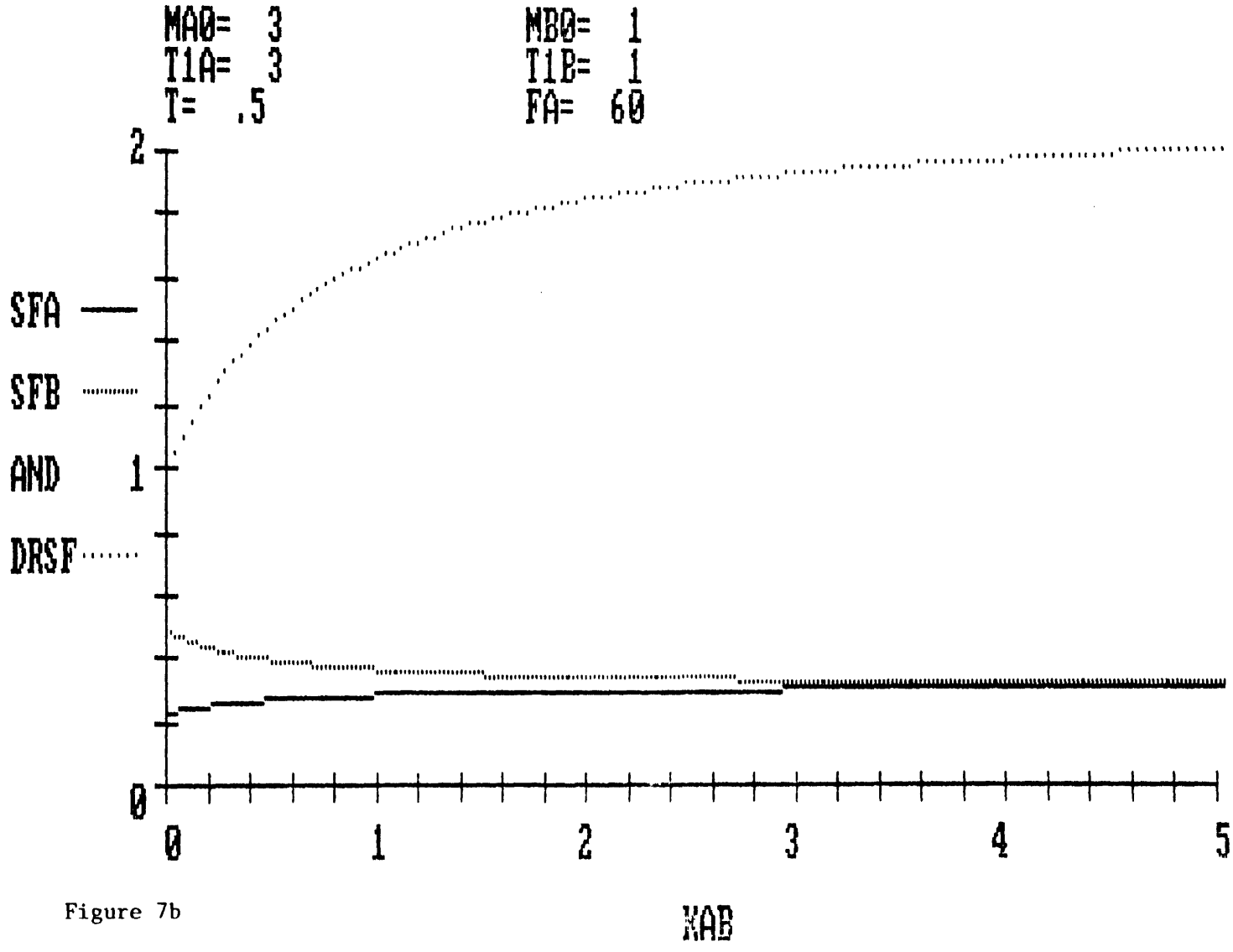

Figure 7b

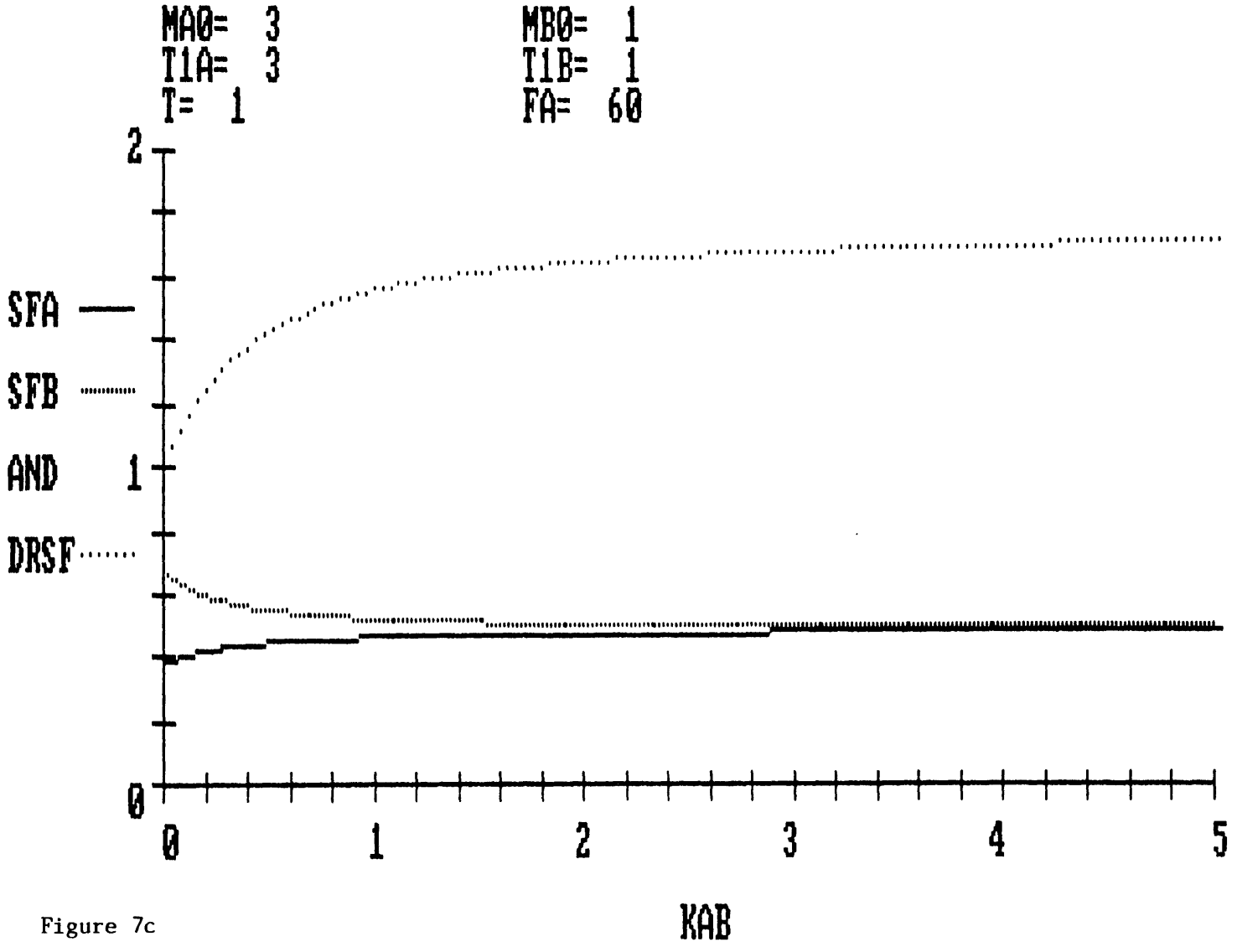

Figure 7c

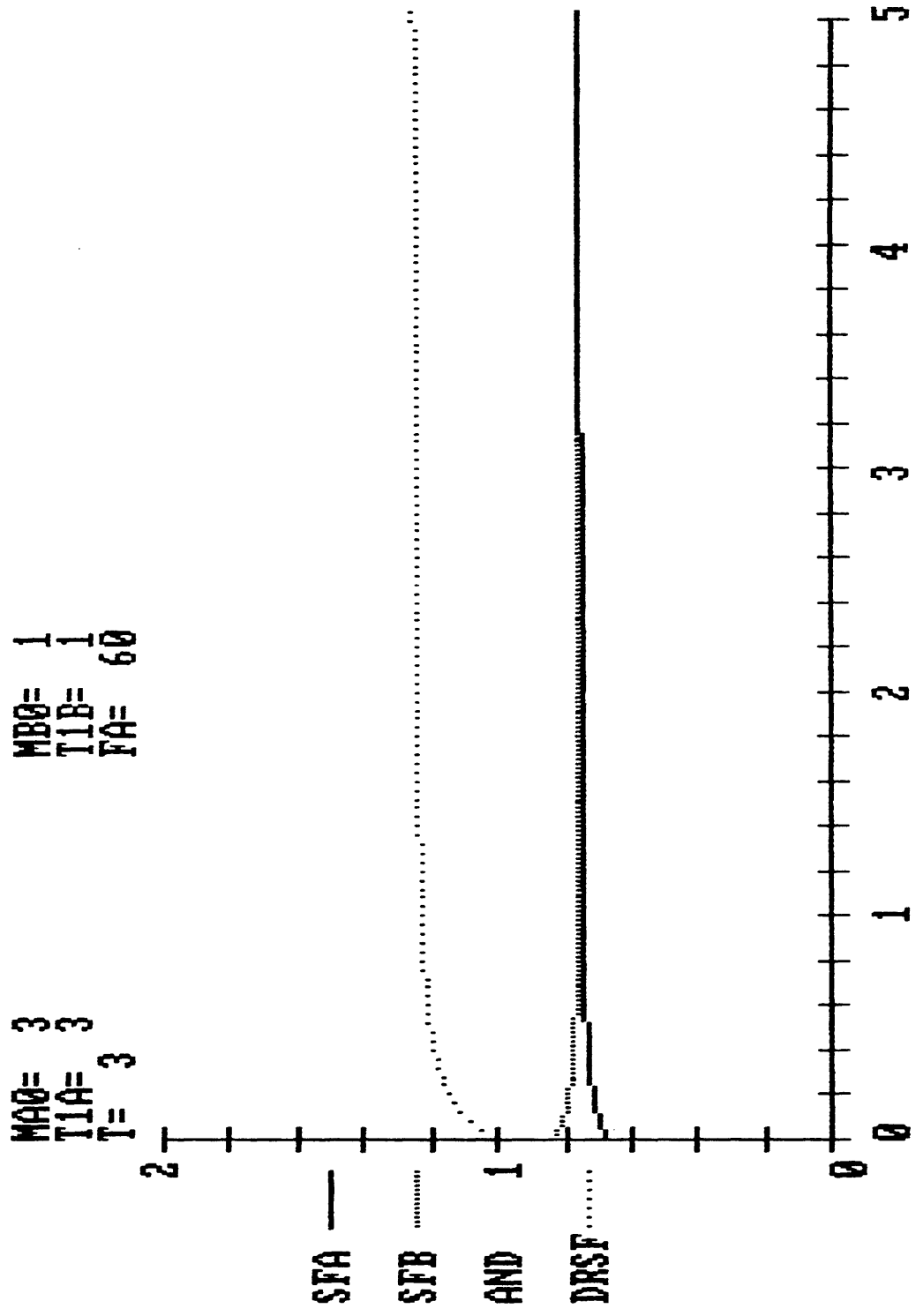

Figure 7d

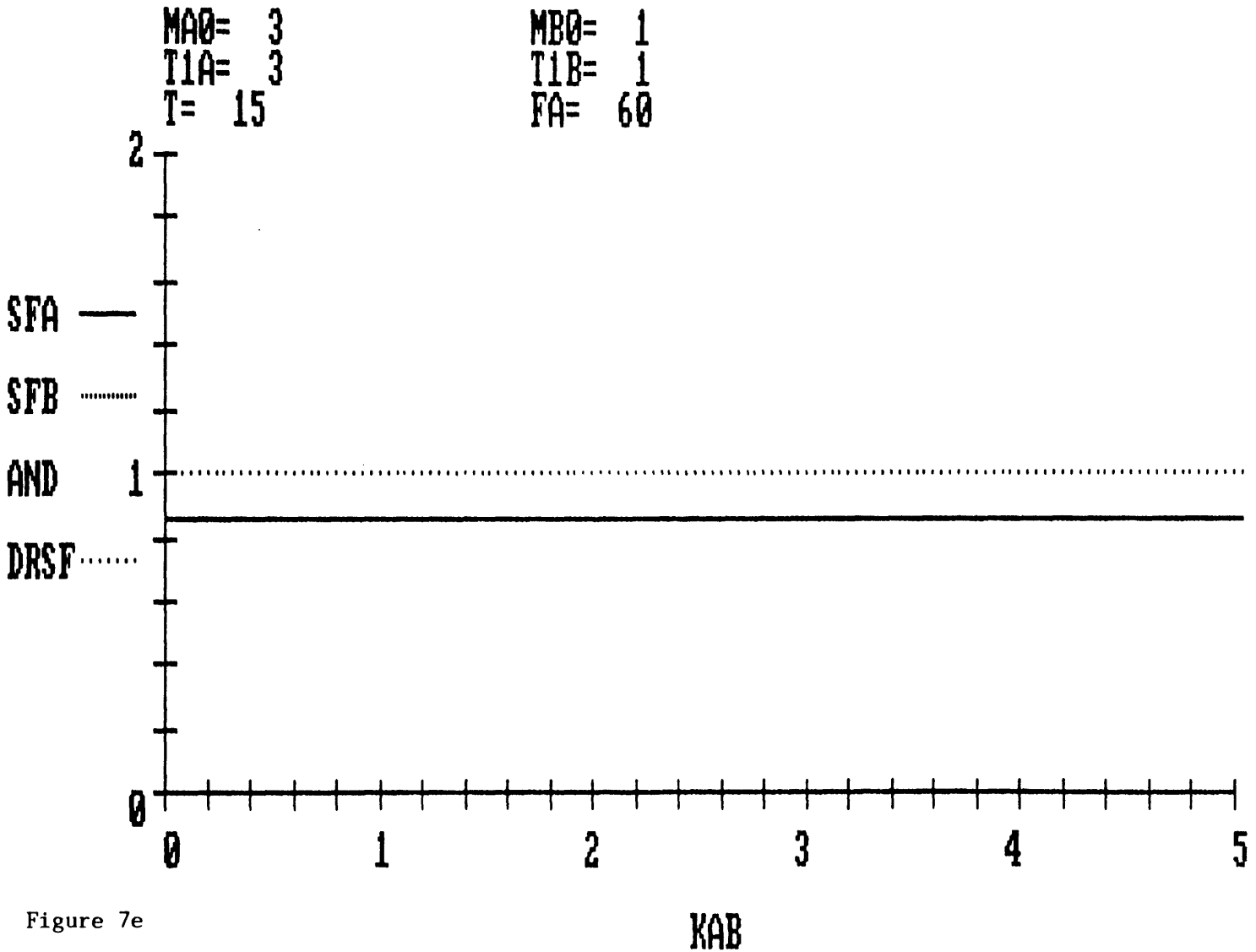

Figure 7e

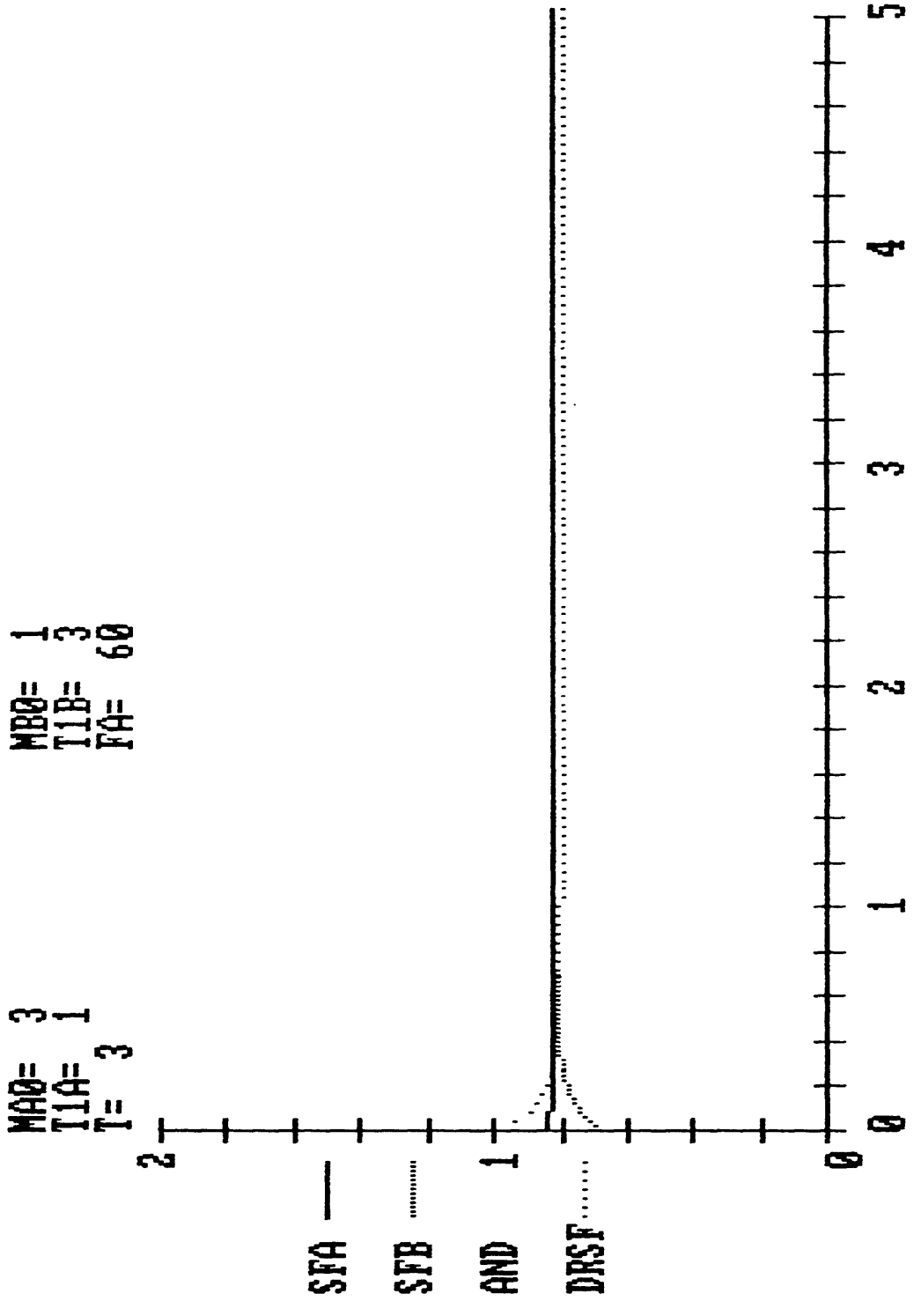

Figure 7f

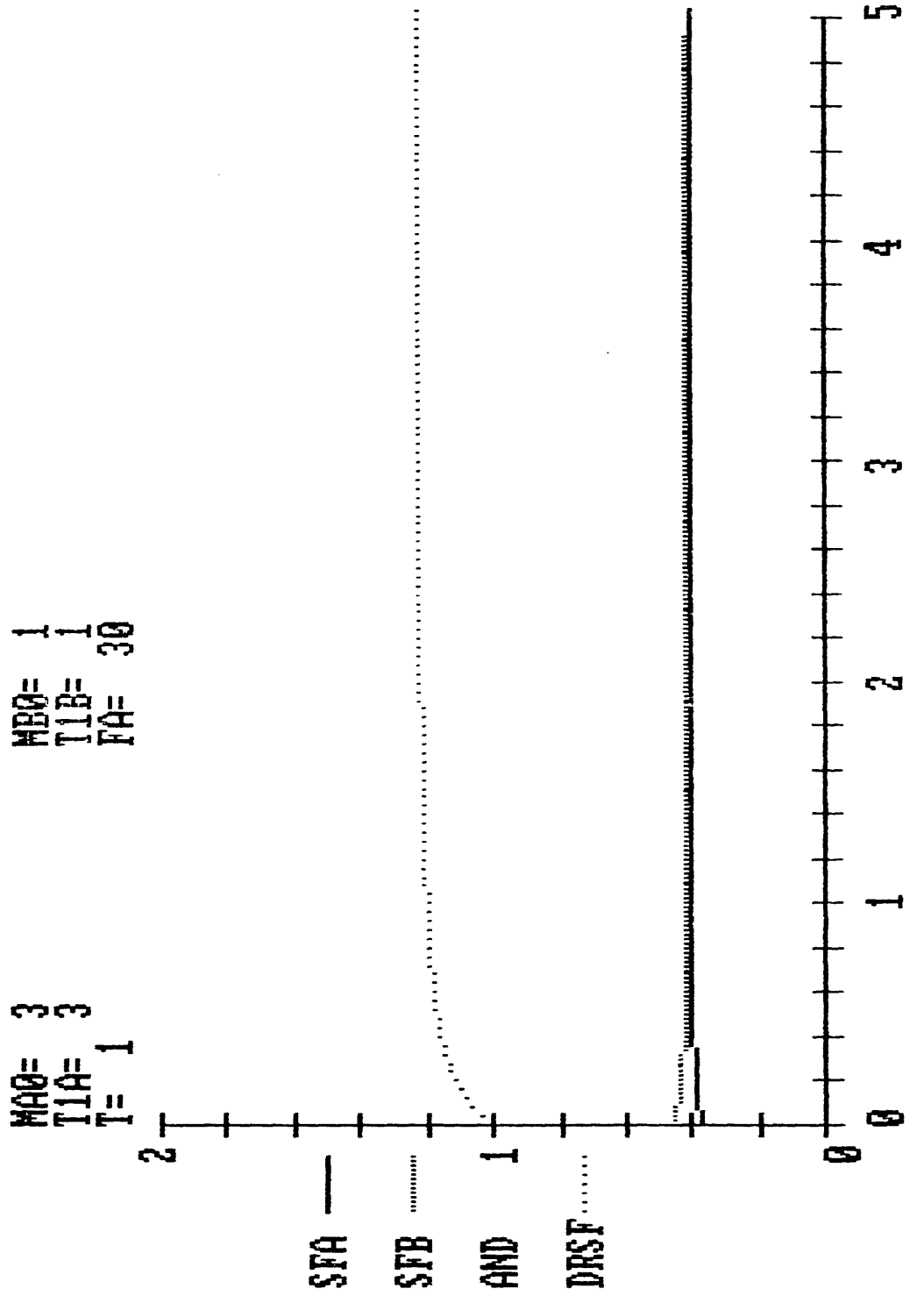

Figure 7g

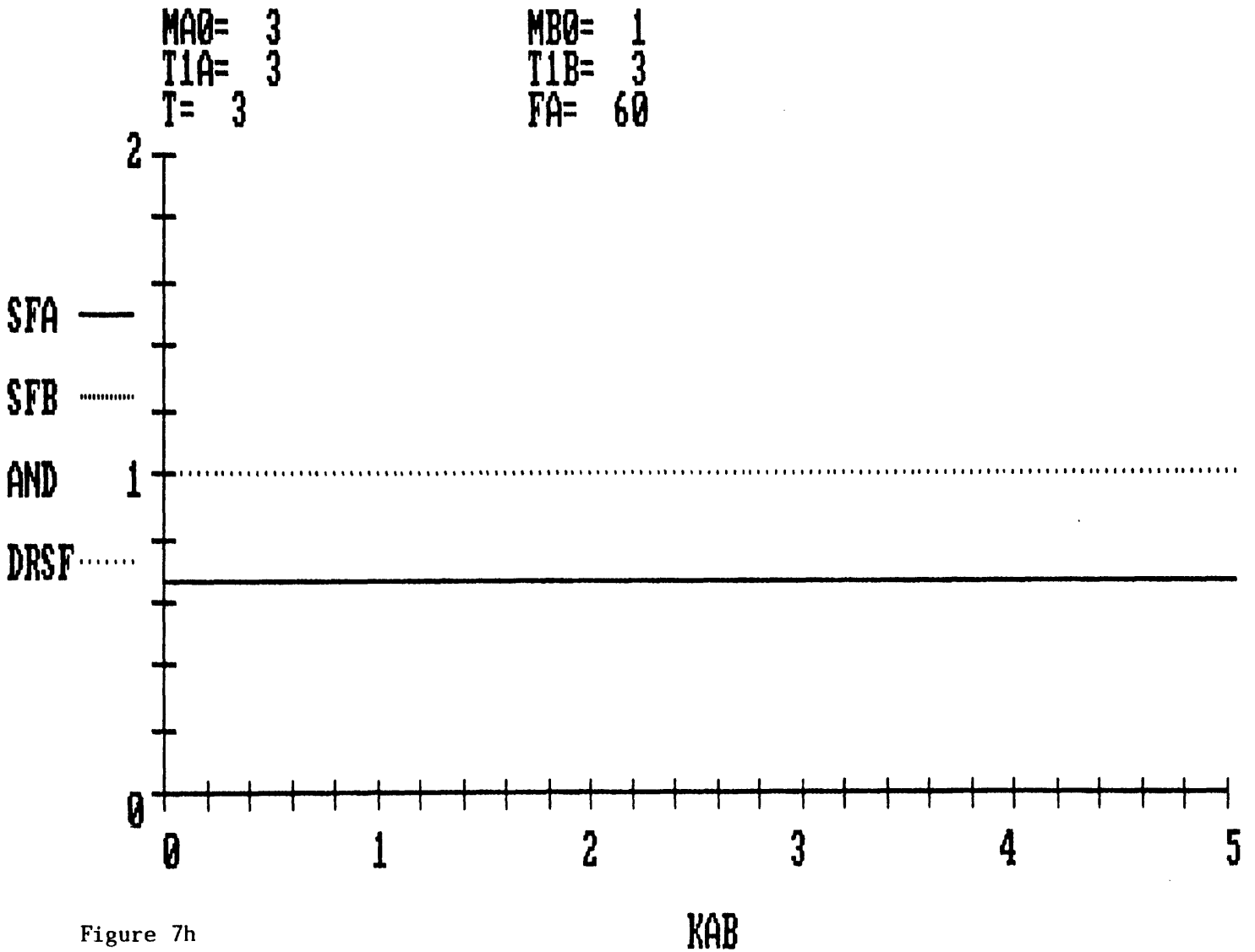

Figure 7h

Figure 8a)-8k). Errors due to neglect of exchange in the assessment of abundances of two interacting species A and B, plotted as a function of changes in Mø(A)/Mø(B), for a variety of pulse, kinetic, and abundance parameters.

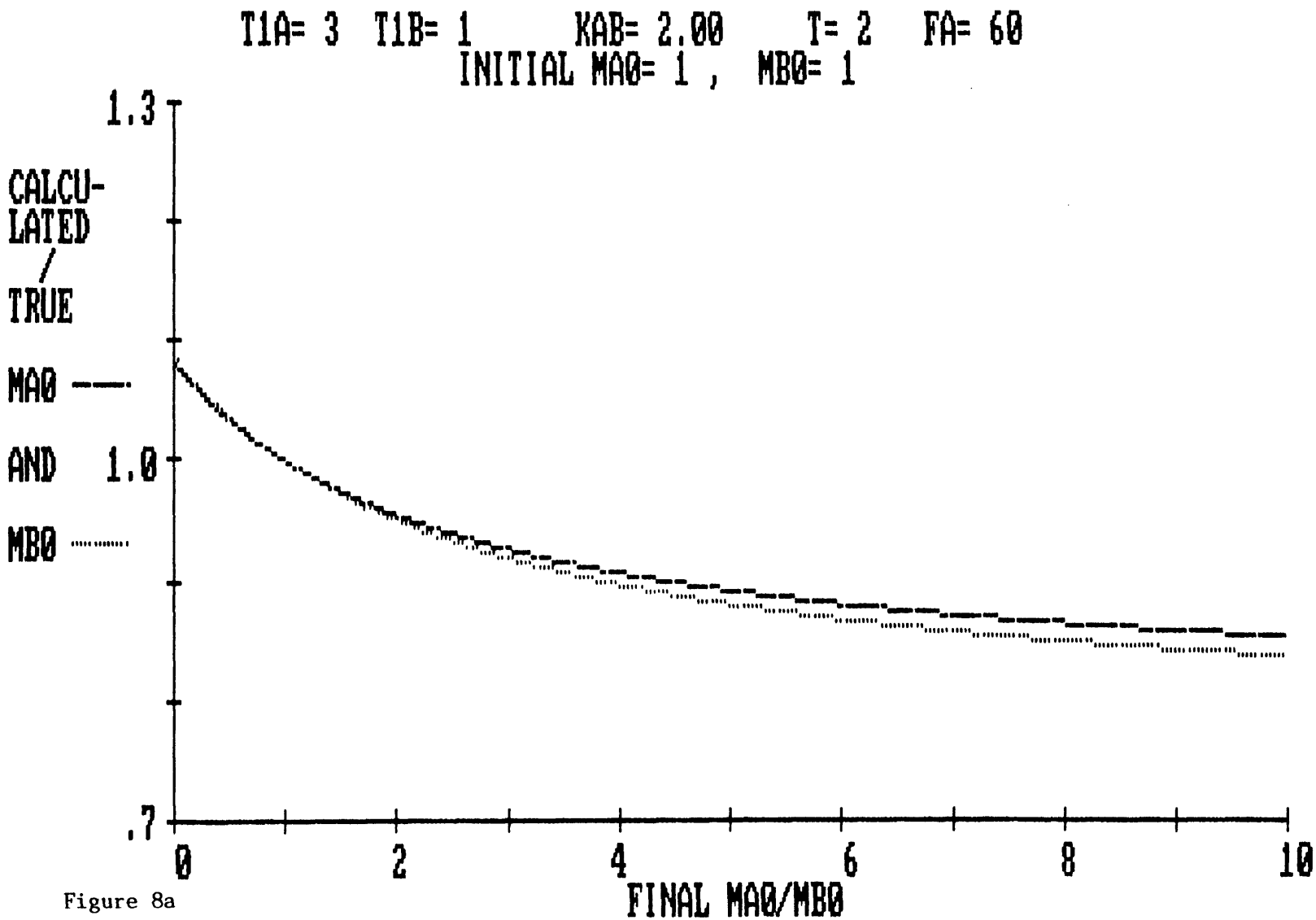
T1A= 3 T1B= 1 KAB= 2.00 T= 2 FA= 60
INITIAL MA0= 1 , MB0= 1
1.3
CALCU-
LATED
/
TRUE
MA0 ——
AND 1.0
MB0 .....
.7
0
2
4
6
8
10
FINAL MA0/MB0

Figure 8a

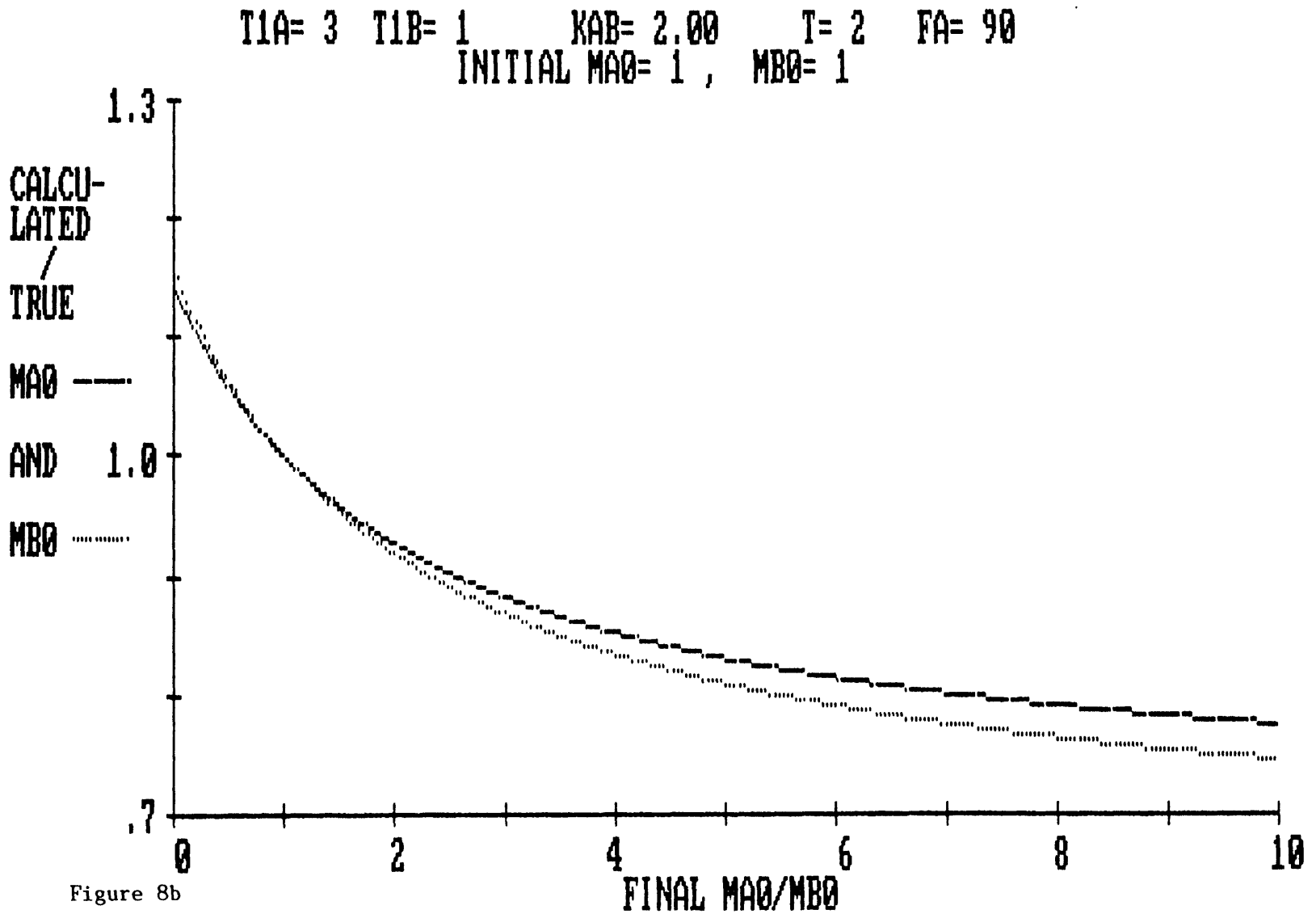
T1A= 3 T1B= 1 KAB= 2.00 T= 2 FA= 90
INITIAL MA0= 1 , MB0= 1
1.3
CALCU-
LATED
/
TRUE
MA0 ——
AND 1.0
MB0 .....
.7
0
2
4
6
8
10
FINAL MA0/MB0

Figure 8b

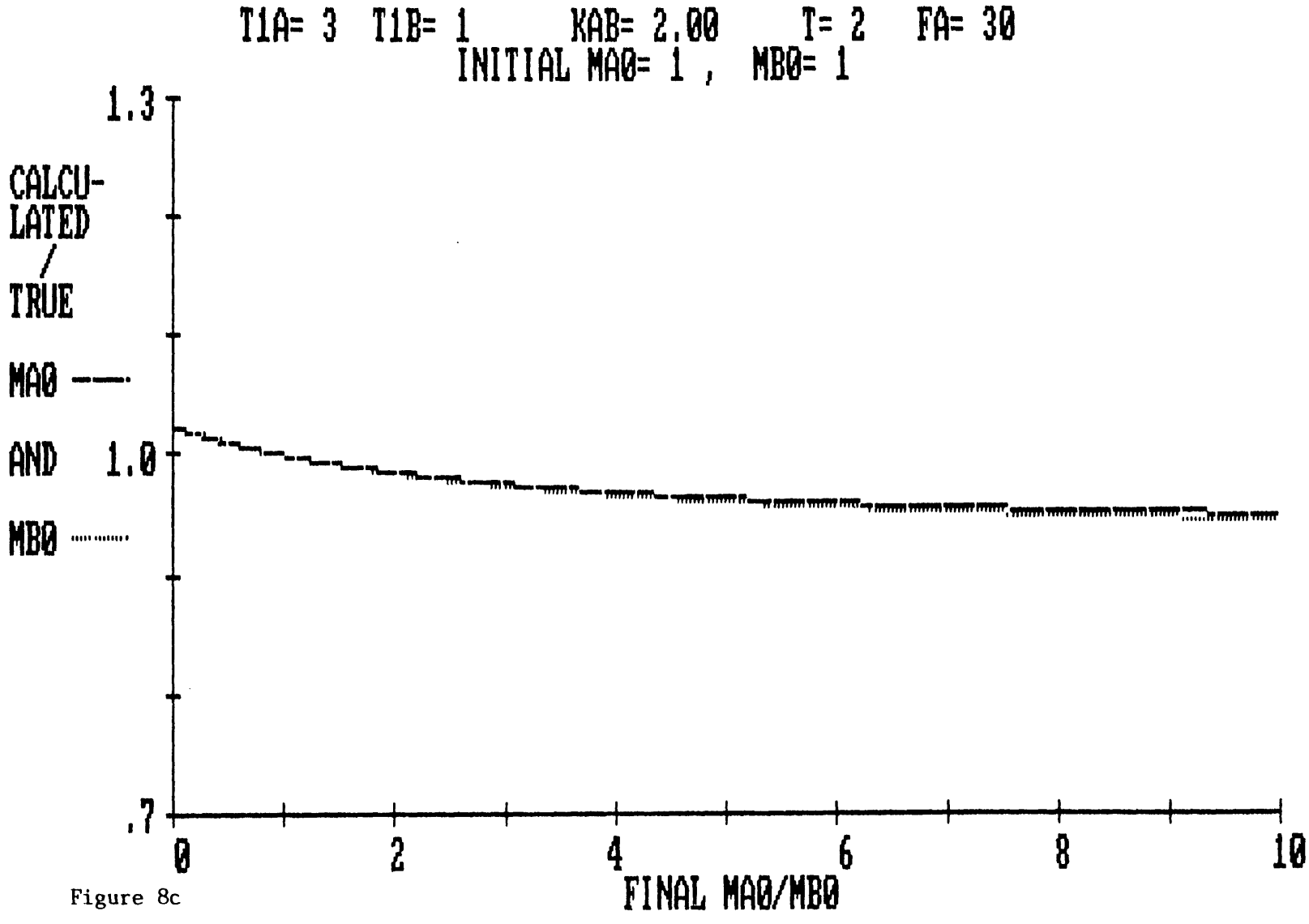
T1A= 3 T1B= 1 KAB= 2.00 T= 2 FA= 30
INITIAL MA0= 1 , MB0= 1
1.3
CALCU-
LATED
/
TRUE
MA0 ——
AND 1.0
MB0 .....
.7
0
2
4
6
8
10
FINAL MA0/MB0

Figure 8c

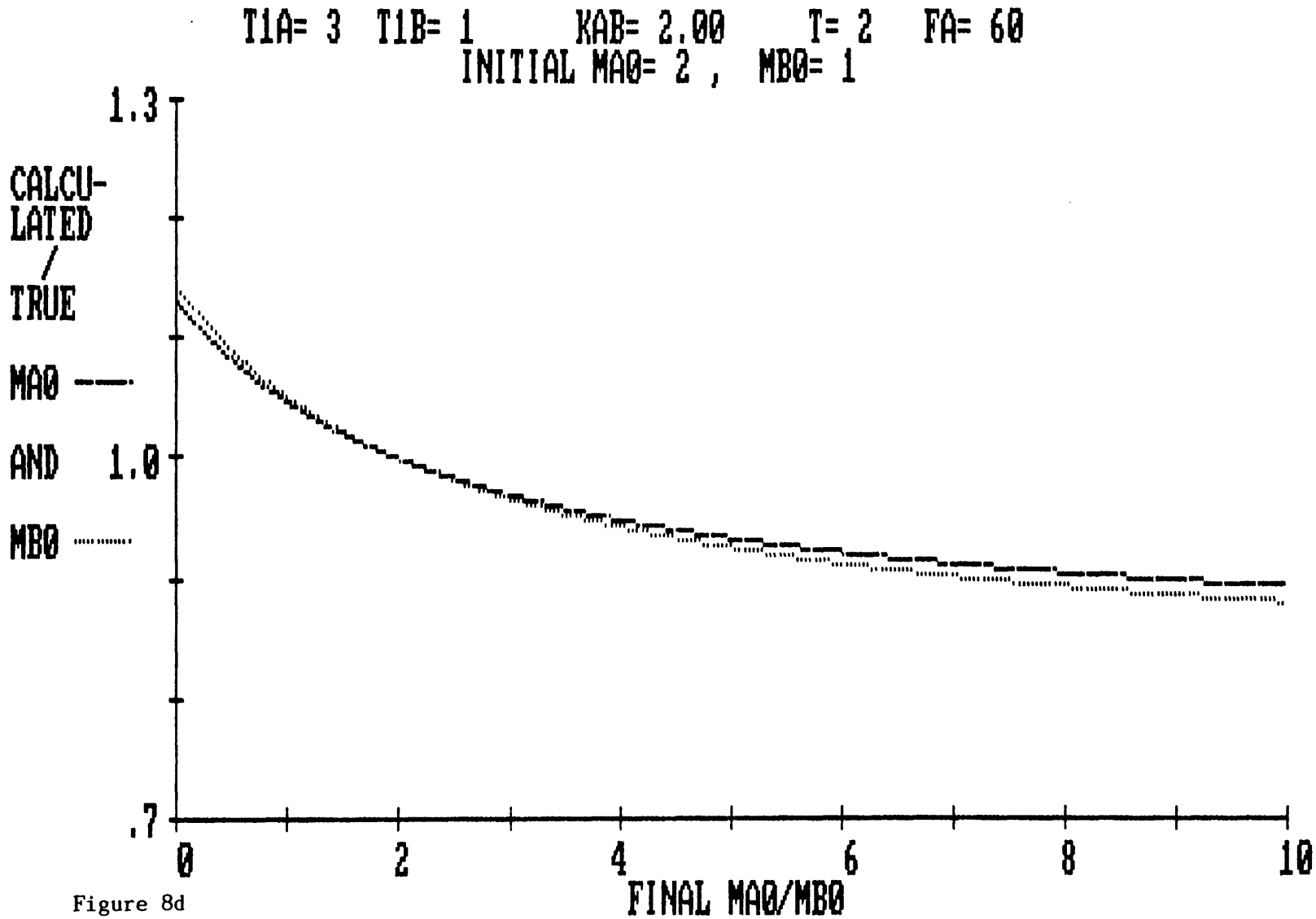
T1A= 3 T1B= 1 KAB= 2.00 T= 2 FA= 60
INITIAL MA0= 2 , MB0= 1
1.3
CALCU-
LATED
/
TRUE
MA0 ——·
AND 1.0
MB0 ·····
.7
0
2
4
6
8
10
FINAL MA0/MB0

Figure 8d

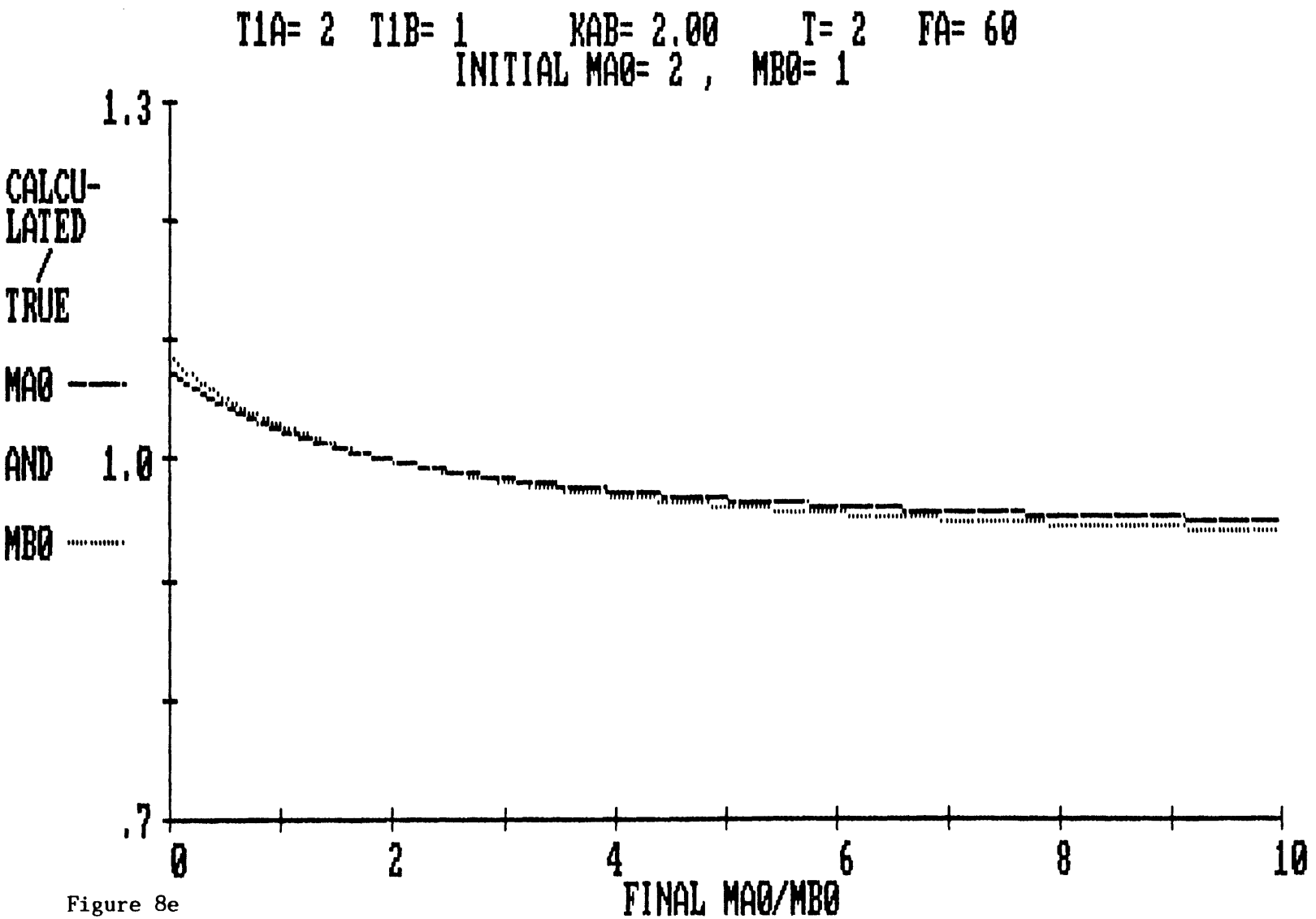
T1A= 2 T1B= 1 KAB= 2.00 T= 2 FA= 60
INITIAL MA0= 2 , MB0= 1
1.3
CALCU-
LATED
/
TRUE
MA0 ——
AND 1.0
MB0 .....
.7
0
2
4
6
8
10
FINAL MA0/MB0

Figure 8e

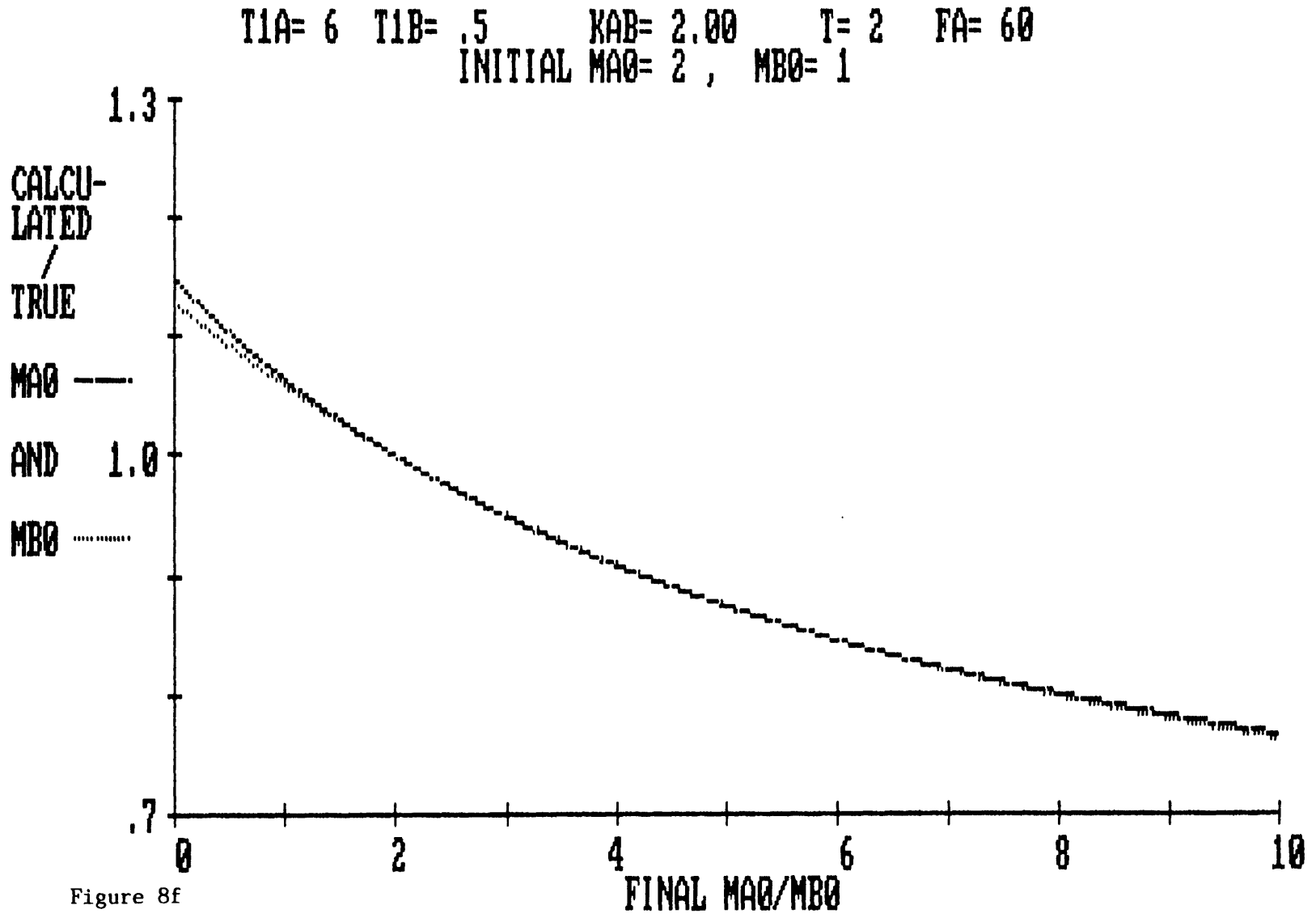
T1A= 6 T1B= .5 KAB= 2.00 T= 2 FA= 60
INITIAL MA0= 2 , MB0= 1
1.3
CALCU-
LATED
/
TRUE
MA0 ——
AND 1.0
MB0 .....
.7
0
2
4
6
8
10
FINAL MA0/MB0

Figure 8f

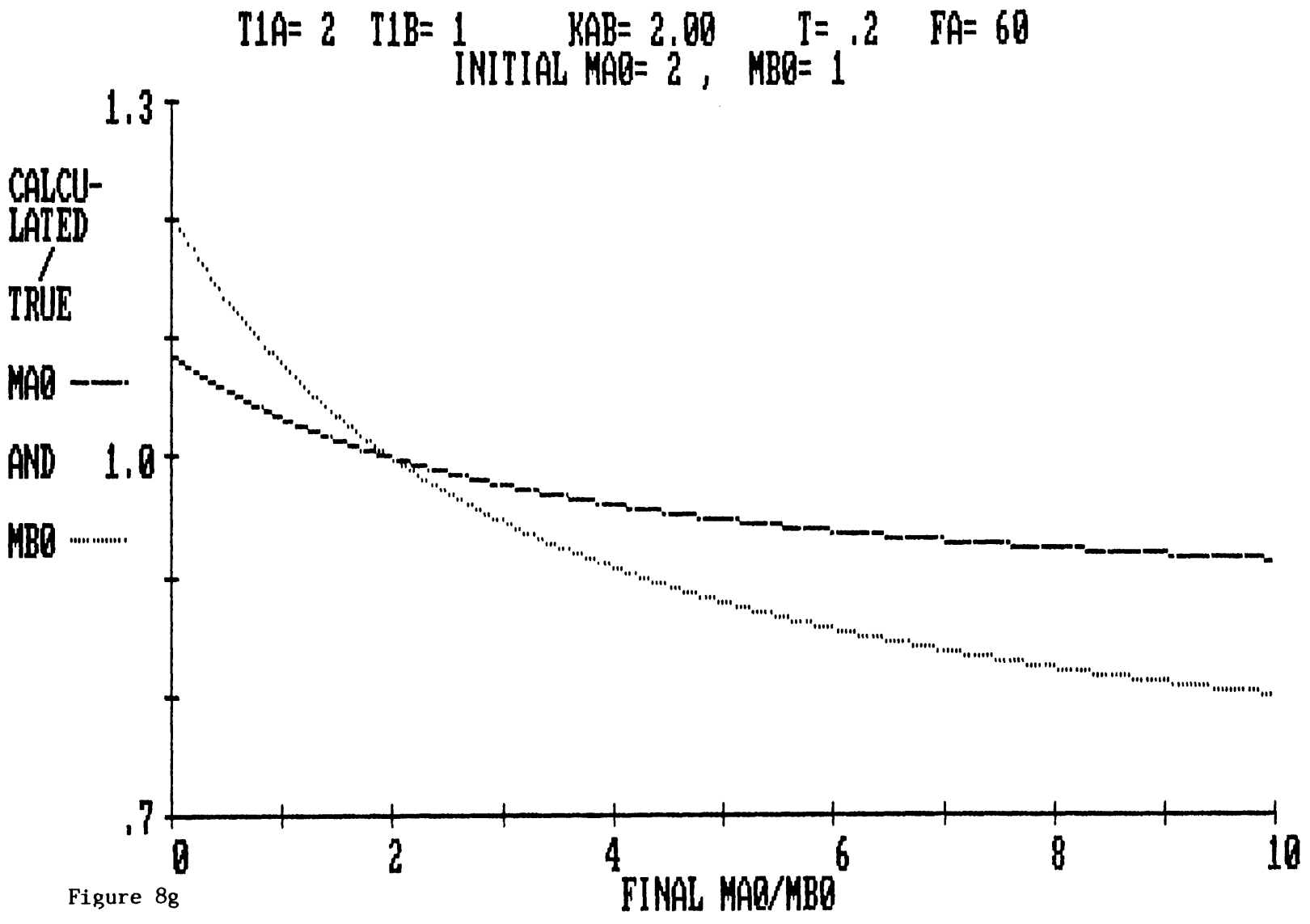
T1A= 2 T1B= 1 KAB= 2.00 T= .2 FA= 60
INITIAL MA0= 2 , MB0= 1
1.3
CALCU-
LATED
/
TRUE
MA0 ——
AND 1.0
MB0 ……
.7
0
2
4
6
8
10
FINAL MA0/MB0

Figure 8g

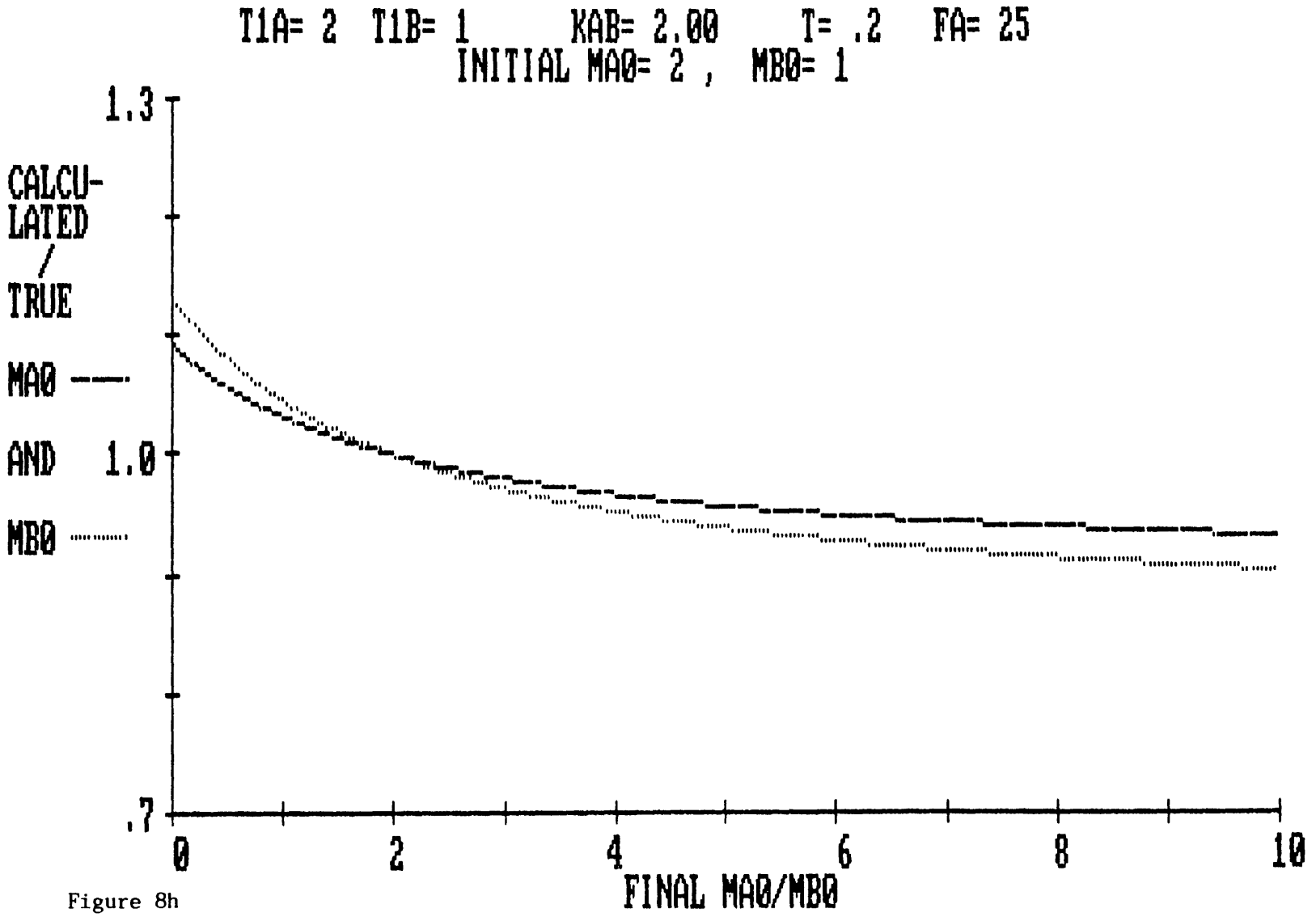
T1A= 2 T1B= 1 KAB= 2.00 T= .2 FA= 25
INITIAL MA0= 2 , MB0= 1
1.3
CALCU-
LATED
/
TRUE
MA0 ——
AND 1.0
MB0 .....
.7
0
2
4
6
8
10
FINAL MA0/MB0

Figure 8h

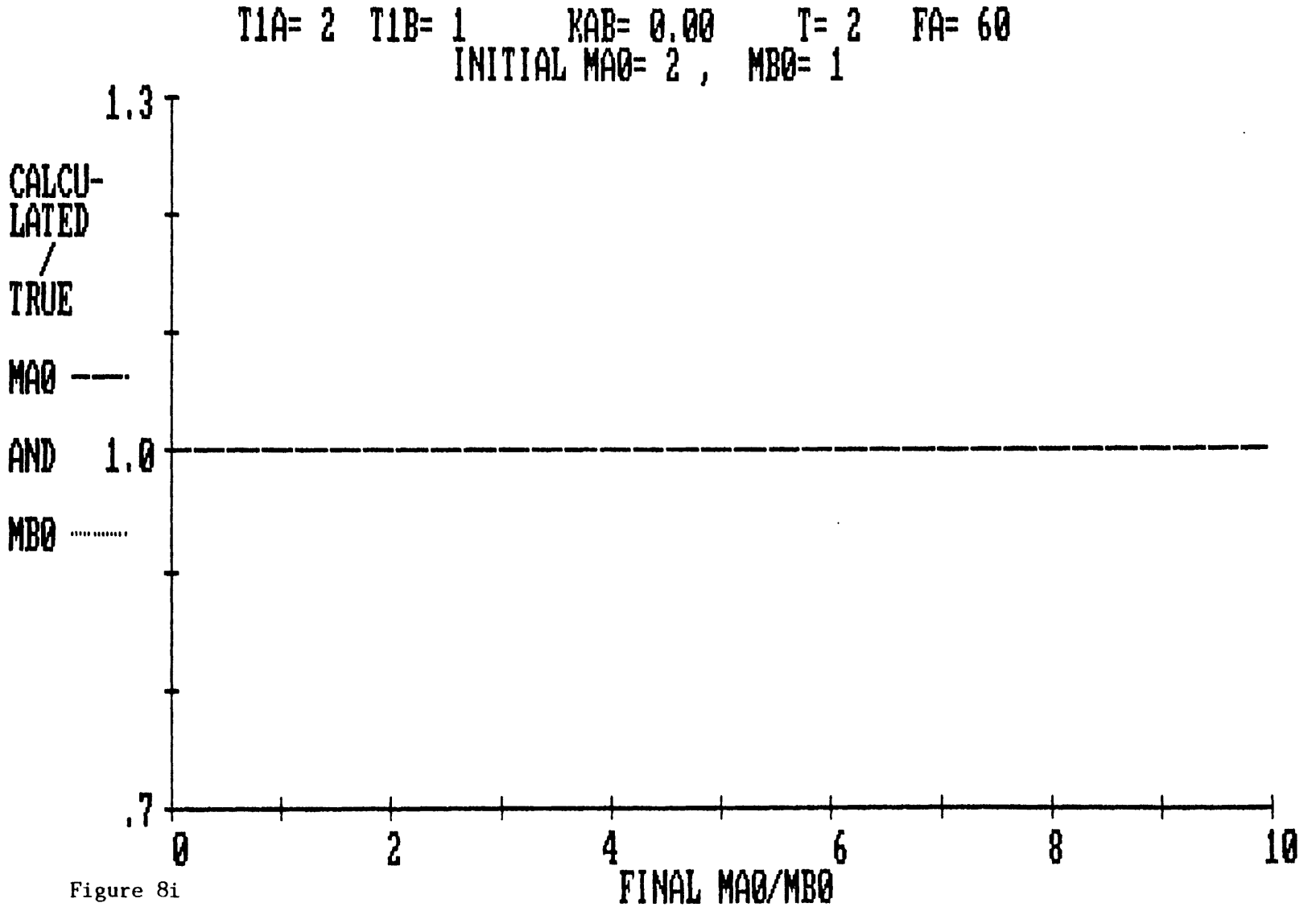
T1A= 2 T1B= 1 KAB= 0.00 T= 2 FA= 60
INITIAL MA0= 2 , MB0= 1
1.3
CALCU-
LATED
/
TRUE
MA0 ——
AND 1.0
MB0 .....
.7
0
2
4
6
8
10
FINAL MA0/MB0

Figure 8i

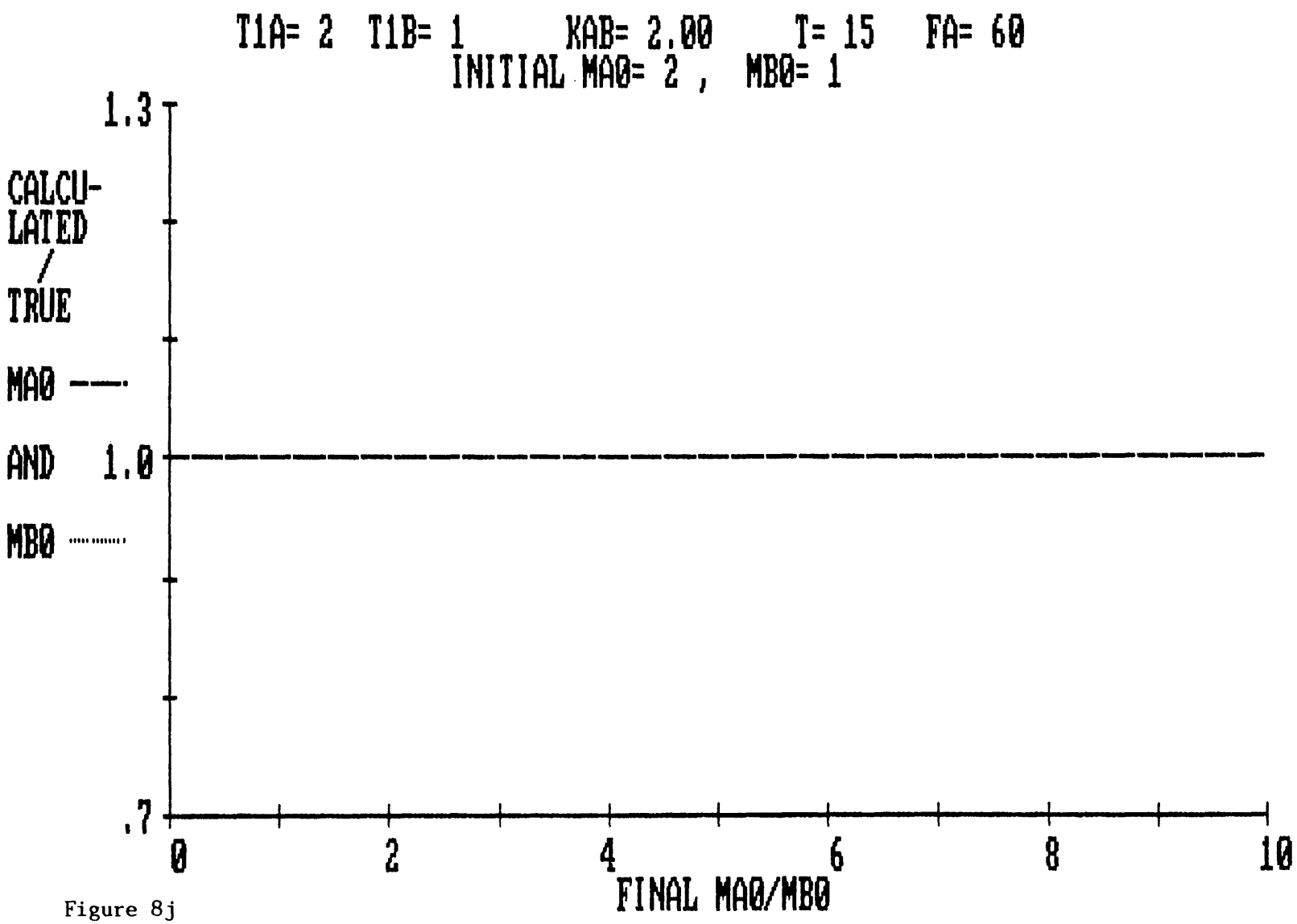
T1A= 2 T1B= 1 KAB= 2.00 T= 15 FA= 60
INITIAL MA0= 2 , MB0= 1
1.3
CALCU-
LATED
/
TRUE
MA0 ——·
AND 1.0
MB0 ·····
.7
0
2
4
6
8
10
FINAL MA0/MB0

Figure 8j

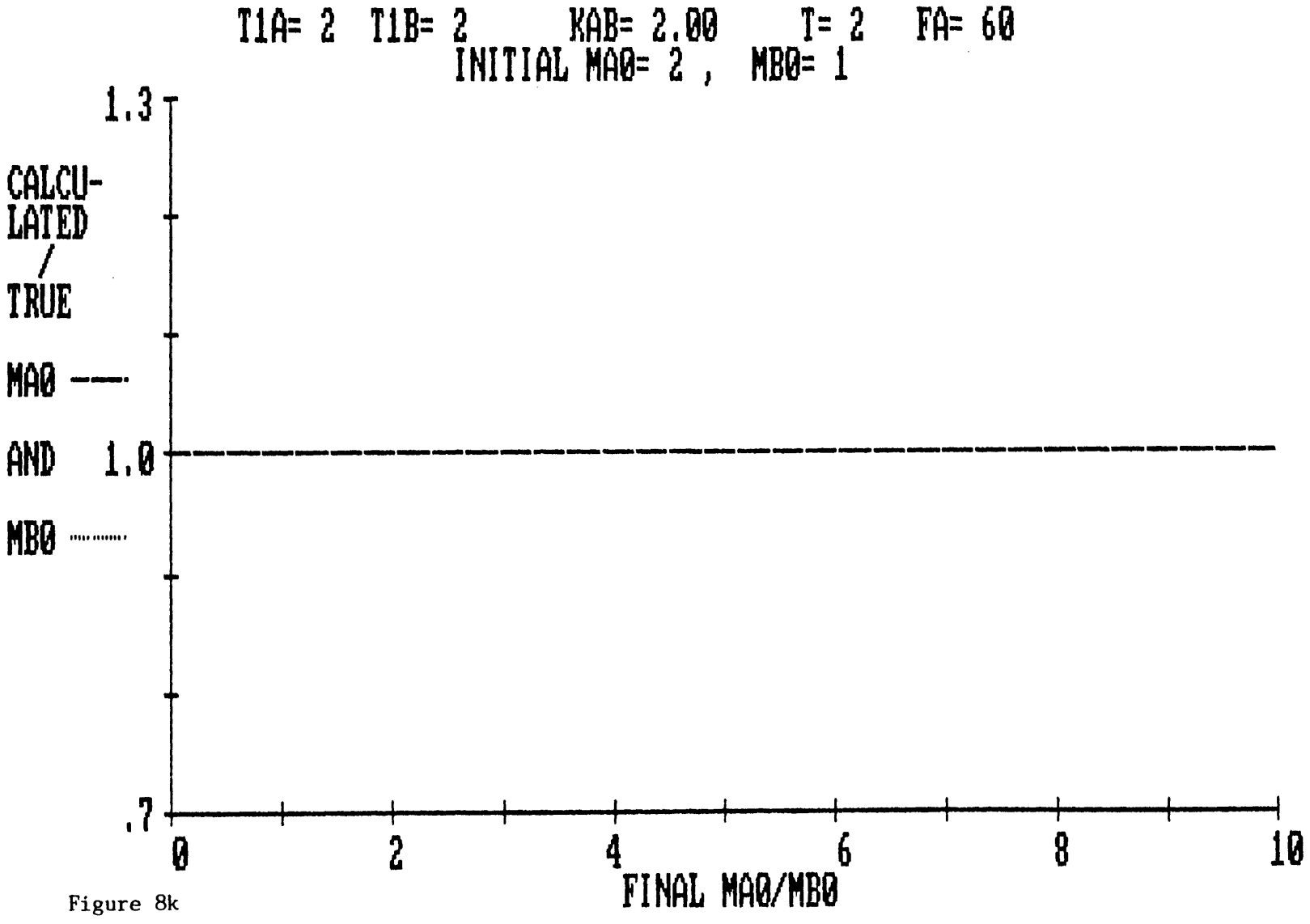
T1A= 2 T1B= 2 KAB= 2.00 T= 2 FA= 60
INITIAL MA0= 2 , MB0= 1
1.3
CALCU-
LATED
/
TRUE
MA0 ——
AND 1.0
MB0 .....
.7
0
2
4
6
8
10
FINAL MA0/MB0

Figure 8k

Chapter 3, Part 1

The Hemodynamic and Metabolic Response to Hypoxia of the Normal and Hypertrophied Rat Heart

Abstract

To define the relationship between metabolic state and hemodynamic function during prolonged global hypoxia in the normal and mildly hypertrophied adult rat heart, we used ^{31}P NMR spectroscopy to measure levels of adenosine triphosphate (ATP) and phosphocreatine (PCr) while monitoring hemodynamic function over a 24-minute period of hypoxia in a paced buffer-perfused isovolumic isolated heart preparation. During this period normal and hypertrophied hearts exhibited a similar and significant loss of high-energy phosphates (final ATP levels approx. 45%, final PCr levels approx. 20%, of control) and a significant degree of systolic and diastolic dysfunction (final left ventricular developed pressure approx. 20% of control value in both groups; end-diastolic pressure rising from 10 to 40 $\pm$ 6 mm Hg in the normal hearts, and to 61 $\pm$ 5 in the hypertrophic hearts). In both groups, the relationship between ATP concentration ([ATP]) and LVEDP, and between PCr concentration ([PCr]) and left ventricular developed pressure (LVDP), was linear throughout hypoxia. Furthermore, although the relationship between ATP concentration and LVEDP was not the same ($p < .01$) for the two groups, the difference could be fully accounted for by the increased muscle mass of the hypertrophied left ventricle: in the control group, LVEDP/LVW = -.69[ATP] + 79, while for the hypertrophied hearts, LVEDP/LVW = -.74[ATP] + 81, where LVEDP/left-ventricular weight (LVW) is in mm Hg/g and [ATP] is in % initial. Similarly, the relationship between [PCr] and LVDP/LVW was indistinguishable between the groups: in the control group, LVDP/LVW = .70[PCr] + 3.6, while for the hypertrophied hearts, LVDP/LVW = .72[PCr] + 1.5, where LVDP/LVW is in mm Hg/g and [PCr] is in % initial ATP concentration. We conclude that during hypoxia in this heart preparation and in this model of hypertrophy, [ATP] is an excellent predictor of diastolic (but not systolic)

dysfunction, while [PCr] is an excellent predictor of systolic (but not diastolic) dysfunction. Further, the additional diastolic stiffening exhibited by the hypertrophied hearts over the control hearts during hypoxia can be accounted for by the increased mass of the hypertrophied left ventricle, without the need to invoke a defect in high energy phosphate metabolism.

Introduction

The nature and extent of the cardiac changes which occur in the hypertrophy response to the increased demand of pressure overload may range from a simple replication of normal structures to a greater or lesser alteration of a variety of processes involving energy synthesis and delivery. Among these are changes in the myosin[1] and creatine kinase[2] enzyme systems, as well as in other biochemical systems. In addition, there is a decrease in capillary reserve in hypertrophy[3,4], as well as other structural changes (for an overall review, see Alpert[5]).

During hypoxia, both systolic and diastolic dysfunction may be exacerbated in the hypertrophied heart. Hypotheses put forth to account for the decrease in systolic pressure early in hypoxia include a failure of the energy-dependent Ca^{++} transporting capability of the sarcolemma[6], and accumulation of intracellular H^{+}[7] or anions[8]. Any of these processes may be accelerated in the hypertrophied myocardium, in which the balance between energy production and delivery on the one hand, and energy requirements on the other, may be compromised even in the well-oxygenated state as a result of the biochemical and structural changes mentioned above. Similarly, many of the processes which enable the myocardium to relax between contractions are energy-dependent[9], and so may be upset to a greater extent when hypoxic injury is imposed on the hypertrophied, as opposed to the normal, heart. Further, in addition to changes in cellular function, the hypertrophied heart is characterized by its overall geometry--expression at the organ level of any given functional or biochemical state of individual myocytes will depend on their number and physical configuration[10]. Indeed, it is likely that the clinically important increased susceptibility of hypertrophied hearts to injury during ischemia[11,12,13] is a direct manifestation of these various cellular and organ-level alterations.

The critical net result of the changes accompanying cardiac hypertrophy may be an alteration in the availability of the two main cardiac high-energy phosphates (HEPs), adenosine triphosphate (ATP) and phosphocreatine (PCr), to structures in the myocyte. Although the precise nature of the relationship between these metabolites is uncertain, it is clear that while each forms a part of the same overall integrated scheme of energy production, delivery, and utilization in the myocyte, the processes in which they are most directly involved may be quite different.

A number of studies have shown that in the presence of functioning CK, it is changes in CP, as opposed to in ATP, which correlate with contractile ability in muscle[14,15], in spite of the fact that ATP is the direct substrate for the reactions of excitation-contraction-relaxation coupling. This latter fact was demonstrated directly in the elegant experiments of Cain and Davies[16], who, studying the levels of HEPs in contracting muscle during CK inhibition with fluorodinitrobenzene, found that PCr levels were unchanged during contraction, while ATP levels fell. In addition, however, the muscle lost its ability to respond to stimulation after only few beats, at a time when ATP levels were still high. This and other evidence points to the conclusion that the ATP involved in contraction is formed primarily from PCr via the CK reaction, although this essential contractile pool may comprise only a small percentage of the total intracellular ATP.

On the other hand, it has also been suggested that the ATP involved in membrane function may not be closely linked to oxidative phosphorylation and the CK reaction, but rather that it is glycolytic ATP which serves this function[17,18]. In addition, it is likely that the activity of the ATP-dependent calcium uptake pumps of the sarcoplasmic reticulum (SR) may be more linked with overall ATP than with that fraction derived from CP. Indeed, a preponderance of recent evidence indicates that diastolic contracture during hypoxia

or ischemia occurs due to a reduction of cellular energy stores, and is related to overall ATP depletion.

In their experiments on the ischemic dog heart, Gudbjarnason et. al. (Ref. 14) observed what they referred to as the "kinetic heterogeneity" of ATP and PCr depletion during ischemia, during which PCr levels fell markedly before there was a significant decrease in ATP content. This greater lability of PCr than of ATP during ischemia and hypoxia has since been well established. However, parallel to these biochemical processes, there is also a "kinetic heterogeneity" in the development of systolic and diastolic dysfunction during hypoxia: a systolic deficit occurs rapidly and reaches its full extent in a matter of minutes, while the onset of contracture occurs later, and develops more gradually[6].

On the basis of the preceding discussion, we sought to formalize the relationship between ATP depletion and diastolic dysfunction, and to construct an analogous relationship between PCr depletion and systolic dysfunction, as metabolic and functional deficits developed during global hypoxia in the perfused rat heart. In addition, we compared normal rat hearts and rat hearts which had hypertrophied secondary to chronic pressure overload to investigate the alterations in the rate of the development of cardiac metabolic and functional deficits during prolonged global hypoxia, and alterations in the relationship between these metabolic and functional deficits, which may occur in the state of mild compensated hypertrophy.

Methods

Animals

Male Sprague-Dawley rats weighing 200-225 grams underwent unilateral nephrectomy under chloral hydrate anesthesia. After a day of post-operative recovery, they were maintained on a diet of standard laboratory rat chow, drank only 0.9% saline in tap water, and were injected subcutaneously 3 times per week with 1.5 mg/100 g body weight deoxycorticosterone. They were maintained on this regimen for 8 to 10 weeks before experimentation, during which cardiac hypertrophy developed secondary to hypertension resulting from this circulatory volume loading[19,20]. The control group consisted of adult male Sprague-Dawley rats. At the end of each experiment the hearts were blotted dry and weighed. All control animals had a heart weight to body weight ratio (HW/BW) $< 3.75 \times 10^{-3}$, while all but one of the hypertensive animals, which was accordingly eliminated from the analysis, exhibited HW/BW $> 4.0 \times 10^{-3}$. The left ventricle was dissected free and weighed separately.

Perfusion

At the time of experimentation, the rats were anesthetized with an intraperitoneal injection of 40 mg sodium pentobarbital. Hearts were then rapidly excised and immersed in ice cold perfusion buffer. The aorta was then dissected free and the heart perfused retrograde through the aorta by 37° phosphate-free Krebs-Henseleit buffer gassed with 95% O_2, 5% CO_2 (pH 7.4) as described previously[21]. The buffer was composed of (mM) NaCl (118), KCl (4.7), EDTA (0.5), $MgSO_4$ (1.2), $CaCl_2$ (1.75), $NaHCO_3$ (25), and glucose (11). A constant-pressure system was used, providing a perfusion pressure of 100 mm Hg under gravity feed for all hearts. The same coronary perfusion pressure was used for the control and the hypertrophied hearts in order to approximately equalize between the two groups the

contribution of perfusion to contractility[22] and diastolic stiffness[23,24,25] in the hypoxic hearts. Initial LVEDP was set to 10 mm Hg in each heart by adjusting the volume of the balloon placed in the left ventricle (see below). Coronary flow was assessed by measuring coronary effluent at three-minute intervals.

Hemodynamic measurements

A water-filled latex balloon was inserted into the left ventricle through an incision into the left atrium, via the mitral valve. The volume of this balloon was adjustable, so that initial LVEDP could be set to 10 mm Hg in all hearts. Pressures were obtained via a water filled tube running from the latex balloon to a pressure transducer, connected to a Hewlett-Packard chart recorder. Systolic and diastolic pressures were recorded at 3-minute intervals throughout the experiment. Hearts were excluded from the analysis if they fibrillated during the experiment.

NMR measurements

The perfused hearts were placed into a 20mm NMR sample tube and inserted into the bore of an Oxford Instruments 360 wide-bore magnet (field strength, 8.45 Tesla), interfaced with a Nicolet 1280 computer. Individual spectra were accumulated over 3 minute periods, averaging data from 76 free induction decays following broad-band pulses of tip-angle 60°. The interpulse delay time was 2.15 seconds. We were thus able to obtain measurements of relative amounts of ATP, PCr, and Pi every three minutes. In addition, intracellular pH was determined by comparison of the chemical shift between Pi and PCr with a standard curve obtained under comparable in vitro conditions[26].

Experimental protocol

All hearts were paced at 4.5 Hz. After hemodynamic stability was attained with LVEDP = 10 mm Hg, six minutes of

control data was obtained during perfusion with the well-oxygenated buffer. The perfusate was then rapidly switched to one identical in composition but gassed with 95% N_2 and 5% CO_2 to induce hypoxia (pO_2 ~ 2Ø Torr). We continued collecting spectra and hemodynamic data over three-minute periods thereafter, up to a total time of 24 minutes of hypoxia.

Statistical analysis

Statistical analyses were performed using the RS/1 software of BBN Research Systems, Cambridge, MA. Means were compared using a 2-tailed Student's t-test. Linear regressions were performed by a weighted least-squares routine, with weights given by the reciprocal of the variance of each point in the ordinate dimension. The uncertainty in the predictor variable was neglected as, in each case, the standard deviation of the range of its values was much greater than the individual standard deviations of the points[27]. All errors are presented as $\pm$ SEM.

Results

Effect of Systemic Hypertension on Cardiac Mass in Prepared Animals

Table 1 shows the effect of systemic hypertension on heart weight (HW) (increased by 44% over control animals), left ventricular weight (LVW) (increased by 39%), ratio of heart weight to body weight (HW/BW) (increased by 24%), and left ventricular weight to body weight (LVW/BW) (increased by 22%). All differences between the two groups were statistically significant.

Hemodynamic Data

Hemodynamic and coronary flow data is summarized in Table 2 and Figures 1 to 7. Fig. 1 shows that the left-ventricular systolic pressure (LVSP) of the hypertrophied hearts was, as expected, markedly greater during control oxygenation, corresponding to the *in vivo* compensation for increased afterload. This overall greater LVSP persisted throughout hypoxia as well, during which a large initial drop in LVSP was followed by an approximately steady-state value for both groups. In that later stage, the ratio of systolic pressures between the two groups was somewhat smaller than during control oxygenation. Normalizing by LVW, however (Fig. 2), we find a different picture; throughout hypoxia, the LVSP generated per gram LVW in the hypertrophied hearts was consistently less than in the controls (though not statistically significant at any given time). This is consistent with a decrease in intrinsic systolic contractile capability in the muscle units of the hypertrophied hearts[28], or may also be accounted for by their relative underperfusion. We note that the data represented in Fig. 2 was derived by calculating each heart's LVSP/LVW at each time, and then averaging these quantities for each time interval, rather than by dividing the curves in Fig. 1 by the average LVW for the control and hypertrophied groups, respectively. The error bars in Fig. 2 therefore reflect the

variation in both LVSP and LVW within groups, and so are larger than those in Fig. 1. Similar comments apply to all data normalized to LVW presented below. The slight increase in LVSP seen in the hypertrophy group is not uncommon in hypoxic perfused heart preparations, and may be due to the development of edema during prolonged hypoxia, resulting in tissue stretch and an effective increase in preload.

Changes in left ventricular diastolic pressure are shown in Fig. 3. Starting from an equal initial LVEDP of 1Ø mm Hg, the hypertrophied hearts exhibited a significantly greater increase in resting tension than did the control hearts throughout all but the earliest stages of hypoxia. However, normalizing by LVW eliminates this difference (Fig. 4). In this figure, the lower control LVEDP/LVW in the hypertensive group reflects an initial LVEDP of 1Ø mm Hg in both groups, and the greater LVW of the hypertrophied hearts. After the control period, there were no significant differences between the two groups. This shows that the degree of additional left ventricular contracture in this model of hypertrophy is directly proportional to the additional muscle mass present. Left ventricular developed pressure (LVDP), defined by LVDP = LVSP - LVEDP, is augmented in the hypertrophied hearts over the controls by their greater systolic pressure, but is diminished by their greater increase in diastolic pressure, during hypoxia. The offsetting nature of these two effects is shown in Fig. 5, in which the close equality of left ventricular developed pressure between the two groups during hypoxia is shown. Because heart rate was fixed throughout these experiments, the ordinate of Fig. 5 may be viewed as either developed pressure or as the rate-pressure product (RPP) = developed pressure x HR, which is an index of total myocardial work output and oxygen consumption in the isolated heart. Thus, we find that both groups of hearts rapidly reach the same, relatively fixed, work and oxygen utilization levels. Fig. 6 shows a lower LVDP/LVW in the hypertrophied hearts, which follows directly from their lower in LVSP/LVW,

and the equality of LVEDP/LVW between the two groups. This can be interpreted as a decrease in the ability of the hypertrophied hearts to utilize oxygen and produce work per unit mass.

As shown in Fig. 7, there was a trend towards lower coronary flow per gram of total heart weight in the hypertrophied hearts during control oxygenation. With the onset of hypoxia, the difference increased and was statistically significant throughout hypoxia. In addition, the figure also shows that the initial vasodilatory response to hypoxia was smaller in the hypertrophied group. These facts are consistent with a decrease in capillary proliferation in the hypertrophied hearts[3]. In this type of heart preparation, the initial vasodilatory response is followed by a decline in coronary flow, which may perhaps be explained by edema formation or by a diminished rate of adenosine production. By the end of the 24 minute hypoxic period, this effect fully offset the vasodilatory response in the hypertrophied hearts, so that coronary flow returned to control levels. In the normal hearts, however, coronary flow remained augmented throughout.

Metabolic Data

High-energy phosphate (ATP and PCr) levels are shown in Figs. 8 and 9, and Table 3. Values are given relative to an initial ATP concentration of 100% in each group. It has previously been shown[29] that the control levels of ATP and PCr are not altered significantly by the method we have used to create cardiac hypertrophy. We see that in the control hearts, the initial concentration of PCr was 1.27 $\pm$ .07 times the initial ATP concentration, while for the hypertrophied group, the value was 1.20 $\pm$ .09 (NS between the two groups). At the end of the hypoxic period, the concentration of PCr in both groups had dropped to approximately 20% of control levels. In addition, it is evident that the most severe drop in [PCr] occurred during the first half of the hypoxic

period. For control hearts, a drop of 74 units of PCr in the first twelve minutes of hypoxia is followed by a drop of only 22 in the second twelve minutes. The numbers for the hypertrophied hearts are similarly disparate, a drop of 83 being followed by a drop of 13. This behavior is reflected in Fig. 9 as the distinct flattening of slope which is seen to occur approximately midway through hypoxia. On the other hand, the rate of change of [ATP] with respect to time is evidently roughly constant throughout the hypoxic period, as seen by the fact that the data points for the curves of Fig. 8 lie approximately on a straight line. The percent of initial concentration of ATP remaining at the end of the experiment was 5Ø $\pm$ 8% for the controls and 42 $\pm$ 6% for the hypertrophied hearts, indicating in both groups a relative preservation of ATP levels at the expense of the more fully depleted PCr stores. The lack of statistically significant differences between the ATP and PCr levels in the two groups during hypoxia may point to a preserved energy production and delivery capability in the hypertrophied hearts, in spite of the hemodynamic derangements documented above.

Fig. 1Ø shows the time evolution of intracellular pH. At no time was the difference between the control and hypertrophied group statistically significant, though the hypertrophied group displayed a trend towards slightly lower pH. The competition of H^+ with Ca^{++} for troponin binding sites may thus explain part of the systolic deficit seen in the hypertrophied hearts.

Relationship between metabolism and function

Fig. 11a shows a graph of LVEDP vs ATP for the two groups. LVEDP as a function of [ATP] is linear for both the control and hypertrophied hearts, but the linear relationship is different ($p<.Ø1$ for slopes) between the two groups. These results show that, for a given ATP deficit, LVEDP is higher in this model of stable, compensated hypertrophy than in normal hearts. This could be due to an intrinsic

metabolic phenomenon in which contractile units of the hypertrophied myocardium have a diminished ability to relax during diastole; alternatively, the impaired ability of contractile units to relax could be the same in the hypertrophied and control hearts, but the overall resting tension increased in hypertrophy simply because of the greater number of such units. This would be consistent with the parallel replication of sarcomeres in concentric hypertrophy, as described by Grossman et al[10]. Evidence that such replication of sarcomeres explains our results is seen in Fig. 12, showing the relationship between LVEDP normalized by LVW and [ATP]. As can be seen, the same linear relation exists for control and hypertrophied hearts. Figures 11a and 12 show that in these experiments, LVEDP (or LVEDP/LVW) and [ATP] are correlated with each other throughout their entire range of variation during hypoxia. Thus, a measurement of either one of them is a reliable index to the value of the other, and we may say that there is a mutually predictive relationship between these two variable.

From Figure 11b we see that LVDP, as opposed to LVEDP, is not predicted by ATP levels. In both groups of hearts, even a large decrease in [ATP], once below approximately 80% of the control value, can occur with only a small change in LVDP. On the other hand, Figure 11c shows that there is a clear mutually predictive (and linear) relation between [PCr] and LVDP during prolonged hypoxia in this preparation. Finally, we also find that [PCr] and LVEDP are not mutually predictive (Fig. 11d).

Discussion

Using P-31 NMR and hemodynamic monitoring, we studied the evolution during prolonged hypoxia of 1) intracellular metabolism, as reflected by [ATP], [PCr], and pH, 2) function, as reflected by systolic and diastolic pressures, and 3) the relationship between metabolism and hemodynamic function, in normal hearts and hearts which had hypertrophied secondary to systemic hypertension. The hypertrophied hearts were observed to maintain a greater peak systolic pressure throughout the 24 minutes of hypoxia, but, normalizing by muscle mass, they showed a lower LVSP developed per gram of myocardium. On the other hand, their greater increase in LVEDP over the control hearts could be attributed directly to their greater mass. Loss of high-energy phosphates during hypoxia was similar in the two groups, and in each, [ATP] was found to be predictive of decreased left ventricular compliance. The predictive relationship between [ATP] and LVEDP/LVW was the same for the two groups. Similarly, systolic function was mutually predictive with [PCr].

Implicit in our discussion has been the assumption that the increased mass of the hypertrophied left ventricle is due to growth of functional myocardial tissue. For example, we have attributed the decreased peak LVSP per gram of left ventricular mass to lower peak force generating capability per contractile unit. An alternative explanation would be proliferation of noncontractile elements; in that case, force generated per unit mass of left ventricle could be lower because of fewer force-producing units per gram, while force generating capability per contractile unit could actually be unimpaired. Similarly, we have attributed increased LVEDP in the hypertrophied group over the control group simply to a greater number of incompletely relaxing contractile units in the former; however, proliferation of stiff connective tissue could in principle lead to the same observation. Even in the absence of actual proliferation[30], a change in the properties

of existing connective tissue, secondary to the stimulus to hypertrophy, could alter function. Evidence on the exact extent and nature of alterations in connective tissue in experimental cardiac hypertrophy is inconclusive, but the changes are small. Thus, this effect is unlikely to be dominant in mild hypertrophy.

Of the multitude of interacting processes which together permit adequate ATP production, we note two which are altered by the hypertrophy process. First, oxygen delivery, already severely compromised but not totally eliminated in our hypoxic buffer (pO2 ~ 20 mm Hg), is further diminished by the defect in microvascularization associated with hypertrophy[3,4]. The hypoxic state is appropriate to investigate this difference in capillary density because the state of mild hypertrophy represents, rather than a condition in which the heart is unable to function under normal conditions, a decrease in cardiac reserve. As is well-known, under normal, well-oxygenated, conditions, a large fraction of capillaries in the heart are closed. In hypertrophy, although the proliferation of capillaries lags behind muscle growth, the proportion of patent capillaries increases, effectively compensating for this. However, relatively fewer closed capillaries then remain, representing a diminished cardiac reserve for oxygen delivery to myocardial tissue. Thus, a physiologic stress, such as hypoxia, may be required to increase the sensitivity of assessing the adequacy of vascularization in the intact hypertrophied heart. Evidence of decreased functional capillary density is seen in Fig. 7. Because hearts from both groups were perfused at the same pressure, these coronary flow measurements reflect total vascular area per gram of heart weight which is presented to the perfusing stream. The smaller initial rise in coronary flow seen in the hypertrophied hearts in response to hypoxia can therefore be interpreted as a diminished cardiac vascular reserve. ATP production for a given amount of oxygen may be reduced also

by the relative decrease in mitochondrial size and number seen in hypertrophied myocardium. In addition, mitochondrial respiratory activity is decreased in stable hypertrophy[31]. These changes can again be regarded as a decrease in cardiac reserve, which may be probed by an appropriate physiologic stress. Indeed, our observations are consistent with a greater decrease in ATP synthesis capability in the hypertrophied than in the normal myocardium during hypoxia: Fig. 8 shows an equal rate of ATP depletion in the two groups, while Fig. 5 implies lower total myocardial ATP hydrolysis. These facts can be reconciled if ATP synthesis is diminished in the hypertrophied group. Unfortunately, direct measurement of ATP synthesis in this system by the standard NMR technique of magnetization transfer is impossible, because the requirement that metabolite levels remain constant over the time scale of the saturation transfer experiment (approximately 20 minutes) is not satisfied.

The mechanisms of diastolic dysfunction during hypoxia have been discussed extensively in the literature[32,33]. The use of P-31 NMR spectroscopy to monitor metabolite levels during hypoxia has extended earlier observations by allowing ongoing measurement at short time intervals during hypoxia. The presence of cellular hypertrophy could influence several processes in the transition from cardiac systole to relaxation to exacerbate the diastolic deficit seen in hypoxia. With the transition to diastole accounting for approximately one-third of the energy requirements of the myocyte, a defect in ATP generation would be likely to result in an increase in LVEDP. Our results, however, indicate that the increased diastolic deficit of the hypertrophied hearts during hypoxia could be attributed directly to a mass effect. Thus, for a given amount of diastolic tension per contractile element, the parallel addition of such elements in a number proportional to the increase in left ventricular mass would be consistent with our observation of an increase in overall

LVEDP (Fig. 3) but equality of LVEDP/LVW (Fig. 4) between the control and hypertrophied hearts.

Apparent stiffness in the isolated perfused heart is due to both intrinsic myocardial tissue properties and a hydraulic erectile effect reflecting fluid perfusion. This erectile effect is in general comparable to or even greater than the contribution of intrinsic myocardial stiffness in the perfused heart[34]. We were unable to specifically assess the relative contribution of intrinsic myocardial stiffness and the extrinsic perfusion effect; this measurement would have required transient ischemia, complicating interpretation of our NMR data. However, we attempted to roughly equalize the erectile effect in the two groups of hearts by perfusing at equal pressures (100 mm Hg, approximating the blood pressure of normotensive rats), so that a difference in LVEDP could be considered as due primarily to myocardial tissue stiffness; perfusion of the hypertrophied hearts at a higher pressure (e.g., 150 mm Hg, reflecting the blood pressure of rats made hypertensive by our protocol), would have made the hydraulic contribution to LVEDP in the two groups clearly different. Our approach, which is most suitable for comparison of metabolic with functional state, does have the effect of exacerbating the relative underperfusion of the hypertrophied hearts discussed above. In addition, it should be noted that the erectile contribution may depend not only on perfusion pressure, but also on the level of edema, degree of vasodilation, myocardial stiffness (stress-strain relationship), and other properties of the myocardium. Kimmel et al[35], in the context of lung elasticity, discuss a tissue model which could incorporate many of these factors.

Finally, we note a possible therapeutic corollary of our results, which imply that the diastolic dysfunction in moderate cardiac hypertrophy is likely to be due at least in part to increased muscle mass. We conjecture from this that medical therapy of hypertension when cardiac hypertrophy coexists may be most likely to reverse the diastolic deficit

when carried out with antihypertensive agents which are known to also reverse hypertrophy. A similar conclusion regarding the desirability of reversing hypertrophy along with reversing hypertension was reached by Wicker and Tarazi[36] in their review of coronary flow data in experimental left ventricular hypertrophy.

In summary, using ^{31}P NMR spectroscopy, we established relationships between high-energy phosphates and function during prolonged hypoxia in the isolated perfused rat heart. We found that for both the control and hypertrophied hearts, [ATP] is predictive of diastolic (but not systolic) function, while [PCr] is predictive of systolic (but not diastolic) function.

1. Mercadier, J., A. Lompré, C. Wisnewsky, J. Samuel, J. Bercovici, B. Swyngehedauw, and K. Schwartz. 1981. Myosin Isoenzymic Changes in Several Models of Rat Cardiac Hypertrophy. Circ. Res. 49:525-532.

2. Ingwall J.S. 1984. The hypertrophied myocardium accumulates the MB-creatine kinase isozyme. Eur. Heart Jour. 5 (suppl. F):129-139.

3. Henquell L., C. L. Odoroff, and C. R. Honig. 1977. Intercapillary distance and capillary reserve in hypertrophied rat hearts beating in situ. Circ. Res. 41:400-408.

4. Alfaro A., T. F. Schaible, A. Malhotra, T. Yipintsoi, and J. Scheuer. 1983. Impaired coronary flow and ventricular function in hearts of hypertensive rats. Cardiovasc. Res. 17:553-561.

5. Alpert, N. R., editor. 1983. Perspectives in Cardiovascular Research, Vol. 7, Myocardial Hypertrophy and Failure. Raven Press, New York. 1-682.

6. Nayler, W.G., P. A. Poole-Wilson, and A. Williams. 1979. Hypoxia and Calcium. J. Molec. Cell. Card. 11:683-706.

7. Katz AM and Hecht HH 1969. The Early "Pump" Failure of the Ischemic Heart, Am J Med 47, 497-502.

8. Kübler W and Katz AM 1977. Mechanism of Early "Pump" Failure of the Ischemic Heart: Possible Role of Adenosine Triphosphate Depletion and Inorganic Phosphate Accumulation, Am J Card 40, 467-471.

9. Winegrad S. (1979). Electromechanical Coupling in Heart Muscle, in Handbook of Physiology, Section 2, Vol 1, Ed. Robert M. Berne.

10. Grossman W., Jones D., McLaurin L.P. 1975. Wall Stress and Patterns of Hypertrophy in the Human Left Ventricle, J Clin Inves 56, 56-64.

11. Sink, J. D., G. L. Pellom, W. D. Currie, R. C. Hill, C. O. Olsen, R. N. Jones, and A. S. Wechsler. 1981. Response of hypertrophied myocardium to ischemia. Thorac Cardiovasc Surg. 81:865-872.

12. Peyton, R. B., R. N. Jones, D. Attarian, J. D. Sink, P. Van Trigt, W. D. Currie, and A. S. Wechsler. 1982. Depressed High-energy phosphate content in hypertrophied ventricles of animal and man. Ann Surg 196:278-284.

13. Menasche, P., C. Grousset, C. S. Apstein, F. Marotte, C. Mouas, and A. Piwnica. 1985. Increased injury of hypertrophied myocardium with ischemic arrest: preservation with hypothermia and cardioplegia. Am. Heart Jour. 110:1204-1209.

14. Pool, P. E., J. W. Covell, C. A. Chidsey, and E. Braunwald. 1966. Myocardial high energy phosphate stores in acutely induced hypoxic heart failure. Circ. Res. 19:221-229.

15. Gudbjarnason, S., P. Mathes, and K. G. Ravens. 1970. Functional compartmentation of ATP and creatine phosphate in heart muscle. Jour. Mol. Cell. Card. 1:325-339.

16. Cain, D. F., and R. D. Davies. 1962. Breakdown of adenosine triphosphate during a single contraction of working muscle. Biochem. Biophys. Res. Comm. 8:361-366.

17. Bricknell, O. L., P. S. Daries, and L. H. Opie. 1981. A relationship between adenosine triphosphate, glycolysis, and ischaemic contracture in the isolated rat heart. Jour. Molec. Cell. Cardiol. 13:941-945.

18. Weiss, J., and B. Hiltbrand. 1985. Functional compartmentation of glycolytic versus oxidative metabolism in isolated rabbit heart. J. Clin. Invest. 75:436-447.

19. Brecher P., Chan C.T., Franzblau C., Faris B., and Chobanian A.V. 1978. Effects of Hypertension and Its Reversal on Aortic Metabolism in the Rat, Circ. Res. 43, 561-569.

20. Beznak M., Korecky B., and Thomas G. 1969. Regression of Cardiac Hypertrophies of Various Origin, Can. J. Physiol. Pharmacol. 47, 579-586.

21. Ingwall J.S. 1982. Phosphorus Nuclear Magnetic Resonance Spectroscopy of Cardiac and Skeletal Muscles, Am. J. Physiol. 242, H729-H744.

22. Arnold G, Kosche F, Miessner E, Neitzert A, and Lochner W (1968). The Importance of the Perfusion Pressure in the Coronary Arteries for the Contractility and the Oxygen Consumption of the Heart, Pflügers Archiv 299, 339-356.

23. Salisbury P.F., Cross C.E., and Rieben P.A. 1960. Influence of Coronary Artery Pressure Upon Myocardial Elasticity, Circ. Res. 8, 794-800.

24. Olsen CO, Attarian DE, Jones RN, Hill RC, Sink JD, Lee KL, and Wechsler AS (1981). The Coronary Pressure-Flow Determinants of Left Ventricular Compliance in Dogs, Circ Res 49, 856-865.

25. Vogel WM, Apstein CS, Briggs LL, Gaasch WH, and Ahn J (1982). Acute Alterations in Left Ventricular Diastolic Chamber Stiffness: Role of the "Erectile" Effect of Coronary Arterial Pressure and Flow in Normal and Damaged Hearts, Circ Res 51, 465-478.

26. Jacobus WE, Pores IH, Lucas SK, Kallman CH, Weisfeldt ML, and Flaherty JT (1982). The Role of Intracellular pH in the Control of Normal and Ischemic Myocardial Contractility: A ^{31}P Nuclear Magnetic Resonance and Mass Spectrometry Study, in Intracellular pH: Its Measurement, Regulation, and Utilization in Cellular Functions, Alan R Liss, Inc, New York.

27. Draper N and Smith H (1981). Section 2.14 in Applied Regression Analysis, Wiley and Sons, New York.

28. Spann JF (1983). Contractile and Pump Function of the Pressure-Overloaded Heart, in Ref. 5.

29. Wexler, L. F., B. H. Lorell, S. Momomura, E. O. Weinberg, C. S. Apstein, and J. S. Ingwall. 1987. Enhanced sensitivity to hypoxia-induced diastolic dysfunction in pressure overload left ventricular hypertrophy in the rat: role of high energy phosphate depletion. Submitted to Circ. Res.

30. Caulfield, JB (1983). Morphologic Alterations of the Collagen Matrix with Cardiac Hypertrophy, in Ref. 5.

31. Sordahl LA (1983). Mitochondrial Changes in Pressure-Overload Hypertrophy and Failure, in Ref. 5.

32. Nayler WG and Williams A (1978). Relaxation in Heart Muscle: Some Morphological and Biochemical Considerations, Eur J Card 7/Suppl, 35-50.

33. Serizawa T, Vogel WM, Apstein CS, Grossman W (1981). Comparison of Acute Alterations in Left Ventricular Relaxation and Diastolic Chamber Stiffness Induced by Hypoxia and Ischemia, J Clin Inves 68, 91-102.

34. Vogel WM, Briggs LL, and Apstein CS (1985). Separation of Inherent Diastolic Myocardial Fiber Tension and Coronary Vascular Erectile Contributions to Wall Stiffness of Rabbit Hearts Damaged by Ischemia, Hypoxia, Calcium Paradox, and Reperfusion, J Mol Cell Cardiol 17, 57-70.

35. Kimmel E, Kamm RD, and Shapiro AH (1986). A Cellular Model of Lung Elasticity, submitted to ASME J of Biomech Eng.

36. Wicker, P. and R. C. Tarazi. 1982. Coronary blood flow in left ventricular hypertrophy: a review of experimental data. Eur. Heart J. 3 (suppl. A):111-118.

Table 1. Heart and Left Ventricle Weights

	HW (g)	LVW (g)	HW/BW x 10^3	LVW/BW x 10^3
Control (n = 7)	1.37 ± .05	.99 ± .05	3.48 ± .08	2.50 ± .06
Hypertensive (n = 7)	1.97 ± .08 (↑ 44%**)	1.38 ± .05 (↑ 39%**)	4.34 ± .16 (↑ 24%**)	3.04 ± .12 (↑ 22%**)

Effects of one kidney DOCA-salt hypertension on heart weight (HW), left ventricular weight (LVW), heart weight-to-body weight ratio (HW/BW), and left ventricular weight-to-body weight ratio (LVW/BW). **p < .01 control versus hypertensive.

Table 2. Effect of Hypoxia on Hemodynamic Variables

	LVSP		LVSP/LVW	
	Control	Hypertrophy	Control	Hypertrophy
Normoxia	122 ± 4.6	**159 ± 9.9	123 ± 4.8	117 ± 9.8
10.5 minutes	67.6 ± 3.5	*82.1 ± 3.8	69.2 + 5.5	60.3 ± 4.1
22.5 minutes	66.7 ± 4.3	**87.1 ± 3.1	68.5 ± 6.2	63.9 ± 3.6

	LVEDP		LVEDP/LVW	
	Control	Hypertrophy	Control	Hypertrophy
Normoxia	10.0	10.0	10.2 ± .31	7.32 ± .28
10.5 minutes	26.1 ± 3.4	*41.0 ± 4.3	27.1 ± 4.3	30.2 ± 3.7
22.5 minutes	40.3 ± 5.6	*61.0 ± 5.3	41.9 ± 6.8	44.9 ± 4.6

	LVDP		LVDP/LVW	
	Control	Hypertrophy	Control	Hypertrophy
Normoxia	112 ± 4.6	**149 ± 9.8	113 ± 4.7	110 ± 9.6
10.5 minutes	41.4 ± 1.7	41.1 ± 2.9	42.1 ± 2.0	**30.0 ± 2.2
22.5 minutes	26.4 ± 1.62	26.1 ± 3.1	26.6 ± 1.1	*19.0 ± 2.2

Values of hemodynamic variables during control oxygenation and at two times during hypoxia. Abbreviations and units are: left ventricular systolic pressure (LVSP), mm Hg; left ventricular weight (LVW), g; LVSP divided by LVW (LVSP/LVW), mm Hg/g; left ventricular end-diastolic pressure (LVEDP), mm Hg; LVEDP/LVW, mm Hg/g; left ventricular developed pressure (LVDP), mm Hg/sec; LVDP/LVW, mm Hg/g/sec. 10.5 and 22.5 minutes correspond respectively to the times at the midpoint of the fourth and eighth ^{31}P spectra.
*$p < .05$, **$p < .01$, control versus hypertrophied hearts.

Table 3. Effect of Hypoxia on Metabolic Variables

	[ATP]		[PCr]	
	Control	Hypertrophy	Control	Hypertrophy
Normoxia	1ØØ	1ØØ	127 ± 7.2	12Ø ± 9.Ø
1Ø.5 minutes	71.8 ± 5.9	76.9 ± 6.1	53.1 ± 6.9	37.3_+ 5.Ø
22.5 minutes	5Ø.Ø ± 7.6	42.3 ± 5.6	3Ø.7 ± 5.9	24.Ø ± 3.7

Intracellular concentrations of adenosine triphosphate (ATP) and phosphocreatine (PCr) during control oxygenation and at two times during hypoxia. Initial [ATP] was set to 1ØØ in each heart, and all other values are given relative to that. 1Ø.5 and 22.5 minutes correspond respectively to the times at the midpoint of the fourth and eighth ^{31}P spectra. None of the differences shown between the two groups was statistically significant.

Figure 1. Time course of left-ventricular systolic pressure (LVSP) for control and hypertrophied hearts during control oxygenation (first data point; -1.5 minutes) and the subsequent 24' of hypoxia (second through ninth data points; 1.5 to 22.5 minutes). The hypertrophied hearts maintained their greater LVSP throughout hypoxia. *p < .Ø5, **p < .Ø1, control versus hypertrophied hearts.

Figure 1

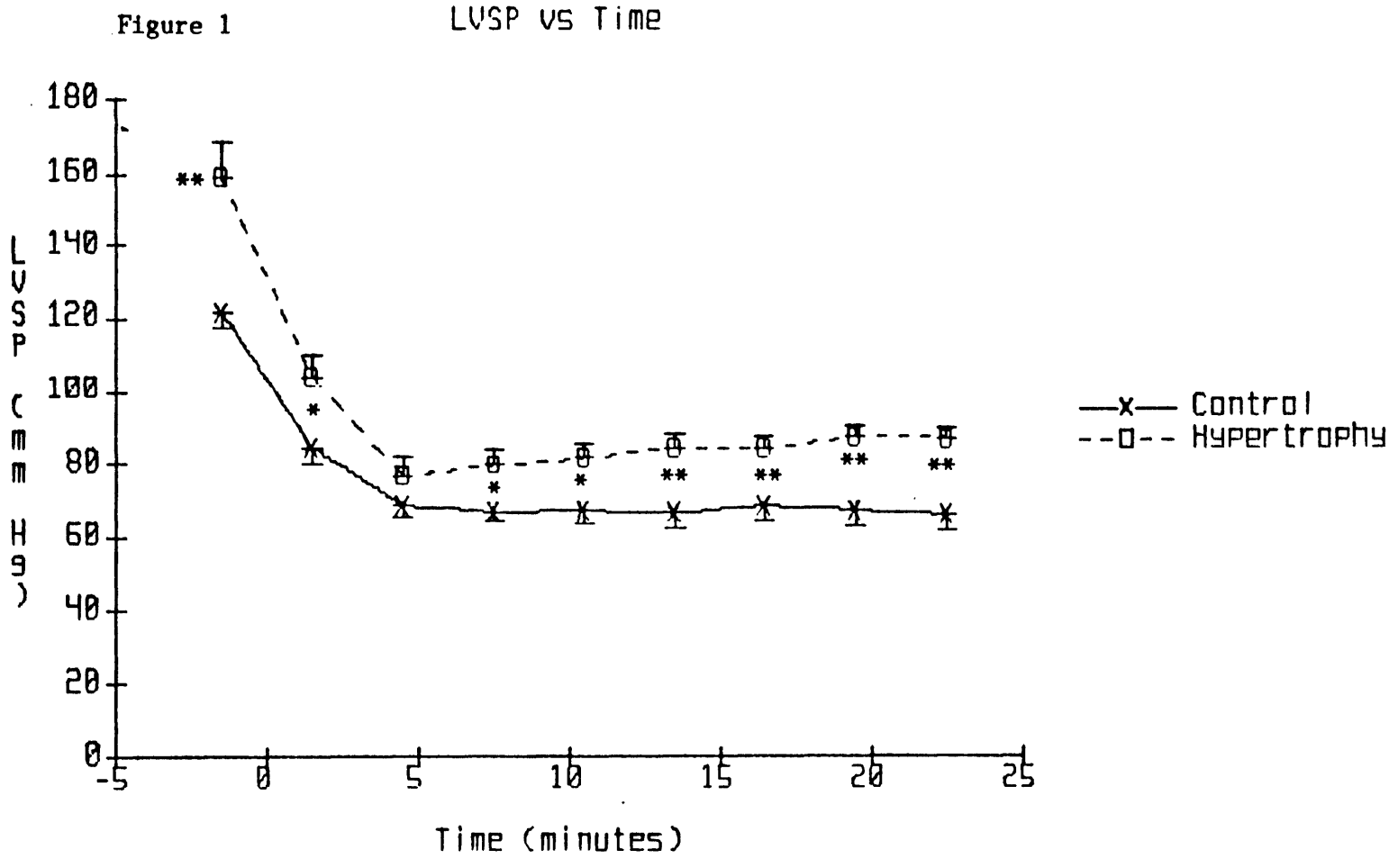
LVSP VS Time
LVSP (mm Hg)
180
160
140
120
100
80
60
40
20
0
-5
0
5
10
15
20
25
Time (minutes)
—x— Control
--□-- Hypertrophy

Figure 2. Time course of LVSP normalized by left ventricular (wet) weight (LVW). Although the difference between the two groups was not significant at any time point, the hypertrophied hearts displayed a tendency to develop less LVSP per gram of LVW than the control hearts. Format and symbols as in Figure 1.

Figure 2

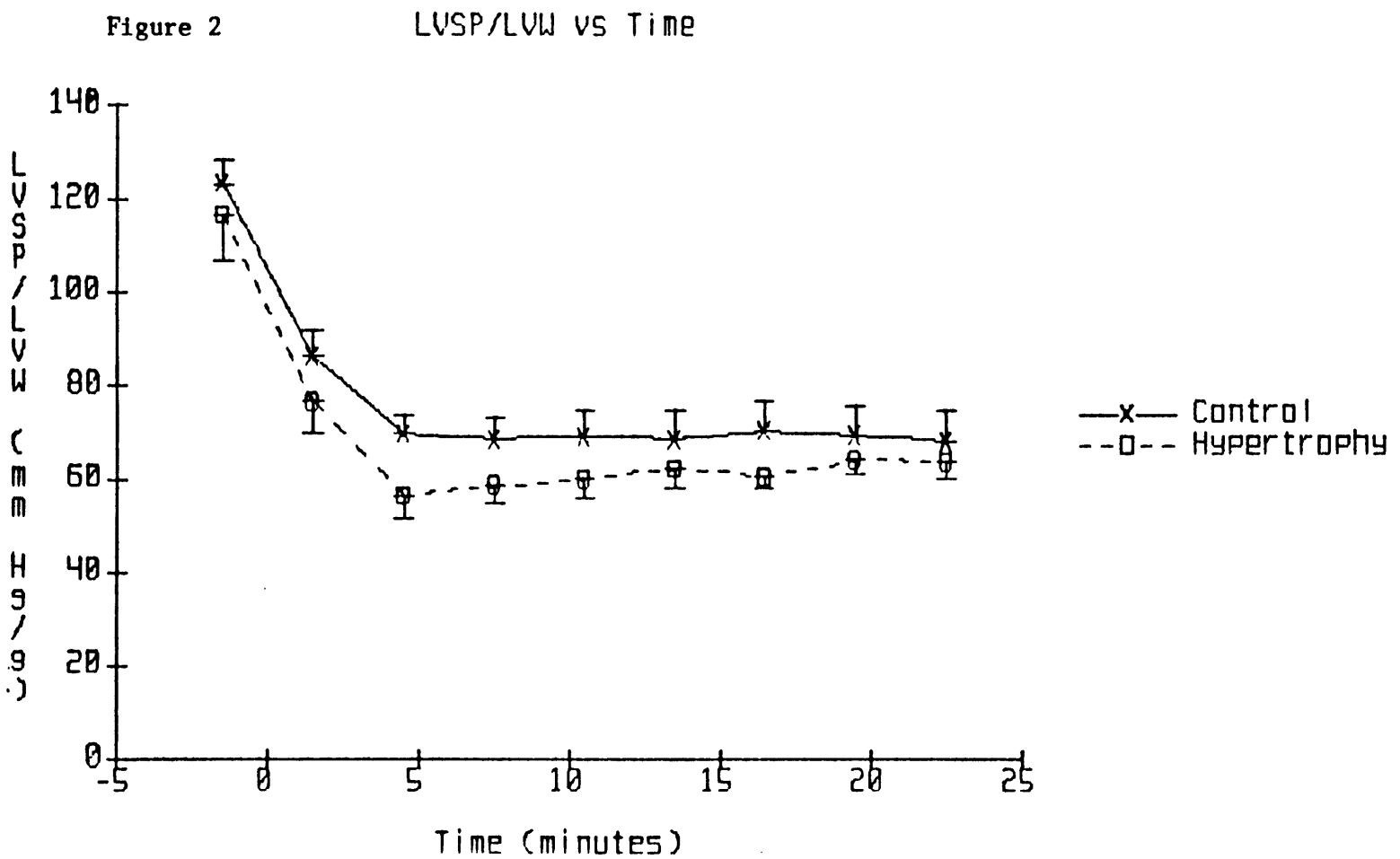
LVSP/LVW vs Time
LVSP/LVW (mm Hg/g)
140
120
100
80
60
40
20
0
-5
0
5
10
15
20
25
Time (minutes)
Control
Hypertrophy

Figure 3. Time course of left ventricular end-diastolic pressure (LVEDP). Starting from an initial LVEDP set to 1Ø mm Hg in both groups during control oxygenation, the hypertrophied hearts developed significantly more contracture during prolonged hypoxia than did the controls. Format and symbols as in Figure 1.

Figure 3

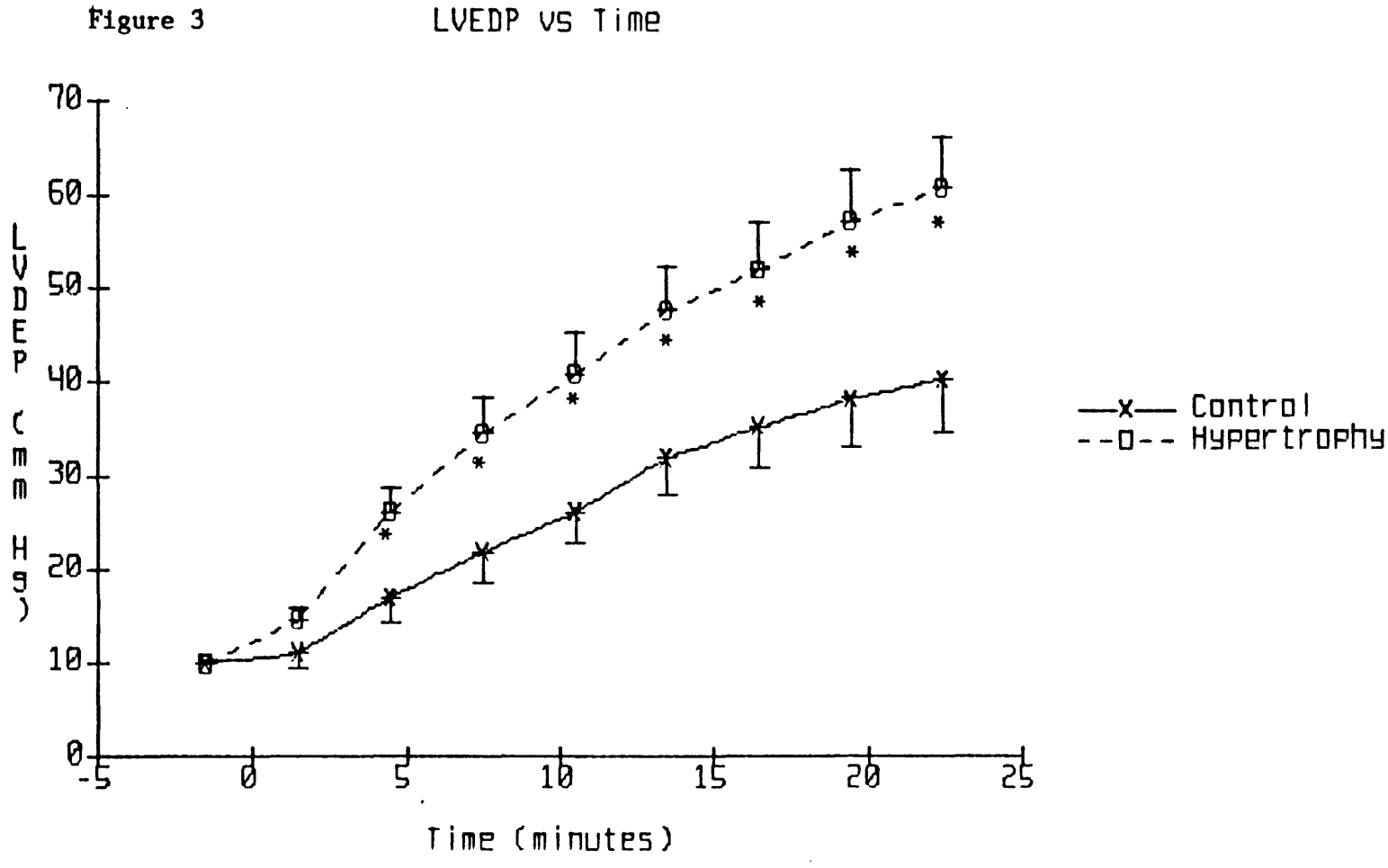
LVEDP vs Time
LVDEP (mm Hg)
70
60
50
40
30
20
10
0
-5
0
5
10
15
20
25
Time (minutes)
Control
Hypertrophy

Figure 4. Time course of left ventricular end-diastolic pressure (LVEDP) normalized by left ventricular weight. The two groups of hearts displayed the same amount of contracture per gram LVW. Format and symbols as in Figure 1.

Figure 4

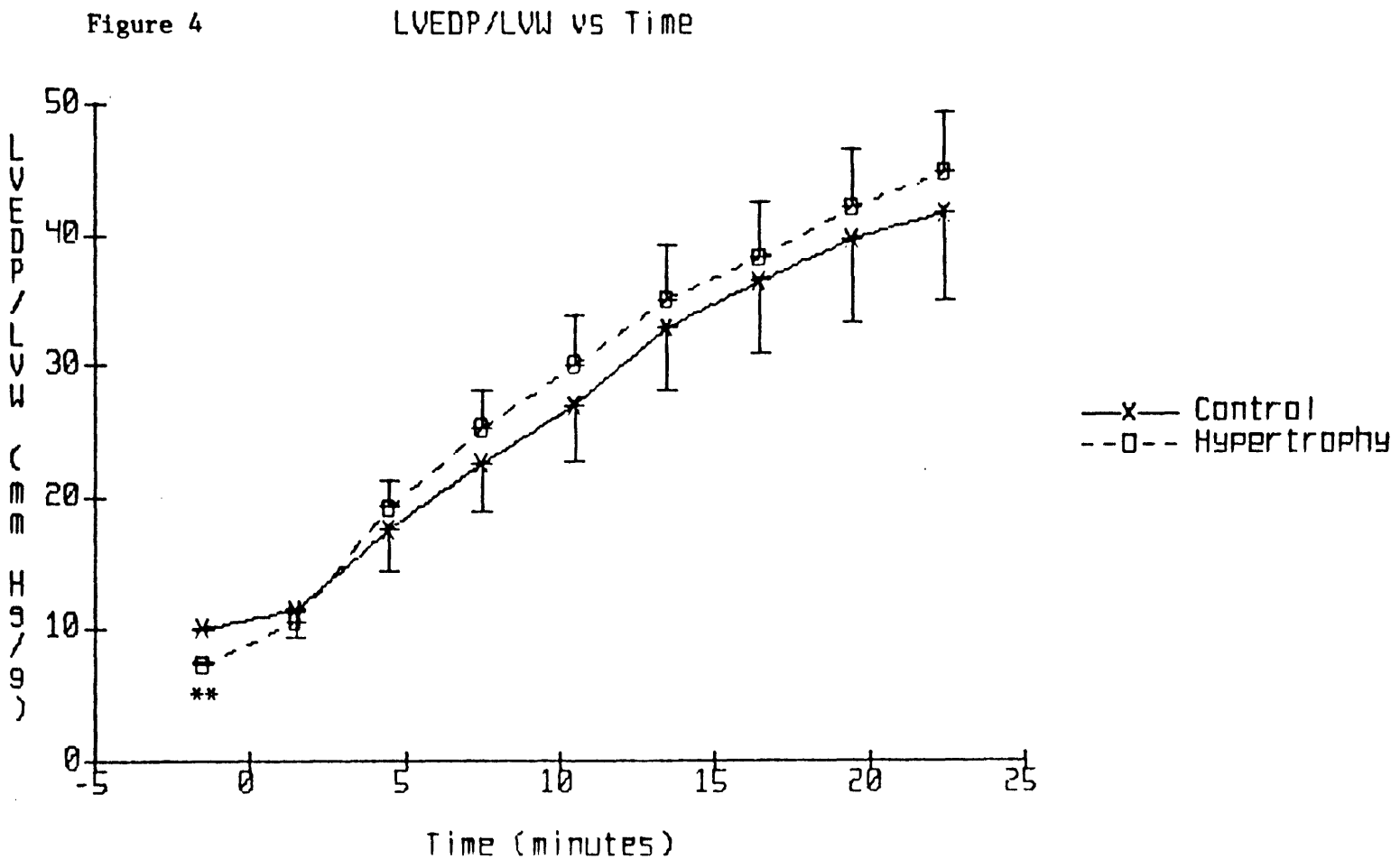
LVEDP/LVW vs Time
LVEDP/LVW (mm Hg/g)
50
40
30
20
10
0
-5
0
5
10
15
20
25
Time (minutes)
**
—x— Control
--o-- Hypertrophy

Figure 5. Time course of left ventricular developed pressure (LVDP) = LVSP - LVEDP. The heart rate was fixed at 4.5 Hz throughout the experiment, so that LVDP is proportional to the rate-pressure product (RPP). Starting from an initially greater LVDP, the hypertrophied hearts rapidly decline to the same level of performance as the control hearts during hypoxia. Format and symbols as in Figure 1.

Figure 5

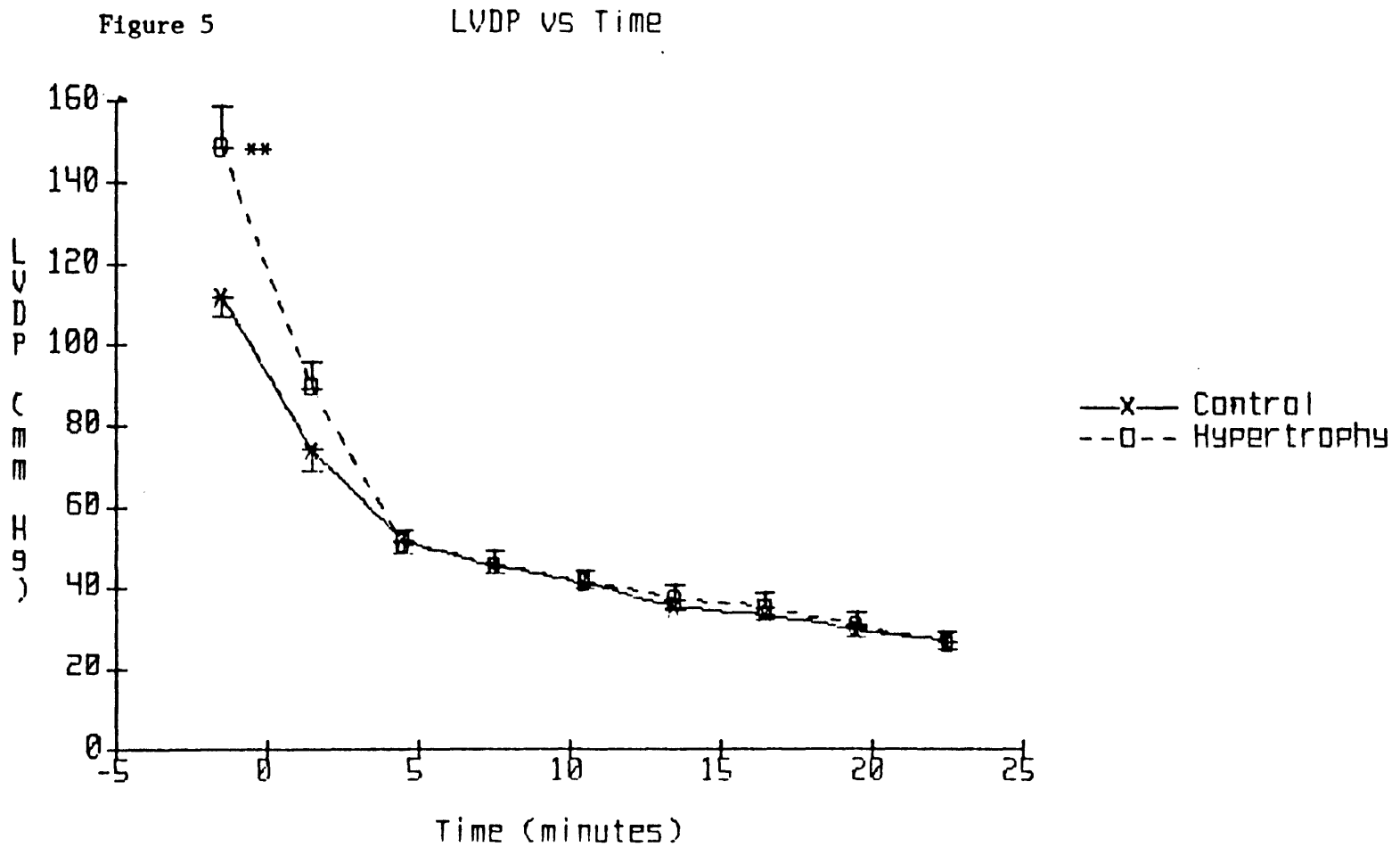
LVDP vs Time
160
140
120
100
80
60
40
20
0
LVDP (mm Hg)
**
-5
0
5
10
15
20
25
Time (minutes)
—x— Control
--o-- Hypertrophy

Figure 6. Time course of LVDP normalized by LVW. During control oxygenation, both groups displayed identical performance per gram of LVW; during hypoxia, the performance of the hypertrophied hearts per gram of LVW was lower than that of the controls. Format and symbols as in Figure 1.

Figure 6 LVDP/LVW vs Time

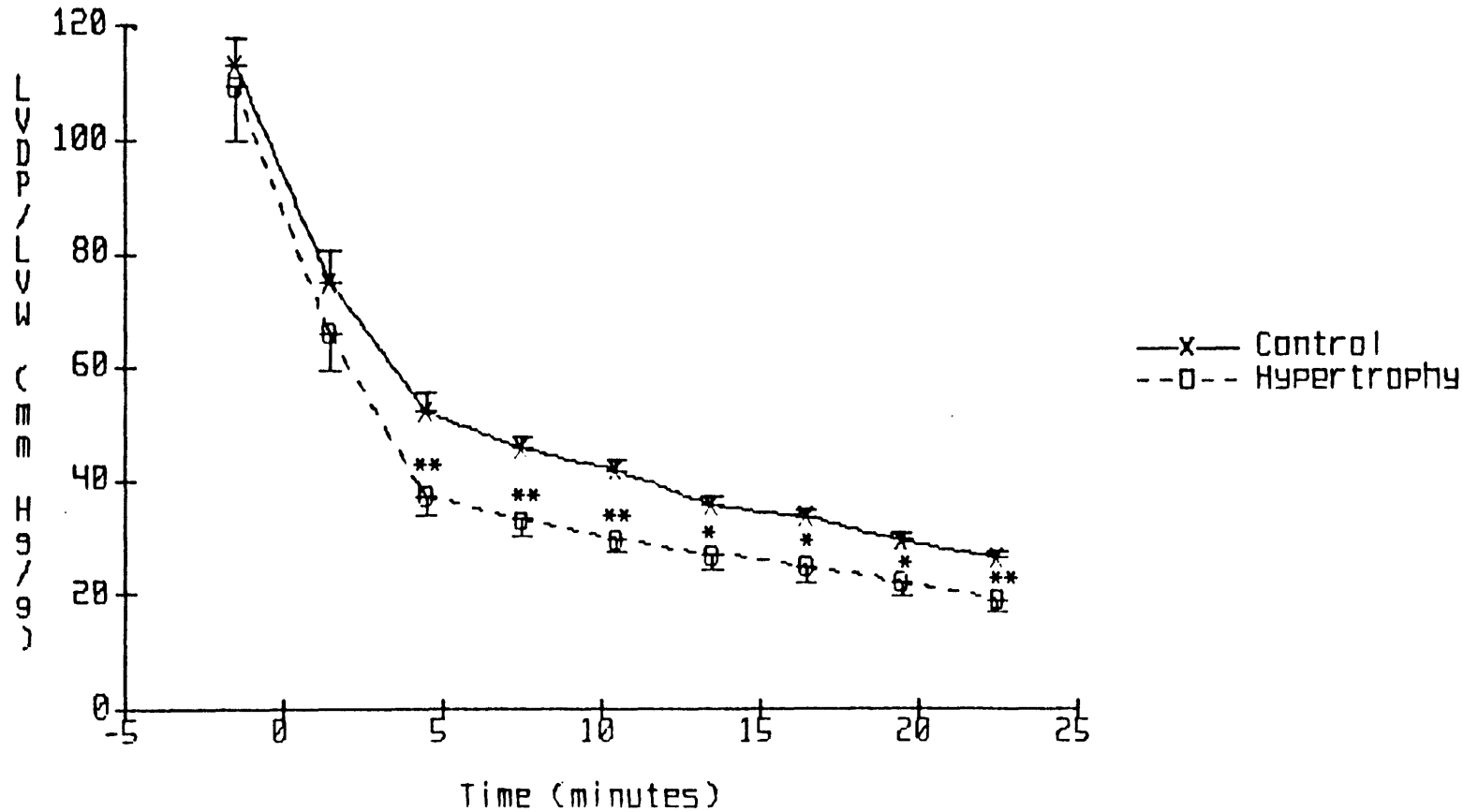

Figure 7. Time course of coronary flow normalized by LVW. All hearts were perfused at 100 mm Hg perfusion pressure; the hypertrophied hearts displayed lower flow per gram of heart weight both before and during hypoxia. Format and symbols as in Figure 1.

Figure 7 CF/HW vs Time

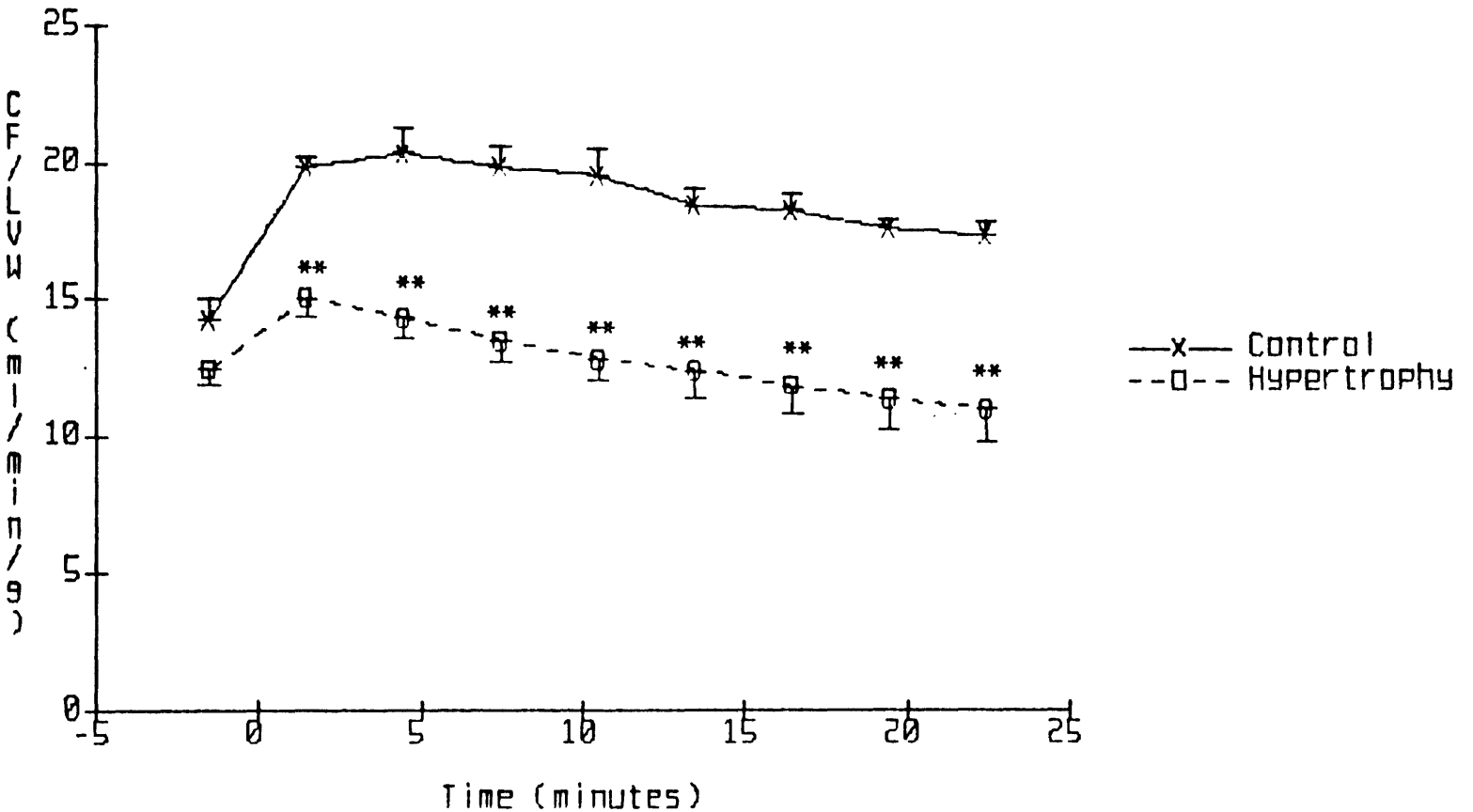

Figure 8. Time course of ATP levels. The rate of depletion of ATP was indistinguishable between the two groups. Format and symbols as in Figure 1.

Figure 8:

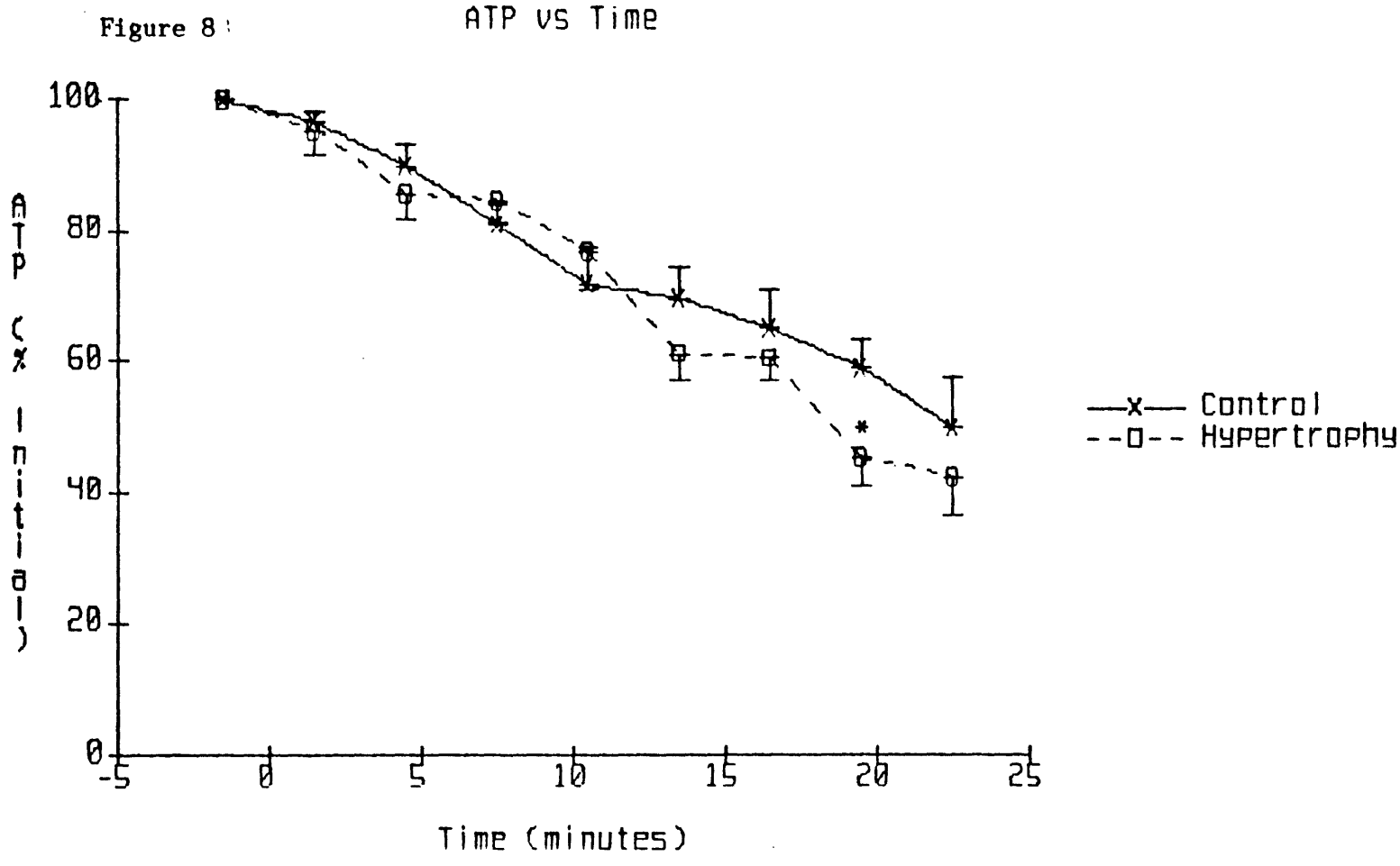
ATP vs Time
ATP (x - nitro-)
100
80
60
40
20
0
-5
0
5
10
15
20
25
Time (minutes)
—x— Control
--o-- Hypertrophy

Figure 9. Time course of PCr levels. The rate of depletion of PCr was indistinguishable between the two groups. Format and symbols as in Figure 1.

Figure 9

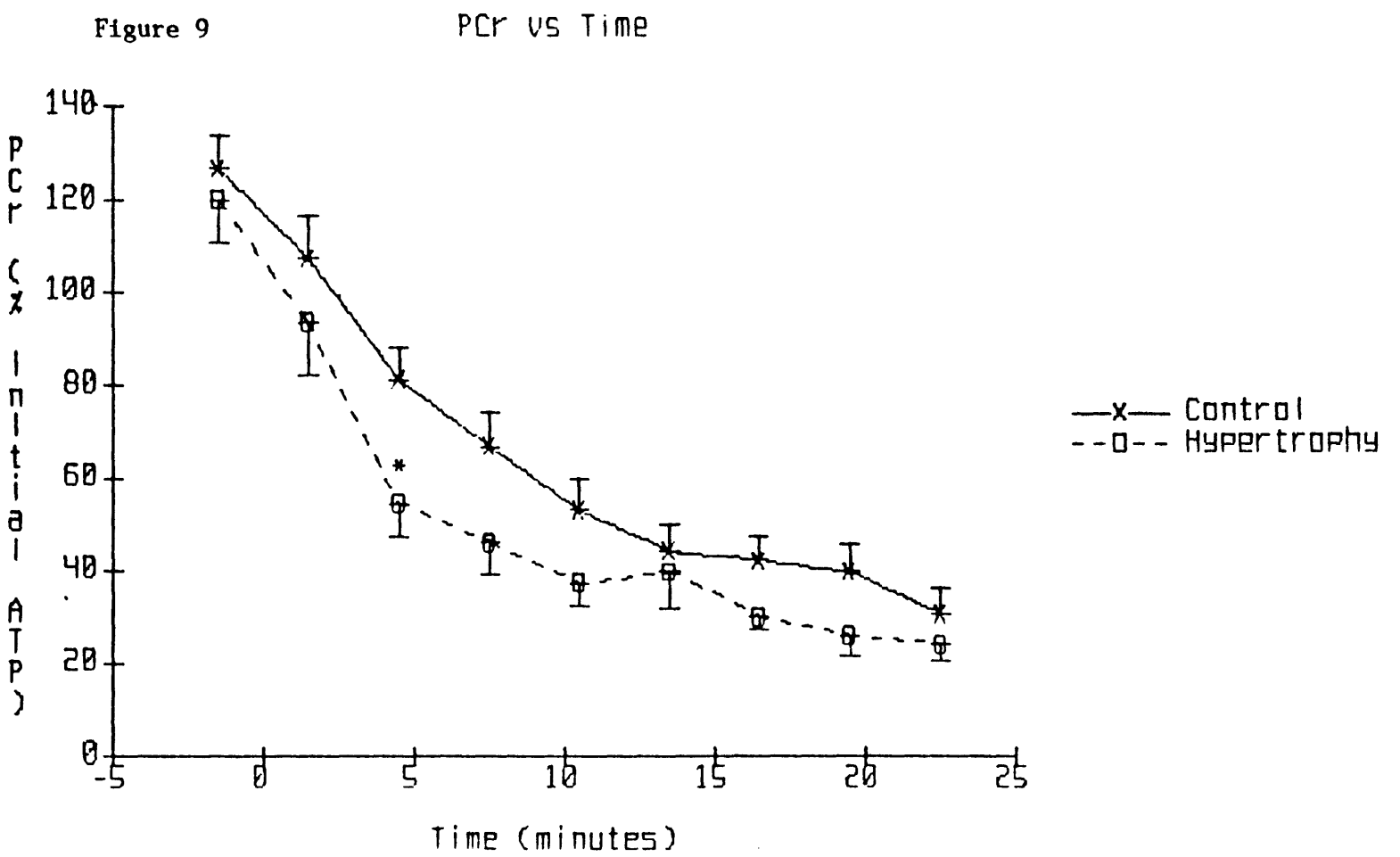
PCr vs Time
PCr (% Initial ATP)
140
120
100
80
60
40
20
0
-5
0
5
10
15
20
25
Time (minutes)
—x— Control
--o-- Hypertrophy

Figure 1Ø. Time course of pH. Although the hypertrophied hearts displayed a trend towards lower pH during hypoxia, the difference between the two groups was small. Format and symbols as in Figure 1.

Figure 10

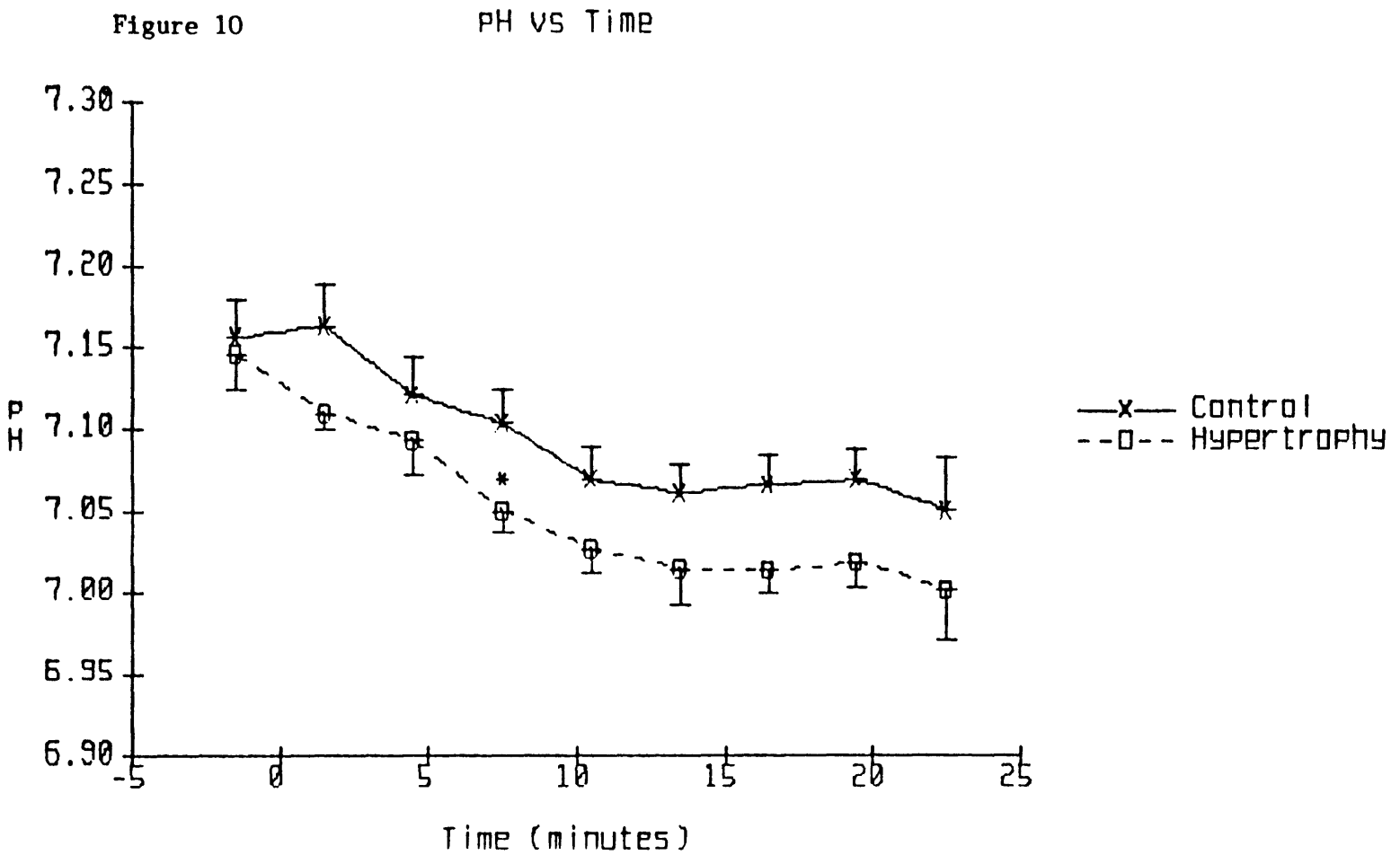
pH VS Time
7.30
7.25
7.20
7.15
7.10
7.05
7.00
6.95
6.90
pH
-5
0
5
10
15
20
25
Time (minutes)
—x— Control
--o-- Hypertrophy

Figure 11. Mutually predictive and non-mutually predictive relationships between cardiac function and metabolite levels.

a: Relationship between LVEDP and [ATP]. The regression equations shown are the results of a variance-weighted fit to the displayed data. The slopes of the two regression equations were different at a level of $p < .01$. LVEDP and [ATP] are correlated throughout their entire range, so that these variables are mutually predictive, in the sense that knowledge of one restricts the possible values of the other to a narrow range.

b: Relationship between LVDP and [ATP]. These variables are not mutually predictive; a large initial decrease in LVDP occurs without a significant decrease in [ATP], while subsequently, LVDP remains nearly constant as [ATP] continues to fall.

c: Relationship between LVDP and [PCr]. The regression equations shown are the results of a variance-weighted fit to the displayed data. The slopes of the two regression equations were different at a level of $p < .05$. LVDP and [PCr] are correlated throughout their entire range, so that these variables are mutually predictive, in the sense that knowledge of one restricts the possible values of the other to a narrow range.

d: Relationship between LVEDP and [PCr]. These variables are not mutually predictive; initially, a large decrease in [PCr] occurs without a correspondingly large increase in LVEDP. During the subsequent slow decrease in [PCr], LVEDP increases by a large amount.

Figure 11a

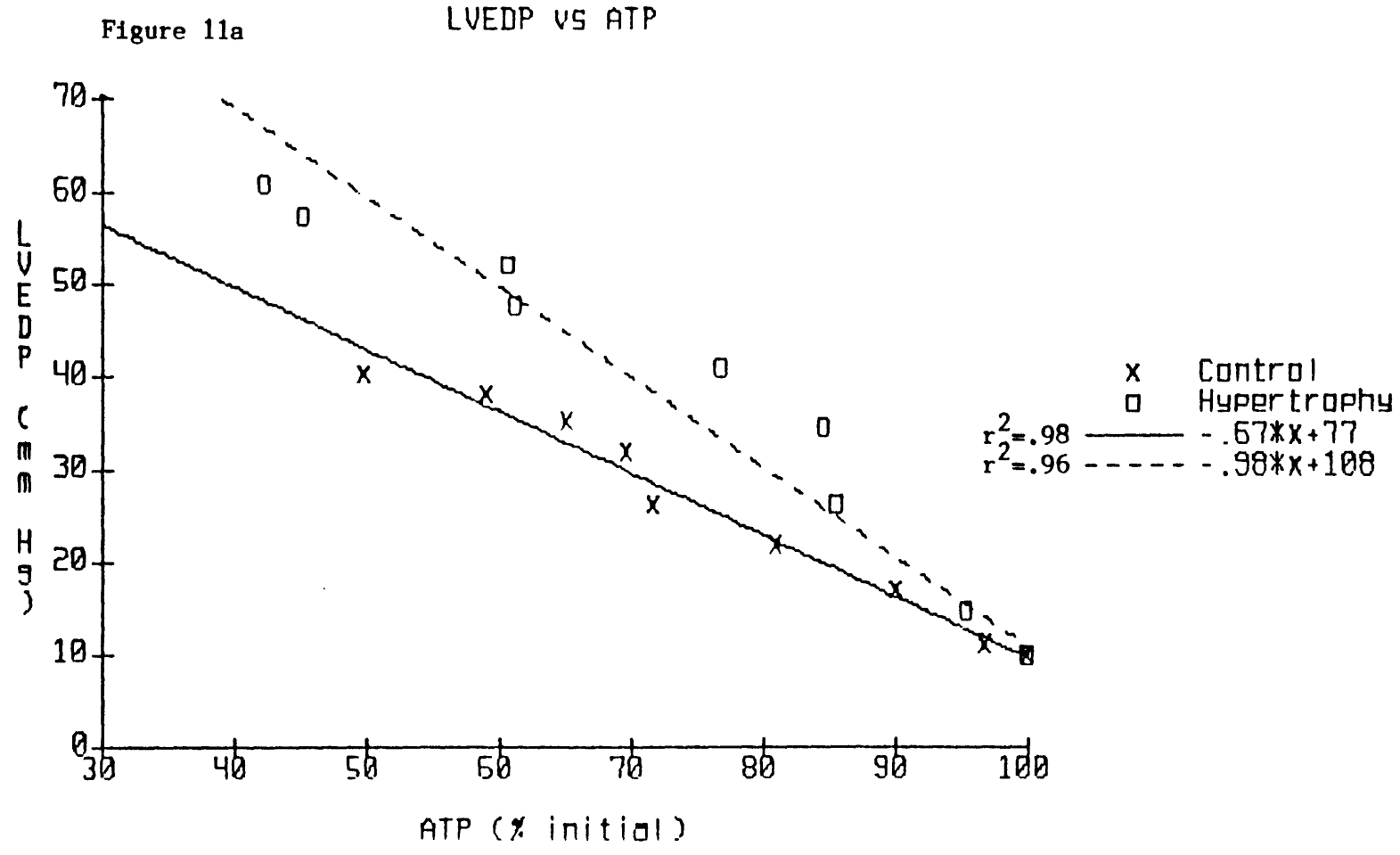
LVEDP VS ATP
LVEDP (mm Hg)
70
60
50
40
30
20
10
0
30
40
50
60
70
80
90
100
ATP (% initial)
x Control
o Hypertrophy
r2=.98 ——— -.67*x+77
r2=.96 - - - - - -.98*x+108

Figure 11b

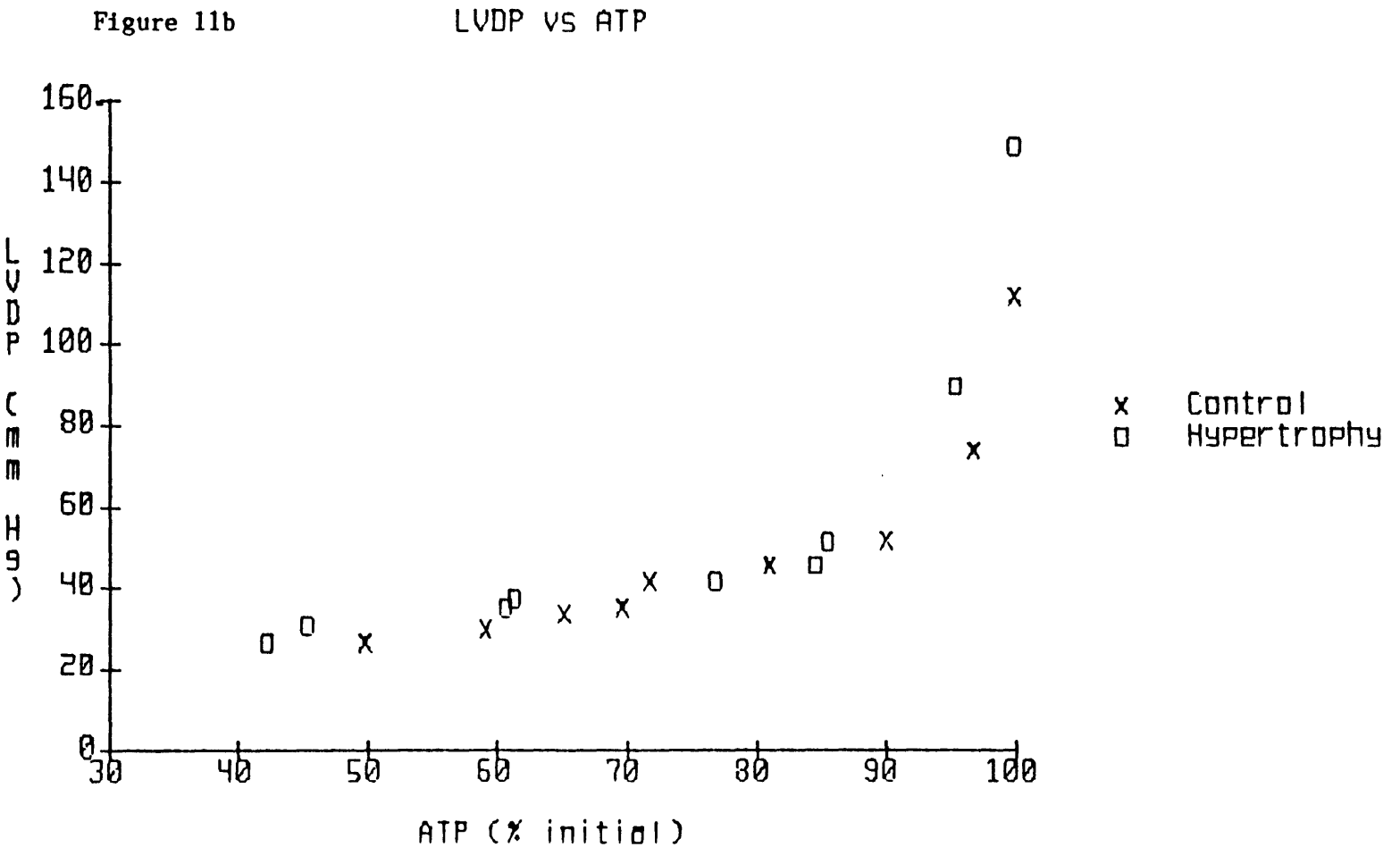
LVDP VS ATP
LVDP (mm Hg)
160
140
120
100
80
60
40
20
0
30
40
50
60
70
80
90
100
ATP (% initial)
Control
Hypertrophy

Figure 11c

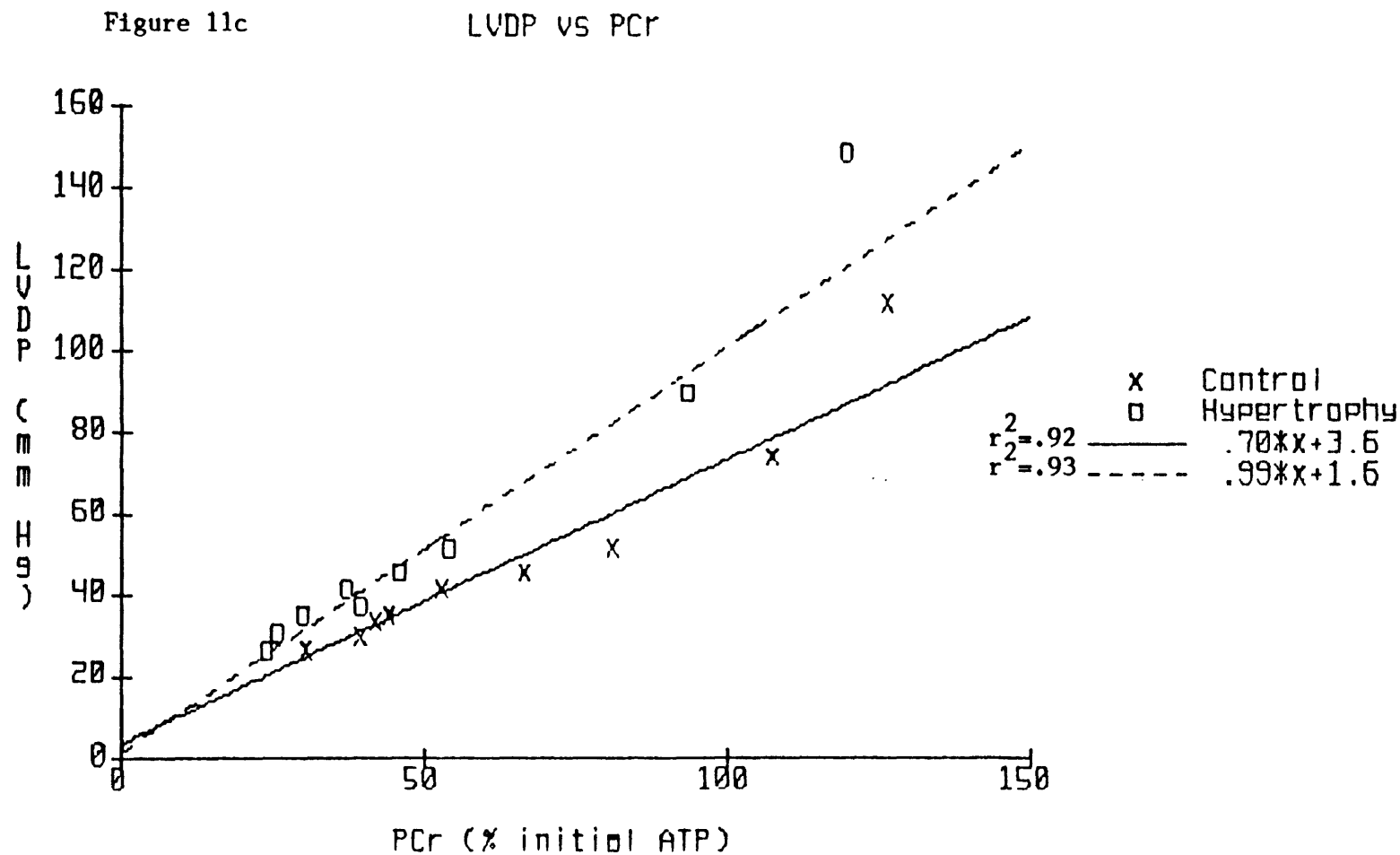
LVDP vs PCr
160
140
120
100
80
60
40
20
0
LVDP (mm Hg)
0
50
100
150
PCr (% initial ATP)
x Control
o Hypertrophy
r2=.92 ——— .70*x+3.6
r2=.93 - - - - - .99*x+1.6

Figure 11d

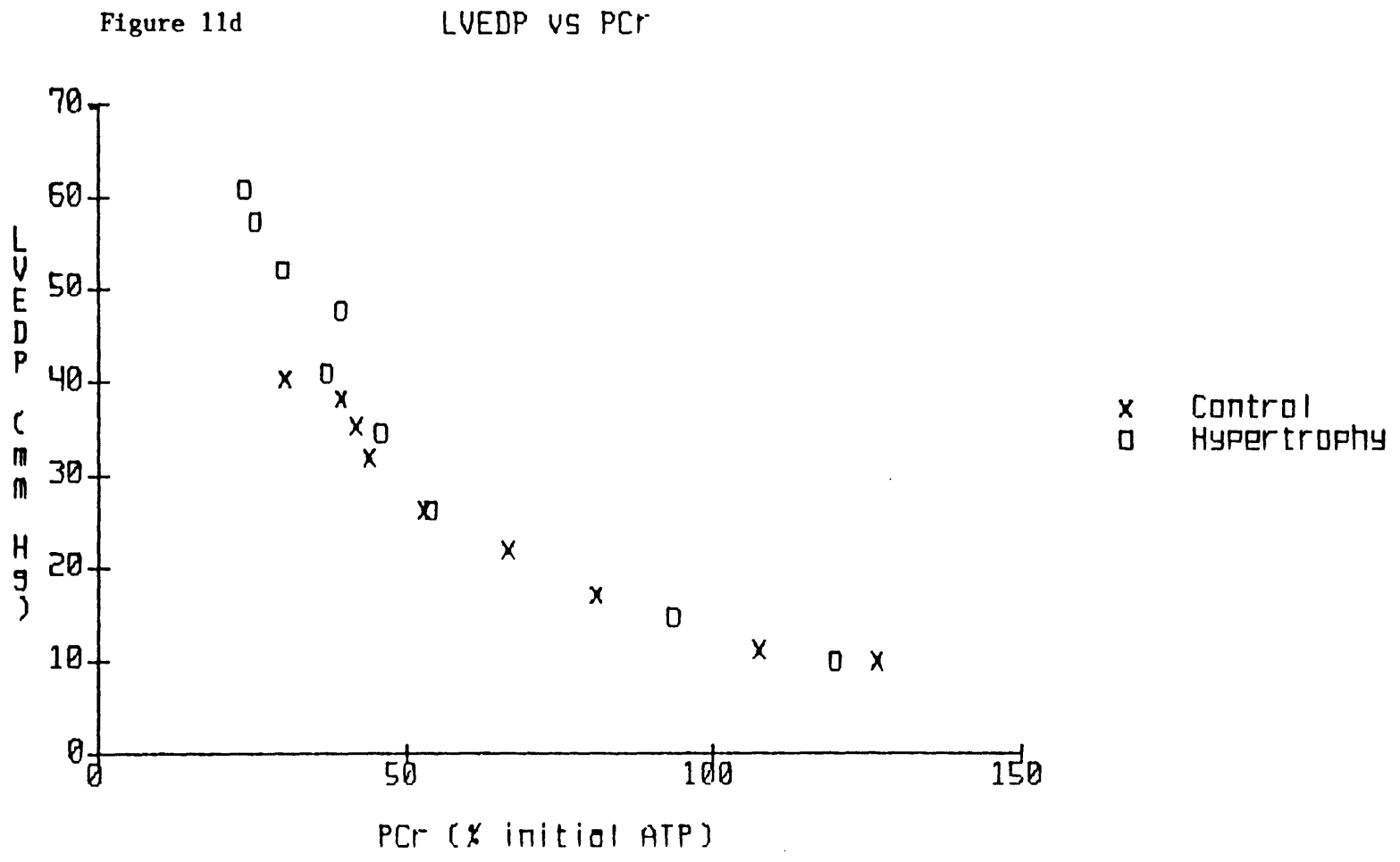
LVEDP vs PCr
LVEDP (mm Hg)
70
60
50
40
30
20
10
0
0
50
100
150
PCr (% initial ATP)
x Control
o Hypertrophy

Figure 12. Relationship between LVEDP normalized by LVW and [ATP]. Neither the slope nor the intercept of the two regression lines shown are significantly different.

Figure 12

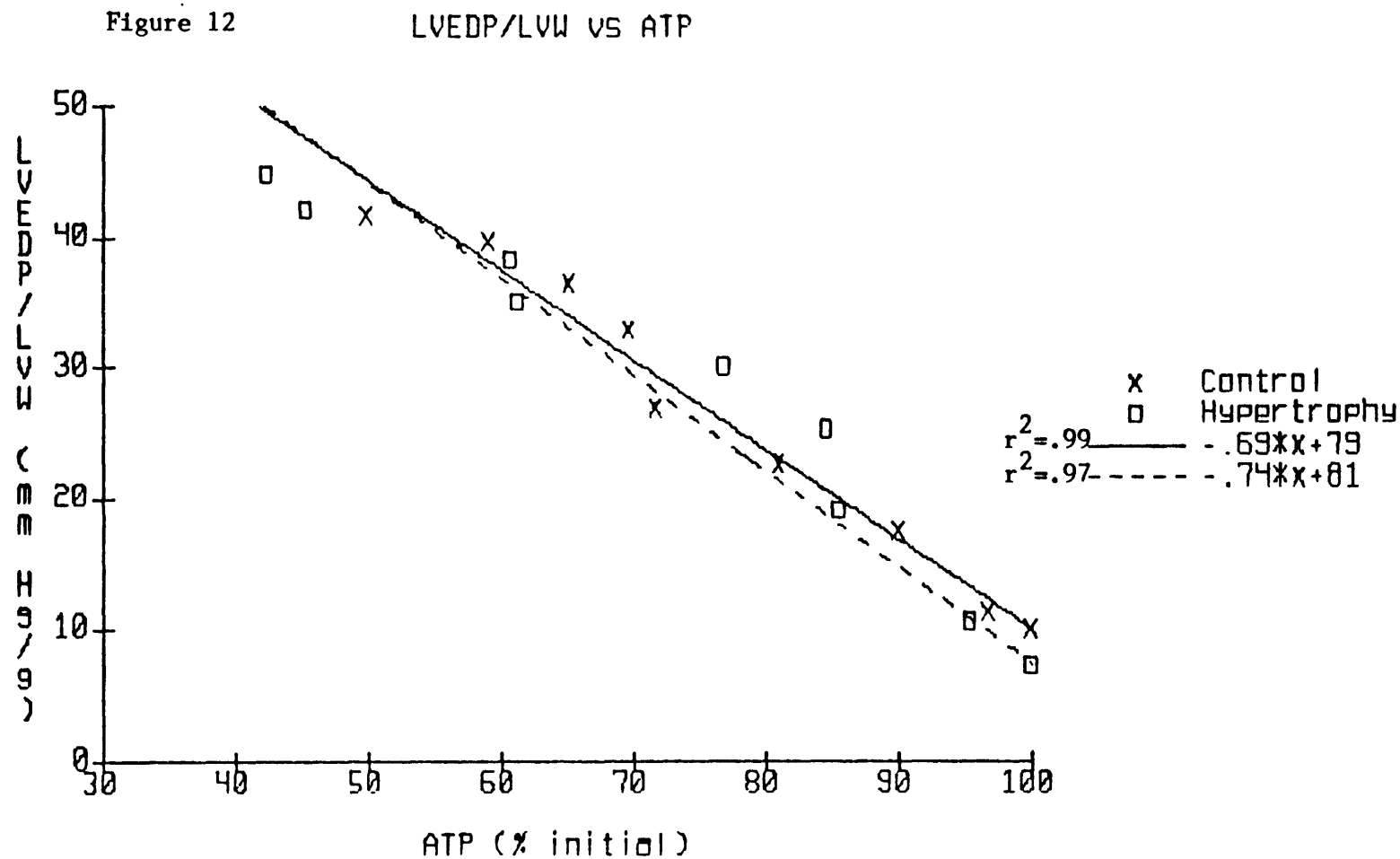
LVEDP/LVW VS ATP
LVEDP/LVW (mm Hg/g)
50
40
30
20
10
0
30
40
50
60
70
80
90
100
ATP (% initial)
x Control
o Hypertrophy
r2=.99 ——— -.69*x+79
r2=.97 - - - - -.74*x+81

Chapter 3, Part 2

The Hemodynamic and Metabolic Response to Hypoxia of the Rat Heart Hypertrophied Secondary to Chronic Exercise

Abstract

Using ^{31}P NMR spectroscopy and hemodynamic monitoring, we compared the development of metabolic and functional deficits in rat hearts hypertrophied secondary to chronic exercise to the development of such deficits in control hearts during prolonged global hypoxia. In addition, we assessed metabolic and functional recovery during reoxygenation. In an isolated, paced, buffer-perfused, isovolumic heart preparation, left ventricular developed pressure fell from a control oxygenation value of 119 ± 3.3 to 1Ø.6 ± 1.6 mm Hg after 16 minutes of hypoxia in control hearts, while in hearts from trained animals, the drop was from 133 ± 5.1 (a control oxygenation value 1.12 times greater than in the control hearts, $p < .Ø5$) to 28.5 ± 3.6 mm Hg (an end-hypoxia value 2.7 times greater than in the control hearts, $p < .Ø1$). The control group also exhibited somewhat less recovery after 32 minutes of reoxygenation (final developed pressure for the control group, 85.6 ± 4.7 mm Hg, 72% of the control oxygenation value; final developed pressure for the trained group, 1Ø7 ± 4.6 mm Hg, 8Ø% of the control oxygenation value). Left ventricular diastolic function was also markedly superior in the trained hearts. In the control group, the end diastolic pressure rose from its control oxygenation value of 1Ø mm Hg to 71.Ø ± 3.3 mm Hg at the end of 16 minutes of hypoxia, and recovered after 32 minutes of reoxygenation to only 19.8 ± 2.8 mm Hg, twice the control oxygenation value; in the trained group, the end diastolic pressure increased from 1Ø to only 55.3 ± 4.8 mm Hg at the end of hypoxia ($p < .Ø5$ versus control hearts), and recovered fully after reoxygenation, to 1Ø.4 ± 1.4 mm Hg ($p < .Ø1$ versus control hearts). These differences in the development of and recovery from functional deficits were not accompanied by differences in the rate of loss of high-energy phosphates; in both groups, ATP fell to approximately 55% of control oxygenation values after 16 minutes of hypoxia and recovered

to approximately 65% of these values after 32 minutes of reoxygenation, while phosphocreatine levels fell to approximately 3Ø% of their control values and recovered to approximately 115%. During hypoxia in both groups, left-ventricular developed pressure was highly correlated with phosphocreatine concentration, while left-ventricular end-diastolic pressure was highly correlated with ATP concentration. The relative preservation of diastolic function of the trained hearts during hypoxia, and their markedly greater recovery during reoxygenation, could not be accounted for either by high-energy phosphate metabolism as reflected by overall abundance measurements or by geometric considerations.

Introduction

In Chapter 3, Part 1, of this Thesis, it was found that rat hearts which had hypertrophied secondary to chronic hypertension exhibited a greater degree of left ventricular contracture during prolonged global hypoxia than did control hearts. We were able to account for this additional diastolic stiffening by the increased mass of the hypertrophied left ventricle, without the need to invoke a defect in high-energy phosphate metabolism. However, cardiac hypertrophy occurs not only in pathologic states, but also secondary to exercise. This may be termed "physiologic" hypertrophy, as opposed to the "pathologic" hypertrophy of a chronic pressure overload such as hypertension[1,2]. Of these two general categories, hypertrophy secondary to disease is by far more commonly seen clinically, accounting for its appropriate domination of the literature on hypertrophy. However, the athletic heart is itself of clinical concern, and even basic clinical issues of adaptive versus maladaptive changes in response to training have yet to be resolved[3,4].

The net effect of the cardiac alterations seen in mild pathologic or physiologic hypertrophy may represent, rather than a change in functional capability during normal activity, a change in the ability of the heart to respond to physiologic stress; for example, one of the chief differences between pathological and physiological hypertrophy, and between these states and the normal, is the degree of vascularization. Thus, although baseline function may be similar, altered cardiac reserve may become apparent with the imposition of an intervention which creates an imbalance between energy supply and demand, such as hypoxia.

As discussed in the Introduction to Part 1 of this chapter, the use of ^{31}P NMR spectroscopy allows for the simultaneous measurement of mechanical function and phosphorous-containing metabolite concentrations, including the high-energy phosphates ATP and phosphocreatine (PCr).

Using this technique, we may therefore assess both the metabolic and functional behavior of the heart, and establish explicit relationships between metabolic and functional parameters.

Many of the cardiac effects of training are undoubtedly independent of the development of hypertrophy[5], but we were specifically interested in further exploring the effect of cardiac mass on diastolic function. Because the increased left ventricular mass of the pathologically hypertrophied hearts studied in Chapter 3, Part 1, may have been directly responsible for their increased diastolic stiffness during hypoxia, we performed a similar investigation of hearts which had undergone hypertrophy secondary to chronic exercise.

In rats, the hypertrophy response to training appears to be most apparent in female, as opposed to male, rats, and with swimming, as opposed to running, as a stimulus[6,7,8]. Accordingly, cardiac hypertrophy was induced in female Wistar rats by subjecting them to chronic swimming, and the hemodynamic and metabolic response to prolonged global hypoxia of these hearts was then compared with that of normal hearts. The development of an additional diastolic deficit proportional to increased muscle mass in these hearts, as was found for pathologically hypertrophied hearts in Chapter 3, Part 1, would be strong evidence for a maladaptation of exercised hearts. Finally, in addition to hypoxia, we studied a reoxygenation period, to examine the ability of the hearts to recover function after the hypoxic injury.

Methods

Animals

Female Wistar rats weighing 150-200 grams were subjected to swim training for 8 - 10 weeks. They swam in groups two times per day for 75 minutes, five days per week. Age-matched control female Wistar rats were fed and housed under identical conditions. At the end of the experiment, all hearts were blotted dry and weighed. In addition, the left and right ventricles were dissected free and weighed separately. Both body weight and right tibia length were recorded for normalization of heart and left ventricle weights.

Perfusion

At the time of experimentation, the rats were anesthetized with an intraperitoneal injection of 25 mg sodium pentobarbital. Hearts were then rapidly excised and immersed in ice cold perfusion buffer. The aorta was then dissected free and the heart perfused retrograde through the aorta by 37° phosphate-free Krebs-Henseleit buffer gassed with 95% O_2, 5% CO_2 (pH 7.4) as described previously[9]. The buffer was composed of (mM) NaCl (118), KCl (4.7), EDTA (0.5), $MgSO_4$ (1.2), $CaCl_2$ (1.75), $NaHCO_3$ (25), and glucose (11). A constant-pressure system was used, providing a perfusion pressure of 100 mm Hg under gravity feed for all hearts. Coronary flow was assessed by measuring coronary effluent at four-minute intervals.

Hemodynamic measurements

A water-filled latex balloon was inserted into the left ventricle through an incision into the left atrium, via the mitral valve. The volume of this balloon was adjustable, so that initial LVEDP could be set to 10 mm Hg in all hearts. Pressures were obtained via a water filled tube running from the intraventricular balloon to a pressure transducer,

connected to a Hewlett-Packard chart recorder. Systolic and diastolic pressures were recorded at 4-minute intervals throughout the experiment.

NMR measurements

The perfused hearts were placed in a 2Ø mm NMR sample tube and inserted into the bore of an Oxford Instruments 36Ø wide-bore magnet (field strength, 8.45 Tesla), interfaced with a Nicolet 128Ø spectrometer. Individual spectra were accumulated over 4 minute periods. The distortion of the relative magnitudes of PCr and ATP was corrected by dividing by the appropriate NMR saturation factors (see, for example, Chapter 1, Part 1, of this Thesis). We were thus able to obtain measurements of relative amounts of ATP, PCr, and Pi every four minutes. In addition, intracellular pH was determined by comparison of the chemical shift between Pi and PCr with a standard curve obtained under comparable <u>in vitro</u> conditions[10].

Experimental protocol

After hemodynamic stability was attained with LVEDP set to 1Ø mm Hg, eight minutes of control data was obtained during perfusion with well-oxygenated buffer. The perfusate was then rapidly switched to one identical in composition but gassed with 95% N_2 and 5% CO_2 to induce hypoxia. We continued collecting spectra and hemodynamic data over four-minute periods thereafter, up to a total time of 16 minutes of hypoxia. The hearts were then perfused with the well-oxygenated buffer for a 32 minute period of reoxygenation. All hearts were paced at 4.5 Hz, except that pacing was turned off during early reoxygenation if it induced arrhythmias.

Statistical analysis

Statistical analyses were performed using the RS/1 software of BBN Research Systems, Cambridge, MA. Means were

compared using the 2-tailed Student's t-test. Linear regressions were performed by a weighted least-squares routine, with weights given by the reciprocal of the variance of each point in the ordinate dimension. The uncertainty in the predictor variable was neglected as, in all cases, the variance of the set of predictor values was much greater than the variances of the individual points[11]. All errors are presented as ± SEM.

Results

Effect of Chronic Swimming on Cardiac Mass

Table 1 shows the effect of swim training on body weight (BW), heart weight (HW) (increased by 38% over control animals), left ventricular weight (LVW) (increased by 33%), and the ratios of the latter two to body weight (HW/BW and LVW/BW) (increased by 30% and 26%, respectively) and right tibia length (HW/TL and LVW/TL) (increased by 37% and 32%, respectively). All of these differences between the two groups were statistically significant.

Hemodynamic Data

Hemodynamic and coronary flow data is summarized in Table 2 and Figures 1 to 5. Note that hemodynamic data is reported for times at the midpoint of the four-minute intervals defined by the acquisition of NMR spectra, so that the hemodynamic values correspond to the averaged metabolic levels measured by NMR. Fig. 1 shows that the left-ventricular systolic pressure (LVSP) of the exercised hearts was slightly (10%) but statistically significantly greater than that of the control hearts during control oxygenation. During the second through fourth four-minute hypoxic periods, there was no difference between the two groups. Upon reoxygenation, however, a dramatic difference was observed: the control hearts exhibited a very gradual increase in LVSP, while the LVSP of the exercised hearts increased sharply, achieving a LVSP not significantly different from their initial control oxygenation values during the first two minutes of reoxygenation, and full recovery of LVSP by six minutes. The gradual rise in LVSP seen in both groups during the latter parts of hypoxia probably reflects either cellular edema or increased vasodilation secondary to the production of adenosine, either one of which may tend to increase myocardial stretch and effective myocardial preload, and hence LVSP. Similarly, the slow decline in LVSP of the

swimming group during reoxygenation may be explained by decreased adenosine production, consistent with the coronary flow data shown in Fig. 5. Note that by the end of the reoxygenation period, LVSP of both groups of hearts had reached a stable level, so that the recovery we observed may be regarded as maximal.

Changes in left ventricular diastolic pressure (LVEDP) are shown in Fig. 2. Starting from an equal initial LVEDP of 1Ø mm Hg, the hearts from trained animals exhibited a smaller increase in resting tension than did the control hearts throughout all of hypoxia. Post-hypoxic recovery was also more rapid and more complete in these animals, with the controls exhibiting a final LVEDP of 19.8 mm Hg after 3Ø minutes of reoxygenation, while the LVEDP of the trained hearts recovered to 1Ø.4 mm Hg, indicating full recovery to control diastolic stiffness. All differences in LVEDP between the control hearts and the trained hearts were statistically significant during hypoxia and reoxygenation. Again, note that by the end of the 32 minute reoxygenation period, both groups had reached a stable LVEDP.

Left ventricular developed pressure (LVDP), defined by LVDP = LVSP - LVEDP, is shown in Fig. 3. Because the trained hearts had either a greater LVSP or smaller LVEDP, or both, throughout the experiment, they showed a greater LVDP throughout. The difference between the two groups was statistically significant at all times. Because heart rate was fixed throughout these experiments, the ordinate of Fig. 3 may be viewed as either developed pressure or as the rate-pressure product (RPP) = developed pressure x heart rate, which is an index of total myocardial work output and oxygen consumption in the isolated heart. Thus, we find that the trained hearts maintained a higher level of work and oxygen utilization. To assess this on a per gram basis, we normalized LVDP by LVW, as shown in Fig. 4. The control oxygenation value of LVDP/LVW for the hearts from trained rats was significantly lower than that of the controls, but

the exercised hearts maintained their LVDP/LVW somewhat better throughout hypoxia, so that by the end of the 16 minute hypoxic period, they showed an LVDP/LVW significantly greater than the controls. This difference was magnified during early reoxygenation, indicating an increased ability of the trained hearts to utilize oxygen and produce work per unit mass during this period. Towards the end of the reoxygenation period, the two groups showed equal LVDP/LVW; this equality follows from the fact that the LVSP/LVW and LVDP/LVW of the trained hearts was smaller than in the controls by approximately the same amount. Note that the data represented in Fig. 4 was derived by calculating each heart's LVDP/LVW at each time, and then averaging these quantities for each time interval, rather than by dividing the curves in Fig. 3 by the average LVW for the control and hypertrophied groups, respectively. The error bars in Fig. 4 therefore reflect the variation in both LVDP and LVW within groups, and so are larger than those in Fig. 3. Similar comments apply to other data normalized to LVW or HW presented below.

Total coronary flow (CF) was significantly greater in the trained hearts throughout the entire experiment. However, normalizing by HW to assess tissue vascularization, we see from Fig. 5 that during control oxygenation, perfusion per gram of heart was equal in the two groups. In addition, they showed a similar sudden increase in flow at the outset of hypoxia. However, the CF/HW was significantly greater in the trained hearts during the second through fourth four-minute hypoxic periods, consistent with a greater coronary reserve in these hearts. The greater CF/HW in the trained hearts persisted throughout reoxygenation as well, but was only statistically significantly greater during the first eight minutes of reoxygenation. The decline in coronary flow during hypoxia following the initial vasodilatory response in both groups may be due to vascular compression secondary to edema formation, or to a decline in adenosine production.

Metabolic Data

High-energy phosphate (ATP and PCr) levels are shown in Figs. 6 and 7, and Table 3. Values are given relative to an initial ATP concentration of 100% in each group. It has previously been shown[1,2] that the control levels of ATP and PCr are not altered significantly by the exercise protocol we have used. We see that in the control hearts, the initial concentration of PCr was 1.30 ± .10 times the initial ATP concentration, while the corresponding value for the trained group was 1.27 ± .05 (not significantly different between the two groups). At the end of the hypoxic period, the concentration of PCr had dropped to 29% and 27% of control levels in the trained and control groups, respectively. As is evident from Fig. 6, the drop in [PCr] was more sudden during the earlier, as opposed to the later, part of the hypoxic period. Both groups exhibited an overshoot in recovery of PCr levels during reoxygenation, with control hearts achieving a maximum [PCr] 31% greater than control oxygenation levels, and exercised hearts achieving a maximum [PCr] 34% greater than their control value. Values of [PCr] greater than control oxygenation levels persisted throughout reoxygenation. There was no statistically significant difference in PCr concentration between the two groups at any time. In contrast to [PCr], the rate of change of [ATP] with respect to time was roughly constant throughout the hypoxic period, as seen in Fig. 7. The percent of initial concentration of ATP remaining at the end of hypoxia was 53 ± 5% for the controls and 59 ± 3%, with neither group demonstrating a substantial repletion of ATP during reoxygenation. At no time was the difference in ATP concentration between the two groups statistically significant.

Fig. 8 shows the time evolution of intracellular pH. The two groups showed an equal small drop in pH during hypoxia, and similar recovery upon reoxygenation.

Relationship between metabolism and function

Figs. 9a-d show the relationships, during control oxygenation and hypoxia, between the two main high-energy phosphates and the hemodynamic parameters reflecting systolic function and diastolic function. The results here are substantially the same as in Figs. 11a-d of Part 1 of this Chapter. We see from Fig. 9a that LVEDP and [ATP] are correlated with each other throughout their entire range of variation during hypoxia, so that we may say that LVEDP and [ATP] are mutually predictive, i.e., that knowledge of either one provides a reliable index to the other. Fig. 9b shows that LVDP and [ATP] are not mutually predictive; a large drop in LVDP occurs with the onset of hypoxia without a significant decrease in [ATP], and, as hypoxia progresses, [ATP] continues to fall even though LVDP is relatively stable. On the other hand, Figure 9c shows that there is a clear mutually predictive relation between [PCr] and LVDP during prolonged hypoxia in this preparation. From Fig. 9d, we see that [PCr] and LVEDP are not mutually predictive, with [PCr] falling at the onset of hypoxia before LVEDP rises, and [PCr] remaining nearly constant as LVEDP continues to rise during late hypoxia. Neither the two slopes nor the two intercepts of the regression lines in Fig. 9a were significantly different. Similarly, the relations shown in Fig. 9c were also not significantly different, although the p-value of the intercepts in Fig. 9c were nearly so ($p = Ø.5Ø2$), reflecting the greater LVDP of the trained hearts, and the nearly identical rate of loss of PCr in the two groups, during hypoxia.

Discussion

Changes in cardiac reserve may be a key feature of the cardiac adaptation to both pathologic and physiologic stimuli. A method of directly assessing altered reserve is to examine response to a fixed insult, the most common examples being hypoxia and ischemia. Indeed, many such studies of the pathologically hypertrophied heart have been carried out (see, e.g., references in Chapter 3, Part 1). Cardiac hypertrophy is an ubiquitous finding in pathologic settings; among others, it is associated with states of primary pressure overload (as seen in, for example, hypertension), primary volume overload (as seen, for example, in arteriovenous shunts), coronary artery disease and other setting of focal cardiac ischemia, and in diffuse cardiomyopathies. All of these conditions are accompanied by cardiac hypertrophy of some form, and in addition, in all of them, the hypertrophy develops in step with the progression of the disease.

Physiologic stimuli to cardiac adaptation are generally due to exercise (leaving aside the issue of maturation of the cardiovascular system). Animal studies imply that hypertrophy is a much less constant companion to exercise than it is to pathology, but it is produced by several animal training protocols, and its occurrence is well-documented in human athletes as well. Clinically, hypertrophy secondary to training is seen relatively infrequently, accounting for the relative infrequency of experimental, and especially clinical, investigations, of this state. In particular, few studies have assessed the physiologic cardiac reserve of hearts hypertrophied secondary to exercise by monitoring their response to ischemia or hypoxia. For a review of cardiac adaptations to exercise, see Schaible and Scheuer[13].

In the present study, isovolumically beating perfused hearts from swim trained rats and from control rats were subjected to global hypoxia for 16 minutes and reoxygenation

for 32 minutes. Hemodynamic function was monitored while phosphorus-containing metabolite levels were measured at four-minute intervals with ^{31}P NMR spectroscopy. In terms of systolic function, the greatest differences between the two groups was seen during reoxygenation, early reoxygenation in particular. However, markedly different diastolic function was observed throughout both hypoxia and reoxygenation. Although, as expected[14], both absolute coronary flow and coronary flow per gram of heart weight were greater in the trained group during hypoxia and reoxygenation, the role of this increased perfusion in the relative preservation and recovery of function demonstrated by the trained hearts is unclear. If the increased oxygen supply (the pO_2 of our hypoxic buffer is approximately 2Ø Torr) or increased delivery of glycolytic substrate resulting from the increased perfusion flow were responsible, one might expect this to be reflected in a relative preservation of high-energy phosphate levels. In fact, however, no such preservation was seen. Similarly, pH differences were small and nonsignificant.

In another study in which trained hearts were exposed to global hypoxia, Carey et al.[15] studied the response to mild hypoxia of living, anesthetized, treadmill-trained rats. They found that it took longer for the trained rats to develop a 5Ø% reduction in contractility (as assessed by $(dP/dt)_{max}$), and, in addition, a greater rate-pressure product was reported for the trained rats during hypoxia, consistent with our findings (Fig. 3). No significant difference was found in the concentrations of high-energy phosphates between nontrained and trained animals after the hypoxic period. However, because the endpoint of the experiment was defined by a predetermined functional deficit, and the time elapsed during the development of this deficit was greater for the nontrained rats, the results of Ref. 13 may imply a more rapid depletion of high-energy phosphates in the untrained animals. This issue was not further addressed in Ref. 13.

Scheuer and Stezoski[16] performed a study more similar in design to the present one. During five minutes of global hypoxia, isovolumic performance was found to be only minimally improved in the hearts from trained rats as compared to hearts from sedentary animals. In addition, the concentration of residual high-energy phosphates was not different between the two groups. However, the hypoxic period may have been too short for differences to fully develop, and the pO_2 during hypoxia was greater than in the present study (pO_2 ~ 140 mm Hg, as opposed to pO_2 ~ 20 mm Hg). Perhaps for these reasons, the ATP concentrations after hypoxia reported in Ref. 14 were still at control levels. It is interesting to note that of the parameters reported, the greatest difference between control and trained hearts in the isovolumic preparation was an increased deficit in diastolic function in the controls. Also, as stated, this diastolic deficit apparently developed in the absence of ATP depletion.

In both of the studies discussed above, metabolite concentrations were measured only once; in the present study, the high time resolution of NMR spectroscopy allowed us to establish relationships between metabolite levels and function. We found that during hypoxia in this sample preparation and in this model of exercise hypertrophy, [ATP] is an excellent predictor of diastolic (but not systolic) function, while [PCr] is an excellent predictor of systolic (but not diastolic) function. However, in neither the other studies we have discussed nor the present one was an underlying mechanism for the markedly improved systolic function during reoxygenation and improved diastolic function during hypoxia and reoxygenation of the trained hearts uncovered. Thus, it appears that an effect more subtle than preservation of net metabolite abundances may be responsible.

In the previous study (Chapter 3, Part 1), the increased diastolic deficit of pathologically hypertrophied hearts during hypoxia could be accounted for by their increased

mass, with the hypothesis that this increased mass was due to parallel addition of normal sarcomeres. The trained hearts in the present study were hypertrophied to the same extent as the pathologically hypertrophied hearts referred to above, but their diastolic behavior during hypoxia was enhanced rather than diminished. However, even apart from any biochemical adaptations, the geometric pattern of exercise-induced hypertrophy, which is eccentric, is quite different from that of pressure overload hypertrophy, which is of the concentric pattern. On this basis alone, one might predict a different degree of diastolic dysfunction during hypoxia. To see this, consider first pure concentric hypertrophy, by which we mean an increase in thickness of the left ventricular wall without a concomitant increase in left ventricular radius. If, during hypoxia, each sarcomere exerted a given resting force, and the histologic pattern of the hypertrophy were the parallel addition of sarcomeres[17], then the total circumferential tension exerted by the left ventricle would be proportional to its increased mass. (See Figure 10.) The observations in the previous study, Chapter 3, Part 1, are completely consistent with this model. On the other hand, if the pattern of hypertrophy were purely a dilatation, with no increase in wall thickness, and the histology of the resultant increase in mass were series addition of sarcomeres (Ref. 15), the total circumferential tension exerted by the left ventricle would not be proportionally increased. (See Figure 11.) This latter pattern of hypertrophy probably does not occur in training, since the ventricular dilatation seen in this setting is generally accompanied by some increase in wall thickness. Nevertheless, it is clear that to whatever extent the increased mass of the trained heart is due to dilatation and series addition of sarcomeres, the additional diastolic deficit during hypoxia would not be expected to be proportional to the increased mass. This picture, while it may account for some of the difference between the hypoxic

contracture of the pathologically and physiologically hypertrophied hearts, certainly cannot account for all of it. In the case of the trained hearts, even if the hypertrophy were solely due to dilatation, with no increase in wall thickness, the model described above would predict that the LVEDP during hypoxia would approximately equal that of the control hearts, while the LVEDP/LVW of the trained hearts would be lower. In fact, this is the result we expected in the present study. However, an overall lower diastolic was in fact observed, rather than just a preservation of diastolic function a per gram.

Thus, the relatively preserved diastolic function of the trained hearts, as we have just discussed in detail, cannot be explained by either attenuation of high-energy phosphate loss or by an overall geometric effect. Accordingly, NMR kinetic studies and enzyme analyses were performed in order to test other possible mechanisms, as discussed in the next section, Chapter 3, Part 3.

1. J. Wikman-Coffelt, W.W. Parmley, and D.T. Mason. The Cardiac Hypertrophy Process, Circ. Res. 45:697-707 (1979).

2. F.Z. Meerson. The failing heart: adaptation and deadaptation, Raven Press, New York (1983).

3. M.H. Crawford and R.A. O'Rourke. The athlete's heart, Adv. Int. Med. 24:311-329 (1979).

4. J.A. Alexander. Athlete's heart, Med. Grand Rounds 4:1-7 (1986).

5. P.M. Buttrick, H.A. Levite, T.F. Schaible, G. Ciambrone, and J. Scheuer. Early increases in coronary vascular reserve in exercised rats are independent of cardiac hypertrophy, J. Appl. Physiol. 59:1861-1865 (1985).

6. T.F. Schaible and J. Scheuer. Effects of physical training by running or swimming on ventricular performance of rat hearts, J. Appl. Physiol.: Respirat. Environ. Exercise Physiol. 46:854-860 (1979).

7. T.F. Schaible, S. Penpargkul, J. Scheuer. Cardiac responses to exercise training in male and female rats, J. Appl. Physiol.: Respirat. Environ. Exercise Physiol. 50:112-117 (1981).

8. T.F. Schaible and J. Scheuer. Cardiac function in hypertrophied hearts from chronically exercised female rats, J. Appl. Physiol.: Respirat. Environ. Exercise Physiol. 50:1140-1145 (1981).

9. J. S. Ingwall (1982). Phosphorus Nuclear Magnetic Resonance Spectroscopy of Cardiac and Skeletal Muscles, Am. J. Physiol. 242:H729-H744.

10. W. E. Jacobus, I. H. Pores, S. K. Lucas, C. H. Kallman, M. L. Weisfeldt, and J. T. Flaherty (1982). The Role of Intracellular pH in the Control of Normal and Ischemic Myocardial Contractility: A ^{31}P Nuclear Magnetic Resonance and Mass Spectrometry Study, in Intracellular pH: Its Measurement, Regulation, and Utilization in Cellular Functions, Alan R Liss, Inc., New York.

11. N. Draper and H. Smith (1981). Section 2.14 in Applied Regression Analysis, Wiley and Sons, New York.

12. J. Scheuer, L. Kapner, C. A. Stringfellow, C. L. Armstrong, and S. Penpargkul. Glycogen, lipid, and high energy phosphate stores in hearts from conditioned rats, J. Lab. Clin. Med. 75:924-929 (1970).

13. T. F. Schaible and J. Scheuer. Response of the Heart to Exercise Training, in Growth of the Heart in Health and Disease, edited by R. Zak. Raven Press, New York (1984).

14. J. Scheuer. Effects of physical training on myocardial vascularity and perfusion, Circ. 66:491-495 (1982).

15. R. A. Carey, C. M. Tipton, and D. R. Lund. Influence of training on myocardial responses of rats subjected to conditions of ischaemia and hypoxia. Cardiovasc. Res. 1Ø:359-367 (1976).

16. J. Scheuer and S. W. Stezoski. Effect of physical training on the mechanical and metabolic response of the rat heart to hypoxia. Circ. Res. 3Ø:418-429 (1972).

17. W. Grossman, D. Jones, and L. P. McLaurin. Wall stress and patterns of hypertrophy in the human left ventricle. J. Clin. Invest. 56:56-64 (1975).

Table 1. Body, Heart, and Left Ventricle Weights

	BW (g)	HW (g)	LVW (g)
Control (n = 13)	276 ± 3.8	.86 ± .Ø3	.64 ± .Ø2
Trained (n = 8)	292 ± 6.6 (↑ 6%*)	1.19 ± .Ø5 (↑ 38%**)	.86 ± .Ø3 (↑ 33%**)

	HW/BW x 1Ø³	LVW/BW x 1Ø³
Control	3.12 ± .Ø7	2.34 ± .Ø5
Trained	4.Ø7 ± .12 (↑ 3Ø%**)	2.93 ± .Ø9 (↑ 26%**)

	HW/TL (g/cm)	LVW/TL (g/cm)
Control	Ø.23 ± .Ø1	Ø.17 ± .ØØ4
Trained	Ø.32 ± .Ø1 (↑ 37%**)	Ø.23 ± .Ø1 (↑ 32%**)

Effects of swim-training regimen, as described in text, on body weight (BW), heart weight (HW), left ventricular weight (LVW), heart weight-to-body weight ratio (HW/BW), left ventricular weight-to-body weight ratio (LVW/BW), heart weight-to-tibia length ratio (HW/TL), and left ventricular weight-to-tibia length ratio (LVW/TL). Percent changes are calculated with data to more significant figures than shown here. *$p < .Ø5$, **$p < .Ø1$ control versus trained.

Table 2. Effect of Hypoxia on Functional Variables

	LVSP		LVSP/LVW	
	Control	Trained	Control	Trained
Normoxia	129 ± 3.3	*143 ± 5.1	2Ø2 ± 7.6	**167 ± 2.5
6 minutes	67.2 ± 3.6	7Ø.4 ± 2.5	1Ø5 + 6.Ø	**82.8 ± 3.Ø
14 minutes	81.9 ± 2.9	83.8 ± 2.Ø	128 ± 5.7	**99.3 ± 5.4
Reoxygen-ation	1Ø5 ± 4.4	117 ± 5.5	167 ± 9.3	*137 ± 5.2

	LVEDP		LVEDP/LVW	
	Control	Trained	Control	Trained
Normoxia	1Ø.Ø	1Ø.Ø	15.7 ± .44	**11.8 ± .5
6 minutes	37.3 ± 2.6	*26.9 ± 2.4	58.1 ± 4.2	**31.6 ± 2.7
14 minutes	71.Ø ± 3.3	*55.3 ± 4.8	111 ± 5.Ø	**65.8 ± 6.8
Reoxygen-ation	19.8 ± 2.8	**1Ø.4 ± 1.4	3Ø.7 ± 3.7	**12.1 ± 1.5

	LVDP		LVDP/LVW	
	Control	Trained	Control	Trained
Normoxia	119 ± 3.3	*133 ± 5.1	187 ± 7.3	**155 ± 2.3
6 minutes	29.9 ± 2.4	**43.6 ± 1.4	46.9 ± 3.9	51.3 ± 1.8
14 minutes	1Ø.6 ± 1.6	**28.5 ± 3.6	17.Ø ± 2.8	**33.6 ± 4.2
Reoxygen-ation	85.6 ± 4.7	**1Ø7 ± 4.6	136 ± 1Ø	125 ± 4.3

Values of functional variables during control oxygenation, at two times during hypoxia, and at the end of the 32 minute

reoxygenation period. Abbreviations and units are: left ventricular systolic pressure (LVSP), mm Hg; left ventricular weight (LVW), g; LVSP divided by LVW (LVSP/LVW), mm Hg/g; left ventricular end-diastolic pressure (LVEDP), mm Hg; LVEDP/LVW, mm Hg/g; left ventricular developed pressure (LVDP), mm Hg/sec; LVDP/LVW, mm Hg/g/sec. 6 and 14 minutes correspond respectively to the times at the midpoint of the second and fourth ^{31}P spectra accumulated during hypoxia. *p < .Ø5, **p < .Ø1, control versus trained hearts.

Table 3. Effect of Hypoxia on Metabolic Variables

	[ATP]		[PCr]	
	Control	Trained	Control	Trained
Normoxia	100	100	130 ± 10	127 ± 5.2
6 minutes	83.6 ± 9.0	81.4 ± 4.7	58.5 ± 8.8	50.8_+ 7.3
14 minutes	53.1 ± 5.5	59.2 ± 3.2	37.1 ± 5.9	34.9 ± 4.1
Reoxygen-ation	67.5 ± 6.8	61.1 ± 2.3	150 ± 8.8	145 ± 8.4

Intracellular concentrations of adenosine triphosphate (ATP) and phosphocreatine (PCr) during control oxygenation, at two times during hypoxia, and at the end of the reoxygenation period. Initial [ATP] was set to 100 in each heart, and all other values are given relative to that. 6 and 14 minutes correspond respectively to the times at the midpoint of the second and fourth ^{31}P spectra accumulated during hypxia. None of the differences shown between the two groups was statistically significant.

Figure 1. Time course of left-ventricular systolic pressure (LVSP) for control and hypertrophied hearts during control oxygenation (first data point; -2 minutes), 16 minutes of hypoxia (second through fifth data points; 2 to 14 minutes), and 32 minutes of reoxygenation (sixth through thirteenth data points; 18 to 46 minutes). LVSP was similar in the two groups until reoxygenation, when the trained hearts displayed a much more rapid recovery. *p < .Ø5, **p < .Ø1, control versus trained hearts.

Figure 1

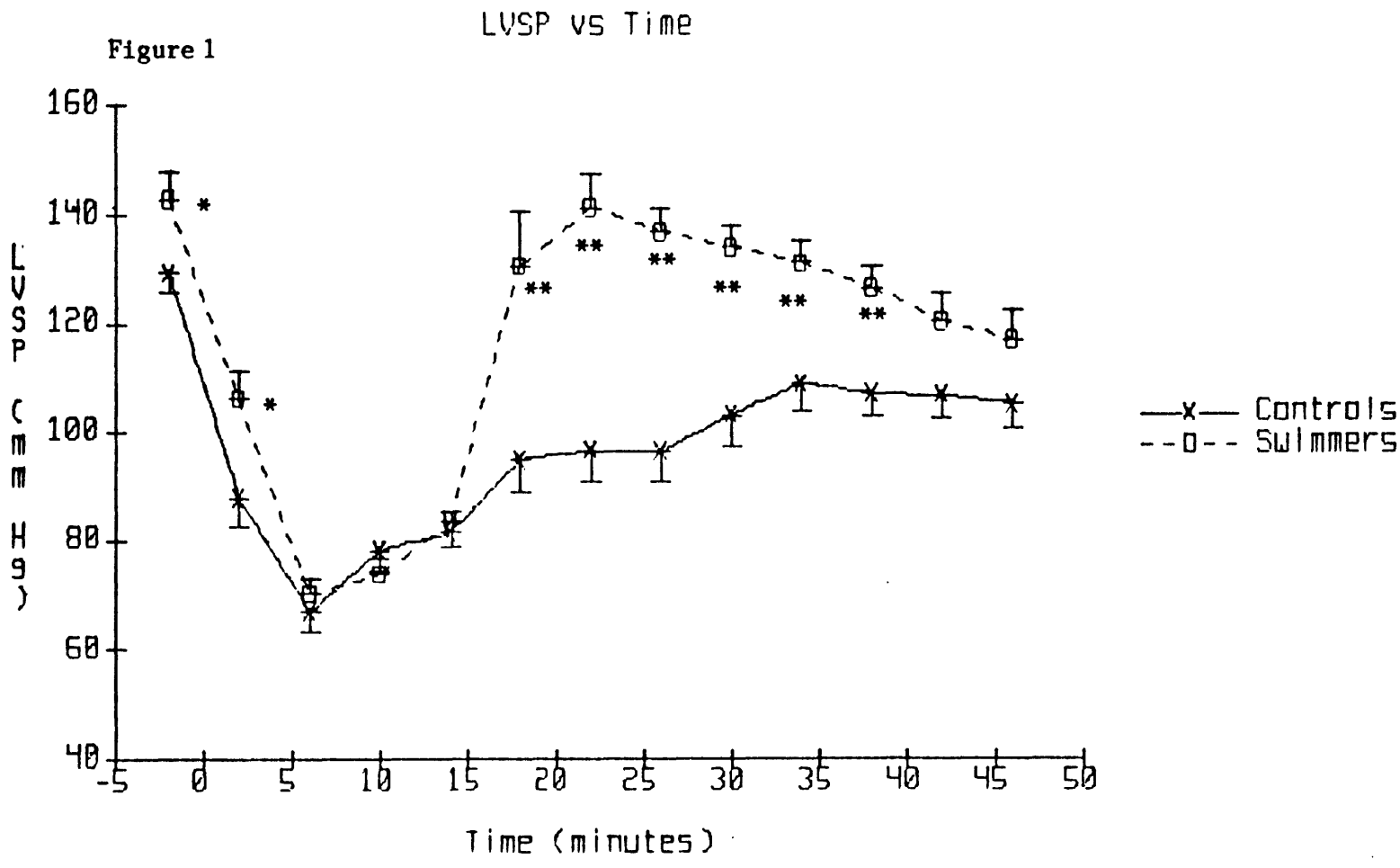
LVSP vs Time
LVSP (mm Hg)
160
140
120
100
80
60
40
-5
0
5
10
15
20
25
30
35
40
45
50
Time (minutes)
—x— Controls
--o-- Swimmers

Figure 2. Time course of left-ventricular end-diastolic pressure (LVEDP). Format and symbols as in Figure 1. Starting from an initial LVEDP set to 1Ø mm Hg in both groups during control oxygenation, the trained hearts developed significantly less contracture during prolonged hypoxia than did the controls, and recovered more rapidly and more completely during reoxygenation.

Figure 2

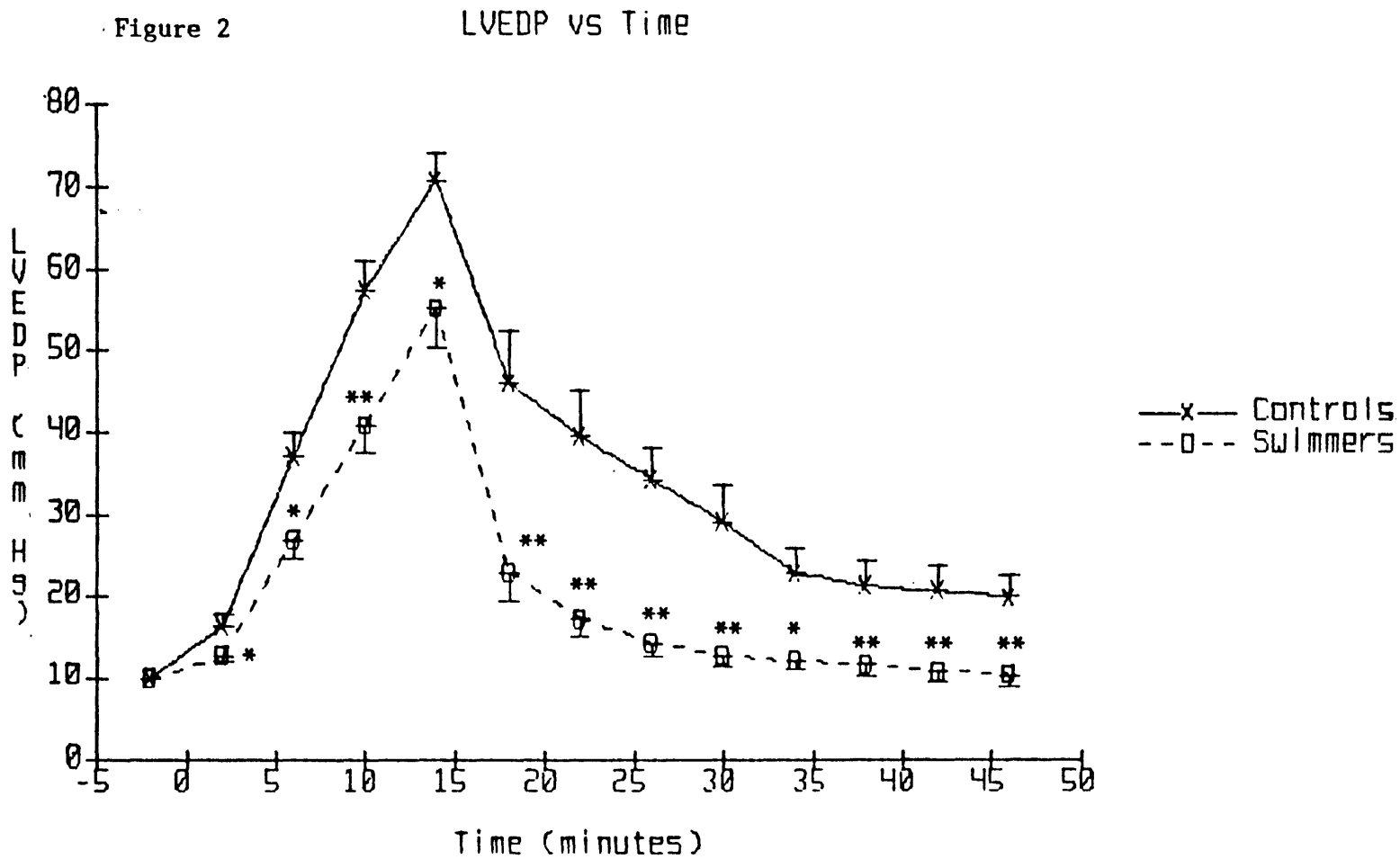
LVEDP vs Time
LVEDP (mm Hg)
80
70
60
50
40
30
20
10
0
-5
0
5
10
15
20
25
30
35
40
45
50
Time (minutes)
—x— Controls
--o-- Swimmers

Figure 3. Time course of left ventricular developed pressure (LVDP) = LVSP - LVEDP. Format and symbols as in Figure 1. The heart rate was fixed at 4.5 Hz throughout the experiment, so that LVDP is proportional to the rate-pressure product. The trained hearts exhibited greater LVDP throughout control oxygenation, hypoxia, and reoxygenation. The difference between the two groups was especially marked upon reoxygenation, when the trained hearts recovered more rapidly and more completely.

Figure 3

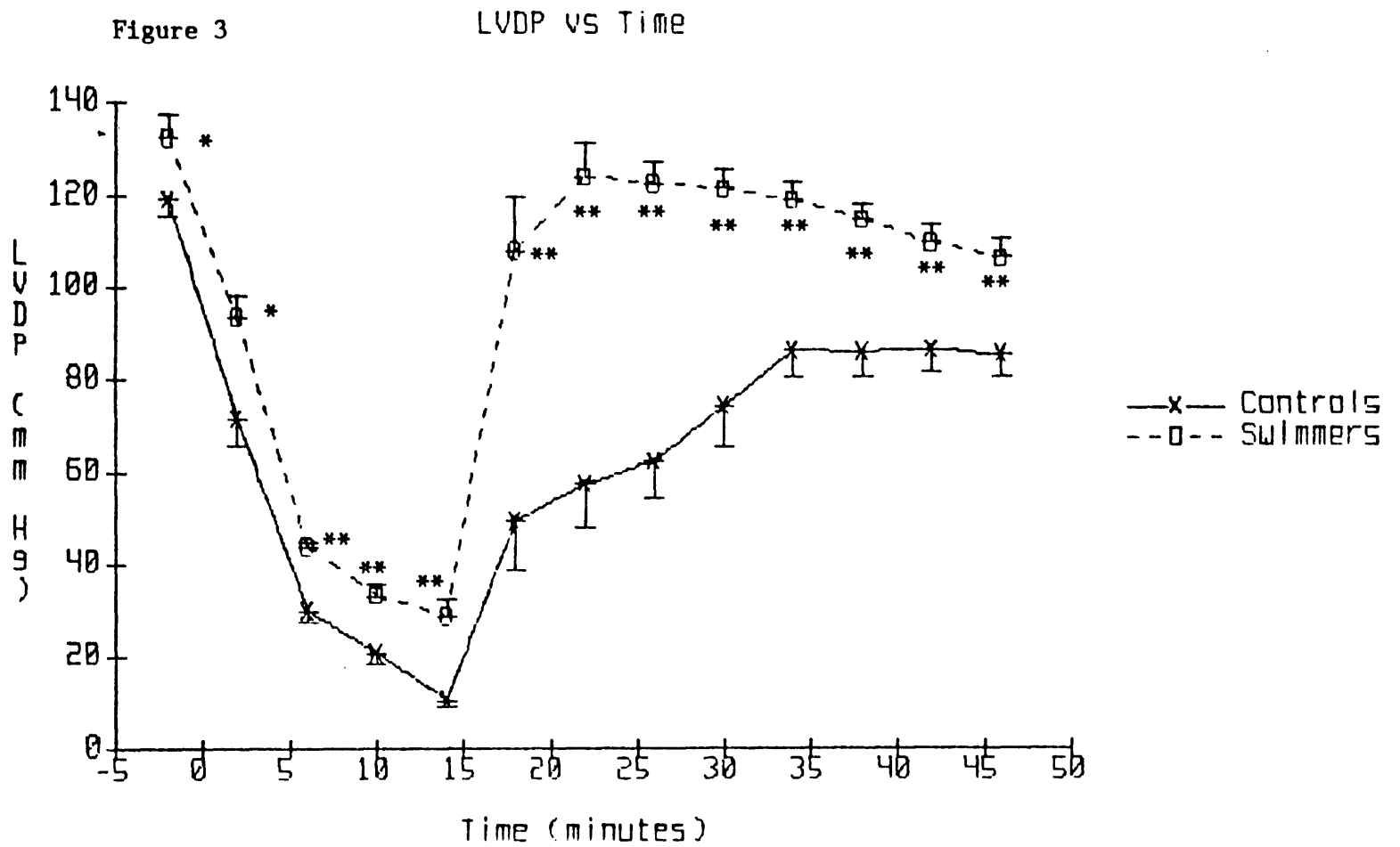
LVDP VS Time
LVDP (cm Hg)
140
120
100
80
60
40
20
0
-5
0
5
10
15
20
25
30
35
40
45
50
Time (minutes)
Controls
Swimmers

Figure 4. Time course of LVDP normalized by LVW. Format and symbols as in Figure 1. During hypoxia and early reoxygenation, the trained hearts were better able to maintain LVDP on a per-gram basis than were the control hearts.

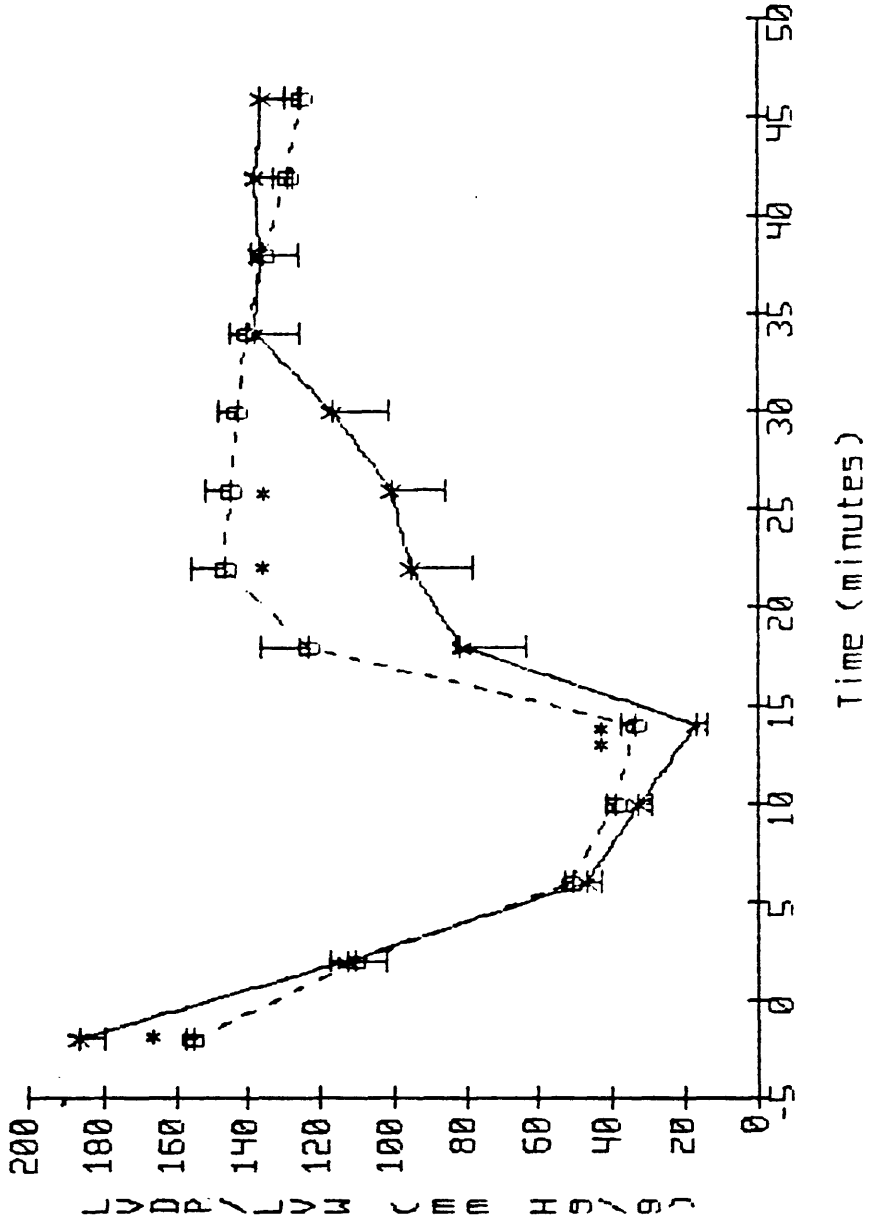
LVDP/LVW vs Time
—x— Controls
--□-- Swimmers
LVDP/LVW (cm Hg/g)
200
180
160
140
120
100
80
60
40
20
0
-5
0
5
10
15
20
25
30
35
40
45
50
Time (minutes)

Figure 4

Figure 5. Time course of coronary flow (CF) normalized by LVW. Format and symbols as in Figure 1. All hearts were perfused at 1ØØ mm Hg perfusion pressure. During control oxygenation, perfusion per gram of heart weight was equal in the two groups; during hypoxia and reoxygenation, the trained hearts showed greater tissue perfusion.

Figure 5

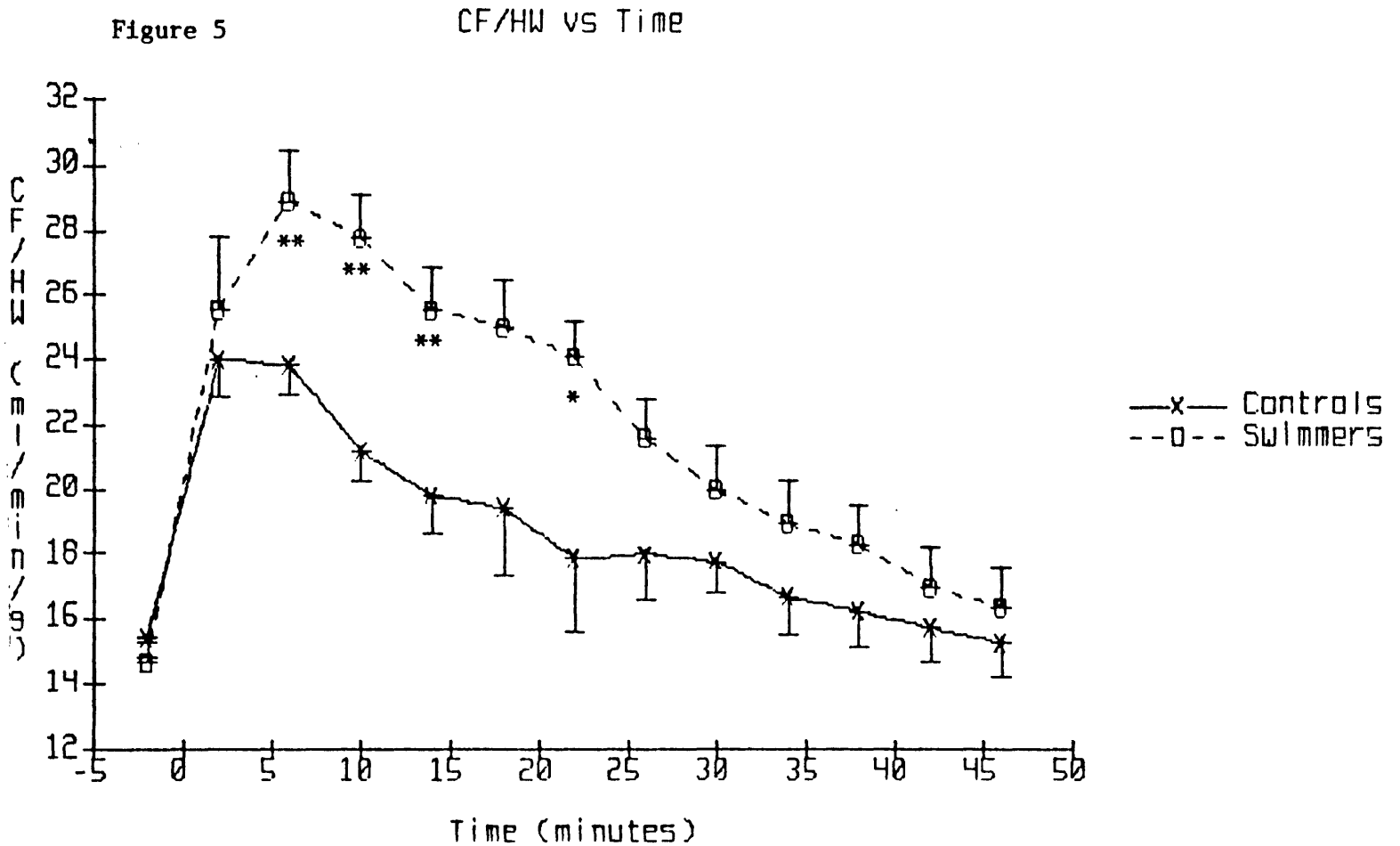
CF/HW vs Time
CF/HW (cm/cm/g)
32
30
28
26
24
22
20
18
16
14
12
-5
0
5
10
15
20
25
30
35
40
45
50
Time (minutes)
**
**
**
*
—x— Controls
--o-- Swimmers

Figure 6. Time course of phosphocreatine (PCr) concentration. Format as in Figure 1. The rate of depletion of PCr was indistinguishable between the two groups.

Figure 6

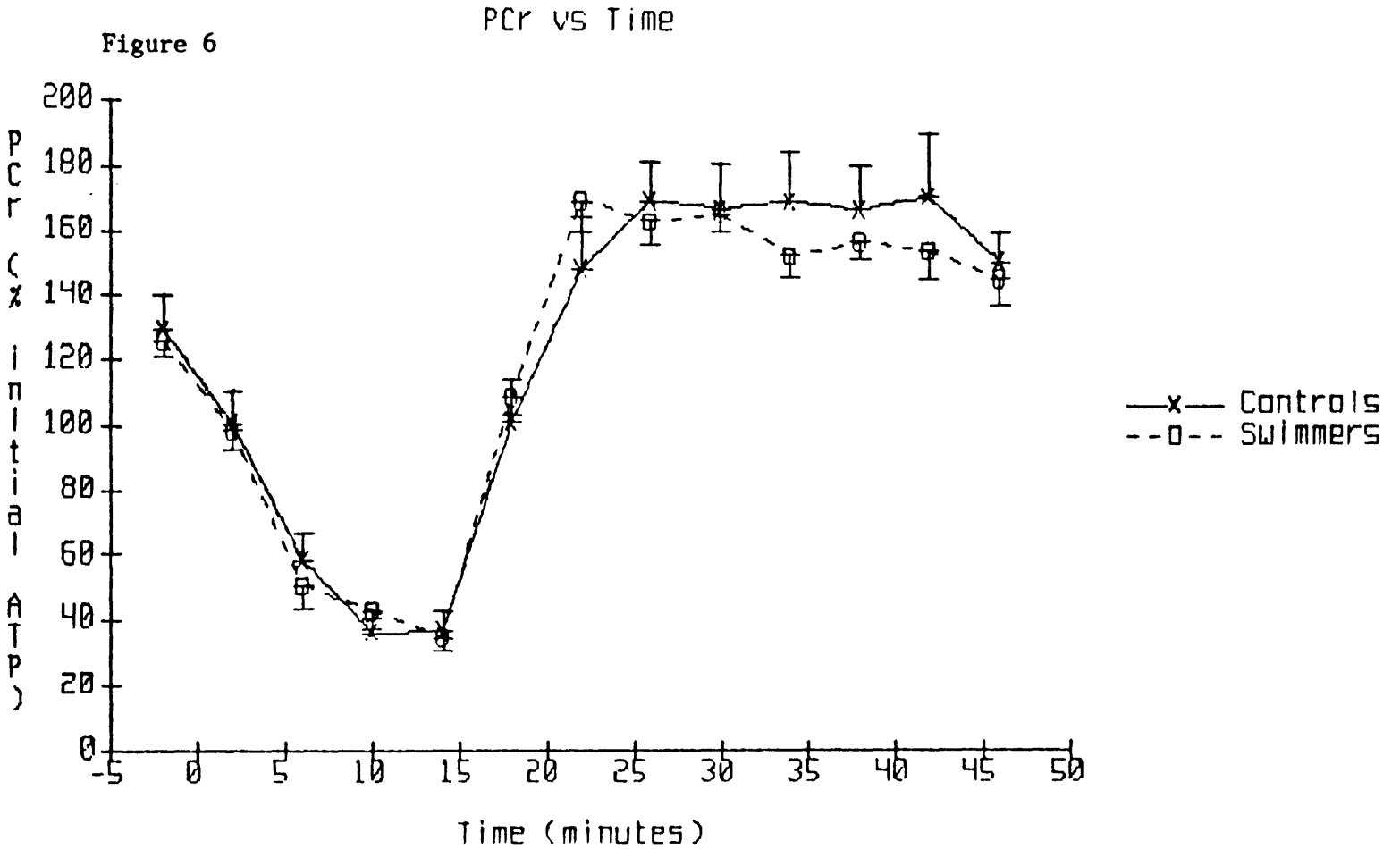
PCr vs Time
PCr (% Initial ATP)
200
180
160
140
120
100
80
60
40
20
0
-5
0
5
10
15
20
25
30
35
40
45
50
Time (minutes)
—x— Controls
--0-- Swimmers

Figure 7. Time course of ATP concentration. Format as in Figure 1. The rate of depletion of ATP was indistinguishable between the two groups.

Figure 7

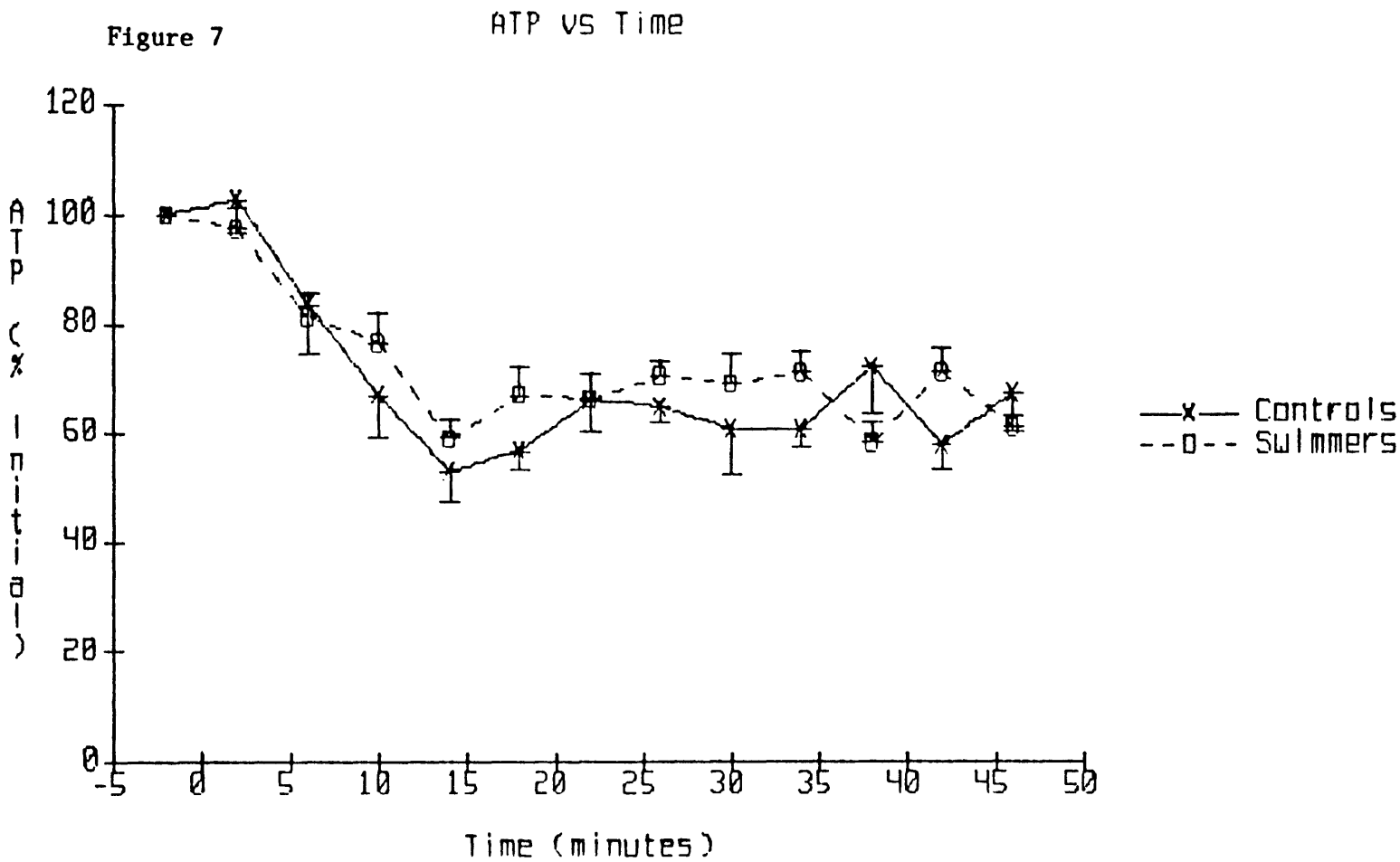
ATP VS Time
120
100
80
60
40
20
0
ATP (% Initial)
-5
0
5
10
15
20
25
30
35
40
45
50
Time (minutes)
Controls
Swimmers

Figure 8. Time course of pH. Format and symbols as in Figure 1. The two groups showed an equal small drop in pH during hypoxia, and similar recovery upon reoxygenation.

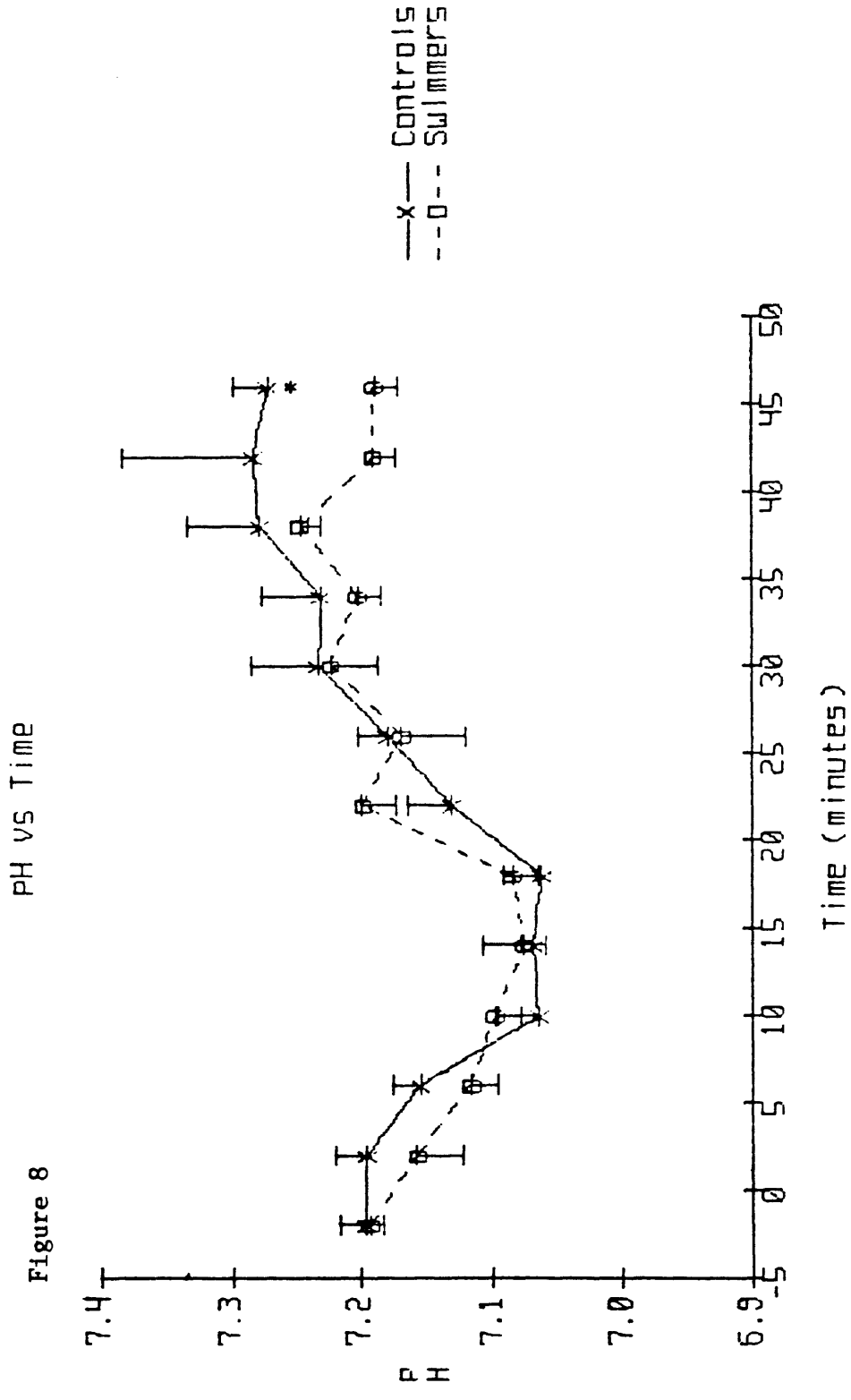
PH vs Time
—x— Controls
--0-- Swimmers
7.4
7.3
7.2
7.1
7.0
6.9
PH
-5
0
5
10
15
20
25
30
35
40
45
50
Time (minutes)

Figure 8

Figure 9. Mutually predictive and non-mutually predictive relationships between cardiac function and metabolite levels during control oxygenation and hypoxia.

a. Relationship between LVEDP and [ATP] during control oxygenation and hypoxia. The regression equations shown are the results of a variance-weighted fit to the displayed data. Neither the slopes not the intercepts of the two regression lines were statistically significantly different. LVEDP and [ATP] are correlated throughout their entire range in this figure, so that these variables are mutually predictive, in the sense that knowledge of one restricts the possible values of the other to a narrow range.

b. Relationship between LVDP and [ATP] during control oxygenation and hypoxia. These variables are not mutually predictive; a large initial decrease in LVDP occurs before a significant decrease in [ATP], while towards the end of hypoxia, LVDP remains nearly constant as [ATP] continues to fall.

c. Relationship between LVDP and [PCr] during control oxygenation and hypoxia. The regression equations shown are the results of a variance-weighted fit to the displayed data. Neither the slopes not the intercepts of the two regression lines were statistically significantly different. LVDP and [PCr] are correlated throughout their entire range in this figure, so that these variables are mutually predictive, in the sense that knowledge of one restricts the possible values of the other to a narrow range.

d. Relationship between LVEDP and [PCr] during control oxygenation and hypoxia. These variables are not mutually predictive; a large decrease in [PCr] occurs at the onset of hypoxia, before LVEDP begins to rise. During the subsequent slow decrease in [PCr], LVEDP increases by a large amount.

Figure 9a

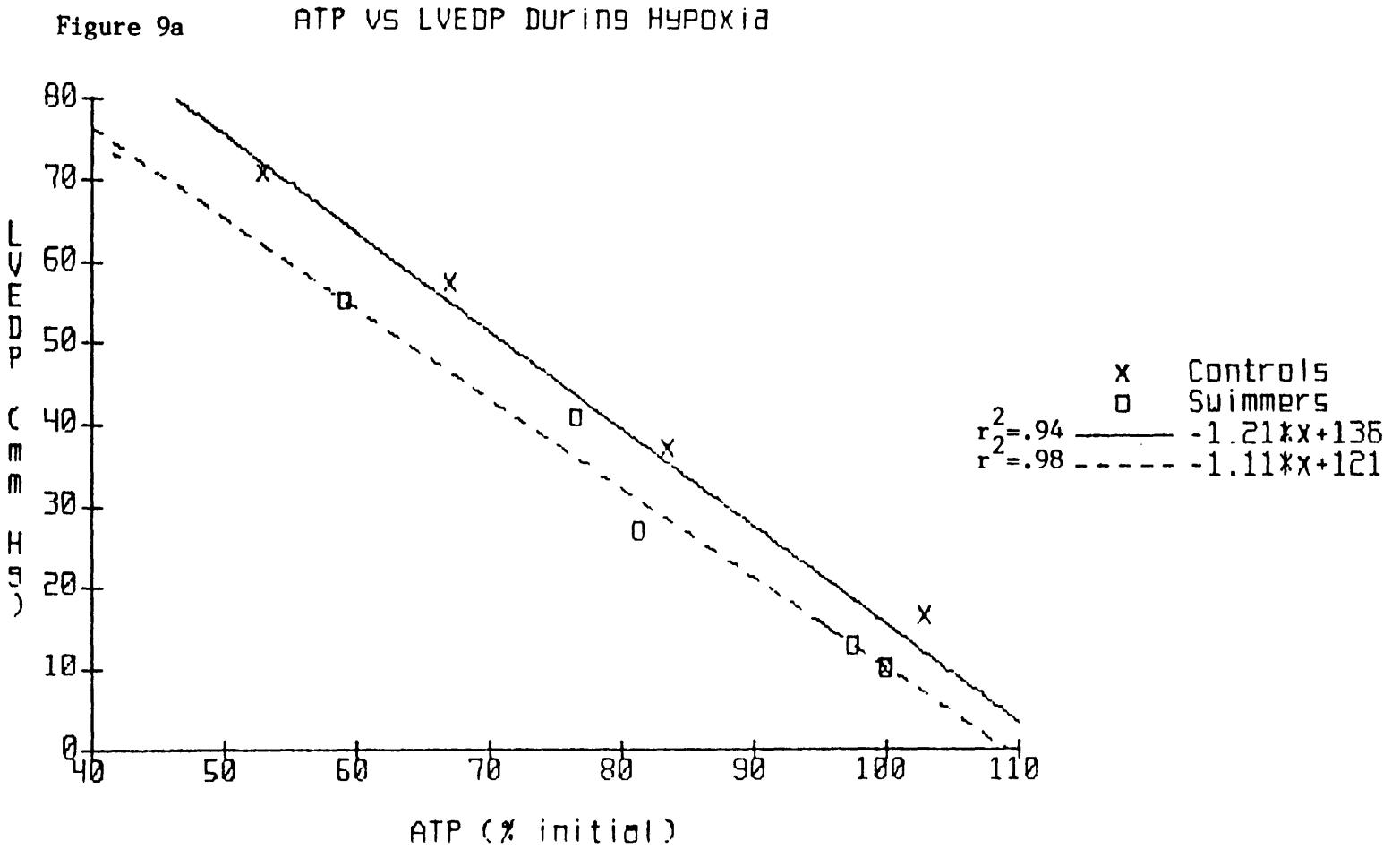
ATP VS LVEDP During Hypoxia
LVEDP (mm Hg)
80
70
60
50
40
30
20
10
0
40
50
60
70
80
90
100
110
ATP (% initial)
X Controls
□ Swimmers
r^2=.94 ——— -1.21*X+136
r^2=.98 - - - - - -1.11*X+121

Figure 9b

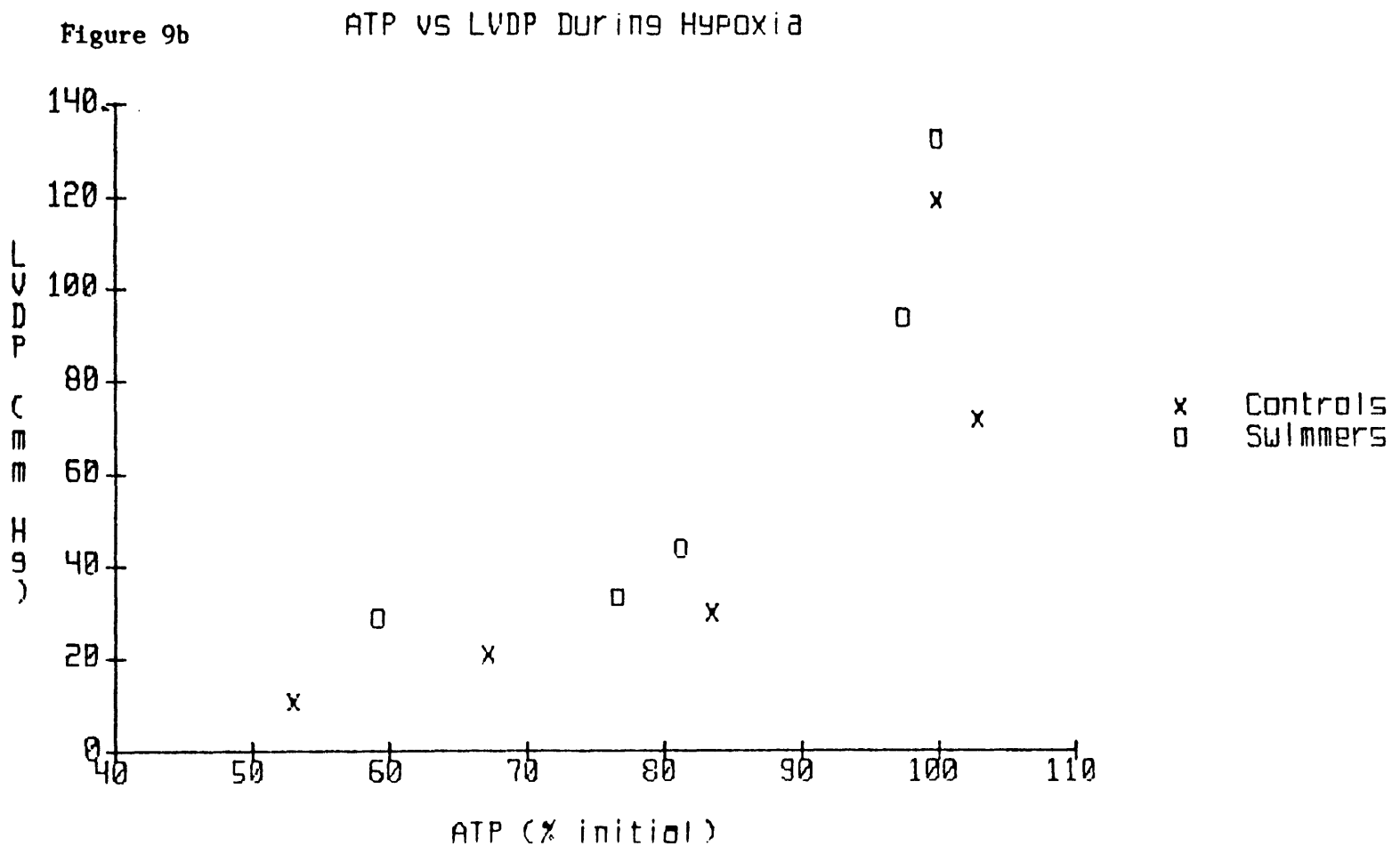
ATP VS LVDP During Hypoxia
LVDP (cm H9)
140
120
100
80
60
40
20
0
40
50
60
70
80
90
100
110
ATP (% initial)
x Controls
0 Swimmers

Figure 9c PCr VS LVDP During Hypoxia

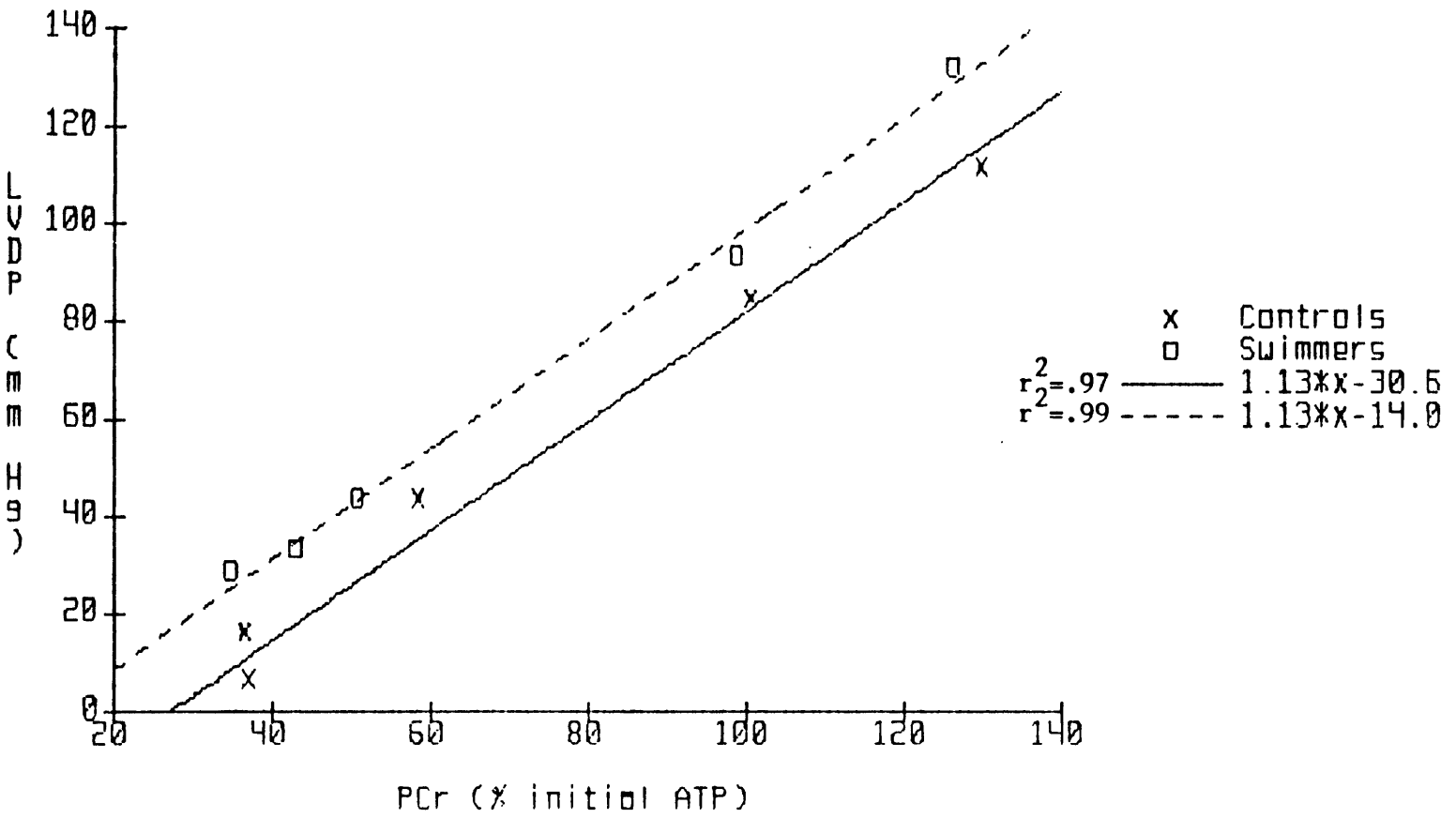

Figure 9d

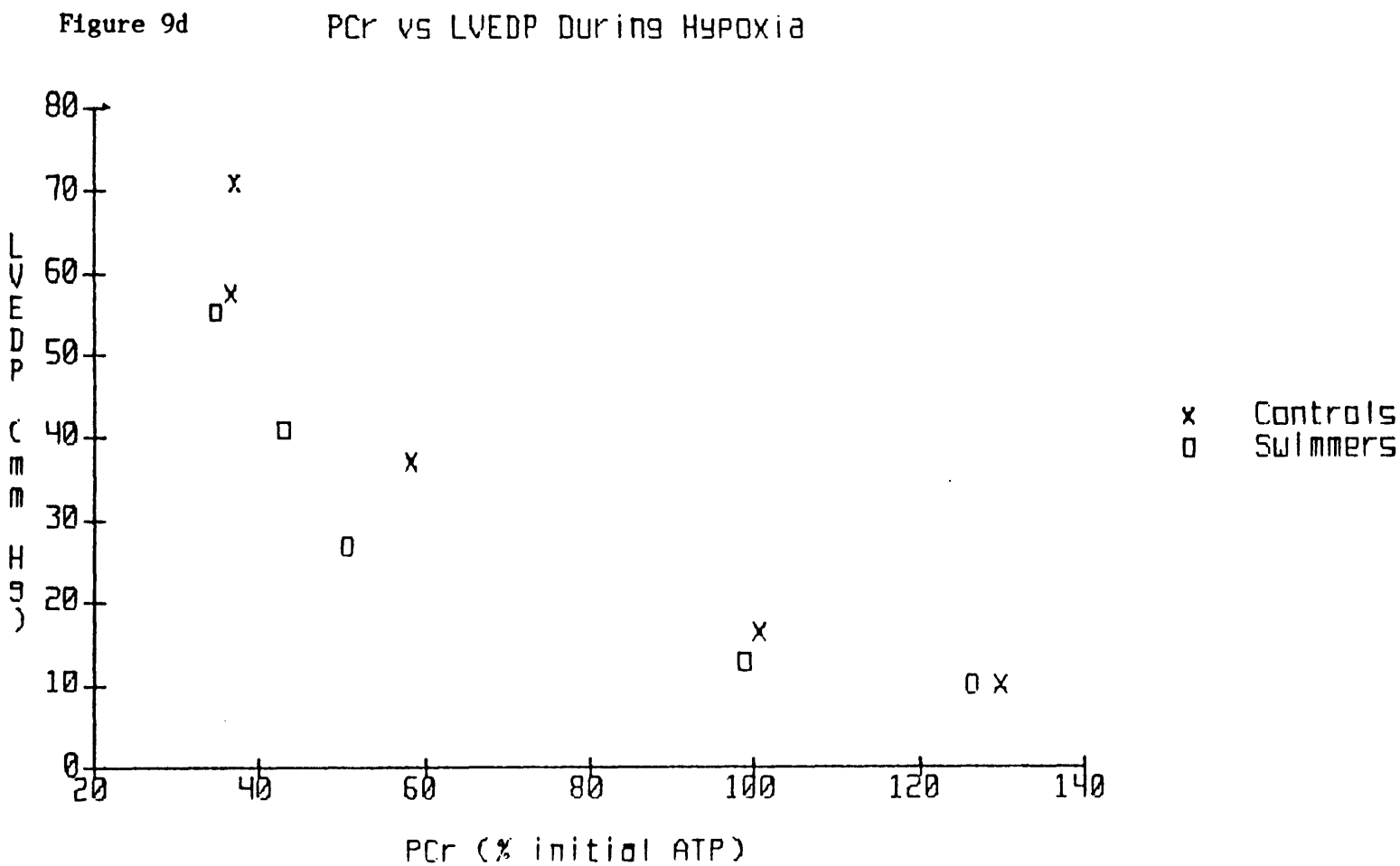
PCr vs LVEDP During Hypoxia
LVEDP (cm Hg)
80
70
60
50
40
30
20
10
0
20
40
60
80
100
120
140
PCr (% initial ATP)
x Controls
o Swimmers

Figure 1Ø. Effect on contracture of an idealized parallel replication of sarcomeres. When identical tension-generating elements, such as sarcomeres during hypoxia, add in parallel, the net tension generated increases in proportion to the number of added elements. As shown, two elements, each generating a tension T, together generate a net tension of 2·T when acting side-by-side. A pattern similar to this may develop in concentric cardiac hypertrophy.

Figure 11. Effect on contracture of an idealized series replication of sarcomeres. When identical tension-generating elements, such as sarcomeres during hypoxia, add in series, the net tension generated is independent of the number of added elements. As shown, two elements, each generating a tension T, together still generate a tension of only T when acting in series. A pattern similar to this may develop in eccentric cardiac hypertrophy.

Figure 1Ø

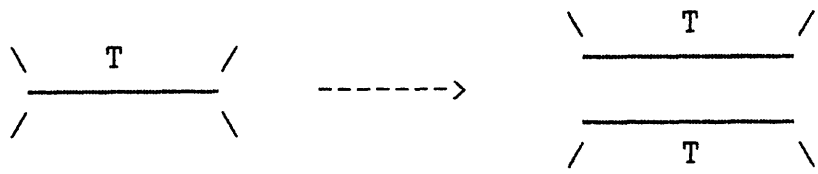

Net tension:

T 2T

Figure 11

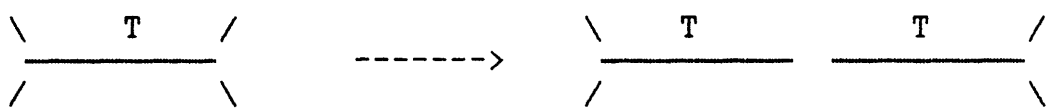

Net tension:

T T

Chapter 3, Part 3

Saturation Transfer and Biochemical Analyses of the Creatine Kinase System in the Trained Rat Heart

Abstract

Using the nuclear magnetic resonance technique of saturation transfer and standard biochemical assays, we analyzed the creatine kinase system in hearts from rats which had been subjected to chronic exercise. The *in vivo* saturation transfer experiments performed with beating hearts showed the rate constant of the creatine kinase reaction in the direction of ATP synthesis to be increased by 18% in hearts from trained animals as compared with sedentary controls. Similarly, there was a trend towards a larger value for this forward rate constant in arrested hearts. In addition, the *in vitro* biochemical analysis showed the concentration of the mitochondrial isozyme of creatine kinase to be increased by 16%. Thus, both of these methods uncovered biochemical changes in the trained hearts, but their magnitude was smaller than functional changes which have previously been observed to result from training.

Introduction

In Chapter 3, Part 1, we described experiments showing that during prolonged global hypoxia, the diastolic function of pathologically hypertrophied hearts was impaired to a greater extent than that of normals; these results could be accounted for by the increased mass of the hypertrophied hearts. On the other hand, as described in Chapter 3, Part 2, the heart hypertrophied secondary to training showed relatively preserved diastolic function during prolonged global hypoxia. This result could not be accounted for either by geometric considerations or by tissue concentrations of high-energy phosphates; however, it is possible that a biochemical alteration more subtle than would be reflected in overall net metabolite abundances is involved.

Alterations in the enzymology and chemical kinetics of the main reactions involving high-energy phosphate synthesis, transport, and utilization may have a profound effect on cardiac physiology. Changes in the creatine kinase system in the pathologically hypertrophied heart have been well documented[1], as have changes in myosin ATPase activity[2]. Myosin changes also occur in the trained heart[2]; they are essentially opposite to those seen in pathologic hypertrophy. To our knowledge, however, the creatine kinase system has not been examined in the trained heart.

The technique of saturation transfer nuclear magnetic resonance (NMR) spectroscopy allows direct measurement of the turnover rates of high-energy phosphates in the functioning heart. Such measurements provide a method of assessing the significance, in terms of the chemical flux of phosphorus, of changes in the steady state myocardial content of creatine kinase isozymes. Although this technique has been applied to the pathologically hypertrophied heart[1], such measurements have yet to be performed in the trained heart.

Accordingly, in this section, we continue our analysis of

the heart hypertrophied secondary to chronic training in order to further characterize this state. As discussed above, we are specifically motivated by the results of the previous section, Chapter 3, Section 2. Creatine kinase enzymology will be described both in terms of biochemical measurements of isozyme activity and in terms of *in vivo* phosphorus fluxes through reactions involving both ATP synthesis and ATP degradation.

Methods

Animals

Female Wistar rats weighing 150-200 grams were subjected to swim training for 8 - 10 weeks. They swam in groups two times per day for 75 minutes, five days per week. Age-matched control female Wistar rats were fed and housed under identical conditions. At the end of each perfusion experiment, the hearts were blotted dry and weighed. In addition, the left and right ventricles were dissected free and weighed separately. Both body weight and right tibia length were recorded for normalization of heart and left ventricle weights.

Heart Perfusion

At the time of the experiment, the rats were anesthetized with an intraperitoneal injection of 25 mg sodium pentobarbital. Hearts, with some adjacent tissue, were then rapidly excised and immersed in ice cold perfusion buffer. The aorta was then dissected free and the heart perfused retrograde through the aorta by 37° phosphate-free Krebs-Henseleit buffer gassed with a mixture of 95% O2 and 5% CO_2 (pH 7.4), as previously described[3]. This buffer was composed of (mM) NaCl (118), KCl (4.7), EDTA (.5), $MgSO_4$ (1.2), $CaCl_2$ (1.75), $NaHCO_3$ (25), and glucose (11). The buffer used to arrest the hearts had an identical composition, only with 30 mM NaCl replaced by 30 mM KCl. A constant-pressure system was used, providing a perfusion pressure of 100 mm Hg under gravity feed.

Hemodynamic measurements

A water-filled latex balloon was inserted into the left ventricle through an incision into the left atrium, via the mitral valve. Pressures and heart rate (HR) were obtained via a water-filled tube running from the latex balloon to a pressure transducer, connected to a Hewlett-Packard chart

recorder. Systolic and diastolic pressures and HR were monitored continuously throughout the experiment. Coronary flow was assessed by collecting coronary effluent.

NMR measurements and experimental protocol

The perfused hearts were placed into a 20 mm NMR sample tube and inserted into the bore of an Oxford Instruments 360 wide-bore magnet (field strength, 8.45 Tesla), interfaced with a Nicolet 1280 spectrometer. Experiments were performed with 60° broad-band observation pulses, and each spectrum was the Fourier transform of the average of at least 80 free-induction decays, with an applied line broadening of 20 Hz. Transient saturation transfer experiments were performed while the hearts were beating, with low-power saturations applied at Γ-ATP for .3, .6, 1.2, 2.4, and 4.8 seconds. Spectra were also acquired without saturation, to obtain relative metabolite abundances. After completion of these measurements, the hearts were arrested by perfusing with the KCl-arrest buffer described above. During arrest, a steady-state saturation transfer experiment was performed, with a low-power saturation signal applied at the Γ-ATP resonance for 10 seconds. Spectra were also acquired without saturation to obtain relative metabolite abundances during KCl arrest. Spillover to the adjacent PCr peak during saturation at Γ-ATP was estimated by moving the saturating frequency upfield of PCr by an amount equal to the frequency separation between Γ-ATP and PCr. Measured in this way, direct spillover saturation of PCr during Γ-ATP saturation was found to be less than 5%. Hearts were excluded from the study if they showed metabolic (as assessed by NMR-measured metabolite levels) or hemodynamic (as assessed by rate-pressure product) instability during the course of the experiment.

Saturation transfer technique

The reaction system we are considering consists of ATP

synthesis and degradation reactions, primarily mitochondrial and myofibrillar, respectively, coupled to the creatine kinase reaction between PCr and ATP:

$$1)\quad ADP + PCr \underset{k_r}{\overset{k_f}{\rightleftharpoons}} ATP + Cr \underset{k_r'}{\overset{k_f'}{\rightleftharpoons}} ADP + P_i\,.$$

We define phosphorus fluxes towards ATP synthesis in this system by $F_f = k_f[PCr]$ and $F_f' = k_f'[P_i]$.

In the reaction network Eq. 1), the Bloch equations describing the evolution of the magnetizations of P_i and PCr following a perturbation are

$$2)\quad \frac{dM(PCr)}{dt} = \frac{M_0(PCr) - M(PCr)}{T_1(PCr)} + k_r M(\Gamma\text{-}ATP) - k_f(PCr)$$

$$3)\quad \frac{dM(P_i)}{dt} = \frac{M_0(P_i) - M(P_i)}{T_1(P_i)} + k_r' M(\Gamma\text{-}ATP) - k_f' M(P_i).$$

The coupling of the evolution of $M(P_i)$ and M(PCr) to $M(\Gamma\text{-}ATP)$ may be eliminated by irradiating the sample with a low-power radio-frequency signal tuned to the resonance frequency of Γ-ATP, thereby eliminating this resonance. During this irradiation, then, the evolution Eqs. 2) and 3) become

$$4)\quad \frac{dM(PCr)}{dt} = \frac{M_0(PCr) - M(PCr)}{T_1(PCr)} - k_f(PCr)$$

$$5)\quad \frac{dM(P_i)}{dt} = \frac{M_0(P_i) - M(P_i)}{T_1(P_i)} - k_f' M(P_i).$$

Because $M(P_i)$ and $M(PCr)$ are not disturbed by the saturation at Γ-ATP, the appropriate initial conditions for Eqs. 4) and 5) are

7) $$M(Cr)(t=\emptyset) = M\emptyset(PCr)$$

6) $$M(P_i)(t=\emptyset) = M\emptyset(P_i)$$

where $M\emptyset$ denotes magnetization amplitudes in the absence of saturation at Γ-ATP. The solution to Eqs. 4) and 6) is

8) $$M(PCr)(t) = M\emptyset(PCr)[\ 1 - k_f \tau(PCr)(1 - \exp(-t/\tau(PCr))\ ]$$

where $\tau(PCr)$ is defined by

9) $$1/\tau(PCr) = 1/T_1(PCr) + k_f .$$

A two-parameter fit to the form Eq. 8) of the magnetization amplitudes $M(PCr)$ of PCr during a transient saturation transfer protocol comprising the full sequence of saturation times given above was performed. From the best-fit values of $\tau(PCr)$ and k_f, $T_1(PCr)$ was calculated according to

1Ø) $$T_1(PCr) = [1/\tau(PCr) - k_f]^{-1} .$$

k_f', $\tau(P_i)$, and $T_1(P_i)$ were obtained in a similar fashion, fitting the magnetization amplitudes of P_i during saturation of Γ-ATP to the solution of Eqs. 5) and 7):

11) $$M(P_i)(t) = M\emptyset(P_i)[\ 1 - k_f'\tau(P_i)(1 - \exp(-t/\tau(P_i))\ ]$$

with parameters k_f' and $\tau(P_i)$, where $\tau(P_i)$ is defined by

12) $1/\tau(P_i) = 1/T_1(P_i) + k_f'$.

$T_1(P_i)$ is then calculated according to

13) $T_1(P_i) = [1/\tau(P_i) - k_f']^{-1}$.

To obtain kinetic constants for the KCl-arrested hearts, the assumption was made that the T_1's of PCr and P_i did not change as a result of the arrest. With this assumption, the rate constants k_f and k_f' appropriate to the arrested state were obtained from the data obtained after KCl arrest from the formulas

14) $k_f = 1/T_1(PCr)[\ M_0(PCr)/M_\infty(PCr) - 1\ ]$

15) $k_f' = 1/T_1(P_i)[\ M_0(P_i)/M_\infty(P_i) - 1]$,

where the T_1's are those obtained prior to the arrest, the M_0's refer to magnetization amplitudes obtained after arrest in the absence of saturation, and the M_∞'s refer to the values of the measured peaks after the 10-second saturation at Γ-ATP. Eqs. 14) and 15) may be derived from considering Eqs. 2) and 3) with a saturation at Γ-ATP of sufficient duration that all metabolite levels reach a steady-state.

Data and statistical analysis

In order to maximize signal-to-noise, free-induction decays from the different hearts in the two groups were summed prior to analysis. Thus, one final spectrum was obtained for each time point (including t = 0) of the transient saturation protocol performed on the beating hearts, for both the trained (n = 7) and sedentary (n = 6) animals. Similarly, for the KCl-arrest experiments, one final spectrum each was obtained for both the 10 second saturation at Γ-ATP and for the data acquired without saturation, for both the trained (n = 6) and sedentary (n =

7) animals. In all of the spectra obtained with saturation, loss of intensity due to saturation transfer to P_i and PCr was assessed by measurement of their respective peak heights.

The two-parameter fits of saturation transfer data to Eqs. 8) and 11) were performed using the nonlinear least-squares routine of the RS/1 software of BBN Research Systems, Cambridge, Mass. The errors reported for the pre-arrest k_f, k_f', $\tau(PCr)$, and $\tau(P_i)$ are the standard errors of the best-fit values obtained from this analysis. The errors in the T_1's obtained from this using Eqs. 10) and 13), and in the values of k_f and k_f' post-arrest obtained from Eqs. 14) and 15), were derived using pythagorean addition of errors[4]. This states that the derived error in a function f of two variables x and y is

$$15) \qquad \sigma_f = \sqrt{[\ (df/dx)^2\sigma_x^2 + (df/dy)^2\sigma_y^2\ ]}$$

where σ_f denotes the standard deviation of the derived quantity f(x,y), σ_x and σ_y are the standard deviations of the independent variables x and y, and the assumption is made that the error in the x variable is independent of the error in the y variable.

Fluxes were obtained by multiplying the appropriate k's with relative metabolite levels obtained by integrating the P_i and PCr peaks of each heart, normalized by the integral of β-ATP, arbitrarily set to 100 magnetization units. Errors in fluxes were derived using Eq. 15).

Oxygen consumption measurements

Using a Clark electrode, oxygen consumption measurements were performed on each heart at two separate times during the protocol, providing a measure of cardiac oxygen consumption while the heart was beating and while it was arrested. The first measurement was taken prior to placing the heart in the magnet, while the second was performed after the heart was removed from the magnet following the KCl-arrest saturation

transfer experiment. The difference between the partial pressure of oxygen (pO_2) in the aortic inflow and the pO_2 of the coronary effluent into the right ventricle was converted into $\mu M\text{-}O_2$/min/gram-dry-weight using the Fick principle.

Biochemical analyses

Biochemical analyses were performed on atrial tissue, which was not separated into left and right atria, the left and right ventricles, and on two skeletal muscles, the gastrocnemius and soleus. The methods have been described previously[1,5]. We obtained values for the activities of the MM, MB, BB, and mitochondrial fractions of creatine kinase, for lactate dehydrogenase (LDH) in the presence of high and low pyruvate concentration, and for citrate synthase. Creatine concentration was also determined, as was milligrams protein per gram of wet weight in each sample, to provide an additional normalization factor.

All errors are presented as $\pm$ SEM.

Results

Effect of Chronic Swimming on Cardiac Mass

Table 1 shows the effect of swim training on body weight (BW) (decreased by 8% as compared to control animals), heart weight (HW) (increased by 27%), left ventricular weight (LVW) (increased by 12%), and the ratios of the latter two to body weight (HW/BW and LVW/BW) (increased by 39% and 22%, respectively) and right tibia length (HW/TL and LVW/TL) (increased by 29% and 14%, respectively). All of these differences between the two groups were statistically significant. In addition, there was a nonsignificant increase in right ventricular weight (23%), and a significant decrease in LVW/HW (12%) in the trained animals, indicating the involvement of the right ventricle in the cardiac hypertrophy process.

Oxygen Consumption Measurements

Table 2 shows the rate-pressure product (RPP; product of developed pressure and heart rate) and oxygen consumption of trained and control hearts both while beating and during KCl arrest (RPP = Ø for KCl arrest). All hearts had a left-ventricular end-diastolic pressure of 1Ø mm Hg during these measurements. The RPP was equal in the two groups, as was their oxygen consumption both while beating and during KCl arrest.

NMR-derived Quantities for Trained and Control Rats

Table 3 shows kinetic constants and metabolite abundances for the trained and control groups, both while beating and during KCl arrest.

The rate constant through the creatine kinase (CK) reaction in the direction of ATP synthesis was slightly (18%) but significantly greater in the trained rats during normal beating. However, the ratio of phosphocreatine to ATP was greater in the controls, so that the forward phosphorus flux,

F_f, through the CK reaction was the same in the two groups. During KCl arrest, k_f was substantially greater (62%) in the controls, but this difference did not reach statistical significance ($p = .Ø51$) due to large errors. In this case as well, the ratio of PCr to ATP was increased in the controls, so that the flux through the CK reaction in the direction of ATP synthesis, though somewhat larger in the trained hearts, was not significantly different between the two groups. The significantly greater τ_1(PCr) of the control hearts over the trained hearts during beating follows from their significantly smaller k_f and the similar values of T_1(PCr) for the two groups.

The rate constant k_f' for ATP synthesis from inorganic phosphate was not different in the two groups during beating or arrest. Although the best-fit value of k_f' during KCl arrest was twice as large in the controls as in the trained animals, the signal-to-noise of the P_i peak during KCl arrest (from measurements of which k_f' during arrest is derived) is extremely poor. Therefore, the standard errors of the fit are quite large, and the difference between the two groups was not statistically significant ($p \approx .5Ø$). Similarly, phosphorus fluxes from P_i to ATP were not different between the two groups during beating or arrest.

Biochemical analyses

Table 4 summarizes the tissue biochemistry results. At the $p < .Ø5$ level, the trained group showed a significant difference in the ratio of mitochondrial CK activity to citrate synthase (CS) activity (increased by 16%) in the left ventricle. Because total CS activity is an index of total mitochondrial mass, this ratio reflects the mitochondrial (as opposed to overall tissue) concentration of mitochondrial CK. In the right ventricle, the trained animals showed a small but statistically significant change in overall CK activity (decreased by 13%), CS activity per gram wet weight (decreased by 12%), milligrams protein per gram wet weight

(decreased by 13%), and a larger change in both the activity (increased by 44%) and percent (increased by 44%) of MB-CK. No significant differences were seen in atrial tissue. In the soleus muscle, there was an increase (18%) in the trained animals as compared with the controls in the ratio of LDH activity in the presence of high pyruvate concentration to activity in the presence of low pyruvate concentration, consistent with slightly increased anaerobic capacity of this red muscle. The increase in this ratio, from .155 in the controls to .183 in the trained animals, represents a very small functional change; a ratio of .8 is characteristic of tissues relying on anaerobic ATP production, while a ratio of .1 to .2 is characteristic of tissues which are predominantly aerobic. In addition, a significant change in the CK isozyme composition of skeletal muscle occurred in one of the trained rats, for which CK-BB appeared in both the gastrocnemius muscle and the soleus. This was the only animal of either group in which skeletal muscle CK-BB was found. Because of the possibility of sarcolemmal damage secondary to hypoxia and reoxygenation, and consequent leakage of enzymes, we did not report results of our enzymatic analyses of the hearts in Chapter 3, Part 2. However, the results were substantially the same, including the development of the BB isoenzyme of CK in the soleus muscle of one of the trained rats.

Discussion

In this study we have assessed both steady-state tissue concentrations of creatine kinase isozymes and the turnover of high-energy phosphate compounds in the myocardium. In both cases, only small differences were seen as compared with controls. This is consistent with previous studies, which have shown that the heart undergoes a smaller adaptive increase in respiratory capacity in response to training than does skeletal muscle[6,7,8]. Holloszy[9] hypothesizes that this is due to the fact that normal heart muscle is, in effect, already adapted for exercise, stating "Because heart muscle contracts continuously and has the highest capacity for aerobic metabolism of any mammalian muscle, it seems reasonable that the levels of activity of the enzymes for the generation of ATP and for the hydrolysis of ATP during muscle contraction are the optimal ones for continuous, vigorous contractile activity."

Previous studies of energy production in the trained heart have focused on a wide variety of processes, including oxygen consumption[10] and glycogen[11,12] and lipid[12,13] metabolism. Enzyme analyses have also been carried out for glycolytic enzymes, including pyruvate kinase[8,14] and lactate dehydrogenase[15], as well as for enzymes of the oxidative pathway[6,8]. However, to our knowledge, no previous studies of the creatine kinase (CK) system in the trained heart have appeared.

In skeletal muscle, Oscai et al.[16] found no increase in creatine kinase activity in gastrocnemius muscle in response to exercise in rats. A more recent study[17] focused on adaptations of the CK system to exercise in humans, finding higher MB isozyme activities in vastus lateralis muscle samples from trained individuals. The significance of this finding is not known; it is of interest to note that in the present study we found a relative accumulation of the same CK isozyme in the right ventricle, and that it also accumulates in both the pathologically hypertrophied heart[1,5] and in

coronary artery disease without hypertrophy[5].

Studies of the cardiovascular effects of exercise generally confirm the presence of training adaptations in experimental animals by examination of skeletal muscle enzymes. An unexplained inconsistency between the present study and previous ones[9] is the lack of significantly increased CS activity in skeletal muscle of the trained animals. This may be due to our use of swimming, as opposed to running, as the training modality; in addition, oxidative enzymes, such as cytochrome oxidase, may be more sensitive indicators of training[18]. In fact, the only clear skeletal muscle adaptation found in the present study was a small change in the LDH isozyme profile of the soleus muscle. However, other studies utilizing the same training protocol have clearly documented functional cardiac adaptations to training[10,19,20,21]. In addition, although cardiac hypertrophy is not a sensitive indicator of a training effect, in the present controlled study it may be regarded as a specific indicator, so that we are confident that training did take place.

We observed a statistically significant increase in the forward rate constant through the CK reaction in the trained hearts while beating, and a nearly ($p = .051$) significant increase during arrest. However, there was an offsetting change in the relative concentrations of [PCr] and [ATP] so that the net phosphorus flux through the CK reaction in the forward direction was the same in both groups. Because the workloads of the two groups were similar (Table 2), and in light of evidence that the main functional determinant of CK flux is workload[22], this result is not unexpected. However, the observed increase in k_f is still consistent with an adaptive biochemical change in the CK system which may become physiologically important at high workload. The ratio of [PCr] to [ATP] decreases with workload in the perfused heart (see Table 3 and Ref. 22); if [PCr]/[ATP] were the same in the two groups at their respective maximal workloads, then

the maximal forward flux through CK might be expected to be greater in the trained hearts by virtue of their larger k_f. Alternatively, since the maximal workload of the trained hearts is likely to be greater than that of the controls, it is possible that their [PCr]/[ATP] at maximal workload may be smaller than in the controls. In this case, the increased k_f of the trained hearts may partly compensate, preventing them from having a lower forward CK flux.

In spite of the changes noted above, the enzymatic and kinetic differences between the control and trained hearts in the present study were much smaller than the differences in the hemodynamic behavior seen in Chapter 3, Part 2. One possible explanation for this is that the hearts in the present study were not stressed, so that an adaptation which may primarily represent an increase in cardiac reserve may not have become apparent. We note, for example, that in Chapter 3, Part 2, coronary flow per gram of myocardium was greater in the trained animals during hypoxia and reoxygenation, but not during control oxygenation. Similarly, we found that rate constants and phosphorus fluxes through the ATPase reactions were the same between the two groups, consistent with their equal oxygen consumptions (Table 2). However, it is known that <u>in vitro</u> myosin ATPase activity is increased by training[2]. These <u>in vitro</u> results may reflect maximal intrinsic activity of the ATPases, not subject to the biochemical control mechanisms of the intact cell and organ. In this regard, and for the other reasons discussed above regarding the [PCr]/[ATP] ratio, it may be of interest to perform studies similar to the present one on hearts which are performing at maximal workloads. Unfortunately, the stress of hypoxia, in spite of its effectiveness as seen in Chapter 3, Part 2, is unsuitable for the types of kinetic measurements we have made here, due to the requirement that metabolite levels remain constant throughout the saturation transfer protocol.

Another possible explanation for the much smaller effects

seen in the present study as compared to Chapter 3, Part 2, is that alterations in the metabolic parameters measured in the present study, primarily CK isozymes and in vivo ATPase and CK kinetics, are not those responsible for the improved performance of the trained heart which is seen in a variety of settings[23]. In fact, in Chapter 3, Part 2, in which the trained hearts displayed remarkably improved performance during hypoxia and reoxygenation, the time-course of high-energy phosphate depletion did not differ between the two groups. This is consistent with the findings of the present study, in which the main reactions involving high-energy phosphate production and utilization were found to be only slightly altered by training.

In Chapter 3, Part 2, the largest functional difference between the control and trained hearts during hypoxia was the relative preservation of diastolic function in the latter. Diastolic function is dependent to a great extent on the ability of the sarcoplasmic reticulum (SR) to sequester calcium, and both calcium binding and calcium transport are increased in the trained heart[24,25]; this adaptation may contribute to their increased rate of relaxation[19]. It is likely that these effects are partly responsible for the findings of Chapter 3, Part 2; however, to be directly relevant to that study, the calcium handling properties of the SR should be studied under conditions of limited ATP substrate.

1. J. S. Ingwall. The hypertrophied myocardium accumulates the MB-creatine kinase isozyme. Eur. Heart Jour. 5(Suppl. F):129-139 (1984).

2. J. Scheuer and A. K. Bhan. Cardiac contractile proteins: adenosine triphosphatase activity and physiological function. Circ. Res. 45:1-12 (1979).

3. J. S. Ingwall. Phosphorus nuclear magnetic resonance spectroscopy of cardiac and skeletal muscles. Am. J. Physiol. 242, H729-H744 (1982).

4. P. R. Bevington. Data reduction and error analysis for the physical sciences, McGraw, (1969).

5. J. S. Ingwall, M. F. Kramer, M. A. Fifer, B. H. Lorell, R. Shemin, W. Grossman, and P. D. Allen. The creatine kinase system in normal and diseased human myocardium. New Eng. J. Med. 313:1Ø5Ø-1Ø54 (1985).

6. L. B. Oscai, P. A. Molé, B. Brei, and J. O. Holloszy. Cardiac growth and respiratory enzyme levels in male rats subjected to a running program. Am. J. Physiol. 22Ø:1238-1241 (1971).

7. L. B. Oscai, P. A. Molé, and J. O. Holloszy. Effects of exercise on cardiac weight and mitochondria in male and female rats. Am. J. Physiol. 22Ø:1944-1948 (1971).

8. J. Scheuer, S. Penpargkul, and A. K. Bhan. Experimental observations on the effects of physical training upon intrinsic cardiac physiology and biochemistry. Am. J. Cardiol. 33:744-751 (1974).

9. J. O. Holloszy and F. W. Booth. Biochemical adaptations to endurance exercise in muscle. Ann. Rev. Physiol. 38:273-291 (1976).

1Ø. S. Penpargkul and J. Scheuer. The effect of physical training upon the mechanical and metabolic performance of the rat heart. J. Clin. Inves. 49:1859-1868 (197Ø)

11. D. R. Lamb, J. B. Peter, R. N. Jeffress, and H. A. Wallace. Glycogen, hexokinase, and glycogen synthetase adaptations to exercise. Am. J. Physiol. 217:1628-1632 (1969).

12. J. Scheuer, L. Kapner, C. A. Stringfellow, C. L. Armstrong, and S. Penpargkul. Glycogen, lipid, and high energy phosphate stores in hearts from conditioned rats. J. Lab. Clin. Med. 75:924-929 (197Ø).

13. S. O. Fröberg. Effects of training and of acute exercise in trained rats. Metabolism 2Ø:1Ø44-1Ø51 (197Ø).

14. J. W. York, D. G. Penney, and L. B. Oscai. Effects of physical training on several glycolytic enzymes in rat heart. Biochim. Biophys. Acta 381:22-27 (1975).

15. P. D. Gollnick, P. J. Struck, and T. P. Bogyo. Lactic dehydrogenase activities of rat heart and skeletal muscle after exercise and training. J. Appl. Physiol. 22:623-627 (1967).

16. L. B. Oscai and J. O. Holloszy. Biochemical adaptations in muscle. II. Response of mitochondrial adenosine triphosphatase, creatine phosphokinase, and adenylate kinase activities in skeletal muscle to exercise. J. Biol. Chem. 246:6968-6972 (1971).

17. E. Jansson and C. Sylvén. Creatine kinase MB and citrate synthase in type I and type II muscle fibres in trained and untrained men. Eur. J. Appl. Physiol. 54:2Ø7-2Ø9 (1985).

18. T. F. Schaible, S. Penpargkul, and J. Scheuer. Cardiac responses to exercise training in male and female rats. J. Appl. Physiol.: Respirat. Environ. Exercise Physiol. 5Ø(1):112-117 (1981).

19. M. M. Bersohn and J. Scheuer. Effects of physical training on end-diastolic volume and myocardial performance of isolated rat hearts. Circ. Res. 4Ø:51Ø-516 (1977).

2Ø. T. F. Schaible and J. Scheuer. Effects of physical training by running or swimming on ventricular performance of rat hearts. J. Appl. Physiol.: Respirat. Environ. Exercise Physiol 46(4):854-86Ø (1979).

21. T. F. Schaible and J. Scheuer. Cardiac function in hypertrophied hearts from chronically exercised female rats. J. Appl. Physiol.: Respirat. Environ. Exercise Physiol. 5Ø(6):114Ø-1145 (1981).

22. J. A. Bittl and J. S. Ingwall. Reaction rates of creatine kinase and ATP synthesis in the isolated rat heart. J. Biol. Chem. 26Ø:3512-3517 (1985).

23. T. F. Schaible and J. Scheuer. Response of the heart to exercise training, in Growth of the heart in health and disease, edited by R. Zap, Raven Press, New York (1984).

24. S. Penpargkul, D. I. Repke, A. M. Katz, and J. Scheuer. Effect of physical training on calcium transport by rat cardiac sarcoplasmic reticulum. Circ. Res. 4Ø:134-138 (1977).

25. A. Malhotra, S. Penpargkul, T. Schaible, and J. Scheuer. Contractile proteins and sarcoplasmic reticulum in physiologic cardiac hypertrophy. Am. J. Physiol 241:H263-H267 (1981).

Table 1.

Effect of Training Protocol on
Body, Heart, and Ventricle Weights

	Control (n = 7)	Trained (n = 7)	Tr/Ctl	p value of difference
Body weight (grams)	278 ± 4.8	254 ± 2.9	.915	< .Ø1
Tibia length (cm)	3.77 ± .Ø36	3.71 ± .Ø51	.985	.38 (NS)
Heart weight (g)	.858 ± .Ø24	1.Ø9 ± .Ø16	1.27	< .ØØ1
LVW (g)	.649 ± .Ø17	.728 ± .Ø28	1.12	< .Ø5
RVW (g)	.167 ± .ØØ95	.2Ø6 ± .Ø21	1.23	.12 (NS)
HW/BWx1Ø^3	3.Ø9 ± .Ø73	4.3Ø ± .Ø64	1.39	< .ØØ1
HW/TL (g/cm)	.228 ± .ØØ62	.294 ± .ØØ64	1.29	< .ØØ1
LVW/BWx1Ø^3	2.34 ± .Ø56	2.86 ± .Ø94	1.22	< .ØØ1
LVW/HW	.756 ± .ØØ45	.668 ± .Ø29	.884	< .Ø5
LVW/TL (g/cm)	.172 ± .ØØ46	.196 ± .ØØ71	1.14	< .Ø5

Effects of swim-training regimen, as described in text, on body weight, heart weight, ventricular weights, and these quantities normalized, as appropriate, by body weight, heart weight, and tibia length. Data shown are means ± SEM. Tr/Ctl of a quantity denotes the ratio of its value for trained animals to its value for control animals. Also shown are the p-values for the differences between the trained group and the control group. Abbreviations are: body weight (BW), right tibia length (TL), heart weight (HW), left ventricle weight (LVW), and right ventricle weight (RVW).

Table 2.

Functional Parameters for Trained and Control Rats

	Control	Trained
Beating		
	(n = 6)	(n = 7)
Rate-pressure product (mm Hg/minx10^{-3})	23.2 ± 7.3	23.1 ± 6.7
VO_2 (μmol/gdw/min)	28.8 ± 8.7	29.5 ± 12.0
KCL arrested		
	(n = 6)	(n = 6)
VO_2 (μmol/gdw/min)	6.79 ± 1.4	7.90 ± 4.0

Rate-pressure product (RPP; product of developed pressure and heart rate) and oxygen consumption (in units of micromoles of O_2 per gram dry weight per minute) of trained and control hearts both while beating and during KCl arrest (RPP = 0 for KCl arrest). Data shown are means ± SEM. None of the differences shown between the two groups was statistically significant.

Table 3. NMR-derived Quantities for Trained and Control Rats

	Control	Trained	p value of difference
Beating	(n = 6)	(n = 7)	
k_f	.83 ± .Ø2	.98 ± .Ø3	< .Ø1
k_f'	.21 ± .Ø6	.22 ± .Ø5	NS
τ_1 (PCr)	.86 ± .Ø3	.72 ± .Ø3	< .Ø1
τ_1 (P_i)	1.38 ± .54	1.33 ± .44	NS
T_1 (PCr)	2.95 ± .41	2.46 ± .37	NS
T_1 (P_i)	1.95 ± 1.1	1.87 ± .89	NS
[PCr]/[ATP]	13Ø	115	
[P_i]/[ATP]	42	46	
$F_f = k_f$[PCr]	1Ø7 ± 3.Ø	113 ± .35	NS
$F_f' = k_f'$[P_i]	8.9 ± 2.44	9.8 ± 2.3	NS
KCl arrested	(n = 7)	(n = 6)	
k_f	.55 ± .Ø77	.89 ± .14	.Ø51
k_f'	.24 ± .13	.12 ± .Ø56	NS
[PCr]/[ATP]	187	15Ø	
[P_i]/[ATP]	41	36	
$F_f = k_f$[PCr]	1Ø3 ± 14	134 ± 2Ø	NS
$F_f' = k_f'$[ATP]	9.7 ± 5.5	4.2 ± 2.Ø	NS

Kinetic parameters and corresponding phosphorus fluxes for trained and control hearts, while beating and during KCl-arrest, derived from saturation transfer experiments as described in text. For definitions of k_f and k_f', see reaction scheme Eq. 1) in text. For definitions of τ_1 (PCr) and τ_1 (P_i), see Eqs. 9) and 12) in text. Units are: for k's, the rate constants, 1/seconds; for τ's, the chemical lifetimes, seconds; for T_1's, the spin-lattice relaxation times, seconds; for F's, the fluxes, magnetization units (with respect to Γ-ATP = 1ØØ) per second.

Data shown are means $\pm$ SEM. Also indicated is the statistical significance of the difference between the two groups for each quantity. Concentrations of phosphocreatine (PCr), ATP, and inorganic phosphate (P_i) were determined by integration of the corresponding spectral resonances. The rate constant through the creatine kinase (CK) reaction in the direction of ATP synthesis was significantly greater in the trained rats during normal beating, and almost significantly greater during KCl arrest. However, in both cases, the ratio of phosphocreatine to ATP ([PCr]/[ATP]) was greater in the controls, so that the forward phosphorus flux, F_f, through the CK reaction was the same in the two groups. The significantly greater τ_1(PCr) of the control hearts over the trained hearts during beating is a result of their significantly smaller k_f and the similar values of T_1(PCr) between the two groups.

Table 4. Summary of Enzymology
Female Wistars
Control Group (n = 7) vs Trained Group (n = 7)

	1 Mean (Ctl)	2 SEM (Ctl)	3	4 Mean (Tr)	5 SEM (Tr)	6 p Value
1			LV			
2 mIUCK/mgWW	1228.143	24.661		1198.571	27.329	
3 IUCK/mgP	7.206	0.259		7.306	0.201	
4 mIULDH/mgWW	512.000	32.572		566.857	59.992	
5 IULDH/mgP	2.963	0.084		3.431	0.321	
6 LDH H/L	0.143	0.013		0.134	0.012	
7 mIUCS/mgWW	166.714	3.490		153.857	5.734	
8 IUCS/mgP	0.978	0.040		0.937	0.032	
9 mgP/mgWW	0.172	0.008		0.165	0.005	
10 nMCr/mgWW	12.671	0.429		12.049	0.784	
11 nMcr/mgP	74.343	3.530		73.100	3.944	
12 %BB	0.614	0.188		0.786	0.351	
13 %MB	9.486	1.251		10.257	1.026	
14 %MM	63.614	1.386		59.914	1.546	0.100
15 %mito	26.286	1.192		29.029	2.083	
16 IUBB/mgP	0.043	0.013		0.057	0.026	
17 IUMB/mgP	0.692	0.108		0.751	0.082	
18 IUMM/mgP	4.576	0.160		4.387	0.206	
19 IUmito/mgP	1.894	0.104		2.106	0.126	
20 mito/CS	1.941	0.094		2.246	0.099	↓.046
21						
22						
23			RV			
24 mIUCK/mgWW	1206.286	55.092		1049.429	37.292	↓.036
25 IUCK/mgP	6.394	0.216		6.384	0.231	
26 mIULDH/mgWW	509.286	30.096		537.143	34.872	
27 IULDH/mgP	2.704	0.146		3.269	0.220	0.054
28 LDH H/L	0.173	0.005		0.173	0.002	
29 mIUCS/mgWW	160.143	6.490		141.571	5.205	↓.045
30 IUCS/mgP	0.850	0.027		0.870	0.034	
31 mgP/mgWW	0.189	0.007		0.165	0.005	↓.011
32 nMCr/mgWW	10.409	0.754		10.651	0.976	
33 nMcr/mgP	55.414	4.095		64.843	6.201	
34 %BB	1.000	0.239		0.871	0.271	
35 %MB	6.314	0.606		9.071	0.801	↓.018
36 %MM	64.386	0.887		62.886	1.997	
37 %mito	28.300	0.895		27.171	1.898	
38 IUBB/mgP	0.065	0.015		0.055	0.016	
39 IUMB/mgP	0.402	0.039		0.580	0.055	↓.022
40 IUMM/mgP	4.116	0.144		4.021	0.212	
41 IUmito/mgP	1.811	0.094		1.726	0.117	
42 mito/CS	2.135	0.098		1.976	0.089	
43						
44						
45			Atria			
46 mIUCK/mgWW	809.143	70.245		691.143	85.589	
47 IUCK/mgP	5.317	0.378		5.071	0.544	
48 mIULDH/mgWW	409.429	38.272		364.000	43.209	
49 IULDH/mgP	2.690	0.218		2.667	0.258	
50 LDH H/L	0.249	0.006		0.239	0.008	

Summary of Enzymology
Female Wistars
Control Group (n = 7) vs Trained Group (n = 7)

	1 Mean (Ctl)	2 SEM (Ctl)	3	4 Mean (Tr)	5 SEM (Tr)	6 p Value
51 mIUCS/mgWW	78.143	2.025		73.950	5.068	
52 IUCS/mgP	0.521	0.025		0.549	0.020	
53 mgP/mgWW	0.151	0.006		0.135	0.006	0.070
54 nMCr/mgWW	6.521	0.831		5.880	1.068	
55 nMcr/mgP	42.786	4.749		43.686	8.258	
56 %BB	9.614	1.111		11.214	2.295	
57 %MB	28.957	2.561		31.171	2.789	
58 %MM	59.100	3.505		55.929	3.440	
59 %mito	2.343	0.722		2.043	0.647	
60 IUBB/mgP	0.525	0.087		0.541	0.106	
61 IUMB/mgP	1.585	0.231		1.655	0.284	
62 IUMM/mgP	3.091	0.204		2.827	0.329	
63 IUmito/mgP	0.115	0.025		0.090	0.023	
64 mito/CS	0.222	0.050		0.185	0.040	
65						
66						
67			Gastroc			
68 mIUCK/mgWW	8170.714	370.241		8153.000	516.039	
69 IUCK/mgP	51.186	3.524		48.343	3.371	
70 mIULDH/mgWW	811.429	38.189		793.714	42.123	
71 IULDH/mgP	5.064	0.308		4.699	0.268	
72 LDH H/L	0.520	0.015		0.505	0.013	
73 mIUCS/mgWW	14.607	1.211		17.303	3.427	
74 IUCS/mgP	0.094	0.013		0.101	0.017	
75 mgP/mgWW	0.165	0.016		0.170	0.038	
76 nMCr/mgWW	37.386	1.851		37.157	1.810	
77 nMcr/mgP	233.286	14.530		213.143	11.444	
78 %BB	0.000	0.000		0.029	0.029	$
79 %MB	0.000	0.000		0.000	0.000	
80 %MM	100.000	0.000		99.971	0.029	$
81 %mito	0.000	0.000		0.000	0.000	
82 IUBB/mgP	0.000	0.000		0.016	0.016	$
83 IUMB/mgP	0.000	0.000		0.000	0.000	
84 IUMM/mgP	51.186	3.524		48.314	3.361	
85 IUmito/mgP	0.000	0.000		0.000	0.000	
86 mito/CS	0.000	0.000		0.000	0.000	
87						
88						
89			Soleus			
90 mIUCK/mgWW	2753.714	96.263		2714.143	153.477	
91 IUCK/mgP	17.186	1.144		17.229	1.543	
92 mIULDH/mgWW	322.143	10.707		325.571	12.851	
93 IULDH/mgP	2.089	0.129		2.049	0.126	
94 LDH H/L	0.155	0.005		0.183	0.005	$$.002
95 mIUCS/mgWW	35.214	2.247		36.471	1.874	
96 IUCS/mgP	0.219	0.015		0.229	0.017	
97 mgP/mgWW	0.164	0.011		0.161	0.009	
98 nMCr/mgWW	26.143	0.373		25.843	1.658	
99 nMcr/mgP	163.429	9.759		162.571	12.558	
100 %BB	0.000	0.000		0.057	0.057	$

Summary of Enzymology
Female Wistars
Control Group (n = 7) vs Trained Group (n = 7)

	1 Mean (Ctl)	2 SEM (Ctl)	3	4 Mean (Tr)	5 SEM (Tr)	6 p Value
101 %MB	0.000	0.000		0.000	0.000	
102 %MM	95.314	0.728		95.886	1.276	
103 %mito	4.543	0.751		4.071	1.288	
104 IUBB/mgP	0.000	0.000		0.012	0.012	$
105 IUMB/mgP	0.000	0.000		0.000	0.000	
106 IUMM/mgP	16.386	1.113		16.597	1.600	
107 IUmito/mgP	0.766	0.132		0.615	0.129	
108 mito/CS	3.493	0.508		2.966	0.842	

Effects of training protocol on cardiac and skeletal muscle enzymes and on other selected biochemical parameters. Means and standard errors are shown for the control and trained group, as well as p values when they are less than .1Ø. *p < .Ø5, ** < .Ø1. $ denotes differences due to the development of CK-BB in the skeletal muscles of one of the trained rats. Abbreviations: Ctl, control group; Tr, trained group; LV, left ventricle; RV, right ventricle; Gastroc, gastrocnemius; (m)IU, (milli-) international units; CK, creatine kinase; mg WW, milligrams wet weight of tissue; mgP, milligrams protein of tissue; LDH, lactate dehydrogenase; LDH H/L, ratio of lactate dehydrogenase activity in the presence of high pyruvate concentration to activity in the presence of low pyruvate concentration; CS, citrate synthase; nM, nanomole; Cr, creatine; BB, MB, MM, mito, the four isozymes of CK; mito/CS, the ratio of mito activity to CS activity. BB, MB, MM, and mito are also given as percent of total CK.

Chapter 4

Attenuation of Hypoxic Contracture by Acidiosis in the Perfused Rat Heart

Abstract

As is well-known, acidosis can attenuate or prevent diastolic contracture during hypoxia. To elucidate the biochemical correlates of this protection, the effects of acidosis on myocardial metabolism and mechanical function during hypoxia were studied in isolated perfused rat hearts. High-energy phosphates (adenosine triphosphate and creatine phosphate), inorganic phosphate, and intracellular pH were measured using ^{31}P nuclear magnetic resonance, and the relationship between these myocardial metabolic parameters and mechanical function during prolonged global hypoxia with and without superimposed acidosis was assessed.

In ten hearts (Group I), after 15 minutes of control perfusion with oxygenated buffer at pH 7.4, the heart was perfused first with hypoxic buffer at pH 7.4 for 30 minutes and then reoxygenated for 15 minutes. In nine hearts (Group II), after control perfusion with oxygenated buffer, the heart was perfused with oxygenated acidotic buffer at pH 6.8 for 15 minutes, hypoxic acidotic buffer at this same pH for 30 minutes, and then finally reoxygenated at pH 7.4 for 15 minutes. Hemodynamic and metabolic measurements were obtained every three minutes during these interventions.

With the onset of hypoxia, the developed pressure of the hearts in Group I dropped sharply, as did the developed pressure in Group II with the onset of acidosis. An additional decrease in developed pressure of Group II hearts was observed during hypoxia, but recovery of developed pressure during reoxygenation was much greater in the Group II hearts (125 $\pm$ 10 mm Hg vs 37 $\pm$ 11 mm Hg at the end of 15 minutes of reoxygenation, $p < .01$). Left ventricular end-diastolic pressure was much higher in the Group I hearts than in the Group II hearts after 30 minutes of hypoxia (69 $\pm$ 8 mm Hg vs 35 $\pm$ 5 mm Hg, $p < .01$) and after 15 minutes of reoxygenation (52 $\pm$ 9 mm Hg vs 15 $\pm$ 2 mm Hg, $p < .01$). Intracellular pH decreased slightly during hypoxia in Group I

(from 7.11 ± .Ø1 before hypoxia to 7.Ø3 ± .Ø2 at 3Ø minutes of hypoxia, $p < .Ø5$), while in Group II, the intracellular pH dropped immediately to the buffer pH at the onset of acidotic perfusion and did not further decrease significantly during hypoxia. In both groups, pH returned to control levels by the end of the reoxygenation period. There was a greater decrease in net ATP concentration during hypoxia in the Group I than in the Group II hearts (remaining ATP after 3Ø minutes of hypoxia 31 ± 6 % of control in Group I vs 54 ± 4 % in Group II, $p < .Ø1$), although ATP levels did not recover significantly in either group upon reoxygenation. In both groups, there was a close linear relation between ATP and left ventricular end-diastolic pressure throughout hypoxia, but the relationship was different between the two groups.

These results indicate that 1) progressive loss of ATP occurs during the development of myocardial contracture during hypoxia and 2) the mechanism by which acidosis protects the myocardium from hypoxic contracture may be through preservation of ATP.

Introduction

In isolated papillary muscle and perfused heart preparations, hypoxia induces a marked decrease in diastolic compliance, known as contracture. Both impaired calcium uptake by the sarcoplasmic reticulum (SR), resulting in an excessive intracellular Ca^{++} load, and persistent interaction between contractile proteins, may contribute to this phenomenon.

As both Ca^{++} uptake by the SR and lysis of actin-myosin bonds require energy derived from high-energy phosphates, the decrease in ATP synthesis during hypoxia, and resultant imbalance between energy supply and demand, may be the primary cause of this increased resting tension. Indeed, Nayler[1] has demonstrated in isolated perfused rabbit hearts that this increase is preceded by a decline in myocardial high-energy phosphates. In isolated muscle, Bing[2,3] and Greene and Weisfeldt[4] have shown that acidosis attenuates diastolic contracture during hypoxia, and facilitates recovery of mechanical function following hypoxia. In addition, Nayler[5] measured high-energy phosphate levels in isolated hearts during hypoxia with and without acidosis, finding a relative preservation of ATP with acidosis. Together, these studies indicate that the protective effect of acidosis on diastolic properties may be through preservation of myocardial ATP stores. However, in these studies, true intracellular pH could not be measured, and the difficulty of obtaining frequent measurements of metabolite concentrations prevented investigation of the relationship between the loss of high-energy phosphates and the development of mechanical dysfunction during hypoxia and reoxygenation.

In contrast, in this study we make use of ^{31}P nuclear magnetic resonance spectroscopy, which permits continual measurement of the concentrations of phosphorus-containing metabolites and intracellular pH in the isolated perfused

heart, while simultaneously monitoring cardiac function. This allows us to explicitly define the relationship between the development of mechanical dysfunction and high-energy phosphate depletion during hypoxia, and, specifically, to test the hypothesis that the attenuation of hypoxic contracture by acidotic perfusion occurs with a preservation of ATP stores.

Methods

Perfusion

At the time of experimentation, adult male Sprague-Dawley rats weighing 350-400 grams were anesthetized with an intraperitoneal injection of 40 mg of sodium pentobarbital. Hearts were then rapidly excised with adjacent tissue and immersed in ice cold perfusion buffer. Adjacent tissue was removed, and the aorta was cannulated with a hard plastic tube and perfused[6] as shown in Fig. 1. The perfusion medium consisted of 37° phosphate-free Krebs-Henseleit buffer (118 mM NaCl, 25 mM $NaHCO_3$, 1.75 mM $CaCl_2$, 4.7 mM KCl, 1.2 mM MgSo4, 11 mM Glucose, and 0.5 mM EDTA) gassed with 95% O_2, 5% CO_2 (pH 7.4). The same buffer was gassed with 95% N_2, 5% CO_2 for hypoxic perfusion at pH 7.4, with 70% O_2, 30% CO_2 for oxygenated acidosis at pH 6.8, and with 70% N_2, 30% CO_2 for hypoxic acidosis at pH 6.8. A latex balloon was placed in the left ventricle via the left atrial appendage; the heart rate and a record of the left ventricular pressure of the isovolumic contraction was obtained via a water filled plastic tube running from the balloon to a Gould Stratham P23 ID pressure transducer. The heart was paced at 4.5 beats/second via a pair of salt bridges (0.5% agarose in 1.0 M NaCl) running from a Grass S44 stimulator to platinum electrodes positioned appropriately on the heart. A 20 mm glass sample tube was then placed around the preparation, allowing the heart to be placed in the magnet for NMR measurements, to be described below. Since the short axis of these hearts was less than 15 mm, there was no contact between the heart and the surrounding tube. Coronary perfusion flow was fixed throughout the experiment at a value which produced a control perfusion pressure of 100 mg Hg, and was measured with a ball type flowmeter. Aortic perfusion pressure was measured via a plastic tube running from the windkessel (see Fig. 1) of the perfusion umbilicus to a pressure transducer. Initial left ventricular end-diastolic

pressure (LVEDP) was set to 1Ø mm Hg in each heart by adjusting the volume of the intraventricular balloon. Left ventricular systolic and diastolic pressures and coronary perfusion pressure were measured every three minutes, to correspond to the time resolution of the NMR measurements. If the initial left ventricular peak systolic pressure of a heart was less than 1ØØ mm Hg, or if it showed hemodynamic instability during control oxygenation, the experiment was discontinued and the heart was not included in the study.

NMR measurements

The perfused heart in its sample tube was inserted into the bore of an 89 mm Oxford Instruments 36Ø superconducting magnet (field strength, 8.46 Tesla) interfaced with a Nicolet 128Ø spectrometer. Phosphorus spectra at 145.75 MHz were obtained using 2K data points and a spectral width of 24ØØ Hz, and each spectrum was the average of 76 free-induction decays with an observation pulse flip angle of 6Ø° and an interpulse delay of 2.15 seconds (total acquisition time per spectrum of three minutes).

Experimental protocol

After placement in the magnet, each heart was monitored until systolic and diastolic pressures were stable (less than 15 minutes), after which control measurements were made. For control hearts (Group I; n = 1Ø), a 15 minute control period was followed by 3Ø minutes of perfusion with hypoxic buffer, and subsequent reoxygenation for 15 minutes, at pH 7.4. For the hypoxia with acidosis protocol (Group II; n = 9), a six minute control period was followed by perfusion with oxygenated acidotic buffer for 15 minutes and hypoxic acidotic buffer for 3Ø minutes, and then reoxygenation at pH 7.4 for 15 minutes. Thus, all hearts were exposed to 3Ø minutes of global hypoxia and reoxygenated for 15 minutes, with Group II hearts differing from Group I hearts in that the former were pretreated with acidotic buffer for 15

minutes before hypoxia was imposed, and the hypoxic buffer itself was acidotic.

Data analysis

^{31}P spectra were obtained from the averaged free-induction decays by Fourier transformation, with a line broadening of 2Ø Hz applied. The relative amounts of ATP, creatine phosphate (CrP), and inorganic phosphate (P_i) were measured by integration of their spectral resonances, using Nicolet software. The ATP measurements were made using the β-ATP resonance, to avoid the possible confounding effects of NADP (at the α resonance) or ADP (at the α and Γ resonances). We were thus able to obtain measurements of relative amounts of ATP, CrP, and P_i every three minutes. In addition, intracellular pH was determined for each spectrum by comparison of the chemical shift between P_i and CrP with a standard curve obtained under comparable <u>in vitro</u> conditions.

Statistical comparisons between Group I and Group II were made using Student's t-test, with statistical significance defined as $p < .Ø5$, and regression equations were determined by linear least squares. All data are expressed as mean ± SEM.

Results

Hemodynamic data

Hemodynamic data is summarized in Figs. 2 to 4. During the initial period of control oxygenation, there were no differences between Groups I and II in left ventricular systolic pressure (LVSP), left ventricular end-diastolic pressure (LVEDP), left ventricular developed pressure (LVDP), coronary perfusion pressure, or perfusion flow rate.

In Group I, LVSP (Fig. 2) fell promptly with hypoxia, from 143 ± 6 mm Hg to a minimum of 65 ± 3 mm Hg after six minutes of hypoxia ($p < .01$), and then increased somewhat, to 83 ± 5 mm Hg, as the hypoxic period progressed. No significant recovery occurred with reoxygenation. LVDP (Fig. 3) decreased from 131 ± 6 mm Hg to 14 ± 5 mm Hg ($p < .01$) during hypoxia, and recovered somewhat, to 37 ± 11 ($p < .01$), during reoxygenation. LVEDP (Fig. 4) rose gradually from the initial control value of 10 mm Hg to 69 ± 8 mm Hg ($p < .01$) at the end of the hypoxic period, and recovered only slightly, declining to 52 ± 9 mm Hg, during reoxygenation. Coronary perfusion pressure fell from the control value of 100 ± 3 mm Hg to a minimum of 82 ± 2 mm Hg ($p < .01$) at 3 minutes of hypoxia, and then gradually increased throughout hypoxia and reoxygenation to 127 ± 11 mm Hg after 15 minutes of reoxygenation.

In group II hearts, LVSP (Fig. 2) fell from a control value of 142 ± 8 mm Hg to 58 ± 2 mm Hg ($p < .01$) during 15 minutes of perfusion with oxygenated acidotic buffer; at the same time, LVDP (Fig. 3) fell from 132 ± 8 mm Hg to 49 ± 2 mm Hg ($p < .01$), while LVEDP (Fig. 4) was essentially unchanged. With the onset of hypoxia, LVDP declined from its immediately prehypoxic acidotic value of 49 ± 2 mm Hg at the end of 15 minutes of oxygenated acidotic perfusion, to 18 ± 1 mm Hg at the end of hypoxia ($p < .01$). This was not significantly different from the value at the end of hypoxia for Group I hearts. At the same time, LVEDP began to rise, increasing

from 9 ± 1 mm Hg when hypoxia was induced to 35 ± 5 mm Hg at the end of the hypoxic period ($p < .01$); this was significantly lower than the LVEDP of Group I hearts at the end of hypoxia ($p < .01$). Upon reoxygenation, LVDP and LVEDP both recovered strikingly, LVDP recovering almost completely to 125 ± 10 mm Hg, and LVEDP falling to 15 ± 2 mm Hg ($p < .01$ vs 30 minutes of hypoxia for both LVDP and LVEDP), at the end of reoxygenation. This value for LVDP at the end of reoxygenation was significantly higher ($p < .01$), and for LVEDP was significantly lower ($p < .01$), than the corresponding values for Group I hearts. Coronary perfusion pressure decreased from 102 ± 2 mm Hg to 79 ± 4 mm Hg ($p < .05$) during oxygenated acidosis, and then increased during hypoxia to 105 ± 4 mm Hg ($p < .05$ compared to 15 minutes of oxygenated acidosis).

Metabolic data

Metabolic data is summarized in Figs. 5 to 8. Initial ATP concentration was set equal to 100 in each heart. During the initial period of control oxygenation, there were no changes in either group, and no differences between Groups I and II, in [CrP], [P_i], or pH.

In Group I, [ATP] decreased to 31 ± 6 % of control levels ($p < .01$) after 30 minutes of hypoxia, and was not significantly repleted after 15 minutes of reoxygenation, rising to only 36 + 4 %. In Group II, [ATP] did not change significantly during perfusion with oxygenated acidotic buffer, rising from 100 % to 107 ± 6 %. After 30 minutes of hypoxia with acidosis, 54 ± 4 % of the initial ATP concentration remained, which was significantly greater than the amount remaining in Group I ($p < .01$). Again, significant ATP repletion was not observed upon reoxygenation, with a final ATP concentration of 60 ± 3 % after 15 minutes.

The ratio of [CrP] to [ATP] was normal in both groups, and not significantly different between them (1.23 ± .17 in

Group I, 1.29 ± .17 in Group II). In Group I, [CrP] decreased to 24 ± 4 % of its initial value by the end of hypoxia, and recovered to 72 ± 9 % by the end of reoxygenation. In Group II, [CrP] fell to 49 ± 5 % of its initial value with oxygenated acidosis ($p < .01$ vs normoxia and normal pH), and further decreased to 20 ± 3 % during hypoxia. After 15 minutes of reoxygenation, CrP levels recovered to a concentration of 86 ± 6 % of control, not significantly different from Group I.

In group II, [P_i] did not change with perfusion by oxygenated acidotic buffer. In both groups, [P_i] increased during hypoxia as [ATP] and [CrP] were depleted, but was significantly higher in Group I after 30 minutes of hypoxia (ratio of [P_i] to [ATP] 201 ± 27 % in Group I, 125 ± 10 % in Group II, $p < .01$). There was no difference between the two groups after 15 minutes of reoxygenation.

Initial intracellular pH was 7.11 ± .01 in Group I, and declined slightly to 7.03 ± .02 after 30 minutes of hypoxia ($p < .05$); the pH did not recover from this value after 15 minutes of reoxygenation. In group II, pH fell promptly from 7.08 ± .02 to 6.82 ± .03 ($p < .01$) after three minutes of perfusion with oxygenated acidotic buffer, and further declined slightly, to 6.76 ± .02, after 30 minutes of hypoxia with acidosis ($p < .05$ vs end of oxygenated acidosis). After 15 minutes of reoxygenation, the pH returned to 7.07 ± .03.

Relationship between metabolism and function

Fig. 9 shows the relationship between [ATP] and LVEDP during hypoxia. There was a close linear inverse relationship between these parameters in both groups: for Group I, LVEDP = .93[ATP] + 92.4, $r^2 = -0.95$; for Group II, LVEDP = .65[ATP] + 72.7, $r^2 = -0.95$; the slopes of these two relationships were significantly different ($p < .01$). The points representing reoxygenation in Group II (the closed triangles in Fig. 9) were the only ones which did not fall on the regression lines established by the hypoxic data; in

effect, the LVEDP was lower during this period than would have been predicted by ATP levels. There was no clear functional relationship between LVEDP and [PCr] (Fig. 1Ø), although these quantities generally varied monotonically with respect to each other. An exception to this monotonic variation was observed during reoxygenation of Group I hearts, in which a greater impairment of diastolic function was observed, given the measured levels of CrP, than would be predicted from the rest of the data.

Discussion

In the normal myocardium with an adequate energy supply, the binding capacity for Ca^{++} by subcellular organelles, i.e., the sarcoplasmic reticulum (SR) and mitochondria, is sufficient to prevent intracellular Ca^{++} overloading and contracture[7]. However, since Ca^{++} uptake by the SR is energy dependent, a decrease in [ATP] production during hypoxia will diminish this Ca^{++} accumulating capability. Nevertheless, the activity of the SR to sequester Ca^{++} will continue despite limited energy production, further consuming ATP, and completing a vicious cycle of increased demand and reduced supply of ATP. The net result of this imbalance may therefore be an increase in cytosolic Ca^{++} and incomplete relaxation, due to formation of persistent crossbridges between actin and myosin, or increased crossbridge cycling, during diastole.

Another mechanism which may be expected to contribute to the Ca^{++} overload of the hypoxic cell and which is related to energy depletion is dysfunction of the sarcolemmal Na^{+}-K^{+} ATPase due to substrate limitation, as a result of which intracellular sodium would tend to increase. Following this, increased Ca^{++} influx through the Na^{+}-Ca^{++} exchange may occur, contributing to the development of hypoxic contracture. Although few studies have been done to directly examine this hypothesis, preliminary results from our laboratory, utilizing Na^{+} NMR spectroscopy, are entirely consistent with it.

Consistent with these ideas, Nayler and Williams[1] demonstrated that ATP and CrP concentrations declined prior to the increase in resting tension during hypoxia in perfused rabbit hearts, and that tissue Ca^{++} accumulation followed both events. From this, they inferred that the Ca^{++} sequestering ability of the SR is impaired due to substrate depletion during hypoxia.

An increased level of cytoplasmic Ca^{++} will result not

only in increased resting tension, but also in the activation of various phospholipases and Ca^{++} sensitive ATPases. In turn, this may precipitate a loss of membrane integrity and increased utilization of the limited ATP still present.

A primary increase in cytosolic Ca^{++} may also be the cause of diastolic contracture; contributions to increased cytosolic Ca^{++} could be augmented Ca^{++} influx from the extracellular space, or Ca^{++} release from subcellular organelles. An example of this may be the normoxic contracture which is induced by ouabain[1,8] in the perfused rabbit heart, which occurs before any decrease in high-energy phosphates[1]. The biochemical mechanism of ouabain and other cardiac glycosides, inhibition of the Na^{+}-K^{+} ATPase resulting in increased Ca^{++} influx through the Na^{+}-Ca^{++} exchange, is consistent with this contracture being caused by a primary increase in Ca^{++} rather than by depletion of ATP. A similar mechanism could also contribute to the contracture seen with hypoxia, since, as discussed above, Ca^{++} influx through the Na^{+}-Ca^{++} exchange may be increased as a result of Na^{+}-K^{+} pump dysfunction in that setting as well. However, the observation that the increase in resting tension precedes a gain in net tissue Ca^{++}[1] may exclude these mechanisms as significant contributors to hypoxic contracture. On the other hand, this does not exclude a possible role for redistribution of intracellular Ca^{++}, without a change in total Ca^{++}, such as could be caused by release of Ca^{++} from the mitochondria. However, the intracellular calcium transient measured with aequorin does not change during hypoxia[9]. In addition, contracture may not occur even in the presence of increased cytosolic Ca^{++}, provided that sufficient ATP is present to serve as substrate for Ca^{++} sequestration by the SR.

In the present study, the close correlation between [ATP] and diastolic pressure favors the hypothesis that it is ATP depletion, rather than increased cytosolic Ca^{++}, which is the initiating cause of hypoxic contracture. Hearse et al.[10]

investigated the relationship between ATP and contracture during ischemia, and, from the observation that contracture appeared to be initiated when ATP content decreased to a certain level, concluded also that ATP depletion is the primary mechanism for ischemic contracture.

Mechanisms which are not directly related to intracellular Ca^{++} may also affect diastolic properties of the heart. In particular, there is a substantial hydraulic turgor effect of coronary vasculature perfusion on diastolic compliance[11]. Thus, changes in coronary vascular resistance during hypoxia could in principle affect the diastolic compliance of the left ventricle. However, since coronary flow was held constant in our experiments, and coronary perfusion pressure was similar between Groups I and II throughout hypoxia, we expect the turgor effect to be comparable in the two groups, and turgor therefore to be a minimal contributor to the differences we observed in LVEDP. The slow development of cellular edema during hypoxia may also stiffen the ventricle, and, although we did not measure the extent of tissue edema in our experiments, it may have occurred to a greater extent in Group I than in Group II hearts. However, the contracture observed in early hypoxia is unlikely to have a substantial component due to edema.

The effects of acidosis on cardiac function have also been extensively investigated in the literature. The negative inotropic effect of acidosis has been observed by many investigators[12,13,14], and several mechanisms have been proposed to account for it. Williamson et al.[15] showed that hydrogen ions can prevent Ca^{++} influx through the sarcolemma, so that Ca^{++} influx into the cell may be directly decreased during extracellular acidosis. It has also been shown[16] that acidosis inhibits the Na^{+}-Ca^{++} exchange mechanism in sarcolemmal vesicle preparations, so that acidosis could affect myocardial systolic function by decreasing inward Ca^{++} movement across the sarcolemma. However, Allen and Orchard[17] found the intracellular Ca^{++} transient to be unchanged during

acidosis. Protons may also compete with Ca^{++} for binding sites on troponin[18], affecting the relationship between local [Ca^{++}] and force generation by contractile units; recently, Blanchard and Solaro[19] showed directly that acidic pH results in a reduction in the affinity of myofibrillar troponin C for calcium.

Relatively few studies have focused on the effect of acidosis on the diastolic properties of the heart[2,3,4,5]. However, a consistent finding has been that mild acidosis prevents or attenuates diastolic contracture and facilitates recovery of function during reoxygenation. Note that ATP depletion may be an important component of, and perhaps the primary mechanism for, hypoxic contracture. For example, as ATP levels decline, the ability of the sarcoplasmic reticulum to sequester calcium through its ATPase activity may be sufficiently impaired to cause diastolic calcium overload, and hence increased rigor bond formation or cross-bridge cycling during diastole. In view of this, it is likely that decreased contractile requirements and relative preservation of ATP levels secondary to the negative inotropic effect of acidosis is responsible in large part for the relative preservation of diastolic function seen with mild acidosis. Indeed, Nayler et al.[5] found that in isolated rabbit hearts, after 60 minutes of hypoxia, ATP was preserved when the pH of the hypoxic buffer was maintained at 6.9 rather than at 7.4, and that the resting tension was lower after 30 minutes of hypoxia at pH 6.9 than at pH 7.4. In addition, functional recovery during reoxygenation was improved in the acidotic preparations. However, in that study, ATP was measured only once, after 60 minutes of hypoxia, and the relationship between high-energy phosphate concentration and diastolic pressure could not be investigated. Furthermore, intracellular pH was unknown.

Lewis et al.[20] and Greene and Weisfeldt[4] demonstrated that even in resting heart muscle preparations, less contracture developed during hypoxia when acidosis was

superimposed; therefore, the protective effect of acidosis on hypoxic contracture may not be due solely to its negative inotropic, energy-sparing effect. Even at a given [Ca^{++}] and [ATP], competition of hydrogen ions for Ca^{++} sites on troponin, or the decreased Ca^{++}-sensitivity of troponin discussed above, could contribute to the protective effect of acidosis by decreasing contractile bond recycling and the formation of rigor bonds.

In the present study, we showed that intracellular pH decreased to the buffer pH of 6.8 immediately upon perfusion of the heart with acidic buffer, and remained at that pH for the duration of hypoxic perfusion. In addition, throughout hypoxia, the lesser amount of contracture of the Group II hearts was accompanied by a relative preservation of ATP stores. This supports the hypothesis that the mechanism of the attenuation of hypoxic contracture is primarily through suppression of ATP consumption, that is, the negative inotropic effect of acidosis leading to a decrease in the rate of ATP hydrolysis at the myofibrils.

The slope of the regression line relating [ATP] and LVEDP during hypoxia was less steep for Group II hearts than for Group I hearts; this may indicate that acidosis alters the relationship between [ATP] and hypoxic contracture. There is other evidence indicating a direct effect of acidosis on relaxation. Mattiazzi et al.[21] showed that the slope of the regression line relating maximal rate of relaxation and maximal rate of force development was higher with acidosis, indicating a relative increase in the rate of relaxation as compared with contraction. In addition, Nakamaru and Schwartz[22,23] showed that acidosis enhances Ca^{++} uptake by the SR in the presence of ATP, again indicating improved relaxation. However, this direct effect on calcium handling by the SR may be less relevant during hypoxia, during which the supply of ATP is limited.

The more rapid decline we observed in CrP than in ATP at the onset of hypoxia was been reported by previous

investigators[24,25]. The lack of correlation of [CrP] with LVEDP during hypoxia was not unexpected, since previous work has demonstrated that [ATP] and LVEDP are correlated during hypoxia or ischemia, while [CrP] is correlated with systolic function[26,27,28].

One of the surprising findings of the present study is the apparent discrepancy between [ATP] and diastolic function seen during reoxygenation of the Group II hearts (Fig. 9). After 15 minutes of reoxygenation, total ATP was not repleted significantly in either Group I or Group II; this is probably due to the loss of adenosine during hypoxia. However, diastolic function recovered strikingly in Group II during reoxygenation, so that LVEDP in that group was much lower than would have been predicted from the ATP-LVEDP relationship established during hypoxia. This is consistent with a preferential repletion of a small ATP compartment directly responsible for relaxation, leading to improved diastolic function without a significant increase in total tissue ATP. It is possible that this effect was seen only in Group II hearts because, for the reasons discussed above, they suffered a smaller increase in intracellular Ca^{++}. It is well-known that Ca^{++} overload is harmful to cellular function, and may cause irreversible cellular damage or cell death[29]; acidosis may prevent such irreversible damage by preventing an excessive increase in cytosolic calcium.

In summary, the present study shows a close negative linear correlation between myocardial ATP stores and LVEDP during hypoxia in the isovolumic rat heart preparation, possibly indicating that depletion of ATP is responsible for hypoxic contracture in this system. In addition, hypoxic contracture is attenuated by mild acidosis, and this protection may be brought about through lowered ATP utilization during acidosis.

1. W. G. Nayler and A. Williams. Relaxation in heart muscle: some morphological and biochemical considerations, Eur. J. Cardiol. 7(suppl):35-5Ø (1978).

2. O. H. L. Bing, W. W. Brooks, and J. V. Messer. Heart muscle viability following hypoxia: protective effect of acidosis, Science 18Ø:1297-1298 (1973).

3. O. H. L. Bing, C. S. Apstein, W. W. Brooks. Factors influencing tolerance of cardiac muscle to hypoxia, in Recent Advances in Studies on Cardiac Structure and Metabolism, Vol. 1Ø, pp 343-354, University Park Press, Baltimore (1975).

4. H. L. Greene and M. L. Weisfeldt. Determinants of hypoxic and posthypoxic myocardial contracture, Am. J. Physiol. 232(5): H526-H533 (1977).

5. W. G. Nayler, R. Ferrari, P. A. Poole-Wilson, and C. E. Yepez. A protective effect of a mild acidosis on hypoxic heart muscle, J. Mol. Cell. Card. 11:1Ø53-1Ø71 (1979).

6. 6. J. S. Ingwall. Phosphorus Nuclear Magnetic Resonance Spectroscopy of Cardiac and Skeletal Muscles, Am. J. Physiol. 242:H729-H744 (1982).

7. R. J. Solaro and F. N. Briggs. Estimating the functional capabilities of sarcoplasmic reticulum in cardiac muscle: calcium binding, Circ. Res. 34:531-54Ø (1974).

8. W. G. Nayler, C. Yepez, and P. A. Poole-Wilson. The effect of adrenoreceptor and Ca^{++} antagonist drugs on the hypoxia-induced increase in resting tension, Cardiovasc. Res. 12:666-674 (1978)

9. D. G. Allen and C. H. Orchard. Intracellular calcium concentration during hypoxia and metabolic inhibition in mammalian ventricular muscle, J. Physiol. 339:1Ø7-122 (1983).

1Ø. D. J. Hearse, P. B. Garlick, and S. M. Humphrey. Ischemic contracture of the myocardium: mechanism and prevention, Am. J. Cardiol. 39:986-993 (1977).

11. W. M. Vogel, C. S. Apstein, L. L. Briggs, W. H. Gaasch, and J. Ahn. Acute alterations in left ventricular diastolic chamber stiffness: Role of the "erectile" effect of coronary arterial pressure and flow in normal and damaged hearts, Circ. Res. 51:465-478 (1982).

12. J. R. Williamson, B. Safer, T. Rich, S. Schaffer, and K. Kobayashi. Effects of acidosis on myocardial contractility and metabolism, Acta Med. Scand. 587(suppl.):95-111 (1975).

13. C. Steenbergen, G. Deleeuw, T. Rich, and J. R. Williamson. Effects of acidosis and ischemia on contractility and intracellular pH of rat heart, Circ. Res. 41:849-858 (1977).

14. W. E. Jacobus, I. H. Pores, S. K. Lucas, C. H. Kallman, M. L Weisfeldt, and J. T. Flaherty. The role of intracellular pH in the control of normal and ischemic myocardial contractility: a ^{31}P nuclear magnetic resonance and mass spectrometry study, in Intracellular pH: Its Measurement, Regulation, and Utilization in Cellular Functions, pp 537-565, Allan R. Liss, New York (1982).

15. J. R. Williamson, M. L. Woodrow, and A. Scarpa. Calcium binding to cardiac sarcolemma, in Recent Advances in Studies on Cardiac Structure and Metabolism, Vol. 5, pp 61-71, edited by A. Fleckenstein and N. S. Dhalla, University Park Press, Baltimore (1975).

16. K. D. Philipson, M. M. Bersohn, and A. Y. Nishimoto. Effects of pH on Na^+-Ca^{++} exchange in canine cardiac sarcolemmal vesicles, Circ. Res. 50:287-293 (1982).

17. D. G. Allen and C. H. Orchard. The effects of changes of pH on intracellular calcium transients in mammalian cardiac muscle, J. Physiol. 335:555-567 (1983).

18. A. M. Katz and H. H. Hecht. The early "pump" failure of the ischemic heart, Am. J. Med. 47:497-501 (1969).

19. E. M. Blanchard and R. J. Solaro. Inhibition of the activation and troponin calcium binding of dog cardiac myofibrils by acidic pH, Circ. Res. 55:382-391 (1984).

20. M. J. Lewis, A. C. Grey, and A. H. Henderson. Determinants of hypoxic contracture in isolated heart muscle preparations, Cardiovasc. Res. 13:86-94 (1979).

21. A. R. Mattiazzi, H. E. Cingolani, and E. Spacapan de Castuma. Relation between calcium and hydrogen ions in heart muscle, Am. J. Physiol. 237:H497-H503 (1979).

22. Y. Nakamaru and A. Schwartz. Possible control of intracellular calcium metabolism by $[H^+]$: sarcoplasmic reticulum of skeletal and cardiac muscle, Biochem. Biophys. Res. Comm. 41:830-836 (1970).

23. Y. Nakamaru and A. Schwartz. The influence of hydrogen ion concentration on calcium binding and release by skeletal muscle sarcoplasmic reticulum, J. Gen. Physiol. 59:22-32 (1972).

24. N. S. Dhalla, J. C. Yates, D. A. Walz, V. A. McDonald, and R. E. Olsen. Correlation between changes in the endogenous energy stores and myocardial function due to

hypoxia in the isolated perfused rat heart, Can. J. Physiol. Pharmacol. 50:333-345 (1972).

25. W. G. Nayler, P. A. Poole-Wilson, and A. Williams. Hypoxia and calcium, J. Mol. Cell. Card. 11:683-706 (1979).

26. P. E. Pool, J. W. Covell, C. A. Chidsey, and E. Braunwald. Myocardial high energy phosphate stores in acutely induced hypoxic heart failure, Circ. Res. 19:221-229 (1966).

27. S. Gudbjarnason, P. Mathes, and K. G. Ravens. Functional compartmentation of ATP and creatine phosphate in heart muscle. J. Mol. Cell. Card. 1:325-339 (1970).

28. R. G. S. Spencer, S. Momomura, W. Grossman, J. S. Ingwall. The hemodynamic and metabolic response to hypoxia of the normal and hypertrophied rat heart, in preparation.

29. J. Y. Cheung, J. V. Bonventre, C. D. Malis, and A. Leaf. Calcium and ischemic injury, New Eng. J. Med. 314:1670-1676 (1986).

Figure 1. Isovolumic perfusion apparatus used in the present study. Ao = aorta, PA = pulmonary artery, RV = right ventricle, LA = left atrium, LV = left ventricle. 1: to transducer for LV pressure measurement; 2: from perfusion pump; 3: to transducer for perfusion pressure measurement; 4: suction drain for coronary effluent. See text for explanation.

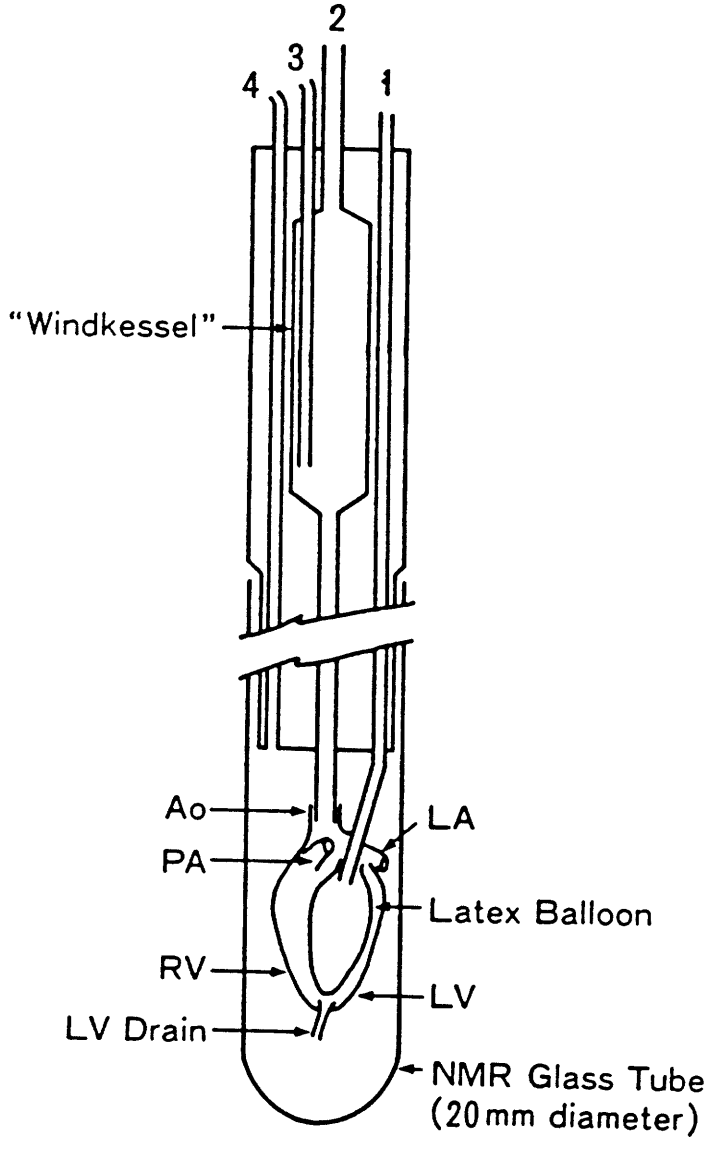
2
3
4
1
"Windkessel"
Ao
LA
PA
Latex Balloon
RV
LV
LV Drain
NMR Glass Tube
(20mm diameter)

Figure 1

Figure 2. Changes in left ventricular peak systolic pressure (LVPSP) in Group I (CONT) and Group II (ACID). Measurements were taken at the midpoint of three minute intervals throughout the experiment, and are plotted on the figure at times corresponding to these midpoints. For Group I, the first five data points reflect control oxygenation measurements, while the sixth is a repetition of the fifth to facilitate direct comparison with Group II. The time from the beginning of control oxygenation for Group I is given in parentheses. For Group II, only the average of the two control measurements is displayed, and is shown as the first point on the ACID curve. Stability in this group was comparable to Group I. The next five data points on the ACID curve represent measurements taken during the 15 minutes of oxygenated acidotic perfusion, with time after onset of oxygenated acidotic perfusion indicated without parentheses. Hypoxia began at the first vertical dashed line, with time after the onset of hypoxia indicated thereafter. Reoxygenation began at the second vertical dashed line, with time after the onset of reoxygenation indicated thereafter.

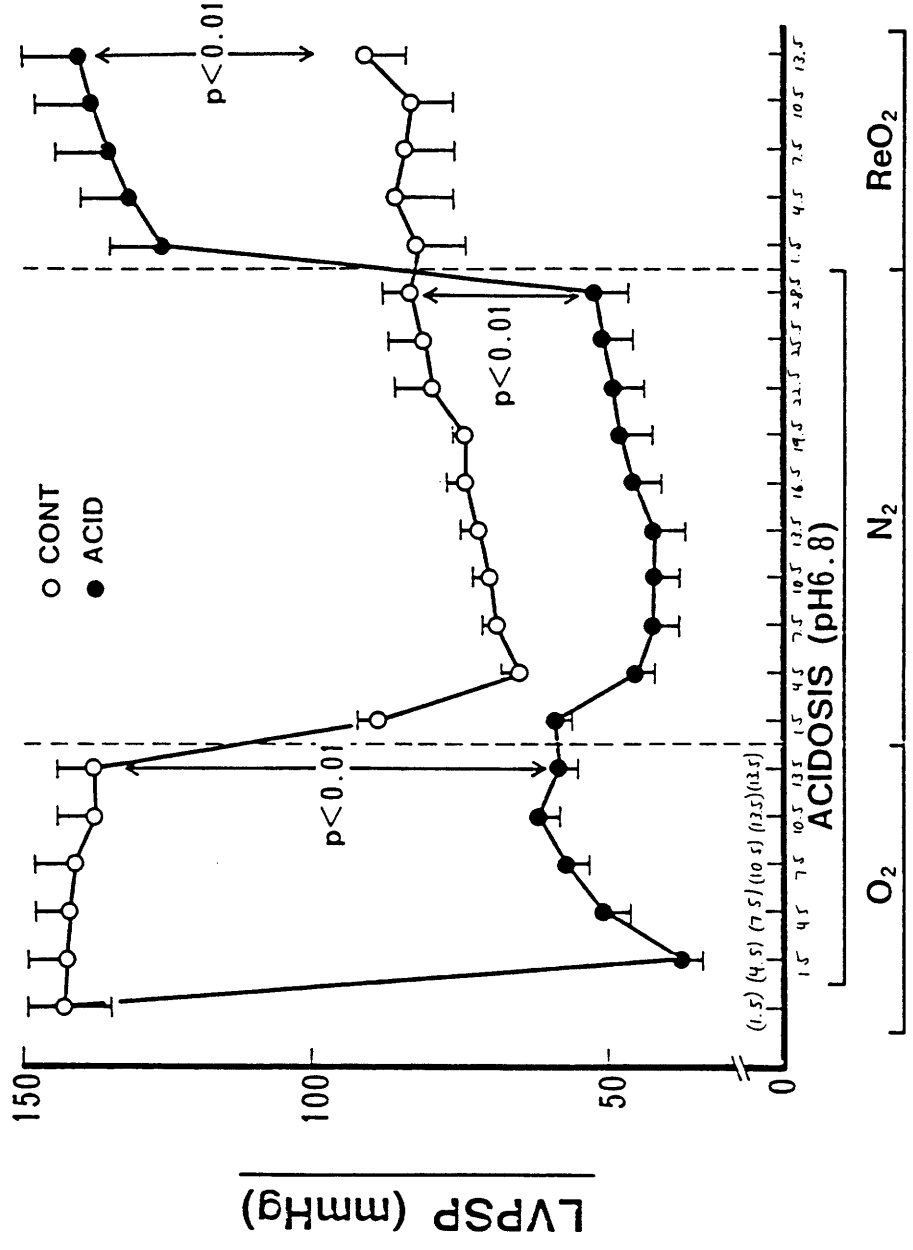
LVPSP (mmHg)
150
100
50
0
○ CONT
● ACID
p<0.01
p<0.01
p<0.01
O2
N2
ReO2
ACIDOSIS (pH6.8)
Time (minutes)

Figure 2

Figure 3. Changes in left ventricular developed pressure (LVDP) in Group I (CONT) and Group II (ACID). Time axis and interventions as described for Fig. 2.

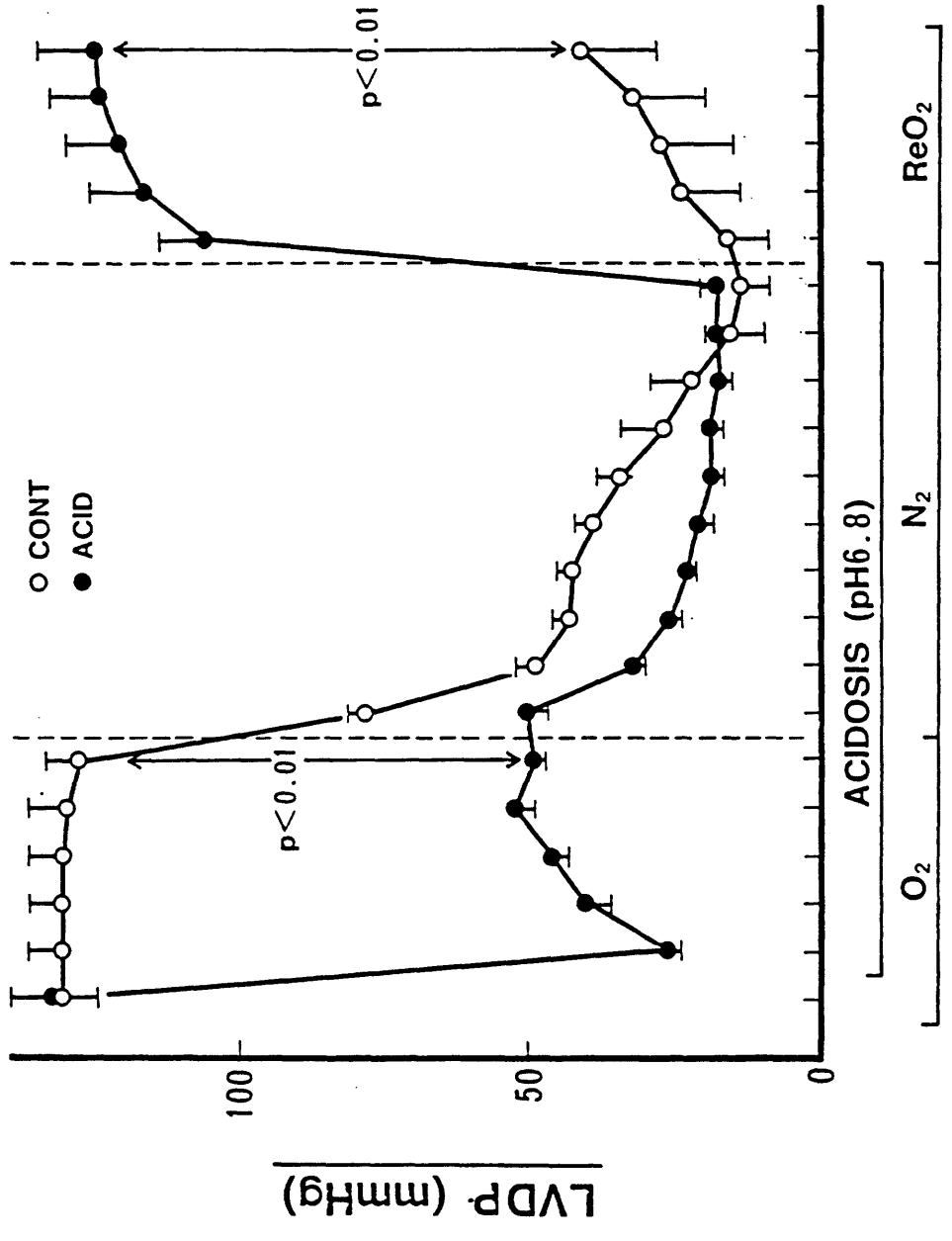
LVDP (mmHg)
100
50
0
O CONT
● ACID
p<0.01
p<0.01
ACIDOSIS (pH6.8)
O2
N2
ReO2
Time (minutes)

Figure 3

Figure 4. Changes in left ventricular end-diastolic pressure in Group I (CONT) and Group II (ACID). Time axis and interventions as described for Fig. 2.

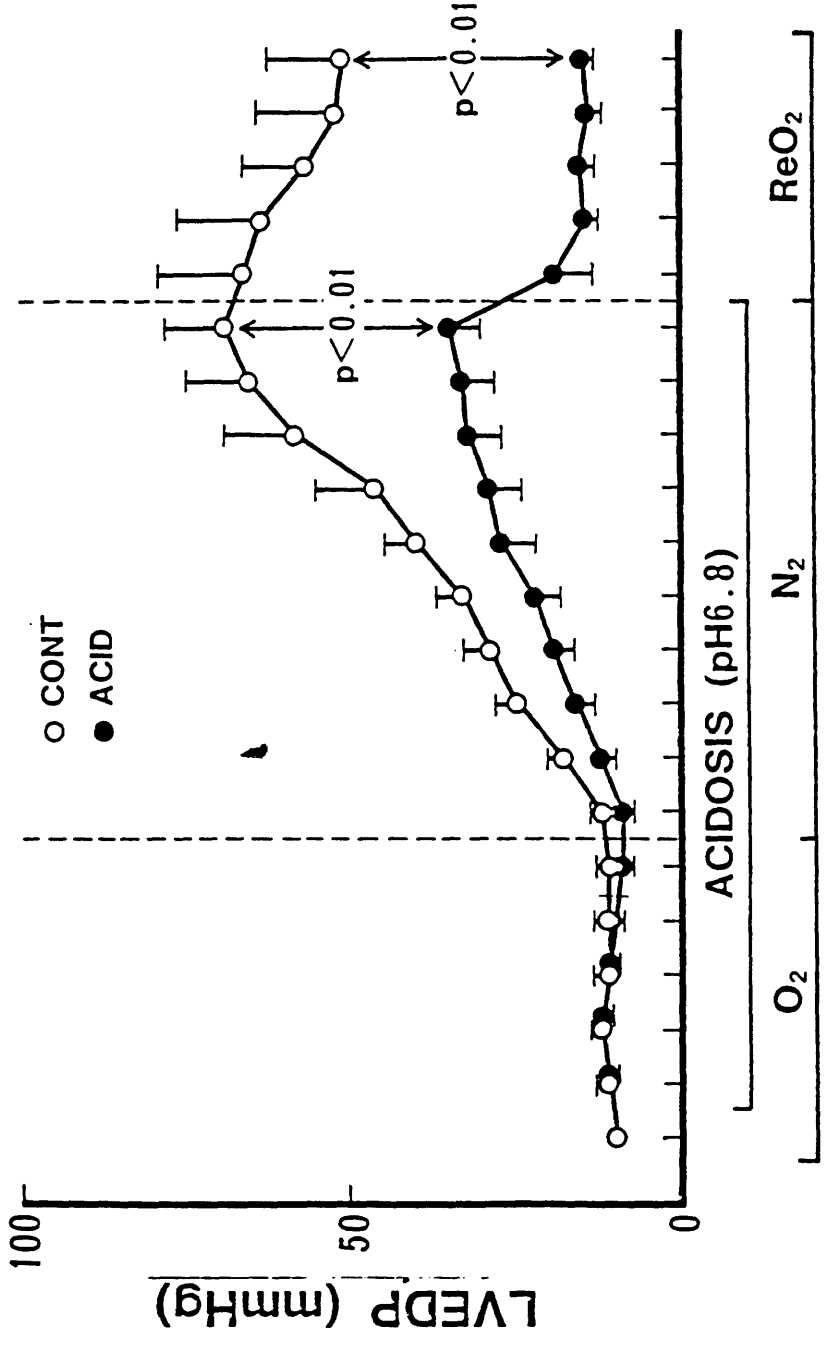
LVEDP (mmHg)
100
50
0
○ CONT
● ACID
p<0.01
p<0.01
ACIDOSIS (pH6.8)
O2
N2
ReO2
Time (minutes)

Figure 4

Figure 5. Total measured concentration of ATP, as percent of control value, in Group I (CONT) and Group II (ACID). Time axis and interventions as described for Fig. 2.

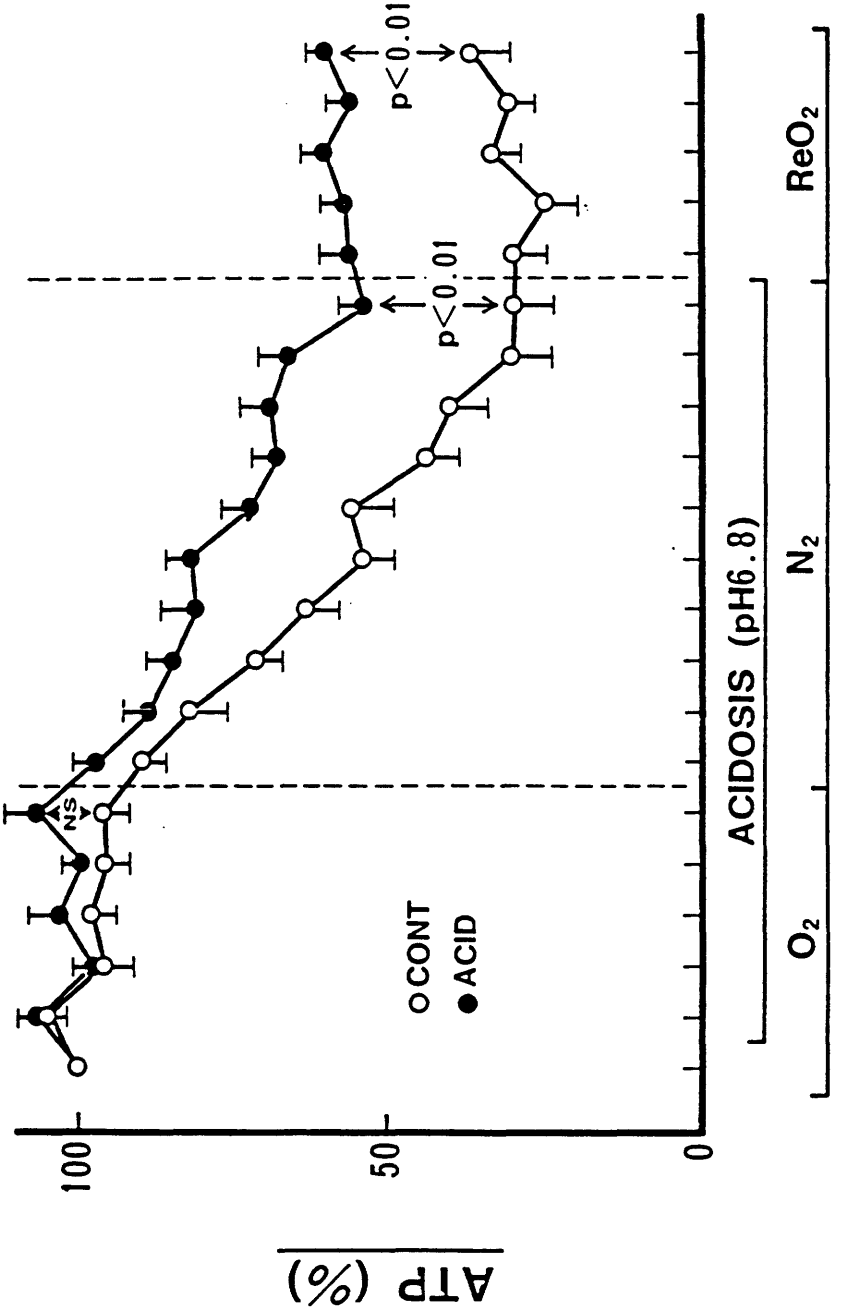
ATP (%)
100
50
0
NS
p<0.01
p<0.01
○CONT
●ACID
O2
N2
ReO2
ACIDOSIS (pH6.8)
Time (minutes)

Figure 5

Figure 6. Total measured concentration of creatine phosphate (CrP), as percent of control concentration of ATP, in Group I (CONT) and Group II (ACID). Time axis and interventions as described for Fig. 2.

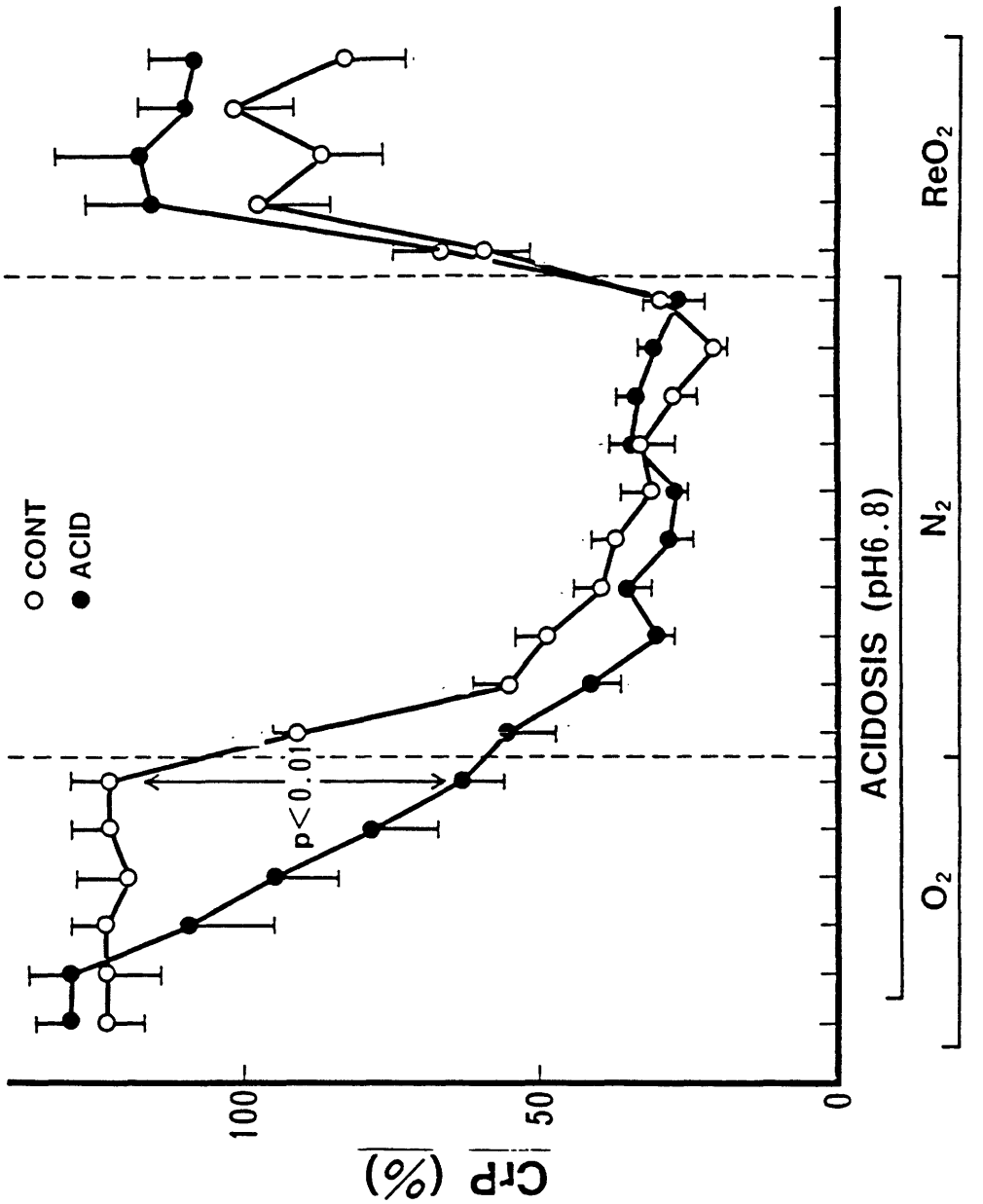
O CONT
● ACID
p<0.01
ACIDOSIS (pH6.8)
O_2
N_2
ReO_2
100
50
0
$\overline{CrP}$ (%)
Time (minutes)

Figure 6

Figure 7. Total measured concentration of inorganic phosphate (P_i), as percent of control concentration of ATP, in Group I (CONT) and Group II (ACID). Time axis and interventions as described for Fig. 2.

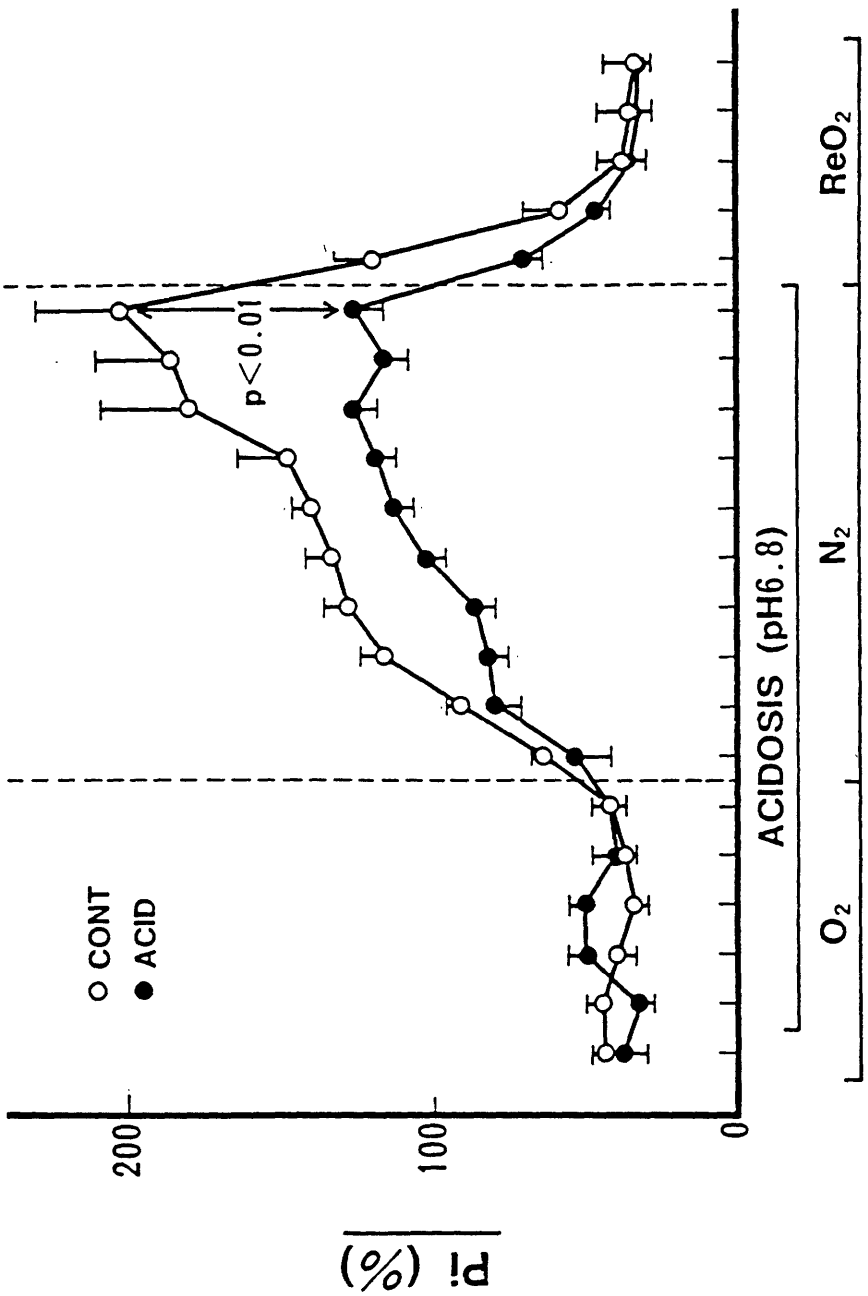
Pi (%)
200
100
0
○ CONT
● ACID
p<0.01
ACIDOSIS (pH6.8)
O2
N2
ReO2
Time (minutes)

Figure 7

Figure 8. Changes in intracellular pH (pH_i) in Group I (CONT) and Group II (ACID). Time axis and interventions as described for Fig. 2.

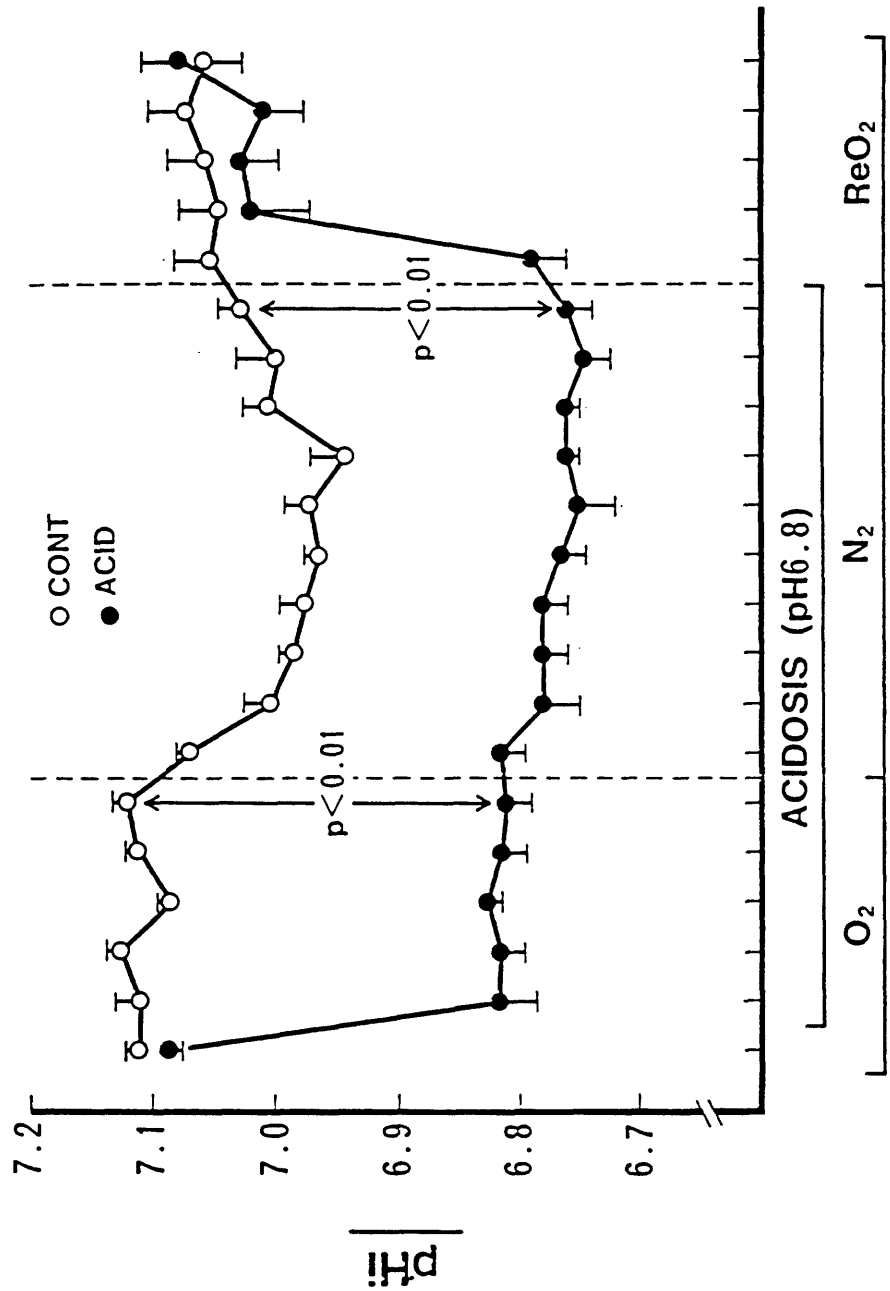
pHi
7.2
7.1
7.0
6.9
6.8
6.7
○ CONT
● ACID
p<0.01
p<0.01
ACIDOSIS (pH6.8)
O2
N2
ReO2
Time (minutes)

Figure 8

Figure 9. Relation between left ventricular end-diastolic pressure (LVEDP) and [ATP] during hypoxia. Solid line indicates the regression line for Group I, while the broken line indicates the regression for Group II.

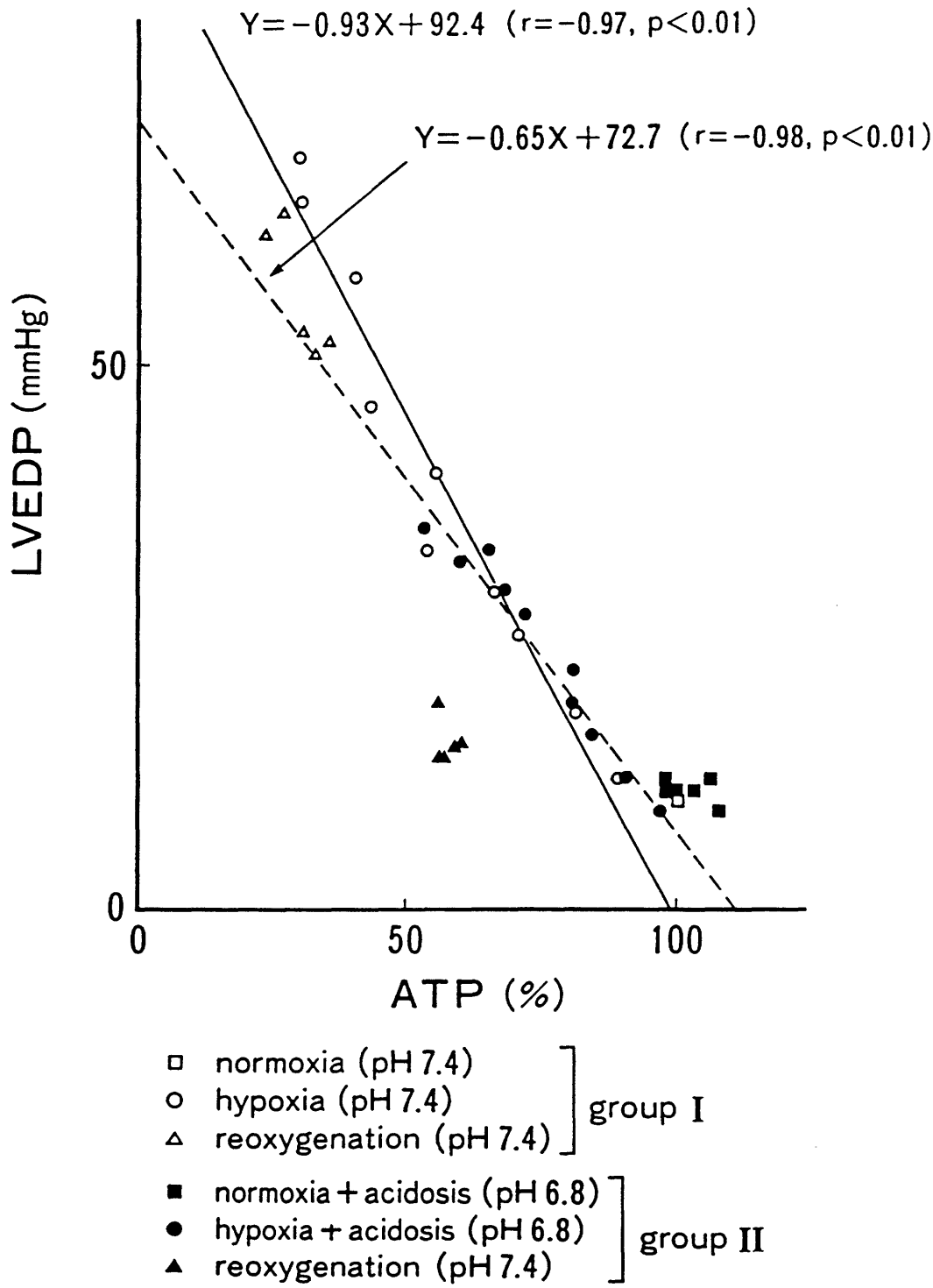
Y=−0.93X+92.4 (r=−0.97, p<0.01)
Y=−0.65X+72.7 (r=−0.98, p<0.01)
LVEDP (mmHg)
50
0
0
50
100
ATP (%)
normoxia (pH 7.4)
hypoxia (pH 7.4)
reoxygenation (pH 7.4)
group I
normoxia + acidosis (pH 6.8)
hypoxia + acidosis (pH 6.8)
reoxygenation (pH 7.4)
group II

Figure 9

Figure 1Ø. Relation between left ventricular end-diastolic pressure (LVEDP) and creatine phosphate (CrP).

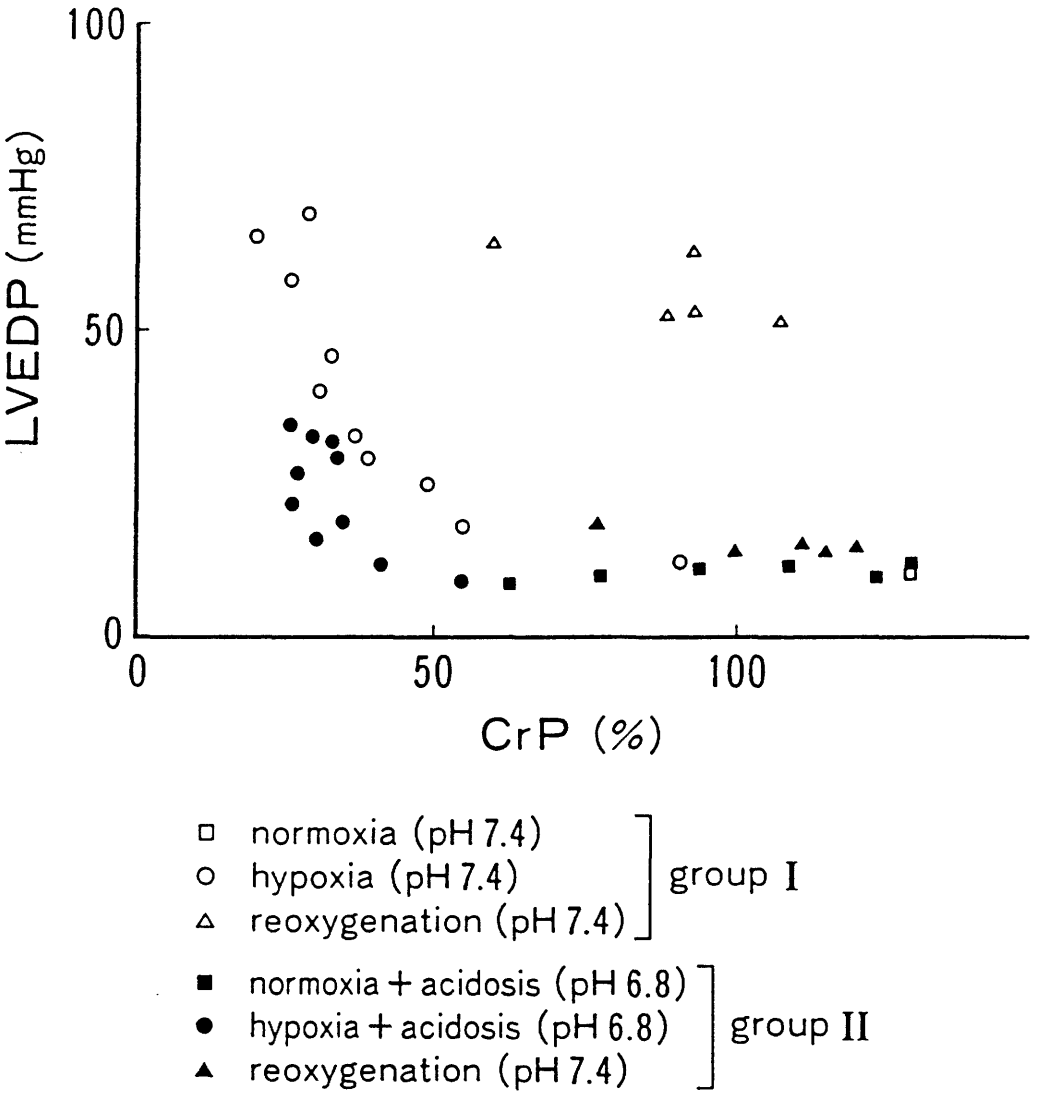
100
50
0
LVEDP (mmHg)
0
50
100
CrP (%)
normoxia (pH 7.4)
hypoxia (pH 7.4)
reoxygenation (pH 7.4)
group I
normoxia + acidosis (pH 6.8)
hypoxia + acidosis (pH 6.8)
reoxygenation (pH 7.4)
group II

Figure 10